How large were the temperature fluctuations in Greenland over the last 70'000 years? New insights from stable isotope ratio measurements on polar ice cores with a novel on-line extraction technique.

Inauguraldissertation

der Philosophisch–naturwissenschaftlichen Fakultät
der Universität Bern

vorgelegt von

Christof Huber

von Krauchthal (BE)

Leiter der Arbeit:
PD Dr. Markus Leuenberger
Prof. Dr. Thomas Stocker

Abteilung für Klima– und Umweltphysik
Physikalisches Institut der Universität Bern

How large were the temperature fluctuations in Greenland over the last 70'000 years? New insights from stable isotope ratio measurements on polar ice cores with a novel on-line extraction technique.

Inauguraldissertation

der Philosophisch–naturwissenschaftlichen Fakultät
der Universität Bern

vorgelegt von

Christof Huber

von Krauchthal (BE)

Leiter der Arbeit:
PD Dr. Markus Leuenberger
Prof. Dr. Thomas Stocker

Abteilung für Klima– und Umweltphysik
Physikalisches Institut der Universität Bern

Von der Philosophisch-naturwissenschaftlichen Fakultät angenommen.

Der Dekan
Prof. Dr. P. Messerli

Bern, den 28. Oktober 2004

Contents

Chapter 1

Introduction and Results Overview

Global change and its impacts on human society has become one of the most important problems concerning our near future. There is now a broad agreement within the scientific community that the observed global temperature change is a result of anthropogenic greenhouse gas emissions from fossil fuel burning. Since the start of the industrialization in the 17th century, atmospheric greenhouse gas concentrations increased rapidly. CO_2 concentration for example, rose from about 280 ppm at 1850 to a value of more than 370 ppm at present. From ice core data we know that in the last 500'000 years CO_2 levels varied between 200 ppm during glacial and 280 ppm during interglacial time periods [42]. Hence the present day CO_2 concentration is the highest level recorded in half a million of years of climate history. 2001 the scientific community reported in the third assessment report of the Intergovernmental Panel on Climate Change IPPC [27] for the first time undoubtable evidence for global climate change. The most important findings: The temperature increase of the last 50 years is human made, and climate model predict a global mean temperature increase of 1.4–5.8°C by the year 2100. Despite this clear evidence political discussion is still the same as years ago. At the international environmental conference of Kyoto 1997 an agreement was made to reduce greenhouse gas emissions mainly of the western industrialized world. Switzerland signed to reduce CO_2 emissions by 8% below the level of 1990 until 2008–2012. But Swiss CO_2 emissions are still increasing, and the parliament still hesitates to take such measures as to increase prices on fossil energy. However, this work not concerns the politics but the physical mechanisms controlling our climate system. This is done by the analysis of historical data obtained from polar ice cores. Particularly the study of rapid climate change events during the last ice age can help to constrain relevant processes.

The earth climate is of a highly complex nature. To reach a better understanding requires the knowledge of the interactions and behavior of the atmosphere, the ocean the marine and terrestrial biosphere, the cryosphere, and the lithosphere. Scientists from different disciplines have to work together in order to better understand how our planets climate behave and what is going to happen to it in our near future. The Climate and Environmental Physics division of the University of Bern is part of the interdisciplinary climate science community. On one hand experimental work is done on climate paleo archives, such as polar and alpine ice cores, firn air, tree rings, and groundwater as well as on recent atmospheric air and hydrological water samples. On the other hand the experimental results are used to calibrate and improve climate models which can be used to predict future climate. The study of

climate history is essential to learn how the system behaves. It is the only way to tackle the relevant processes driving the highly complex climate on our planet.
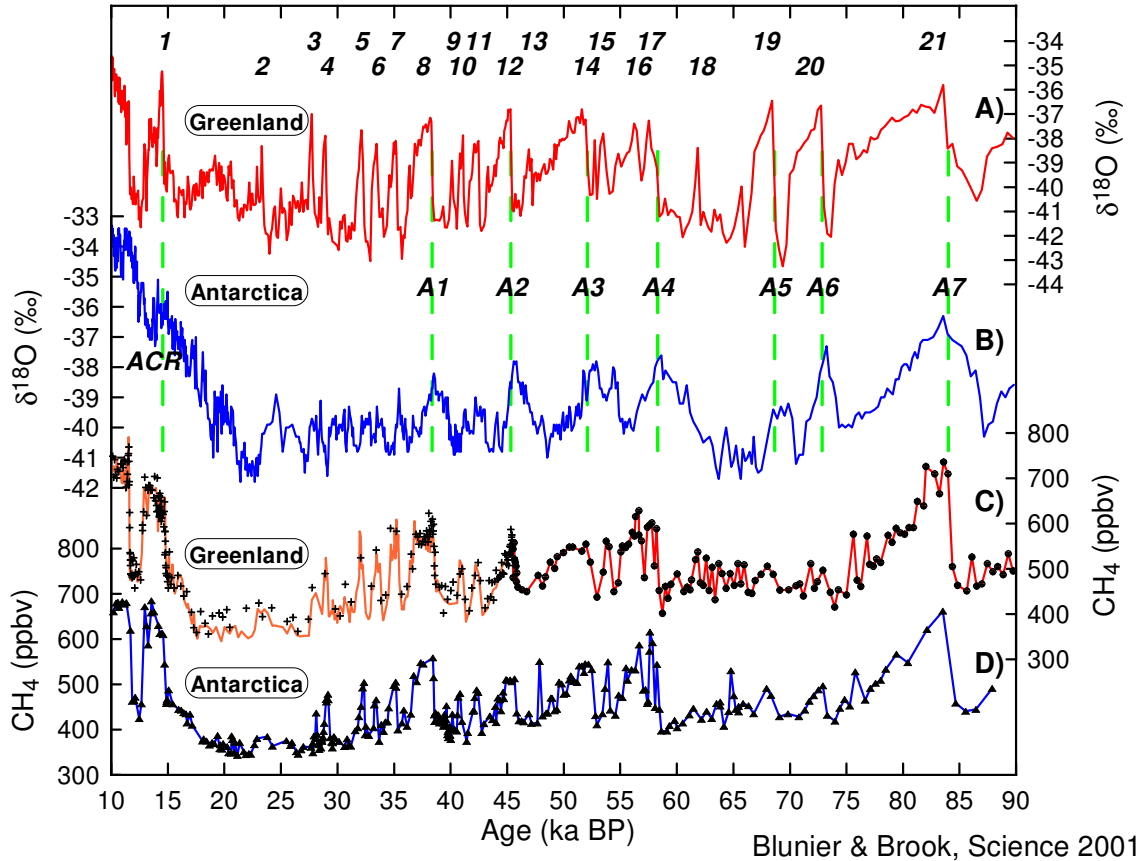

Figure 1.1: Figure taken from Blunier and Brook [8]. Isotopic and CH_4 data from Greenland and Antarctica on the GISP2 timescale. DO events are recorded in the Greenland $\delta^{18}O_{ice}$ record (A). They are labelled with numbers 1–21. Dashed lines indicate the onset of the major DO events, event A1–A4 correspond with H-events. $\delta^{18}O_{ice}$ is a proxy for temperature. The records from GISP2 Greenland (A), and Byrd station Antarctica (B) are compared to CH_4 data from GISP2 and GRIP Greenland (C) and Byrd Antarctica (D). The CH_4 concentration from both hemispheres is closely related to temperature changes in Greenland.

The complexity can be seen for example on the many abrupt temperature shifts during the last ice age (10'000–110'000 years BP) revealed in Greenland ice cores, by measurements of the stable isotope composition of water. 24–25 so called Dansgard/Oeschger (DO) events are recorded in Greenland ice cores. DO events are characterized by an abrupt warming of up to 16°C within only a few decades [34, 31], followed by a more gradual cooling. Antarctic ice cores show much less pronounced temperature variability. Only the biggest DO events have a clear counterpart in the Antarctic ice cores. Antarctic temperature was increasing during the cold phase of the DO event and falling after Greenland warming started. This contradictional behavior of the two hemispheres has been called the seesaw effect [51]. It probably has its origin in ocean circulation. The big DO events are preceded by massive ice surges from the northern hemispheric ice sheets, so called Heinrich (H) events. H events are documented by ice rafted debris deposition in North Atlantic sediments. The huge

amount of fresh water released with the ice caused a reduction or even a collapse of the North Atlantic deep water formation (NADW) that could reduce or stop the northward transportation of warm tropical waters by the Thermohaline Circulation (THC) [30]. Synchronization of Greenland and Antarctic ice cores suggests that these H-DO tandems are closely related to global greenhouse gas concentration like CO_2 and CH_4. The residence time of CH_4 in the atmosphere is about 10 years. The CH_4 concentration follows the changes observed in Greenland temperature. Hence CH_4 can be used to synchronize records from both hemispheres [8] (Figure 1.1).

This work focuses mainly on the study of rapid climate change happening during the last ice age. In this framework we developed new on-line techniques for analyses of (i) the elemental and isotopic composition of ancient atmospheric air, extracted from polar ice cores and polar firn, as well as of (ii) the stable isotopic composition of water samples taken from ice cores. The stable isotope composition of both, water and air, can be used to reconstruct ancient temperature evolution.

1.1 Isotopes

Atoms consist of a positive charged nucleus surrounded by orbiting negative charged electrons. The mass of the atom mainly depends on the number of nucleons, A, i.e. neutrons and protons, present in the nucleus, since electrons have much less mass than nucleons. Protons are positive charged whereas neutrons carry no charge. Elements are defined by their number of protons, Z, and are listed in the Element System. Isotopes are atoms of different masses within an element that is defined by its atomic number, Z. The isotopes of one element differ from each other in the number of neutrons. There are stable and unstable (radioactive) isotopes. This work focuses only on the analysis of stable isotopes. The elements and molecules and the corresponding isotopes, which are investigated in this work, are listed in Tables 1.1 and 1.2.

Table 1.1: Natural abundance of the stable isotopes of the elements discussed in this work.

Element	Isotope (natural abundance in %)		
Hydrogen	^{1}H (99.985)	^{2}H (0.015)	
Helium	^{4}He (99.99986)	^{3}He (0.00014)	
Carbon	^{12}C (98.90)	^{13}C (1.10)	
Nitrogen	^{14}N (99.63)	^{15}N (0.37)	
Oxygen	^{16}O (99.762)	^{18}O (0.200)	^{17}O (0.038)
Argon	^{40}Ar (99.600)	^{36}Ar (0.337)	^{38}Ar (0.063)

1.2 Mass Spectrometry

There exist different techniques to measure either absolute or relative isotope abundance, such as interferometry, obtical spectrometry, gas chromatography (GC), and mass spectrometry. In this study all measurements are performed using isotope ratio mass spectrometry (IRMS). It is an expensive but very reliable technique. To measure the isotope ratios of

Table 1.2: Isotopic composition and molecular masses of the molecules discussed in this work.

Molecule	Isotopic composition (molecular mass in g/mol)		
Molecular Hydrogen	$^1\text{H}_2(2)$	$^1\text{H}^2\text{H}$ (3)	
Molecular Nitrogen	$^{14}\text{N}_2(28)$	$^{14}\text{N}^{15}\text{N}$ (29)	
Molecular Oxygen	$^{16}\text{O}_2$ (32)	$^{16}\text{O}^{17}\text{O}$ (33)	$^{16}\text{O}^{18}\text{O}$ (34)
Carbon dioxide	$^{12}\text{C}^{16}\text{O}_2$ (44)	$^{13}\text{C}^{16}\text{O}^{18}\text{O}$ and $^{12}\text{C}^{16}\text{O}^{17}\text{O}$ (45)	$^{12}\text{C}^{16}\text{O}^{18}\text{O}$ (46)
Nitrous oxide	$^{14}\text{N}_2^{16}\text{O}$ (44)	$^{15}\text{N}^{14}\text{N}^{16}\text{O}$ and $^{14}\text{N}_2^{17}\text{O}$ (45)	$^{14}\text{N}_2^{18}\text{O}$ (46)

gaseous substances within a molecular mass range from 2 to 100 amu, usually sector field IRMS is used. Such IRMS consist of the following main compounds (Figure 1.2).

- (a) The ion source: The gas sample is ionized by electron impact and accelerated in an electric field. The velocity depends on the mass/charge ratio, m/z, of the ion. From $E = zU = mv^2/2$ follows $v = \sqrt{2U/(m/z)}$.

- (b) The ion separation: The accelerated ions are deflected in an electro magnetic field, B. The deflection force is proportional to charge, z, and the velocity, v, of the ion: $F = zvB = mv^2/r$, where r is the the radius of the ion tracks in the magnetic field. r can be expressed as follows: $r = (m/z)(v/B)$. Hence the ions are sorted according their m/z ratio. Generally, $z = 1$.

- (c) The ion detection: After the deflection, the ions are detected and counted in faraday collector cups. The electric current, or the voltage measured over a resistor, is directly proportional to the number of ions collected per time unit. In an IRMS typically an array of collector cups is placed in a way that the ions of interest can be detected simultaneously on different cups. In one of our IRMS, a FinniganMAT Delta Plus XL, 8 different mass/charge ratios can be analyzed at the same time (m/z=28, 29, 32, 33, 34, 36, 40, 44). Hence it is possible to measure the isotopic and elemental composition of the main air compounds, nitrogen, oxygen, argon, and CO_2 simultaneously.

The relative variability of the isotopic ratios of the analyzed gases is only in the order of a few tenth of a per mil or less. In order to achieve a measurement precision which is high enough to resolve such small variations, isotope ratios are always measured relative to a known standard. Isotope ratio determinations are expressed in the so called δ-notation:

$$\delta = \frac{R_{SA} - R_{ST}}{R_{ST}} \times 1000^0\!/\!_{00} \tag{1.1}$$

where R_{SA} and R_{ST} are the isotope ratio of the sample and the standard, respectively (e.g $R =^{15}\text{N}/^{14}\text{N}$ for nitrogen). The results are expressed against international standard material, which are Vienna-PDB (carbonate from Peedee Belemnite), Vienna-SMOW (Standard Mean Ocean Water), and Vienna-SLAP (Standard Light Antarctic Precipitation). The V-PDB scale is mostly used for ^{13}C isotope determinations of CO_2, whereas the SMOW/SLAP scale is used for oxygen and hydrogen isotope determinations from water and CO_2 samples. Nitrogen and argon measurements are referenced to ambient air, since the natural variability is very low [37].
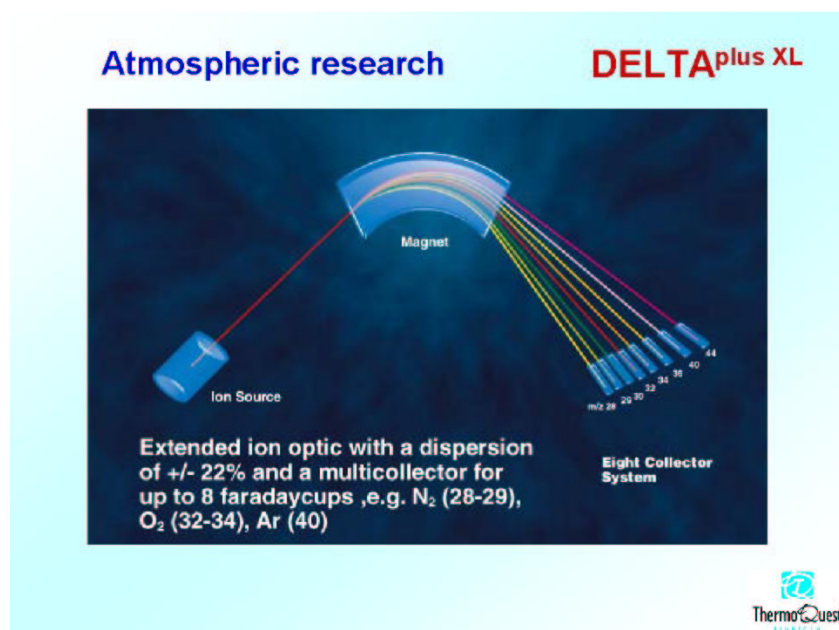
Figure 1.2: FinniganMAT Delta Plus XL isotope ratio mass spectrometer with an array of eight collector cups for the simultaneous detection of the isotopic and elemental composition of the main air compounds, nitrogen, oxygen, argon, and CO_2.

Of great importance is the sample inlet system. Samples can be of solid, fluid or gaseous state. In our laboratory we admit only gaseous samples to the IRMS, however, several peripherals exist to convert solids and liquids into gases. For IRMS usually a dual inlet system is used consisting of two bellows one containing the sample and the other the standard. The volume of the bellows is adjustable in order to maintain equal pressures on both sides. Measurements are performed by switching frequently between sample and standard.

1.2.1 On-Line Techniques

In order to couple peripheral systems, like for example GC columns, combustion or reduction ovens, to an IRMS novel inlet techniques were developed, which no longer use the dual inlet technique for the gas supply. On-line techniques usually use a carrier gas, mostly helium (He), to transport the sample gas from the extraction through the peripheral system and a so called open-split into the mass spectrometer. The open-split (Figure 1.3) consists of a tiny glass tube over which several capillaries are connected. The sample capillary is coming from the peripheral system carrying the sample. The MS capillary connects the open-split with the ion source of the mass spectrometer. Due to the open geometry of the glass tube, the pressure gradient between open-split and ion source, and hence the sample flux to the IRMS, remains constant. A third capillary carries pure He. It can be used to dilute the sample depending on the position of this capillary within the open-split. Usually the split ratio, sample flow/MS flow is in the order of 50:1 [25]. Hence most of the sample is waste and leaves the open-split to atmosphere. This waste flow is important, since it prevents

contamination with ambient air. Nevertheless, on-line techniques allow smaller sample size and higher sample throughput than off-line methods. **In chapter 2 and 3 new on-line extraction and analyzing methods are described, which were developed during this work.** The purpose of the new methods is to melt a long piece ice continuously at one end and subsequently analyze either the water isotopes $\delta^{18}O$ [35] and δ^2H [22] of the melted ice, or extract the air from the melt water and measure the air elemental and isotopic composition [25, 23]. This allows for the first time to perform high resolution isotope measurements on ice cores with a continuous flow technique.
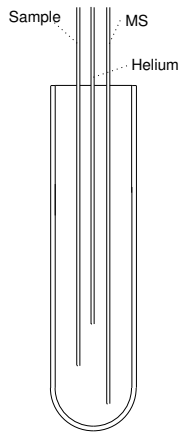

Figure 1.3: The open-split consists of a tiny glass tube over which several capillaries are mounted. It connects peripheral on-line systems with the mass spectrometer (MS)

1.3 Polar Ice Sheets as Climate Archives

Direct climate monitoring is restricted to about 1–2 centuries. Therefore, to go back in time information has to be extracted from climate archives, such as ice cores, firn air, tree rings, sediments, corals, ground water, stalagmites, historical documents etc. **The archives used in this work are polar ice cores (chapter 5) and firn air (chapter 4).** The timescale of these archives is rather different. Polar ice cores reach back several 100'000 years as far as nearly one million, whereas firn air studies document the last century. A big advantage of both archives is the more or less direct climate information and the high temporal resolution. The polar ice sheets of Greenland and Antarctica are enormous storages of ancient ice. A schematic view on an ice sheet is given in Figure 1.4. The thickness in the center of the ice sheet, the dome, is about 3–4 km. Depending on the accumulation rate and the ice flow at a specific site, this corresponds to about 100–200 kyr in Greenland and about 500–1000 kyr in Antarctica. Due to the ice flow from the dome towards the edges of the ice sheet, the ice is thinning out with depth. As a result of the ice thinning, the time resolution decreases with depth.
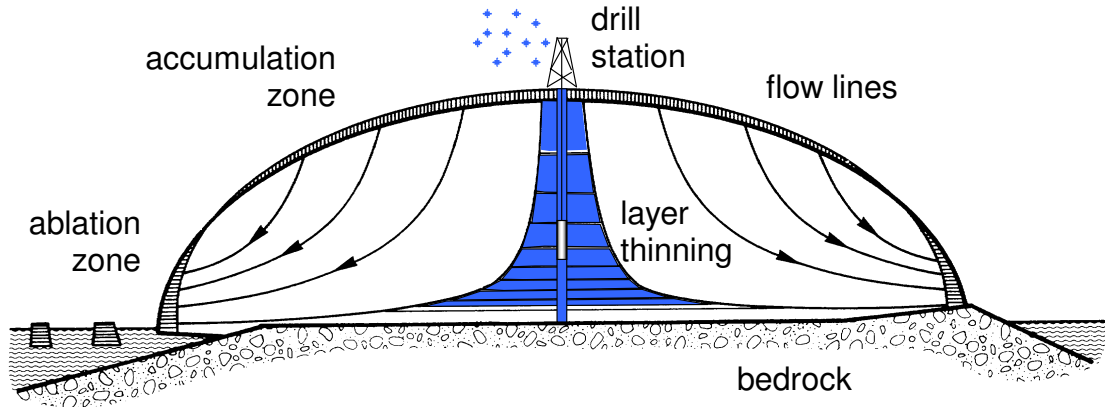
Figure 1.4: A schematic view on a polar ice sheet with a drill station on the dome. The snow is accumulated in the accumulation zone on the center of the ice sheet. It is slowly transported by ice flow towards the costal ablation zone. This leads to a thinning of the ice layers with depth.

1.3.1 The Transformation of Snow to Ice

The uppermost part of an ice sheet is called the firn (Figure 1.5). It describes the transformation zone from snow to ice. Firn is a porous media. The density and porosity structure depend on site conditions like accumulation rate and temperature [20, 38, 44]. The ice crystals are reorganized first geometrically in the upper 5–10 m and then, when density reaches about $550\,kg/m^3$, by increasing its size during a sintering process. Herron [20] developed an empirical model which describes the relation of density, accumulation and temperature. The air can move trough the upper part of the firn and is locked-in at a given density, experimentally found to be $818\,kg/m^3$. The depth where this density is reached varies for different sites. It depends mainly on the temperature and the accumulation rates. Lower temperatures and associated lower accumulation rates cause deeper close-off depths [38, 43, 46, 45]. Close-off depth can vary between 50–120 m. The main transport mechanism within the porous firn column is molecular diffusion. As a consequence of the diffusive movement of air in the firn column, the age of the entrapped air is much younger than the age of the surrounding ice. The exact determination of this gas age-ice age difference (Δage) is essential in order to compare data from different climate records. One approach to deduce the Δage is to model the firn densification and air diffusion. The porous firn column can be divided into three different zones (Figure 1.5). (i) A convective zone at the top, where the air in well mixed by convection and wind driven air flow, followed by (ii) a diffusive zone, where the composition of the air is altered due to vertical diffusion, and finally (iii) a non-diffusive zone, where no vertical mixing occurs anymore but horizontal moving is still possible. Convective zones are normally only a couple of meters deep or even not existent. Deep convective zones are only detected at very cold low accumulation sites on the Antarctic continent, like for example Vostok or Dome Fuji (8–10 m convective zones). But during ice ages when temperature was more than 20°C colder, accumulation rates were very low, and winds were stronger, the presence of deep convective zones was probably more likely. However, there is no consistent theory which explains convective zones. Lock-in depth (LID) predictions from models disagree with measurements at nearly all Antarctic sites during
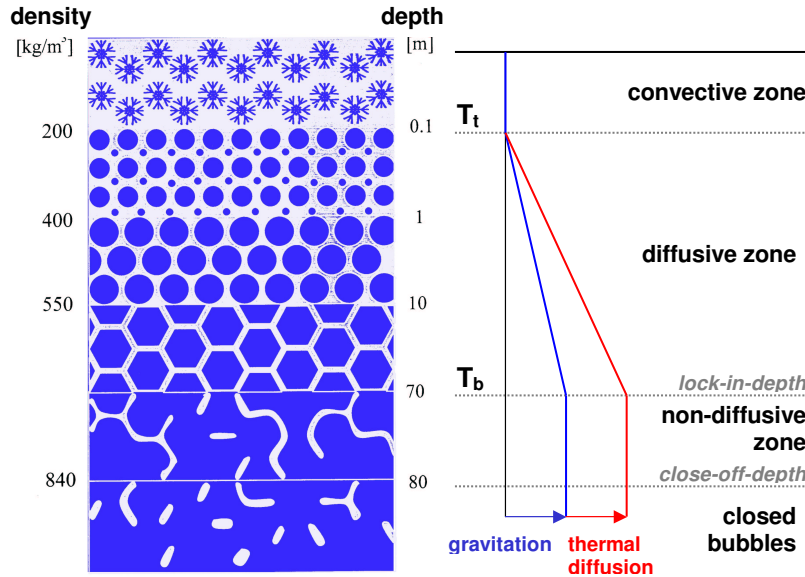
Figure 1.5: The firn structure. Snow is accumulated at the surface and gradually transformed to ice by a sintering process. During this process atmospheric air is trapped in bubbles in the ice. The isotopic composition of the air is altered in the diffusive column of the firn by gravitational settling and thermal diffusion.

glacial periods, measurements being lower. Since model do not incorporate convective zones the difference could be explained by more pronounced convective zones during glacials. But of course other mechanisms could be responsible for the discrepancies. Till now it is an unsolved problem. **In chapter 5 this problem is discussed for measurements made on the NorthGRIP ice core [40, 24] and a possible solution is presented.**

1.3.2   Climate Information from Firn Air

Alterations of the air composition in the diffusive firn column can be described by three effects, which are (i) the gravitational settling [43, 9], (ii) the molecular concentration diffusion (ordinary diffusion) [14, 52], and the thermal diffusion [50, 36, 34]. The gravitational settling is driven by the earth gravity acceleration, g, the molecular mass of the gas, m, and the depth off the firn column, z, according to the Barometric formula. Relative enrichment of two elements or isotopes can well be linearly approximated by the diffusive column height (DCH) and the mass difference, Δm, between two molecular species:

$$\delta = \left(e^{\Delta mgz/RT} - 1\right) \times 1000^0\!/_{00} \cong \Delta mgz/RT \times 1000^0\!/_{00} \tag{1.2}$$

where T is the temperature and R the ideal gas constant. Heavy molecules will be enriched at the lock-in depth at the bottom of the firn column. Ordinary diffusion is driven by a atmospheric concentration gradient. Thermal diffusion, finally, is active when temperature is not constant over the diffusive firn column. A temperature gradient, ΔT, between the top (T_t) and the bottom (T_b) of the diffusive firn column, can be the result of a rapid changing

surface temperature as it happened during Dansgaard/Oeschger events [24] (see chapter 5). Thermal diffusion forces lighter molecules to move toward the warmer end of the firn column. The strength of the fractionation due to thermal diffusion can be calculated by the following equation:

$$\delta = \left[\left(\frac{T_t}{T_b} \right)^{\alpha_T} - 1 \right] \times 1000^0\!/\!_{00} \cong \Omega \Delta T \qquad (1.3)$$

where α_T is the the temperature dependent thermal diffusion factor, and $\Omega = \alpha_T/T$ the thermal diffusion sensitivity [16, 17, 36]. For nitrogen isotopes, $\delta^{15}N$, the fractionation is about $0.014^0\!/\!_{00}$/K at -50°C. Therefore, a rapid increase of the surface temperature will result in an increase of the isotope ratio at the bottom of the firn column. This is only the case for rapid temperature changes. When temperature is changing slowly (<1°C/100 yr), no thermal gradient is manifested in the firn and hence no thermal diffusion will be detected. Seasonal temperature variations do only affect the upper 20–30 m of the firn column. Thermal fractionation can be detected when sampling air from shallow depths. Deeper down seasonal effects are smoothed out [48].

The age of the air at the bubble close-off depends on the site conditions. It can reach up to about 100 years. The direct air sampling from the firn column gives access to those archived compositions. The first firn air samples were taken by Schwander et al. [44]. In the following years a number of firn air studies have been done. It is an archive that covers the human industrialization and is therefore important closing the gab between ice core data and direct atmospheric measurements, especially for greenhouse gases like CO_2 and CH_4 [2] as well as isotopes [14]. Firn air is the only direct archive for human made trace gases, such as CFC's, SF_6, etc. Furthermore, firn air measurements help to better understand the processes occurring in the firn column which alter the composition of the air finally trapped in the ice. **In chapter 4 a size dependent fractionation process during bubble close-off is investigated using firn air measurements.** Hence, beside the climate information coming from direct measurements, firn air studies are very important to improve our knowledge about the reliability of ice cores as archive for ancient atmospheric air. The effect of gravitational enrichment and thermal diffusion applies for both elemental as well as isotopic compositions. However, for elemental compositions these effects are in the order of the measurements precision. In contrast the extremely high precision of isotopic determinations allows us to clearly detect such firn process influences.

Regarding the composition of trace gases, such as CO_2, CH_4, and N_2O, ice cores are a direct atmospheric archive [26, 41, 13]. On the other hand, for the elemental ratios O_2/N_2 and Ar/N_2, the process of size dependent fractionation during the bubble-close off is dominant [3, 4, 21]. Hence these ratios do not reflect atmospheric values.

1.3.3   What can we learn from the Isotopic Composition of Ice Cores?

Stable Isotopes of the Ice as a Temperature Proxy

The stable isotope composition of the ice itself, as well as of the entrapped air is carrying an enormous amount of information about ancient climate. Water isotopes, $\delta^{18}O$ and δD, are usually used as a proxy for the temperature at the site of the ice core. The isotopic composition of the precipitation depends on temperature. The lower the temperature, the

more depleted the precipitation. Heavy water molecules condense earlier than light ones, resulting in a constant isotopic depletion of the clouds during its transport from the source region over the ocean to the continental precipitation sites.

Concerning the climate system, we can learn a lot from $\delta^{18}O$ and δD. In Figure 1.1 the $\delta^{18}O$ from the Greenland site GISP2 is compared to an Antarctic record of Byrd [8]. It is nicely documented that the last glacial period lasted from about 110 kyr BP to 15 kyr BP. In Greenland the cold climate was interrupted by several warm events (DO-events), whereas in Antarctica the temperature remained more or less constantly cold. 20 kyr ago, the temperature started to rise, first in Antarctica then abruptly in Greenland. The following warm period in Greenland is called the Bølling-Allerød. During this time the rise of the Antarctic temperature was interrupted (Antarctic Cold Reversal). Later on, Greenland climate shifted into the last cold period (Younger Dryas) which lasted about 1000 years, before the temperatures in both hemispheres inevitably rose into the long and constant warm period, the Holocene. This 10'000 year warm period was essential for the development of modern cultures. To investigate these different time frames ice core drilling projects were organized.

A new deep drilling operation has been completed in 2003 in North Greenland at the NorthGRIP site [40] (75.1°N, 42.3°W), 324 km North-North-West of the summit site where the GRIP [18] and GISP2 [19] ice cores were retrieved (see Figure 1.6). The oldest ice found in NorthGRIP belongs to the last interglacial (Eem) 120 kyr BP. The high rates of basal ice melting restrict the thinning of the ice layers and the possibility of ice disturbance in the bottom part of the core. It is the first Greenland ice core that reveals undisturbed ice from the Eemian period. The isotope ratios imply substantially warmer (by 5°C) conditions than present day at that time. Furthermore a new DO event (DO 25) has been found in the stable isotope record $\delta^{18}O_{ice}$ of NorthGRIP. **This record is discussed in detail in chapter 5 [40].**

In contrast to Greenland, Antarctic ice cores reach far further back in time. The new Dome C core drilled in the framework of the European Project for Ice Coring in Antarctica (EPICA) provides a climate record extending 740 kyr back in time [39]. Eight glacial interglacial cycles are documented in the climate record. The completion of the drilling will offer a record of nearly one millon years. The climate of the last 500 kyr was characterized by extremely strong 100 kyr cyclicity. During the earlier part of the Quartenary (before 1 million years BP), cycles of 41 kyr dominated. The period in between shows intermediate behavior. The observed frequencies arise from parameters of the Earth's orbit that control the amount, and the seasonal and latitudinal distribution, of solar radiation [6]. The reason for the dominance of the 100 kyr (eccentricity) over the 41 kyr (obliquity) band in the later part of the record, and the amplifiers that allow small changes in radiation to cause large changes in global climate, are not well understood.

In order to deduce temperature information from isotope data, one has to know the relationship on which both parameter depend. For present day conditions a linear relationship between temperature and $\delta^{18}O$ and δD, respectively can be found. It is obtained by measuring the isotopic composition of precipitation at various sites lying on a trajectory between the evaporative regions and the high latitudes where the snow precipitates. This linear relationship is called the spatial slope, $\alpha_{spatial}$. It is about $0.67^0/_{00}/°C$ for Greenland $\delta^{18}O$ [11]. Using this relationship as a paleothermometer relies on the assumption that the spatial
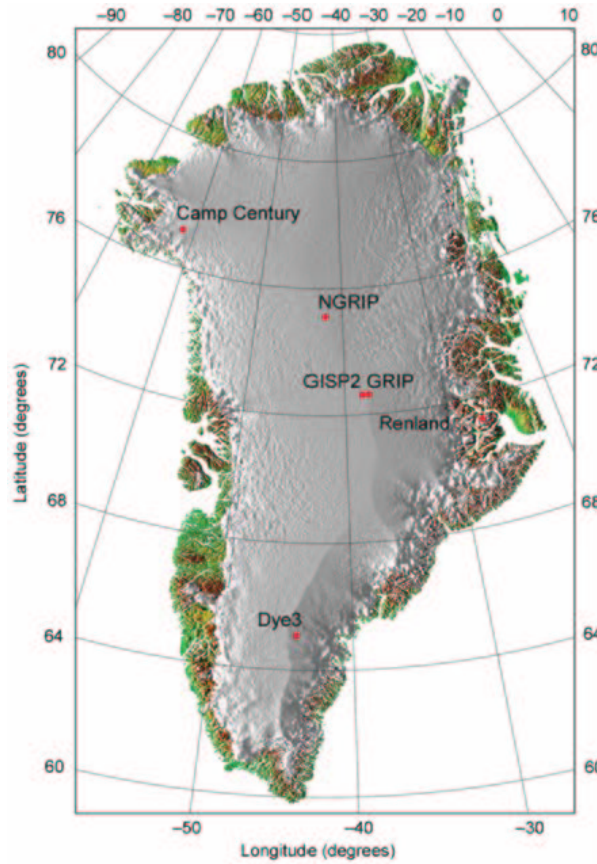
Figure 1.6: Map of Greenland with the deep ice core drilling sites NorthGRIP (75.1°N, 42.3°W), GRIP (72.5°N, 37.3°W), GISP2 (72.5°N, 38.3°W), Dye3 (65.2°N, 43.8°W), Renland (71.3°N, 26.7°W), and Camp Century (77.2°N, 61.1°W). The Figure is taken from [40]

relationship does not change with time and consequently that the spatial and temporal slopes are the same which is clearly not the case for Greenland as shown from comparison with independent estimates of temperature changes [28]. Such an independent estimate can be borehole temperature measurements. This method showed that the interpretation of the δ^{18}O profile using the spatial slope underestimates the Last Glacial Maximum (LGM) (21 kyr BP) to Holocene temperature change by about 12°C or 100%. The temporal slope during the LGM was $\alpha_{temporal}$=0.32^0/$_{00}$/°C [10], probably due to changes in the seasonality of the precipitation between glacial and interglacial periods with huge decreases of winter snowfall during glacial periods [53]. For Antarctic cores this effect is less pronounced and spatial and temporal slopes do not differ significantly [29].

Surface Temperature Reconstruction from Nitrogen and Argon Isotopes

Greenland borehole temperature reconstructions, however, allow to assess past temperature variations only on long timescales. The temporal resolution decreases rapidly with age [1]. Air isotopic measurements of δ^{15}N and δ^{36}Ar, which are altered in the firn column at times of rapid temperature changes, complement the borehole reconstructions on short timescales.

For stable climatic conditions the enrichment of the nitrogen as well as the argon isotope ratios in the ice, which are stable in the atmosphere [37] over long time periods, can be used to calculate the height of the diffusive column DCH. During a rapid climate shift, an additional change of the δ^{15}N composition, due to thermal diffusion occurs. By measuring the isotopic composition of both, nitrogen and argon, the thermal and the gravitational signal can be separated. Thus the amplitude of past surface temperature changes can be assessed by the combined measurement of these isotopes [47, 15, 32]. With the technique we use in our laboratory [23], it is not possible to measure argon isotopes with the required precision. Hence, we use another approach to deduce temperature information from δ^{15}N measurements alone [24, 34, 36]. **In chapter 5 a detailed temperature reconstruction over 9 consecutive DO events on the NorthGRIP ice core is presented.** The reconstruction covers the time period from 64 to 38 kyr BP with a temporal resolution of 50 to 100 yr. This study implies that the idea of a constant linear relationship between δ^{18}O$_{ice}$ and temperature has to be modified [24]. Landais et al. [31] came to same conclusion for the time period of 74 to 62 kyr BP on NorthGRIP.

In the last years several similar studies on the assessment of rapid temperature changes in Greenland were done [47, 34, 36, 49, 15, 32, 24, 31, 33]. A summary of those studies is given in Table 1.3. It documents, that this work contributed a significant part to the knowledge on Greenland temperature. With a nearly complete high resolution δ^{15}N record from about 125–38 kyr BP (DO 25–DO 8), the NorthGRIP ice core is of great importance regarding past temperature evolution.

Table 1.3: Compilation of rapid temperature changes (ΔT) in Greenland. The uncertainty of the ΔT determinations is about $\pm 3°$C.

Event	Ice core	Approx. age (kyr BP)	ΔT ($°$C)	Reference
8200 yr event	GRIP	8.2	-7.4	[36]
YD-transition	GISP2	11.5	10	[50]
YD-transition	GISP2	11.5	12	[15]
Bølling-transition	GISP2	14.5	11	[50, 49]
Bølling-transition	GISP2	14.5	16	[15]
DO 9	NorthGRIP	40	9	[24]
DO 10	NorthGRIP	42	11.5	[24]
DO 11	NorthGRIP	44	15	[24]
DO 12	NorthGRIP	48	12.5	[24]
DO 12	GRIP	45	12	[32]
DO 13	NorthGRIP	50	8	[24]
DO 15	NorthGRIP	57	10	[24]
DO 16	NorthGRIP	59	9	[24]
DO 17	NorthGRIP	60	12	[24]
DO 18	NorthGRIP	65	11	[31]
DO 19	NorthGRIP	73	16	[31]
DO 19	GRIP	70	16	[34]
DO 20	NorthGRIP	77	11	[31]
DO 23	NorthGRIP	103	10	[33]
DO 24	NorthGRIP	105	16	[33]

The Oxygen Cycle

Another important parameter that can be obtained from air measurements on ice cores is the isotopic composition of atmospheric oxygen, $\delta^{18}O_{atm}$. It is inferred from $\delta^{18}O$ measurements corrected for gravitational settling and thermal diffusion using $\delta^{15}N$. Dole [12] has found that the isotopic composition of water oxygen is lower compared to atmospheric oxygen. The difference of $23.5^0/_{00}$ is known as the Dole effect. Bender [5] showed that on long timescales $\delta^{18}O_{atm}$ variations go parallel to changes of the global ice volume, since the isotopic signature of the oceanic water, which depends on the extent of the isotopically depleted polar ice sheets, is transmitted via the biosphere to the atmosphere by photosynthesis/respiration activities. These processes can be summarized by the simplified equation as follows:

$$CO_2 + H_2O \rightleftarrows CH_2O + O_2 \qquad (1.4)$$

In Figure 1.7 a compilation of oxygen isotope data obtained during this work is compared to existing records. Since oxygen is perfectly mixed within the atmosphere, $\delta^{18}O_{atm}$ can be used to synchronize timescales of ice core records from different hemispheres. The atmospheric ratio of the lighter oxygen isotope, $\delta^{17}O_{atm}$, should behave accordingly. However, an anomaly in $\delta^{17}O_{atm}$ is observed caused by stratospheric O_2-CO_2 exchange [7]. The relative rates of biologic O_2 production and stratospheric processing determine the relationship between $\delta^{17}O$ and $\delta^{18}O$ of O_2 in the atmosphere. The parameter

$$\Delta^{17}O = (\delta^{17}O_{atm} - 0.52\delta^{18}O_{atm}) \times 1000 \, \text{per meg} \qquad (1.5)$$

can be used to asses the strength of biological productivity. The measurement precision, however, has to be very high, since $\Delta^{17}O$ variations are in the order of only a few per meg (1/1000 of a per mil!).

Changes of the atmospheric oxygen concentration are anti-correlated to CO_2 changes, due the biological processes described in eq. 1.4 as well as fossil fuel burning. Fossil fuel oxidation can be described as follows:

$$CH_2O(S) + O_2 \rightarrow CO_2 + H_2O + (SO_2) \qquad (1.6)$$

For biogenic processes, taking fertilizers into account, about 1.1 mol of O_2 is required to produce 1 mol of CO_2 for the terrestrial biosphere and about 1.3–1.4 for the marine biosphere. For fossil fuel burning about 1.4 mol of O_2 is consumed for 1 mol of CO_2. This factor depends on the type of fossil fuel and has changed during the industrial period.

In order to learn more about the origin of atmospheric CO_2 variations at preindustrial times, it has been tried to measure the oxygen composition of ancient atmospheric air extracted from ice cores. However, elemental ratios like O_2/N_2 of the air from ice cores are heavily fractionated due to processes during bubble close-off. Therefore, unfortunately atmospheric oxygen concentration variations can not be resolved from ice core data. Even though, elemental ratio measurements on ice cores can provide valuable information. Bender et al. [3] recently described a phenomenon that O_2/N_2 ratios measured on the Antarctic Vostok ice core varies on orbital timescales of 19–21 kyr. Therefore, elemental ratios like O_2/N_2 or Ar/N_2 can be used as a synchronization tool for ice cores. The reason for this correlation is unclear. A better understanding of the processes involved during bubble close-off is essential. **In in chapter 4 new findings about size dependent fractionation of firn air are described.**
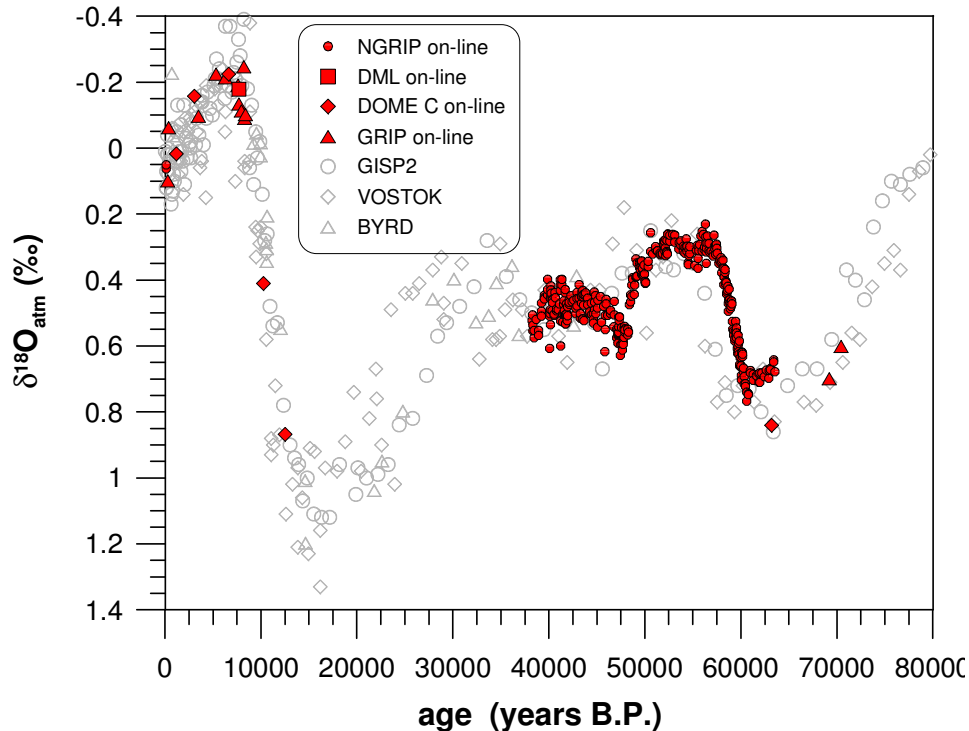
Figure 1.7: Compilation of oxygen isotope data obtained during this work compared to existing records from Vostok and GISP2. The different data is plotted on their individual chronologies which are different. NorthGRIP data older than 40 kyr BP shows an age shift of 2000 to 3000 years compared to the GISP2 and Vostok data.

Bibliography

[1] R. Alley and B.R. Koci. Recent warming in central Greenland? *Annals of Glaciology*, 14:6–8, 1990.

[2] M Battle, M Bender, T Sowers, P P Tans, J H Butler, J W Elkins, J T Ellis, T Cornway, N Zhang, P Lang, and A D Clarke. Atmospheric gas concentrations over the past century measured in air from firn at the South Pole. *Nature*, 383:231–235, 1996.

[3] M Bender. Orbital tuning chronology for the Vostok climate record supported by trapped gas composition. *Earth and Planetary Science Letters*, 204:275–289, 2002.

[4] M Bender, T Sowers, and V Lipenkov. On the concentraion of O_2, N_2, and Ar in trapped gases from ice cores. *Journal of Geophysical Research*, 100(D9):18651–18660, 1995.

[5] M. L. Bender, L. Labeyrie, B. Raynaud, and C. Lorius. Isotopic composition of atmospheric O_2 in ice linked with deglaciation and global primary productivity. *Nature*, 318:349–352, 1985.

[6] A. Berger and M. F. Loutre. Insolation values for the climate of the last 10 million years. *Quaternary Science Reviews*, 10:297–317, 1991.

[7] T Blunier, B Barnett, M.L Bender, and M.B Hendricks. Biological oxygen productivity during the last 60,000 years from triple oxygen isotope measurements. *Glob. Biogeochem. Cycles*, 16:10.1029/2001GB001460, 2002.

[8] T. Blunier and E. Brook. Timing of millennial-scale climate change in Antarctica and Greenland during the last glacial period. *Science*, 291:109–112, 2001.

[9] H. Craig, Y. Horibe, and T. Sowers. Gravitational separation of gases and isotopes in polar ice caps. *Science*, 242:1675–1678, 1988.

[10] Kurt M. Cuffey, Richard B. Alley, Pieter M. Grootes, John M. Bolzan, and Sridhar Anandakrishnan. Calibration of the δ^{18}O isotopic paleothermometer for central greenland, using borehole temperatures. *Journal of Glaciology*, 40(135):341–349, 1994.

[11] W Dansgaard. Stable isotopes in precipitation. *Tellus*, 16:436–468, 1964.

[12] M Dole. The relative atomic weight of oxygen in water and air. *J. Am. Chem. Soc.*, 57:2731–2745, 1935.

[13] J. Flückiger, T. Blunier, B. Stauffer, J. Chappellaz, R. Spahni, K. Kawamura, J. Schwander, T. F. Stocker, and D. Dahl-Jensen. N_2O and CH_4 variations during the last galcial epoch: Insight into global processes. *Glob. Biogeochem. Cycles*, GB 1020:doi:10.1029/2003GB002122, 2004.

[14] R. J. Francey, M. R. Manning, C. E. Allison, S. A. Coram, D. Etheridge, R. L. Langenfelds, D. C. Lowe, and L. P. Steele. A history of delta C-13 in atmospheric CH_4 from the Cape Grim air archive and Antarctic firn air. *J. Geophys. Res*, 104:23,631–23,643, 1999.

[15] C. Goujon, J. M. Barnola, and C. Ritz. Modeling the densification of polar firn including heat diffusion: Application to close-off characteristics and gas isotope fractionation for Antarctic and Greenland sites. *J. Geophys. Res*, 108:doi:10.1029/2002JD003319, 2003.

[16] A. Grachev and J. P. Severinghaus. Determining th termal diffusion factor for ^{40}Ar/^{36}Ar in air to aid paleoreconstruction of abrupt climate change. *J. Phys. Chem. A*, 107:4636–4642, 2003.

[17] A. Grachev and J. P. Severinghaus. Laboratory determination of thermal diffusion constants for $^{29}N_2$/$^{28}N_2$ in air at temperatures from -60 to 0°C for reconstruction of magnitudes of abrupt climate changes using the ice core fossil-air paleothermometer. *Geochimica et Cosmochimica Acta*, 67(3):345–360, 2003.

[18] GRIPmembers. Climate instability during the last interglacial period recorded in the GRIP ice core. *Nature*, 364:203–207, 1993.

[19] P M Grootes, M Stuiver, J W C White, S Johnsen, and J Jouzel. Comparison of oxygen isotope records from the GISP2 and GRIP Greenland ice cores. *Nature*, 366:552–554, 1993.

[20] M M Herron and Jr. Langway, C C. Firn densification: An empirical model. *J. Glaciol.*, 25:373–385, 1980.

[21] C. Huber, U. Beyerle, M. Leuenberger, J. Schwander, R. Kipfer, R. Spahni, J. Severinghaus, and K. Weiler. Evidence for gas fractionation in firn air derived from noble gases, oxygen, and nitrogen measurements. *Earth and Planetary Science Letters*, submitted 2004.

[22] C. Huber and M Leuenberger. Fast high-precision on-line determination of hydrogen isotope ratios of water or ice by continuous-flow isotope ratio mass spectrometry. *Rapid Communications in Mass Spectrometry*, 17:1319–1325, 2003.

[23] C. Huber and M. Leuenberger. Measurements of isotope and elemental ratios of air from polar ice with a new on-line extraction method. *Geochemistry Geophysics Geosystems*, in press, 2004.

[24] C. Huber, M. Leuenberger, J. Schwander, R. Spahni, J. Flückiger, T. F. Stocker, S. J. Johnsen, A. Landais, and J. Jouzel. Isotope calibrated Greenland temperature record over Marine Isotope Stage 3 and its relation to CH_4. *Nature*, submitted 2004.

[25] C. Huber, M. Leuenberger, and O. Zumbrunnen. Continuous extraction of trapped air from bubble ice or water for on-line determination of istotope ratios. *Analytical Chemistry*, 75(10):2324–2332, 2003.

[26] A. Indermühle, T. F. Stocker, F. Joos, H. Fischer, H. J. Smith, M. Wahlen, B. Deck, D. Mastroianni, J. Tschumi, T. Blunier, and B. Stauffer. Holocene carbon-cycle dynamics based on CO_2 trapped in ice at Taylor Dome, Antarctica. *Nature*, 398:121–126, 1999.

[27] IPCC, editor. *Climate Change 2001: The science of climate change. Contribution of working group I to the Third Assessment Report of the Intergovernmental Panel on Climate Change.* Cambridge University Press, Houghton, J. T. et al. edition.

[28] J. Jouzel, R. B. Alley, K. M. Cuffey, W. Dansgaard, P. Grootes, G. Hoffmann, S. J. Johnsen, R. D. Koster, D. Peel, C. A. Shuman, M. Stevenard, M. Stuiver, and J. White. Validity of the temperature reconstruction from ice cores. *J. Geophy. Res.*, 102(C12):26471–26487, 1997.

[29] J. Jouzel, F. Vimeux, N. Caillon, G. Delaygue, G. Hoffmann, V. Masson-Delmotte, and F. Parrenin. Magnitude of isotope/temperature scaling for interpretation of central antarctic ice cores. *J. Geophy. Res.*, 108(D12):4361, doi10.1029/2002JD002677, 2003.

[30] R. Knutti, J. Flückiger, T. F. Stocker, and A. Timmermann. Strong hemispheric coupling of glacial climate through freshwater discharge and ocean circulation. *Nature*, 430:851–856, 2004.

[31] A. Landais, J.M. Barnola, V. Masson-Delmotte, J. Jouzel, J. Chappellaz, N. Caillon, C. Huber, M. Leuenberger, and S. J. Johnsen. A continuous record of temperature evolution over a whole sequence of Dansgaard-Oeschger during Marine Isotope Stage 4 (76 to 62 kyr BP). *Geophys. Res Lett.*, submitted 2004.

[32] A. Landais, N. Caillon, C. Goujon, A. Grachev, J.M. Barnola, J. Chappellaz, J. Jouzel, V. Masson-Delmotte, and M. Leuenberger. Quantification of rapid temperature change during DO event 12 and phasing with methane inferred from air isotopic measurements. *Earth and Planetary Science Letters*, 225:221–232, 2004.

[33] A. Landais, V. Masson-Delmotte, J. Jouzel, D. Raynaud, S. J. Johnsen, C. Huber, M. Leuenberger, J. Schwander, and B. Minister. The glacial inception recorded in the NorthGRIP Greenland ice core: information from air isotopic measurements. *Climate Dynamics*, submitted 2004.

[34] C. Lang, M. Leuenberger, J. Schwander, and S. Johnsen. 16°C rapid temperature variation in central Greenland 70000 years ago. *Science*, 286:934–937, 1999.

[35] M. Leuenberger and C. Huber. On-line determination of oxygen isotope ratios of water or ice by mass spectrometry. *Analytical Chemistry*, 74:4611–4617, 2002.

[36] M. C. Leuenberger, C. Lang, and J. Schwander. Delta 15N measurements as a calibration tool for the paleothermometer and gas-ice age differences: a case study for the 8200 B.P. event on GRIP ice. *Journal of Geophysical Research*, 104(D18):22163–22170, 1999.

[37] A. Mariotti. Atmospheric nitrogen is a reliable standard for natural 15N abundance measurements. *Nature*, 303:685–687, 1983.

[38] P Martinerie, V Y Lipenkov, D Raynaud, J Chappellaz, N I Barkov, and C Lorius. Air content paleo record in the vostok ice core (Antarctica): A mixed record of climatic and glaciological parameters. *J. Geophys. Res.*, 99:10565–10576, 1994.

[39] EPICA Community Members. Eight glacial cycles from an antarctic ice core. *Nature*, 429:623–628, 2004.

[40] NorthGRIP Members. High resolution climate record of the northern hemisphere reaching into the last glacial interglacial period. *Nature*, 431:147–151, 2004.

[41] E. Monnin, A. Indermühle, A. Dällenbach, J. Flückiger, B. Stauffer, T. F. Stocker, D. Raynaud, and J.-M. Barnola. Atmospheric CO_2 concentrations over the last glacial termination. *Science*, 291:112–114, 2001.

[42] J. R. Petit, J. Jouzel, D. Raynaud, N. I. Barkov, J.-M. Barmola, I. Basile, M. Bender, J. Chapppellaz, M. Davis, G. Delaygue, M. Demotte, V. M. Kotlyakov, M. Legrand, V. Y. Lipenkov, C. Lorius, L. Pépin, C. Ritz, E. Saltzman, and M. Stievenard. Climate and atmospheric history of the past 420000 years from the Vostok ice core, Antarctica. *Nature*, 399:429–436, 1999.

[43] J. Schwander. The transformation of snow to ice and the occlusion of gases. In H. Oeschger and C C Langway Jr., editors, *The Environmental Record in Glaciers and Ice Sheets*, pages 53–67. John Wiley, New York, 1989.

[44] J. Schwander, J M Barnola, C Andrié, M Leuenberger, A Ludin, D Raynaud, and B Stauffer. The age of the air in the firn and the ice at summit, Greenland. *J. Geophys. Res.*, 98:2831–2838, 1993.

[45] J Schwander and B Stauffer. Age difference between polar ice and the air trapped in its bubbles. *Nature*, 311:45–47, 1984.

[46] J Schwander, B Stauffer, and A Sigg. Air mixing in firn and the age of the air at pore close-off. *Annals of Glaciology*, 10:141 – 145, 1988.

[47] J. P. Severinghaus and E. J. Brook. Abrupt climate change at the end of the last glacial period inferred from trapped air in polar ice. *Science*, 286:930–934, 1999.

[48] J. P. Severinghaus, A. Grachev, and M. Battle. Thermal fractionation of polar firn by seasonal temperature gradients. *Geochemistry Geophysics Geosystems*, 2:2000GC000146, 2001.

[49] J. P. Severinghaus, A. Grachev, B. Luz, and N. Caillon. A method for precise measurement of argon 40/36 and krypton/argon ratios in trapped air in polar ice with applications to past firn thickness and abrupt climate change in Greenland and at siple dome, Antarctica. *Geochimica et Cosmochimica Acta*, 67(3):325–343, 2003.

[50] Jeffrey P Severinghaus, T Sowers, E J Brook, R B Alley, and M L Bender. Timing of abrupt climate change at the end of the Younger Dryas interval from thermally fractionated gases in polar ice. *Nature*, 391:141–146, 1998.

[51] T. F. Stocker. The seesaw effect. *Science*, 282:61–62, 1998.

[52] C M Trudinger, I G Enting, D M Etheridge, R J Francey, V A Levchenko, L P Steele, D Raynaud, and L Arnaud. Modelling air movement and bubble trapping in firn. *J. Geophys. Res.*, 102(D6):6747–6763, 1997.

[53] M. Werner, M. Heimann, and G. Hoffmann. Isotopic composition and origin of polar precipitation in present and glacial climate simulations. *Tellus*, 53B:53–71, 2001.

Chapter 2

New On-Line Techniques for Stable Isotope Ratios of Water or Ice

2.1   On-Line Determination of Oxygen Isotope Ratios of Water or Ice by Mass Spectrometry

Markus Leuenberger[1] and Christof Huber[1]

Abstract

Oxygen isotope ratio determination on any of the water phases (water vapour, water, ice) is of great relevance in different research fields such as climate and paleoclimate studies, geological surveys and hydrological studies. The conventional technique for oxygen isotope measurement involves equilibration with carbon dioxide gas for a given time with a subsequent isotope determination. The equilibration technique is available in different layouts but all of them are rather time-consuming. Here we report a new on-line technique that processes water samples as well as ice samples. The same principal, CO_2 hydration, is used but speeded up by (i) a direct injection and full dissolution of CO_2 in the water, (ii) an increased isotope exchange temperature at $50°C$ and (iii) a rapid gas extraction by means of an air-permeable membrane into a continuous helium flux supplying the isotope-ratio mass spectrometer (IRMS) with the sample gas. The precision is better than $0.1^0/_{00}$ which is only slightly larger than with the conventional equilibration technique. This on-line technique allows analysis of 1 m of ice with a resolution of 1–3 cm, depending on the melt-water flux, within 1 hour. Similarly, continuous and fast analysis can be performed for aqueous samples for hydrological, geological and perhaps medical applications.

---

[1]Climate and Environmental Physics, Physics Institute, University of Bern, Sidlerstrasse 5, CH-3012 Bern, Switzerland

On-Line Determination of Oxygen Isotope Ratios of Water or Ice by Mass Spectrometry

M. Leuenberger* and C. Huber

Climate and Environmental Physics, Physics Institute, University of Bern, Sidlerstrasse 5, 3012 Bern, Switzerland

Oxygen isotope ratio determination on any of the water phases (water vapor, water, ice) is of great relevance in different research fields such as climate and paleoclimate studies, geological surveys, and hydrological studies. The conventional technique for oxygen isotope measurement involves equilibration with carbon dioxide gas for a given time with a subsequent isotope determination. The equilibration technique is available in different layouts, but all of them are rather time-consuming. Here we report a new on-line technique that processes water samples as well as ice samples. The same principal, CO_2 hydration, is used but speeded up by (i) a direct injection and full dissolution of CO_2 in the water, (ii) an increased isotope exchange temperature at 50 °C, and (iii) a rapid gas extraction by means of an air-permeable membrane into a continuous helium flux supplying the isotope ratio mass spectrometer with the sample gas. The precision is better than 0.1‰ which is only slightly larger than with the conventional equilibration technique. This on-line technique allows analysis of 1 m of ice with a resolution of 1–3 cm, depending on the meltwater flux, within 1 h. Similarly, continuous and fast analysis can be performed for aqueous samples for hydrological, geological, and perhaps medical applications.

Measurement of the oxygen isotopic composition of water is a key parameter in many research fields such as hydrology, limnology, geology, and paleoclimatology. $\delta^{18}O$ obtained from Greenland and Antarctic ice cores is a proxy for regional temperature at the time of the snow/ice formation and hence is a central measurement to detect past changes of climate. For a rapid advancement of the science in all areas of climate reconstruction based on ice cores, a field-based analysis method along with the coring operation would be of tremendous value.

The general method for analyzing water isotopes is based on equilibrating isotopes of gaseous carbon dioxide with those of the water at a given temperature in a vacuum-tight sample container. During this equilibration, oxygen isotopes of the water and CO_2 exchange via HCO_3^- and CO_3^{2-}. The equilibration process may be accelerated by shaking these containers.[1] The precision of these measurements is 0.05‰.

Using this conventional method in paleoclimatology is time-consuming: the ice core has to be cut in small sections, which are separately packed. Preparation and measurement is done on each sample later in the laboratory. For the more than 3000-m-long ice core from the Greenland Ice Core Project (GRIP), this corresponds to more than 100 000 single samples. With the increasing demand to produce high-resolution records, we have developed an on-line technique that is capable of processing 1 m of ice within ~1 h with a precision similar to that obtained by a conventional system. Here we describe this new rapid method for oxygen isotope analysis on aqueous solutions.

METHOD AND MATERIALS

The new on-line technique (Figure 1) is based on our continuous flow analysis (CFA) experience.[2,3] For ice samples, we use a melting device similar to that developed for the chemical components (it is bypassed for water sample analysis). This melting device has undergone several improvements and was very successfully used during many field seasons in Greenland and in the Antarctic as well as in different laboratories.[3,4] An ice bar of 10–100 cm in length with a square area of 2 × 2 cm is slightly forced onto a heated device, where the ice continuously melts. The meltwater is pumped off through a borehole (1 cm²) in the center of the melting device. Therefore, only ~25% of the meltwater is used for the actually measurement; the rest is used to seal the melted air–water mixture from ambient air. This is, however, more important for measurement on the air components than for the water isotope determination.[5] The water, both sample and standard, is pumped off by a multichannel tubing pump (Ismatec SA) that has an adjustable pumping speed. A four-way rotary valve (Rheodyne Inc.) is used to change between sample and standard water. In a bubble generator, CO_2 gas is injected either into the sample water or into the standard water stream, depending on the valve position. To obtain a rapid dissolution of the admixed CO_2 in the water, we used a short and thin capillary (15 cm in length with 35 μm in diameter applying a pressure of 3 bar) to produce tiny CO_2 bubbles. The CO_2–water mixture then entered a thin, 0.75-mm-diameter, 2-m-long PEEK ($^1/_{16}$-in. tubing,

* Corresponding author: (phone) ++41 31 631 44 70; (fax) ++41 31 631 87 42; (e-mail) leuenberger@climate.unibe.ch.
(1) Epstein, S.; Mayeda, T. *Geochim. Cosmochim. Acta* **1953,** *4,* 213–224.

(2) Sigg, A.; Fuhrer, K.; Anklin, M.; Staffelbach, T.; Zurmuhle, D. *Environ. Sci. Technol.* **1994,** *28,* 204–210.
(3) Röthlisberger, R.; Bigler, M.; Hutterli, M.; Sommer, S.; Stauffer, B.; Junghans, H. G.; Wagenbach, D. *Environ. Sci. Technol.* **2000,** *34,* 338–342.
(4) Fuhrer, K.; Neftel, A.; Anklin, M.; Maggi, V. *Atmos. Environ.* **1993,** *27A,* 1873–1880.
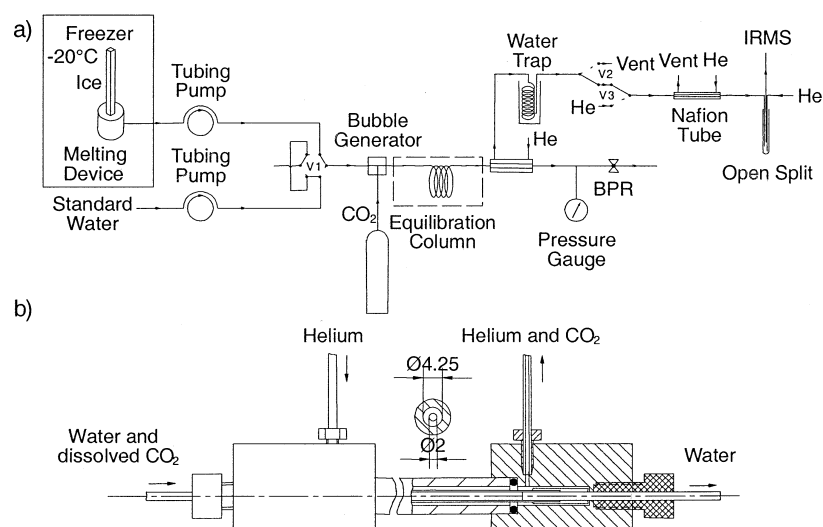(5) Huber, C.; Leuenberger, M., to be submitted.

Figure 1. (a) System layout of the on-line determination of oxygen isotope ratio for water samples and (b) the degassing unit, as described in the Method and Materials section.

Omnilab AG) column where CO_2–H_2O isotope exchange for equilibration immediately starts. This column is immersed into a water bath held at 50 °C. This allows a quick equilibration between the CO_2 and water oxygen isotopes. The residence time in this column is dependent on the pumping rate (melting velocity) defining the pressure gradient applied to the system (in our case, the flux is 1 mL/min corresponding to ~60-s transfer time). The degassing unit (Figure 1b) consists of a gas-permeable membrane (Accurel, Microdyn Techn. Inc.), of 5–10 cm in length and a diameter of 2 mm, that is placed into a plexiglass tube of the same length. Both are fixed on aluminum bodies to seal it from ambient air. The volume between the membrane and the plexiglass tube is flushed with helium, which carries the CO_2 diffusing out of the water flux through the membrane due to the partial pressure difference (pressure of the water is ~0.5 atm above the helium pressure). Seals consists of Teflon tubing and Delrin connectors ($^1/_{16}$-in. Delrin nut, Omnilab AG). The helium flux is sealed with small Viton O-rings pressed onto an aluminum body. The helium–CO_2 mixture (20 mL/min) passes through a water trap (see Figure 1a) held at dry ice temperature (−78 °C) for drying. With a two-position switching valve (V2 and V3 in Figure 1a), one can change between bypass helium and the system helium flux; this allows us to determine the background signals in the isotope ratio mass spectrometer (IRMS) and to remove the degassing unit and the water trap for maintenance without breaking the helium flux of the interface, which connects our measuring system with the IRMS. Into this interface (a GP-Interface, Finnigan MAT) is placed a second drying column (Nafion tubing, Perma Pure Inc.) in front of the open split where the helium–CO_2 mixture enters the IRMS capillary. Only a small percentage of the main flux enters the IRMS capillary. The open split also allows us to dilute the sample gas in order to match the specific requirements of the IRMS. An important unit is the back-pressure regulator (BPR) at the end of the water flux (Jour Backpressure Regulator 0–7 bar, OmniLab AG). It guarantees an adjustable overpressure in the degassing

unit. We usually set it to ~0.5 atm above the helium pressure. A manometer (Mano Gauge 1–10 bar range, Keller AG) is used to continuously monitor the pressure and its fluctuations. Our experience has shown that large pressure fluctuations can lead to a leak in the degassing unit, compromising the measurements.

RESULTS

Hydration Dynamics. A prerequisite for on-line determination of oxygen isotopes of water samples is a fast isotopic exchange between water and added carbon dioxide. However, a complete equilibration between water and carbon dioxide is not required as shown by several test runs. The measured difference with the on-line device, $\Delta\delta^{18}O_{on-line}$, between two water samples did not linearly increase with increasing isotope exchange time. But for a fixed isotope exchange time the ratio of the conventionally to the on-line measured differences is constant. This corresponds to a linear dependence of the on-line to the conventional obtained values. The measurements can therefore be corrected by applying a scaling factor γ according to the eq 1, where $\Delta\delta^{18}O_{on-line}$ and

$$\gamma = \Delta\delta^{18}O/\Delta\delta^{18}O_{on-line} \qquad (1)$$

$\Delta\delta^{18}O$ correspond to the difference between two water samples of oxygen δ-values for the on-line and the conventional system, respectively.

This linear dependence is demonstrated in Figure 2 for three different isotope exchange times, 106, 300, and 1215 s. The slope of the linear dependence corresponds to the inverse scaling factor with which the measured values have to be corrected. The dynamics of the hydration process determines these slopes, i.e., the dependence of those slopes on the isotope exchange time between water and CO_2 isotopes. Dissolved CO_2 is hydrated
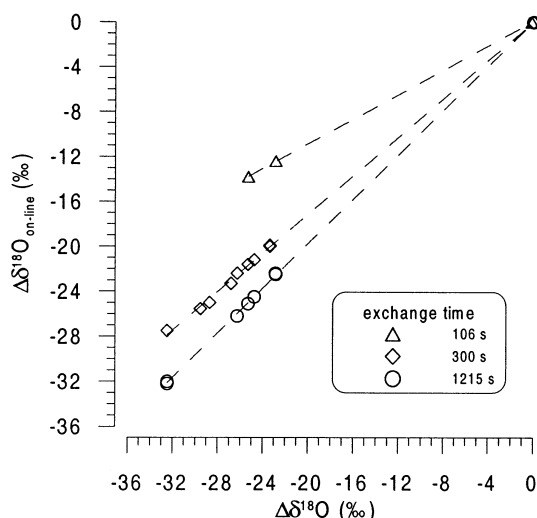
Figure 2. Linear dependence between on-line and conventionally measured differences for three chosen isotope exchange times (106, 300, and 1215 s). The slopes correspond to the inverse scaling factor, γ from eq 1, with which the measured values have to be adjusted to obtain the conventionally measured values.

Table 1. Kinematics of the Hydration of CO_2[a]

T (°C)	k_{CO_2}	$t_{1/2}$ (s)			
		pH = 5	pH = 6	pH = 6.5	pH = 7
0	0.002[pim]	8.9	72	158	251
10	0.007[pim]	3.4	26	52	77
15	0.012[pim]	2.1	16	32	46
20	0.019[pim]	1.5	11	21	29
25	0.030[pim]	0.9	6.5	13	18.5
30	0.055[i]	0.6	4.0	7.5	10.5
30	0.040[m]	0.8	5.5	10.5	14.5
40	0.105[i]	0.3	2.2	4.1	5.5
40	0.070[m]	0.5	3.3	6.1	8.3
50	0.270[i]	0.1	0.9	1.6	2.2
50	0.110[m]	0.3	2.2	3.9	5.3

[a] k_{CO_2} and $t_{1/2}$ are given as functions of the temperature and pH. The multiple values for a given temperature corresponds to the different data fitting procedure as described in Kern[6] and in this study (see also Figure 4). Indexes p, i, and m correspond to photometric, isotopic, and manometric techniques, respectively.
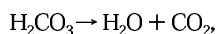
through two paths. Below a pH of 8, the direct hydration is dominant[6,7]

$$CO_2 + H_2O \rightarrow H_2CO_3 \qquad (2)$$

$$H_2CO_3 + OH^- \rightarrow HCO_3^- + H_2O \qquad \text{(immediate)} \quad (3)$$
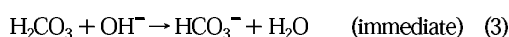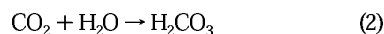
The rate of hydration is

$$-\frac{d[CO_2]}{dt} = k_{CO_2}[CO_2], \quad k_{CO_2} = 0.019 \text{ s}^{-1} \ (T = 20 \text{ °C})$$

The corresponding dehydration processes is

(6) Kern, D. J. Chem. Educ. **1960**, 37, 14–23.
(7) Stumm, W.; Morgan, J. J. Aquatic Chemistry; Wiley-Interscience: New York, 1981.

$$H_2CO_3 \rightarrow H_2O + CO_2,$$

$$k_{H_2CO_3} = k_{CO_2}K \cong 13 \text{ s}^{-1} \ (T = 20 \text{ °C}) \quad (4)$$

For full equilibration, $H_2CO_3 \leftrightarrow CO_2 + H_2O$, $K = [CO_2]/[H_2CO_3]$ $= k_{H_2CO_3}/k_{CO_2}$ is ~700.

Table 1 comprises values for k_{CO_2} as a function of temperature obtained by a variety of techniques for the hydration dynamics that are described in Kern.[6]

For a pH above 10, the direct reaction with OH^- is dominant:

$$CO_2 + OH^- \rightarrow HCO_3^- \qquad (5)$$

$$HCO_3^- + OH^- \rightarrow CO_3^{2-} + H_2O \quad \text{(immediate)} \quad (6)$$
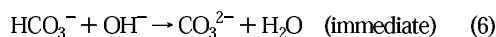
The rate of this reaction is

$$-\frac{d[CO_2]}{dt} = k_{OH}[OH^-][CO_2], \quad k_{OH} = 6300 \text{ s}^{-1}(\text{mol}/L)^{-1}$$
$$(T = 20 \text{ °C})$$

The second path is not important for most of our samples (water samples as well as ice core samples) since they have a pH value of less than 8. Therefore, we investigate in the following the isotopic equilibration processes through the direct hydration according to the eqs 2 and 3. For each hydrated CO_2 molecule according to (2) a new CO_2 molecule is produced by eq 4 as soon as the chemical equilibrium for these two reactions is reached. This newly formed molecule now carries a mixed oxygen isotope signal (one-third from the water signal and two-thirds from the CO_2 signal). This means that the isotopic exchange rate, $k_{isotope}$, is only a third of the CO_2 hydration rate, k_{CO_2}.

With the isotopic exchange rate we can investigate the dynamics of the isotope equilibration process:

$$-\frac{d(\delta^{18}O_{CO_2} - \delta^{18}O_{H_2O} - \epsilon_q)}{dt} =$$
$$k_{isotope}(\delta^{18}O_{CO_2} - \delta^{18}O_{H_2O} - \epsilon_q) \quad (7)$$

where $\delta^{18}O_{CO_2}$ and $\delta^{18}O_{H_2O}$ are the isotopic compositions of CO_2 and H_2O and ϵ_q is the equilibrium fractionation between CO_2 and H_2O.

Assuming that $\delta^{18}O_{H_2O}(t) = \delta^{18}O_{H_2O}$ is constant, we obtain

$$\delta^{18}O_{CO_2}(t) = \delta^{18}O_{H_2O} + \epsilon_q + (\delta^{18}O_{CO_2} -$$
$$\delta^{18}O_{H_2O} - \epsilon_q)\exp(-k_{isotope}t) \quad (8)$$

The measured difference between two samples then corresponds to

$$\Delta\delta^{18}O_{on-line} = \Delta\delta^{18}O(1 - \exp(-k_{isotope}t)) \quad (9)$$

Based on these considerations, we obtain the scaling factor defined by eq 1:

$$\gamma = \frac{\Delta\delta^{18}O}{\Delta\delta^{18}O_{on-line}} = \frac{1}{1 - \exp(-k_{isotope}t)} \qquad (10)$$

This means that this factor is only dependent on the isotopic exchange rate. For a temperature of 20 ± 1 °C, $k_{isotope}$ yields $(6.3 \pm 1.0) \times 10^{-3}$ s^{-1}, since k_{CO_2} is (0.019 ± 0.003) s^{-1}.[6] By fitting our measured values for five different water samples according to eq 9, we obtain a mean value for $k_{isotope}$ of $(6.3 \pm 0.2) \times 10^{-3}$ s^{-1}. For this determination, we reanalyzed samples that previously were measured by a conventional water equilibration system. They cover a $\delta^{18}O$ range of 10‰, when including the reference (-11‰ on the V-SMOW scale), the range widens up to 34‰. Figure 3 shows the isotope exchange as a function of time for these water samples. By normalizing the measured on-line $\delta^{18}O$ values to the previously measured $\delta^{18}O$ values, an additional estimate for $k_{isotope}$ can be derived by fitting the scaling factor (see eq 10) against the applied isotope exchange time. The best fit is obtained for $k_{isotope} = (6.37 \pm 0.11) \times 10^{-3}$ s^{-1} rejecting four values; three of them are values for an isotope exchange time of 1200 s. Both estimates are in very good agreement with the mean literature value for a temperature of 20 °C as given above.[6] In an additional experiment, we extended the isotopic exchange rate value to 40 and 50 °C, as seen in Figure 4, to check which of the two sets of values (photometric and manometric techniques [8]) mentioned by Kern[6] corresponds better with our measured values. From Figure 4, our values depend linearly on the inverse temperature in the logarithmic plot in agreement with measurements of Mills and Urey[9] using the isotope exchange method.

Signal Dispersion. From Figure 3, it is also obvious that for precise measurements a long isotope exchange time is required, ensuring a rather complete isotopic equilibrium. If this is not the case, small variations in the isotope exchange time (occurring through variations in the pumping force and alteration in dissolution velocity of CO_2 in water) or variations in the exchange rate (dependent on pH or temperature variations) will lead to significant changes in the measured signal. On the other hand, the larger the isotope exchange time is the higher the signal dispersion becomes, which has a direct influence on the resolution of the system. In our system, the water passes through a pipe with radius, R. For our settings, we can assume that the flux is laminar. After Navier–Stokes, a parabolic velocity profile is expected with the central fluid parcel having twice the mean velocity and is sticking at the edges. Based on these large velocity gradients within the pipe, a dispersion builds up that increases with the isotope exchange time. However, the Navier–Stokes approach leads to far too high dispersion times compared to values obtained from our measurements. This can be understood by the fact that molecular diffusion in a radial direction dampens the developing dispersion. Molecular diffusion forces the dissolved CO_2 molecule to diffuse toward the edges of the pipe, where the velocity is lower than in the center. Taylor[10,11] and Aris[12] investigated the dispersion of a dissolved material in a fluid, which is now referred to as the Taylor–Aris dispersion. After Taylor, the mean concentration

Figure 3. (Top) On-line $\delta^{18}O$ measurements plotted against the isotope exchange time for five different water samples. The curves are calculated after eq 9 by adjusting $k_{isotope}$. (Bottom) Normalized measurements of the top panel according to eq 10 versus the isotope exchange time. This normalized values correspond to the scaling factors. The curve is fitted to the values through eq 10 by varying $k_{isotope}$.

$c(z, t)$ of the dissolved material over the square area of the pipe can be given by a diffusion equation such as

$$\frac{\partial c}{\partial t} + u\frac{\partial c}{\partial z} = D\frac{\partial^2 c}{\partial z^2} \quad \text{where} \quad D = D_{CO_2}\left(1 + \frac{1}{48}\frac{u^2 R^2}{D_{CO_2}^2}\right) \qquad (11)$$

where R, z, and D_{CO_2} denote the pipe radius, the coordinate along the pipe, and the diffusion coefficient of CO_2 in water. The mean velocity of the dissolved matter is u with a Gaussian distribution that becomes larger with $(Dt)^{0.5}$. The main contribution to the dispersion is given by the term $1/48(u^2R^2/D_{CO_2})$ that is inversely proportional to the diffusion constant of CO_2. For a constant water flux, F, the mean velocity $u(R, F)$ becomes $F/\pi R^2$. The dispersion time, T, is $4[D(R)t]^{0.5}/u(R, F)$. According to eq 11, the increase

(8) Pinsent, B.; Roughton, F. *Trans. Faraday Soc.* **1951**, *47*, 263−269.

(9) Mills, G.; Urey, H. *J. Am. Chem. Soc.* **1940**, *62*, 1019−1026.

(10) Taylor, G. *Proc. R. Soc. London* **1953**, *A219*, 186−203.

(11) Taylor, G. *Proc. R. Soc. London* **1954**, *225*, 473−477.

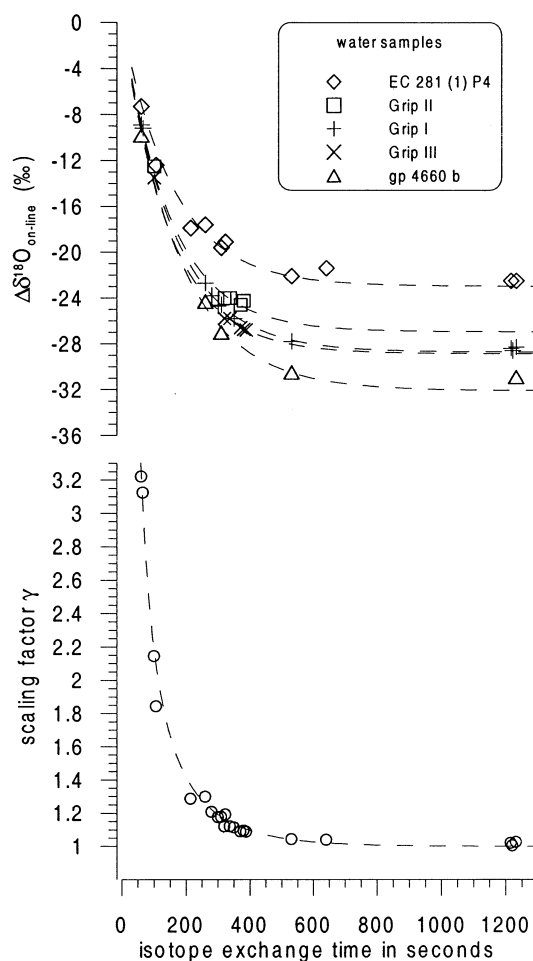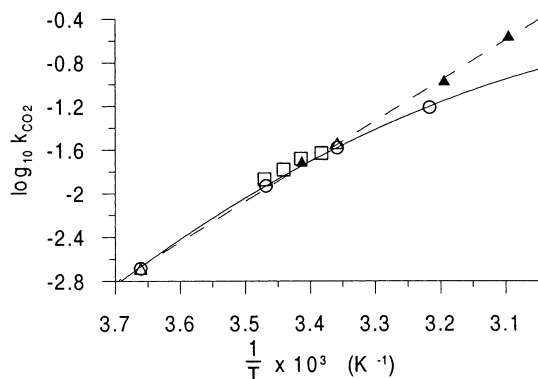(12) Aris, R. *Proc. R. Soc. London* **1956**, *235*, 67−77.

Figure 4. Logarithmic plot for k_{CO_2} versus the inverse temperature. Squares and circles correspond to previously published values obtained by the photometric and manometric hydration techniques, respectively.[8] Triangles corresponds to values obtained by the isotope exchange technique (filled triangles refer to our values for three different temperatures, open triangles is from Mills and Urey[9]). The solid line follows the manometric data. The dotted line is obtained by a linear fit through our data completed by the two isotopic data points from Mills and Urey,[9] which are in good agreement.

becomes proportional to R and $t^{0.5}$ when the product uR is large compared to D_{CO_2}. Hence, for a minimal dispersion influence, one requires not only a short isotope exchange time but also a small pipe radius. However, the pipe cannot be too small in diameter because the pumping resistance will grow as $\propto R^{-4}$. This optimization problem has to be solved according to the specific needs of the applications, either an excellent precision (long isotope exchange times, mean pipe diameter) or high resolution in time (short isotope exchange time, small pipe diameter).

Our measured dispersion values can be understood with Taylor's theory. However, besides the Taylor dispersion in a pipe, there are other mechanisms leading to an enhanced widening of our signal. In particular, the length of the Accurel membrane and the direction of the helium carrier flux are important. In Figure 5b, two estimates of dispersion times of our system for a steplike signal are shown, for a 10-cm Accurel membrane with a backflush helium carrier and a 5-cm Accurel membrane with an unidirectional helium carrier flux. The dispersion is, as expected, smaller for the second case by 5 s. About 70% of this reduction comes from the shorter Accurel membrane and about 30% is due to the equal direction helium carrier flux since the carrier gas moves the same direction as the signal. However, a disadvantage of shorter membrane is a lower degassing efficiency, implying a higher admission of CO_2 gas, which could lead to a longer dissolution of CO_2. This could finally lead to a lower reproducibility.

Resolution of Ice Core Measurements. Resolution of the conventional equilibration method used for discrete samples must be chosen prior to sampling. For the GRIP samples were targeted to a 2-cm resolution. This corresponds to an enormous amount of samples to be measured ($\sim$100 000). The resolution of our system depends mainly on (i) the melting velocity of the ice, (ii) the dispersion in the equilibration column as described above, (iii) the dispersion associated with gas extraction membrane and the direction of carrier flux, and (iv) the open split characteristic. The melting velocity of the ice is commonly set to $\sim$3 cm/min
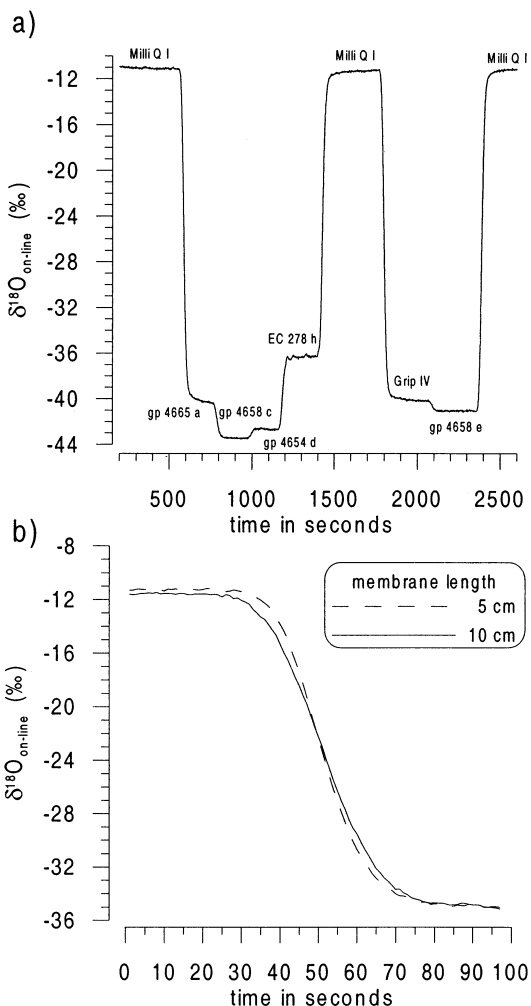
Figure 5. (a) Continuous measurement of oxygen isotope ratio for a sequence of Greenland ice core water samples. Our standard (Milli-Q I) is purified tap water with a δ-value of $-11.10\%_0$ against V-SMOW. Sample description is given for each signal level. (b) Dispersion of our measuring system for a steplike signal, for a 10-cm-long Accurel membrane combined with a backflush helium carrier (flux directions are opposite, solid line) and for a 5-cm-long Accurel membrane combined with a helium carrier set to the same flux direction (dashed line).

(temperature of the melting device 25 °C). However, it would be possible to lower this velocity by lowering the melting device temperature. A water flux of 1 mL/min, corresponding to 1 cm/ min for our melting device with an area of 1 cm^2, is sufficient. Therefore, the melting velocity allows us to adjust the resolution such that it meets the application needs. For a fixed water flux, the resolution is actually determined by the dispersions either in the equilibration column, in the degassing unit, or in the open split. The main contribution comes from the dispersion in the equilibration column since a compromise between dispersion time and equilibration percentage must be found. Full equilibration leads to longer tubes and therefore higher dispersion times (see also below). The dispersions associated with the open split and

Table 2. Compilation of Seven On-Line Measuring Sequences (A−H) of Overall 13 Different Greenland Ice−Water Samples Previously Measured with the Conventional Equilibration Technique[a]

ice−water sample	conventional measured $\delta^{18}O(^0/_{00})$	difference between on-line and conventional measurements $(\delta^{18}O_{on-line} - \delta^{18}O(^0/_{00}))$									
		A	B	C	D	E	F	G	H	mean	std dev
Eiswasser I/2	−35.50	0.15	0.10							0.13	0.04
EC 278 f	−35.76								0.36	0.36	
EC 278 h	−36.25			−0.05	0.15					0.05	0.10
EC 278 k	−36.28					0.08	0.08	−0.02		0.05	0.05
gp 4666 a	−38.92	0.02	0.22							0.12	0.10
gp 4658 b	−40.26	0.16								0.16	
gp 4665 a	−40.39			0.09						0.09	
Grip IV	−40.58			0.38						0.38	
gp 4658 e	−41.36			0.26	0.06		0.36			0.23	0.12
gp 4654 d	−42.67			0.02			−0.03	−0.13	0.07	−0.02	0.07
gp 4658 c	−43.48			0.08	−0.02	0.08				0.05	0.05
gp 4662 b	−43.63		0.08							0.08	
gp 4659 e	−43.89	0.04								0.04	

[a] As standard we used purified tap water (Milli-Q) with a $\delta^{18}O$ of −11.10‰ on the V-SMOW scale.

the degassing unit are mainly dependent on the geometrical dimensions that can be adjusted. They are in our case lower than the dispersion in the equilibration column. Our system gives us a dispersion of ∼30 s defined as the time between 8 and 92% of the isotope signal change (Figure 5b). Therefore, an ice melting velocity of 3 cm/min corresponds to a core resolution of ∼1.5−2 cm dependent on the $\delta^{18}O$ range of the sample. This can be improved by lowering the melting device temperature and therefore the melting velocity. With the present melting device, a maximum core resolution slightly larger than 0.5 cm is possible.

Precision of Measurements. As mentioned above, precision depends on several variables of the system. One important parameter is the percentage of equilibration. From Figure 3 it is obvious that a nearly complete equilibration leads to a better precision due to minimal changes in the scaling factor. To improve precision without having counteracting influences on the dispersion, we increased the equilibration temperature to 50 °C. This leads to a more than 14.5-fold shorter time for complete equilibration compared to ambient temperature of 20 °C. An example of such a measurement is given in Figure 5a (corresponds to sequence C in Table 2). It is a continuous measurement of oxygen isotope ratios for a sequence of Greenland ice core water samples over a measuring time of ∼45 min. The δ-value range of those samples is more than 9‰, when including the standard (Milli-Q I), it extents to more than 30‰, which is much larger than actual changes in ice cores. Therefore, this plot underestimates the precision but allows us to determine the dispersion (defined as 8−92% signal time) rather well. Table 2 shows a compilation of seven measuring sequences (capital letters A−H on the top of the columns) of different Greenland ice−water samples that were previously measured with the conventional equilibration technique. As standard we used purified (Milli-Q system) tap water with a $\delta^{18}O$ = −11.10‰ on the V-SMOW scale. For each measuring sequence, at least one standard water check was performed prior and after the sample sequence (see Figure 5a). The Greenland samples vary between −34 and −44‰ V-SMOW. The values obtained by the conventional method are given in column two. The differences between on-line and conventional determinations of oxygen isotope ratios for are given in columns
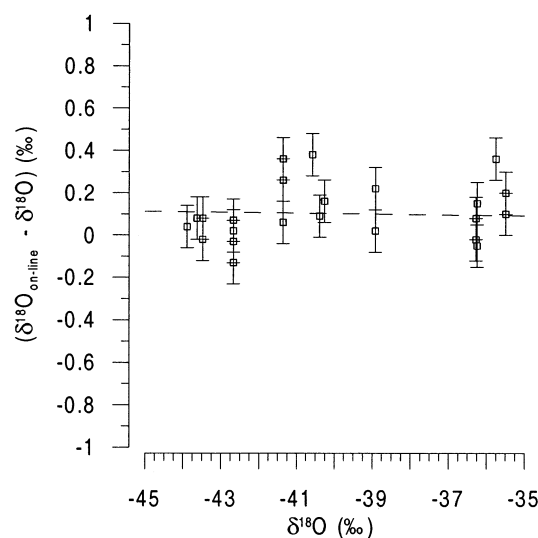
Figure 6. Measurement precision of on-line oxygen isotope determination as derived from 14 different water samples (squares). The precision of the measurements as obtained from replicate determinations is ∼0.1‰ (error bars). An indication of the accuracy of those values is given by the standard deviation of the differences between on-line and conventional determinations, which is 0.13‰. The small offset from zero can be explained by a slightly incomplete equilibration (see text).

A−H. They vary in the range of −0.13 to +0.38‰. The values are on average 0.1‰ too high. This can be explained by a slightly incomplete equilibration (99.6%) of the order of a few per mil (scaling factor 1.004 ± 0.001). The means and standard deviations of replicates of those water samples are given in the last columns. The standard deviation for a single sample difference is 0.13‰. The standard deviation of replicates is lower, namely, 0.08‰. Since the former number includes the uncertainty of the conventional method of 0.05‰, the precision as well as the accuracy are similar, i.e., 0.1‰ (Figure 6).

Complications with Impurities in the Ice. Ice water samples are not as clean as our standard, purified tap water. In particular,

ice from glacial times carries more impurities than ice from interglacial times. Furthermore, Greenland ice contains many more impurities than Antarctic ice.[13] Chemical impurities have to be checked in this respect since they have the potential of altering the pH value of the melted ice. In the worst case, a buffering of the expected pH drop during the addition of CO_2 may lead to a different path of hydration which could influence our isotope determination. However, our experience with Greenland ice–water samples (Table 2) does not support this view. The kinematics of the CO_2 hydration is very fast (<2.5 s) for pH 5–7 at a temperature of 50 °C (Table 1.). Therefore, no major problems should be expected from chemical impurities. Perhaps more important could be major impurities with particles (dust), which could affect the permeability of the Accurel membrane. However, we did not experience this problem during our test measurements.

CONCLUSIONS AND OUTLOOK

The presented on-line measuring system is capable of handling a wide range of aqueous solutions for precise and rapid oxygen isotope ratio determinations (patent pending). The authors can foreseen several applications in the fields of glaciology, hydrology, geology, pharmacy, and medicine, since the new method allows a simple and fast analysis procedure in a fully continuous or semicontinuous mode (switching between single samples). In glaciology, we see the following advantages: (i) continuous measurements on ice sections and thus high-resolution isotope profiles along the ice core can be obtained; (ii) isotope field measurements may become possible soon; (iii) can be coupled to a CFA melting device. Such a system combined with a benchtop mass spectrometer may allow one to continuously measure the water isotopes in the field shortly after the ice core retrieval. This would be a major step forward in establishing an age scale already in the field.

(13) Anklin, M.; Barnola, J. M.; Schwander, J.; Stauffer, B.; Raynaud, D. *Tellus* **1995**, *47 B*, 461–470.

2.2 Fast High-Precision On-Line Determination of Hydrogen Isotope Ratios of Water or Ice by Isotope Ratio Mass Spectrometry

Christof Huber[1] and Markus Leuenberger[1]

Abstract

In this paper a new fast high-precision on-line technique is described for the determination of hydrogen isotope ratios of water by continuous-flow mass spectrometry. This technique completes our new on-line $\delta^{18}O$ technique described in the previous section. For the first time H_2/H_2O-equilibration using a platinum catalyst has been used in a fully continuous process. A significant reduction of the H_2/H_2O-equilibration time is achieved by a complete vaporization of the water and by increasing the exchange temperature to $100°C$. The analysis time is only ~ 5 minutes per sample which includes equilibration and processing. Measurement precision and accuracy are better than $1^0\!/_{00}$ and sample consumption is only ~ 5 mL. This new technique allows measuring a wide range of aqueous samples either in a semi-continuous way (discrete samples are injected one after another) or in a fully continuous way. This allows us, for the first time, to make continuous measurements of ice cores.

---

[1]Climate and Environmental Physics, Physics Institute, University of Bern, Sidlerstrasse 5, CH-3012 Bern, Switzerland

RCM

Fast high-precision on-line determination of hydrogen isotope ratios of water or ice by continuous-flow isotope ratio mass spectrometry

C. Huber* and M. Leuenberger

Climate and Environmental Physics, Physics Institute, University of Bern, Sidlerstrasse 5, 3012 Bern, Switzerland

Received 7 March 2003; Revised 14 April 2003; Accepted 14 April 2003

A new fast high-precision on-line technique is described for the determination of hydrogen isotope ratios of water by continuous-flow mass spectrometry. For the first time H_2/H_2O-equilibration using a platinum catalyst has been used in a fully continuous process. A significant reduction in the H_2/H_2O-equilibration time is achieved by a complete vaporization of the water and by increasing the exchange temperature to 100°C. The analysis time is only ~5 min/sample which includes equilibration and processing. Measurement precision and accuracy are better than 1‰ and sample consumption is only ~5 μL. This new technique allows the measurement of a wide range of aqueous samples either in a semi-continuous way (discrete samples are injected one after another) or in a fully continuous way. This allows us, for the first time, to make continuous measurements of ice cores. Copyright © 2003 John Wiley & Sons, Ltd.

The measurement of the isotopic composition of water is one of the most important applications in a wide variety of disciplines, such as paleoclimatology, hydrology, geology, atmospheric chemistry, biology and medicine. Water consists of oxygen and hydrogen, thus the isotopic ratios of oxygen $^{18}O/^{16}O$ ($\delta^{18}O$), $^{17}O/^{16}O$ ($\delta^{17}O$) and hydrogen D/H (δD) can be determined. Isotopic ratios are commonly expressed as deviations relative to a standard using the delta notation: $\delta = (R_{sample} - R_{standard})/R_{standard} \times 1000‰$, where R is the abundance ratio of the isotopes (e.g. $R = {}^{18}O/{}^{16}O$).

Many different techniques exist to measure δD or $\delta^{18}O$ of water. Traditionally, most of the methods make use of an isotope ratio mass spectrometer (IRMS). Due to the fact that water vapor is strongly absorbed onto the walls of vacuum systems, large memory effects are observed if water is introduced directly into an IRMS. Therefore, water has to be converted into hydrogen (for δD) or CO_2 (for $\delta^{18}O$) which can be analyzed in an IRMS. Molecular hydrogen, H_2, can be produced by reduction of water over hot uranium,[1] zinc,[2] magnesium or chromium.[3,4] The classical chromium reduction method needs about 1 μL of water to measure δD with a precision better than 1‰ by conventional dual-inlet mass spectrometry. Recently, Morrison *et al.*[5] described an on-line method for the measurement of small water samples using chromium, and reported a precision of 0.5‰ on water samples of 0.5 μL.

Alternatively, there are equilibration techniques available: (i) H_2/H_2O-equilibration using a platinum catalyst for hydrogen isotopes,[4,6,7] and (ii) CO_2/H_2O-equilibration for oxygen isotopes.[8] The advantage of the equilibration techni-

que is the high precision of <1‰ for δD and <0.1‰ for $\delta^{18}O$. Disadvantages are the time-consuming equilibration process, about 1 h for H_2/H_2O-equilibration and up to 24 h for the CO_2/H_2O-equilibration, and the rather large sample consumption (1–5 mL). In addition, Begley *et al.*[9] described an on-line pyrolysis technique able to measure δD and $\delta^{18}O$ on small samples (down to 1 μL) with a good precision (~2‰ for δD and ~0.3‰ for $\delta^{18}O$). Furthermore, a new spectroscopic technique for the simultaneous determination of δD, $\delta^{17}O$ and $\delta^{18}O$ is able to deal with 10 μL of water with a precision of 0.7‰ for δD and 0.5‰ for $\delta^{17}O$ and $\delta^{18}O$.[10]

In paleoclimatology the determination of the isotopic composition of water obtained from Greenland and Antarctic ice cores is a central measurement to detect past changes in climate since water isotopes of polar precipitation are affected by regional temperature and moisture source as well as circulation patterns. Due to the enormous length of these ice cores an enormous effort is required to obtain a highly resolved isotope record by conventional equilibration techniques. For the more than 3000-meter long ice core from the Greenland Ice Core Project (GRIP), more than 100 000 single samples had to be cut and analyzed separately. Therefore, a fast continuous melting and analysis technique would be of tremendous value. Besides paleoclimatology, water isotope measurements are also important in the hydrological study of groundwater systems, in physiological studies of metabolism by means of labeled water, and in food authenticity studies.

In this paper we describe a new fast on-line technique for the determination of δD of an aqueous solution in a fully continuous way. Coupled to a melting device, this technique is able to measure ice samples continuously. The sample analysis time is only ~5 min with a sample consumption of ~5 μL and a measurement precision better than 1‰. This

Correspondence to: C. Huber, Climate and Environmental Physics, Physics Institute, University of Bern, Sidlerstrasse 5, 3012 Bern, Switzerland.
E-mail: huber@climate.unibe.ch

1320   C. Huber and M. Leuenberger

technique complements our previously described fast on-line $\delta^{18}O$ technique,[11] which deals with about 5 mL of water and achieves a precision of ~0.1‰.

EXPERIMENTAL

Principles and instrumentation
The technique is based on the exchange reaction (Eqn. 1) between water vapor and hydrogen using a platinum catalyst.

$$H_2O(v) + HD \leftrightarrow HDO(v) + H_2 \qquad (1)$$

Hydrogen in equilibrium is very depleted in deuterium. The isotope distribution in the gas phase is given by the equilibrium constant, K_1.

$$K_1 = \frac{[HDO].[H_2]}{[HD].[H_2O]} = \frac{R_{H_2O}}{R_{H_2}} \qquad (2)$$

The equilibrium constant, K_1, is about 3.53 at 25°C. The fractionation factor α between H_2 and liquid water is slightly higher, about 3.81 at 25°C.[12,13] The natural abundance of deuterium in water is only 0.016% (155.76 ppm for the V-SMOW standard[14]). After conventional equilibration at 25°C the remaining deuterium content is only 0.004%; this corresponds to $\delta D = -737.5‰$ (vs. V-SMOW). This depletion in deuterium makes the precise determination of the D/H ratio difficult. Furthermore, this fractionation is highly temperature-dependent, ~6‰ per degree at 25°C and ~3.3‰ per degree at 100°C,[12,13] and therefore temperature control to ±0.1°C or better is necessary.

Since the exchange reaction (1) occurs only between water vapor and hydrogen and the fractionation is lower at elevated temperatures, we concluded that for a fast exchange with a slightly lower deuterium depletion, a completely vaporized water sample and a high exchange temperature would be needed. The equilibrium constant, K_1, at 100°C is 2.58.[12,13] This corresponds to $\delta D = -612.4‰$.

A schematic of the new on-line technique is given in Fig. 1. The principle of the new technique requires continuous and stable injection of water and H_2 into an equilibration chamber held at a controlled temperature of 100°C, where the water vaporizes immediately and a platinum catalyst supported on a hydrophobic polymer (Hokko beads, Shoko Co. Ltd., Japan)

actuates the exchange reaction. Helium (He), the carrier gas, flushes the equilibration chamber constantly. After the equilibration chamber the gas is dried and continuously injected via an open split into an IRMS. We used a DELTA^{plus}XL isotope ratio mass spectrometer (Thermo Finnigan MAT GmbH, Germany). This IRMS is optimized for the on-line measurement of D/H isotope ratios in a He carrier gas stream, with the complete suppression of the interference of the $^4He^+$ carrier peak with the neighboring HD peak on m/z 3 and a very low H_3^+ production rate in the ion source. We used a $1 \times 10^9 \, \Omega$ resistor on m/z 2 and a $1 \times 10^{12} \, \Omega$ resistor on m/z 3.

Standards and samples
Three different water samples, seawater ('Meerwasser': $\delta D = 1.05 \pm 0.40‰$) and polar ice water ('Dye III': $\delta D = -210.30 \pm 0.40‰$ and 'Dome C': $\delta D = -428.04 \pm 0.40‰$), were calibrated against V-SMOW and were used as our working standards. Another internal water standard ('Standard 91 HD': $\delta D = -83.25 \pm 0.40‰$ vs. V-SMOV) and eight external IAEA (International Atomic Energy Agency) water standards were used to test the new system.

Additionally, we re-analyzed different rainwater samples, which had previously been measured by the conventional chromium reduction technique (H/Device coupled to a MAT 250, Thermo Finnigan MAT). These water samples cover a δD-range from −14‰ to −203‰ vs. V-SMOW.

Samples and standards were stored in glass containers sealed with a rubber membrane (BGB Analytik AG, Switzerland). The volume of the containers was 2 mL for samples and 37 mL for standards.

Procedure
The water is injected continuously into the system (Fig. 1). The rubber membrane of the glass containers is punctured by a hollow needle that is connected with a multi-channel tubing pump (IP Series, Ismatec SA, Switzerland) through which the water (1–2 μL/min) is injected into an equilibration chamber. Its volume of 5 mL is filled with 50–100 Hokko beads of 0.5–1 mm diameter. H_2 (1–2 mL/min) is added directly from a high-pressure cylinder through a very fine fused-silica capillary to obtain a constant flux. Additionally, the equilibration chamber is constantly flushed with He
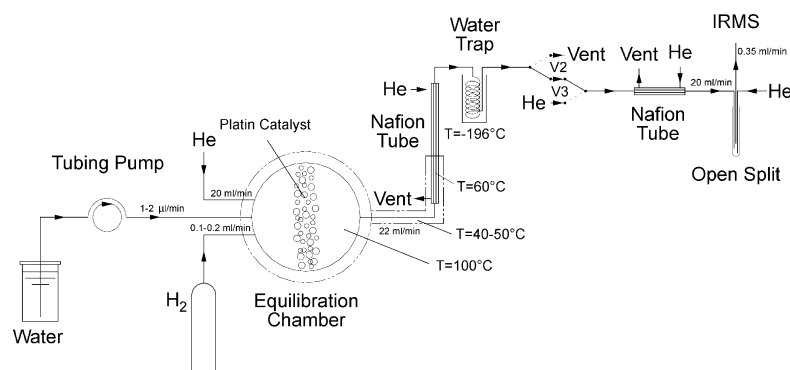

Figure 1. Schematic diagram of the on-line determination system for hydrogen isotope ratio on water samples.

RCM

(20 mL/min). The temperature of the equilibration chamber is held at 100°C by a Jumo-regulator (Jumo dTRON 16.1) which controls four 100-W heating cartridges. After the equilibration chamber the water vapor is removed using a Nafion drying column (0.36 mm i.d. × 60 cm; Perma Pure Inc., USA) and a subsequent cold trap held at liquid nitrogen temperature ($T = -196°C$). Tubing between the equilibration chamber and the Nafion drying column is heated at a temperature of 40–50°C, to prevent condensation of water vapor on the walls. With a two-position switching valve (V2 and V3 in Fig. 1) one can select between the bypass He and the system He flux; this allows us to determine the background signals of the IRMS, and to remove the equilibration chamber and the water trap for maintenance without breaking the He flux of the interface which connects our measuring system to the IRMS. Into this interface (GP-Interface, Finnigan MAT) a second Nafion drying column (0.36 mm i.d. × 18 cm) is placed in front of the open split where the He/H$_2$ mixture enters the IRMS capillary. Only a small percentage of the main flux enters the IRMS capillary. The open split also allows us to dilute the sample gas in order to match the specific requirements of the IRMS.

Corrections

At least two standards were measured at the beginning and end of a measuring sequence to apply the different corrections. Standards and samples were injected sequentially without interrupting the water flux. The following corrections were applied.

Background correction

Background signals were determined prior to a measurement by venting the IRMS with pure He and measuring the signal intensities of the m/z 2 and m/z 3 ion beam. We measured rather large m/z 2 signal intensities of ~0.2–0.6 V due to ^{4}He^{2+} production (He pressure of 2×10^{-6} mbar). However, this signal was very stable during measurement and could be corrected easily. Due to the complete suppression of ^{4}He$^+$ ions the signal intensities on m/z 3 (^{3}He$^+$) were only ~1–15 mV.

H$_3^+$ correction

Measurement of δD in an IRMS is influenced by the formation of H$_3^+$ ions in the ion source. H$_3^+$ ions contribute to the m/z 3 signal. There is a linear relationship between the measured ratio, $R_{m/z\,3/2}$, of the ion intensities for m/z 3 and m/z 2, and the pressure of H$_2$ in the ion source (signal intensity on m/z 2, $I_{m/z\,2}$). We measured this relationship, k, daily by varying the injected H$_2$ flux to the ion source (see Fig. 2). H$_3^+$-factors were between 8 and 30 ppm/nA. The H$_3^+$-corrected isotope ratio, R_{H_2}, was calculated by:

$$R_{H_2} = R_{m/z\,3/2} - k \cdot I_{m/z\,2} \qquad (3)$$

Correction of the influence of the original isotopic composition of the H$_2$

A linear correction had to be applied to correct for the influence of the original isotopic composition of the H$_2$. The molecular H$_2$/H$_2$O mixing ratio, as in conventional methods using H$_2$/H$_2$O-equilibration, is usually between 1/100 and 1/1000.
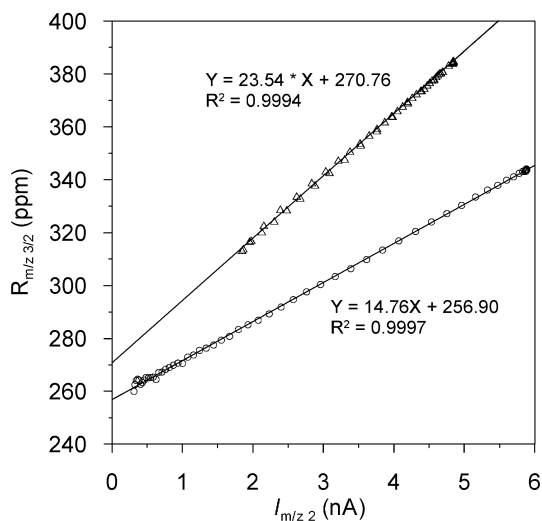
Figure 2. Effect of H$_3^+$ production in the ion source. The ratio of the ion beam intensities for m/z 3 to m/z 2 ($R_{m/z\,3/2}$) is plotted against the ion beam intensity on m/z 2 ($I_{m/z\,2}$) for two different measuring periods.

The influence of the H$_2$ isotopic composition is therefore less than 1% and can be neglected if the difference of the isotopic composition between H$_2$ and H$_2$O is not too large. In contrast, we equilibrated a liquid water flux (B) of only about 1 μL/min water (1 μL liquid water corresponds to ~1.2 mL STP water vapor) with a H$_2$-flux (A) of about 0.1 mL STP/min. Therefore, our H$_2$/H$_2$O mixing ratio, $X = A/B$, was about 1/10, meaning that the original isotopic composition of the H$_2$ contributes significantly to the final isotope ratio of the measured H$_2$. The isotope balance of the process (1), where A and B are the molecular fluxes of H$_2$O and H$_2$, respectively, can be expressed as follows:

$$A \cdot R_{H_2}^{orig} + B \cdot R_{H_2O}^{orig} = A \cdot R_{H_2} + B \cdot R_{H_2O} = (A + B \cdot K_1)R_{H_2} \qquad (4)$$

Equation (4) gives the isotope ratio of H$_2$, R_{H_2}, at the end of the equilibration, which is governed by the original isotopic composition of H$_2$ and H$_2$O and the equilibrium constant K_1 from Eqn. (3). According to Eqn. (4), and due to the fact that the H$_2$/H$_2$O mixing ratio ($X = A/B$) was constant for sample and standard, we can write the original isotopic composition of the water in the δ-notation:

$$\delta D_{H_2O}^{orig} = \left(\frac{R_{H_2O(sample)}^{orig}}{R_{H_2O(standard)}^{orig}} - 1 \right) \cdot 1000(‰) = C \cdot \delta D_{H_2} \qquad (5)$$

$$C^{-1} = 1 - \frac{X \cdot R_{H_2}^{orig}}{(X + K_1) \cdot R_{H_2(standard)}} \qquad (6)$$

From Eqns. (5) and (6) it follows that the isotopic composition of H$_2$ after the equilibration is directly proportional to the original isotopic composition of H$_2$O. Therefore, the measured δD_{H_2}-values have to be corrected with a constant scaling factor C to obtain the original δD_{H_2O}-values

1322   C. Huber and M. Leuenberger

of the water. To determine this scaling factor we measured at least two different standards during a measuring sequence and performed a two-point calibration, similar to what is done for linear V-SMOV-SLAP calibration.[14] We obtained scaling factors C between 1.06 and 1.12 ($R_{H_2}^{orig} \cong 0.25 \times 10^{-3}$, $R_{H_2(standard)} \cong 0.15 \times 10^{-3}$, $X \cong 0.1$ and $K_1 \cong 2.58$), depending on the settings of the H_2- and H_2O-fluxes.

To achieve a precision of the V-SMOV-SLAP calibration better than $\pm 1‰$ the relative variability of the scaling factor C should be lower than $((428 \pm 1)/428 - 1) \times 1000‰ = \pm 2.3‰$ during a measuring sequence. According to Eqn. (6), variability of C can be caused by an unstable H_2/H_2O mixing ratio X, and variations of the equilibrium constant K_1. Since the equilibration temperature is controlled at $100 \pm 0.1°C$ (corresponds to $K_1 = 2.580 \pm 0.001^{12,13}$), the relative variability of C caused by temperature variations is less than $\pm 0.03‰$ and can be neglected. Therefore, the variability of C depends mainly on the variability of the H_2/H_2O mixing ratio X. The relative variability of the H_2/H_2O mixing ratio should be smaller than $\pm 3.5\%$ to reach the required precision (see Eqn. (6)). In our case the H_2 flux remains very stable, since pressure variations are small. Moreover, the relative variability of the rotor speed of the tubing pump (IP Series, Ismatec SA, Switzerland) that we used to pump the water is smaller than 5 and 2.5% for flow rates of 1 and 2 µL/min, respectively. Therefore, it is possible to reach the required stability with our system. By using a tubing pump of the IP-N Series (Ismatec SA), the relative variability of the rotor speed could be reduced by a factor of 4.

Drift correction
Drifts can be caused for example by slight room temperature variations or ambient pressure changes through time, or due to water accumulations in the cold trap and/or in the ion source. Since we measured standards at the beginning, during, and at the end of a measuring sequence, we were able to observe drifts during analysis. Standards were measured at least every hour. We observed maximum drifts of about 3.5‰/h. We obtained good results by correcting drifts linearly between two neighboring standard measurements.

RESULTS AND DISCUSSION

Dispersion and memory effects
Since standards and samples are processed sequentially without interrupting the water flux, a mixing of the gases during the process causes a dispersion of the signal. The dispersion could be observed at the transition from one sample to another (Fig. 3). For a step function the dispersion time, t_{disp}, is defined as the time required to increase the signal from 16 to 84% of full step height. An estimate of the dispersion time is given by the residence time of the gas in the system. The over-all volume of the system is ~ 13 mL (equilibration chamber 5 mL, tubing ~ 1 mL, cold trap ~ 7 mL), the He carrier gas flux is 20 mL/min, resulting in a mean residence time of about 39 s. The measured dispersion time was 35 s. Assuming a Gaussian distribution of the dispersed signal, after $t = 2 \times t_{disp}$ the influence of the previous sample to the actual measurement (memory effect) would be about 2% and after $t = 3 \times t_{disp}$ only about 1‰. To avoid mem-
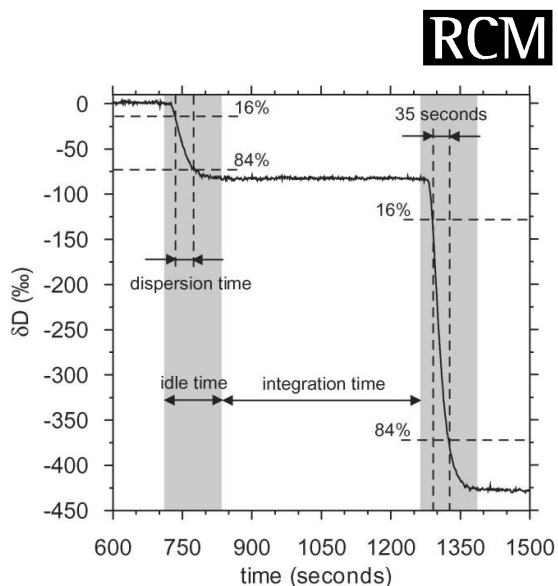
Figure 3. Dispersion of the signal due to mixing of the gas passing through the system. For a step function the dispersion time, t_{disp}, is defined as the time required to increase the signal from 16 to 84% of full step height. In order to avoid memory effects, an idle time of $(3 - 4)t_{disp}$ is applied prior to signal integration.

ory effects we include an idle time at the onset of the transition before we start the integration. Depending on the δD-difference between the consecutive waters, the idle time was between 100 and 150 s (corresponds to $3 \times t_{disp}$ to $4 \times t_{disp}$). A reduction in the cold trap volume to 1.5 mL would result in a lower dispersion time of about 20 s. Therefore, the idle time could be reduced to about 60–80 s.

When the new system is used for continuous measurements, the dispersion time limits the achievable resolution of the measurement. The dispersion has the same impact on the continuous data record as a Gaussian filter with a time constant t_{disp} would have.

Analysis time
In Fig. 4 an example of a measuring sequence of eight rainwater samples is plotted. At the beginning and at the end of the sequence three standards were measured. Each standard was injected for 400 s, of which 250 s was integration time and 150 s was idle time due to the dispersion of the system. Each sample was injected for 300 s, 200-s integration time and 100-s idle time. This gives a total analysis time of 80 min for eight samples corresponding to 10 min/sample.

However, for an improved system, the analysis time could be reduced significantly due to the following reasons: (i) tests showed that the integration time can be reduced to 150 s for standards and 100 s for samples without any loss of precision; (ii) additionally the reduced dispersion time allows shorter injection times (300 s for standards and 200 s for samples); and (iii) measuring more samples per sequence reduces the analysis time per sample, since only one additional standard has to be measured about every hour for drift correction. Therefore, we are able to measure a sequence of 18 samples in about 90 min (~ 5 min/sample), or a sequence of 36 samples in about 150 min (~ 4 min/sample).

RCM
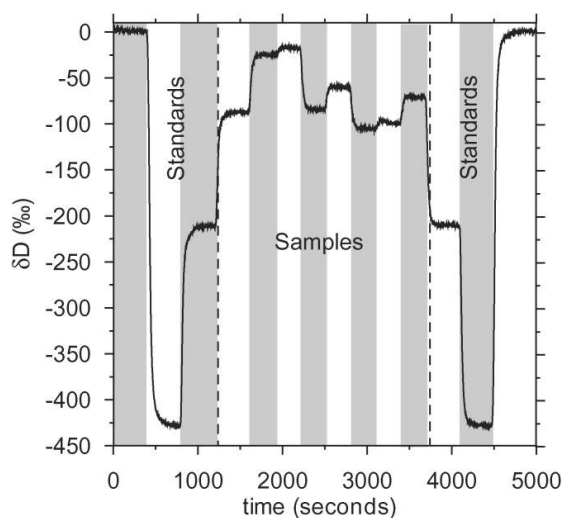
Figure 4. Example of a continuous measuring sequence of eight different rainwater samples. At the beginning and at the end of the sequence three working standards were measured without interrupting the water flux to the system.

Accuracy and precision

Replicate measurements of internal standards

The accuracy and precision of the new technique were determined for the two internal standards 'Dye III' and 'Standard 91 HD' (Table 1). The data in Table 1 have been corrected and scaled to a V-SMOV-SLAP linear calibration by our working standards 'Meerwasser' ($\delta D = -1.05‰$) and 'Dome C' ($\delta D = -428.04‰$). The precision (1 SD) of the measurement of replicate injections was 0.8‰ for 'Dye III' (n = 14) and 0.9‰ for 'Standard 91 HD' (n = 7). Note that this SD corresponds to measurements distributed over several series, and could be lower for consecutive measurements. The deviation of the mean from the expected value was −0.05‰

Table 1. Accuracy and precision of replicate standard measurements

Nr.	Dye III (‰)	Standard 91 HD (‰)
1	−209.1	−81.3
2	−209.9	−84.2
3	−210.8	−82.6
4	−210.0	−83.5
5	−211.8	−83.4
6	−209.3	−82.5
7	−210.5	−83.0
8	−210.4	
9	−210.2	
10	−210.2	
11	−212.0	
12	−210.0	
13	−210.7	
14	−210.0	
Mean	−210.35	−82.93
SD	0.81	0.92
δD-expected	−210.30	−83.25
Offset	−0.05	0.32

for 'Dye III' and 0.32‰ for 'Standard 91 HD', implying that the applied correction method is valid and accuracy of measurements is very good.

Evaluation of the precision including all available data

As mentioned above we re-analyzed eight external IAEA water standards and 23 rainwater samples, which had previously been measured by the conventional chromium reduction technique. Each sample was measured between 1 and 5 times. Including the measurements of the internal standards, a total of 93 measurements were performed. To assess the precision of the on-line technique we calculated the differences of the on-line data from the conventional measured data (Fig. 5). The mean ±1 SD of the differences including all measurements is −0.09 ± 1.03‰ (n = 93). Considering a mean error of the conventional measured values of ~0.40‰, the resulting precision of the on-line values is 0.95‰ ($1.03^2 - 0.40^2 = 0.95^2$). For internal standards the precision is 0.97‰ (n = 23), for external IAEA standards 0.56‰ (n = 16), and for rainwater samples 1.04‰ (n = 54) (see Table 2 and Fig. 6).
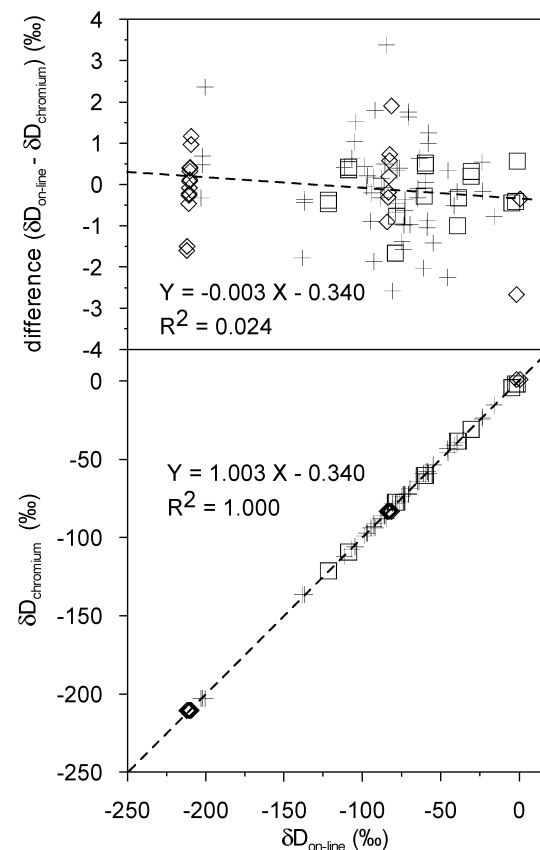
Figure 5. Top: Differences in the on-line measurements from conventional measured reference values ($\delta D_{on-line} - \delta D_{chromium}$) versus on-line measurements $\delta D_{on-line}$. Bottom: Relationship between conventional measured and on-line measured deuterium values. Internal standards (diamonds), IAEA standards (squares) and rainwater samples (crosses).

1324   C. Huber and M. Leuenberger

RCM

Table 2. Assessment of the accuracy and the precision of the new on-line technique

|	All	Internal standards	IAEA standards	Rainwater samples
Number of measurements (n)	93	23	16	54
Mean of differences (offset)[a] (‰)	−0.09	−0.06	−0.18	−0.07
Variation of differences (1 SD)[a] (‰)	1.03	0.97	0.63	1.16
Precision of reference[b] (‰)	0.4	0.1[c]	0.3[d]	0.5[e]
Precision of on-line technique[f] (‰)	0.95	0.97	0.56	1.04

[a]Differences in the on-line measurements from conventional measured reference values (accuracy estimate).
[b]Standard deviation of the mean obtained by replicate measurements with the chromium reduction technique.
[c]n > 25.
[d]n = 3–4.
[e]n = 1–2.
[f](Precision of on-line technique)^2 = (variation of differences)^2 − (precision of reference)^2.

Influence of sample storage

Fifteen of the 23 rainwater samples we analyzed were stored in 2-mL glass containers sealed with a rubber membrane (crimp-top vial with 6.1 mm mouth and 11 mm crimp cap with septa rubber/PTFE; BGB Analytik AG, Switzerland); these are the containers used to supply the autosampler of the chromium reduction measuring device (H/Device, Finnigan MAT). Sixteen months after the measurements using the chromium reduction technique, we analyzed them for the first time with the new on-line system. Another 14 months later we analyzed them for the second time with the new on-line technique. One month later, we re-measured all samples with the chromium reduction technique. In Fig. 7 the deviations of the re-analyses from the initial value obtained by the chromium reduction technique are plotted against the storage time. There is a clear trend toward enriched δD-values with increasing storage time (~1–2‰ after 2.5 years), indicating a leaking membrane. This could either be due to the repeated perforation of the rubber membrane or due to permeation through the membrane. This process could explain the smaller precision of the rainwater measurements compared with standard measurements.

From these findings we conclude that the new on-line method is able to measure δD of water with a precision and accuracy better than 1‰ for a single measurement. The precision and sample analysis time of our technique can be

Figure 7. Influence of sample storage in 2-mL glass containers. The deviations in the measured δD from the initial measurement are plotted against the storage time. Diamonds indicate measurements with the chromium reduction technique and triangles indicate measurements with the new on-line technique.

Figure 6. Assessment of the precision of the new on-line technique, using the differences in the on-line measurements from conventional measured reference values according to Table 2.

compared with those of the on-line chromium method described by Morrison et al.,[5] for which the SD varied between 0.9 and 0.2‰ for consecutive measurements of the same sample.

Continuous ice measurements

Since we are interested in paleoclimatology the new technique will allow us to perform continuous measurements of the stable isotope composition of ice in a fashion similar to that described in our $\delta^{18}O$ publication.[11] To obtain continuous ice measurements the system could be coupled to a melting device as was developed for measurements of the chemical components of the ice.[15,16] This melting device has undergone several improvements and has been used very successfully during many field seasons in Greenland and in Antarctica as well as in different laboratories.[16,17] This melting device works as follows. A piece of ice, 10–100 cm in length with a square area of 2×2 cm, is gently forced onto a

RCM

heated device where the ice continuously melts. The melting water is pumped off permanently through a bore hole in the center of the melting device using a tubing pump. Thereafter, it can be analyzed continuously in our system. The design of the melting device prevents contamination with ambient air and water vapor because only the innermost part of the core section (1 cm^2), which is fully sealed against the atmosphere, is used for the analyses.[11,18] Typically, the sample flux exiting the melting device is 3 mL/min, corresponding to a melt velocity of 3 cm/min. This sample flux has to be split, since water consumption of the new technique is only 1 µL/min, which is controlled by a precise tubing pump. The remaining sample can be used for further analyses. Consequently, one could conceive a combined analysis, δD and $\delta^{18}O$, at the same time using two isotope ratio mass spectrometers, to achieve continuous D-excess ($d = \delta D - 8 \cdot \delta^{18}O$) profiles. For a melt velocity of 3 cm/min, the depth resolution in the ice core would be better than 3 cm. The resolution could be increased, by reducing the melt velocity. The precision of the D-excess would be better than the estimated upper limit of our system of 1.3‰ ($[1^2 + (8 \times 0.1)^2]^{0.5}$).

CONCLUSIONS AND OUTLOOK

A new fast on-line technique has been described which allows fast and precise measurements of δD on microsamples of water by continuous-flow isotope ratio mass spectrometry (patent applied for). For the first time the H_2/H_2O-equilibration technique has been used in a fully continuous process. It has been shown that, by complete vaporization of the water and by increasing the temperature to 100°C, H_2/H_2O-equilibration can be achieved within a few seconds. This new technique allows the measurement of a wide range of aqueous samples either in a quasi-continuous way (discrete samples are injected one after another, for example, using an auto-sampler) or in a fully continuous way. Measurement precision and accuracy for discrete samples on a natural abundance deuterium level are better than 1‰ for a sample volume of ~5 µL. For a measuring sequence of 20 or more samples, the required analysis time can be reduced to less than 5 min/sample, which includes equilibration and processing. Our technique is cost-saving since no dual-inlet system is used and hardly any consumables are necessary (the platinum catalyst has a long useful life). Direct measurements of samples with dissolved salts (e.g. seawater, saline groundwater, beverages or body fluids) should be possible with minor adaptations. Salt deposition upon evaporation of the sample in the equilibration chamber could influence the per-

formance of the system (e.g. blocking of the water flow). Here an exchangeable equilibration chamber would be useful.

Due to the new approach of the technique we are able, for the first time, to make truly continuous δD measurements of ice cores or rain water. Together with our on-line method for $\delta^{18}O$,[11] continuous measurements of the D-excess could be achieved. The precision of such a combined D-excess measurement would be better than 1.3‰, with a depth resolution in the ice core of up to 1 cm. This gives access to new insights into dynamic processes.

REFERENCES

1. Bigeleisen J, Perlman ML, Prosser HC. *Anal. Chem.* 1952; **24**: 1356.
2. Friedman I. *Geochim. Cosmochim. Acta* 1953; **4**: 89.
3. Gehre M, Hoefling R, Strauch G. *Anal. Chem.* 1996; **68**: 4414.
4. Brand WA, Awak H, Seedorf R, Hofmann D, Conradi T. *Isotopes Environ. Health Stud.* 1996; **32**: 263.
5. Morrison J, Brockwell T, Merren T, Fourel F, Phillips AM. *Anal. Chem.* 2001; **73**: 3570.
6. Horiota J. *Chem. Geol.* 1988; **72**: 89.
7. Coplen TB, Wildman JD. *Chen J. Anal. Chem.* 1991; **63**: 910.
8. Epstein S, Mayeda T. *Geochim. Cosmochim. Acta* 1953; **4**: 213.
9. Begley IS, Scrimgeour CM. *Anal. Chem.* 1997; **69**: 1530.
10. Kerstel ERT, van Trigt R, Dam N, Reuss J, Meijer HAJ. *Anal. Chem.* 1999; **71**: 5297.
11. Leuenberger M, Huber C. *Anal. Chem.* 2002; **74**: 4611.
12. Rolston JH, den Hartog J, Butler JP. *J. Phys. Chem.* 1976; **80**: 1064.
13. Bardo RD, Wolfsberg M. *J. Phys. Chem.* 1976; **80**: 1068.
14. Gonfiantini R. *Nature* 1978; **271**: 534.
15. Sigg A, Fuhrer K, Anklin M, Staffelbach T, Zurmuhle D. *Environ. Sci. Technol.* 1994; **28**: 204.
16. Röthlisberger R, Bigler M, Hutterli M, Sommer S, Stauffer B, Junghans HG, Wagenbach D. *Environ. Sci. Technol.* 2000; **34**: 338.
17. Fuhrer K, Neftel A, Anklin M, Maggi V. *Atmos. Environ.* 1993; **27A**: 1873.
18. Huber C, Leuenberger M. *Anal. Chem.* 2003; in press.

2.3 Measurements of Water Isotopes and Deuterium Excess on Ice Cores with a Combined On-Line Technique

In the previous sections the techniques to measure either δ^{18}O or δD, continuously on ice are presented. In this section a combination of the two on-line techniques is described, that allows us to analyze both water isotopes on the same sample, using only one mass spectrometer.

By determining both water isotope ratios, δ^{18}O and δD, on the same sample, a third parameter can be derived, the deuterium excess d. The deuterium excess is important for the interpretation of climate signals from water isotopes of ice cores. It is defined as follows:

$$d = \delta\mathrm{D} - 8 \cdot \delta^{18}\mathrm{O} \tag{2.1}$$

It would be of great value to perform continuous high resolution measurements of d on ice cores. To reach this one could split the sample flux and use two isotope ratio mass spectrometers (IRMS) simultaneously. However this is a very expensive and somehow unsatisfactory solution, but of course it can be done when two IRMS are available. Another possibility is to measured the two isotope ratios one after the other. To achieve this, processing of one parameter has to be delayed for about 40 minutes, e.g. using a delay column. The experimental setup of the latter possibility is shown in Figure 2.1.

A piece of ice is melted continuously. The melt-water flux is splitted in the ratio 1 to 500 (hydrogen equilibration flux to oxygen equilibration flux). The smaller flux (1–2 μl/min)
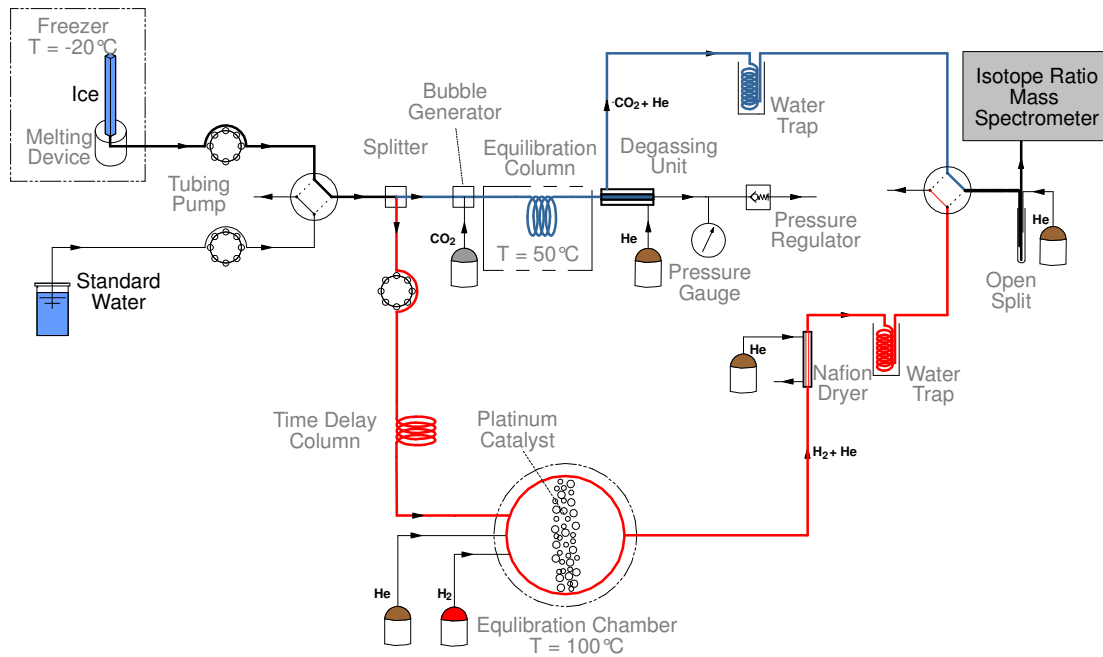
Figure 2.1: Experimental setup for the continuous determination δ^{18}O, δD, and the deuterium excess $d = \delta\mathrm{D} - 8 \cdot \delta^{18}\mathrm{O}$ on a ice core, using only one mass spectrometer.

enters a tubing that delays hydrogen equilibration by about 40 minutes, whereas the oxygen equilibration immediately starts. Using this setup it is possible to process and measure both water isotopes on the same sample with only one mass spectrometer. That leads to a continuous determination of the deuterium excess d. It is possible to process and measure a bag of ice (50–100 cm) within 80–110 minutes. As been shown in the earlier sections, the reproducibility of standard and discrete sample measurements is about $\pm 0.1^0/_{00}$ for $\delta^{18}O$, and $\pm 1^0/_{00}$ for δD. Hence the precision for d should be better than $1.3^0/_{00}$. The measurement resolution depends mainly on the melting velocity and the geometry of the tubing. It is normally about 1–3 cm. The time delay column has of course a negative influence on the resolution of the measurement. It causes a stronger dispersion of the δD signal, which reduces the resolution to about 2–6 cm for this parameter. For a time delay of 40 min we used a specially knotted low dispersion PTFE tubing (1/16" with an inner diameter of 0.25 mm and a length of 2 m). The knots should cause a better radial mixing of the liquid stream in the tube, due to frequent shifts in flow direction. However, because the flow rate of our sample was extremely low (1–2 μl/min), the positive effect of this sophisticated tubing on the dispersion was rather small, compared to an ordinary (not knotted) tubing of the same dimensions.

In order to test the feasibility of the proposed setup, tests with rainwater samples were performed. In Figure 2.2 a compilation the measurements of four different rainwater samples with the new combined on-line technique is shown. The values are compared with conventional measurements of the same samples. Except for Sample 1, reproducibility of the
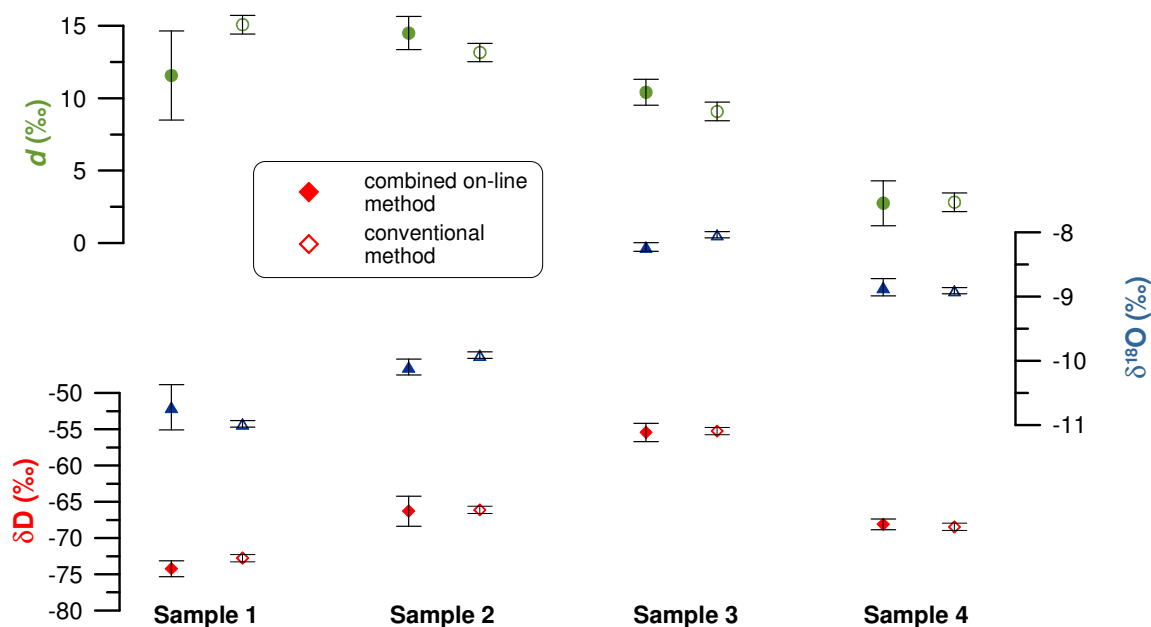
Figure 2.2: A compilation of replicate measurements (n = 3) of four different rainwater samples with the new combined on-line technique. Mean values with the respective error (1 σ) are plotted and compared with conventional measurements.

combined on-line method is comparable with measurements described in [1, 2]. The delayed hydrogen equilibration process worked nicely without altering the δD-values notably.

Thus we went a step further and performed first measurements on ice samples. We took samples from Dome C, since for this ice the deuterium excess has been measured by conventional techniques [3]. However the resolution of the available data corresponds to bag means only. Four pieces of Dome C ice from different depths, each with a length between 23 and 27 cm, were measured with the combined on-line technique. The results are presented in Figure 2.3.
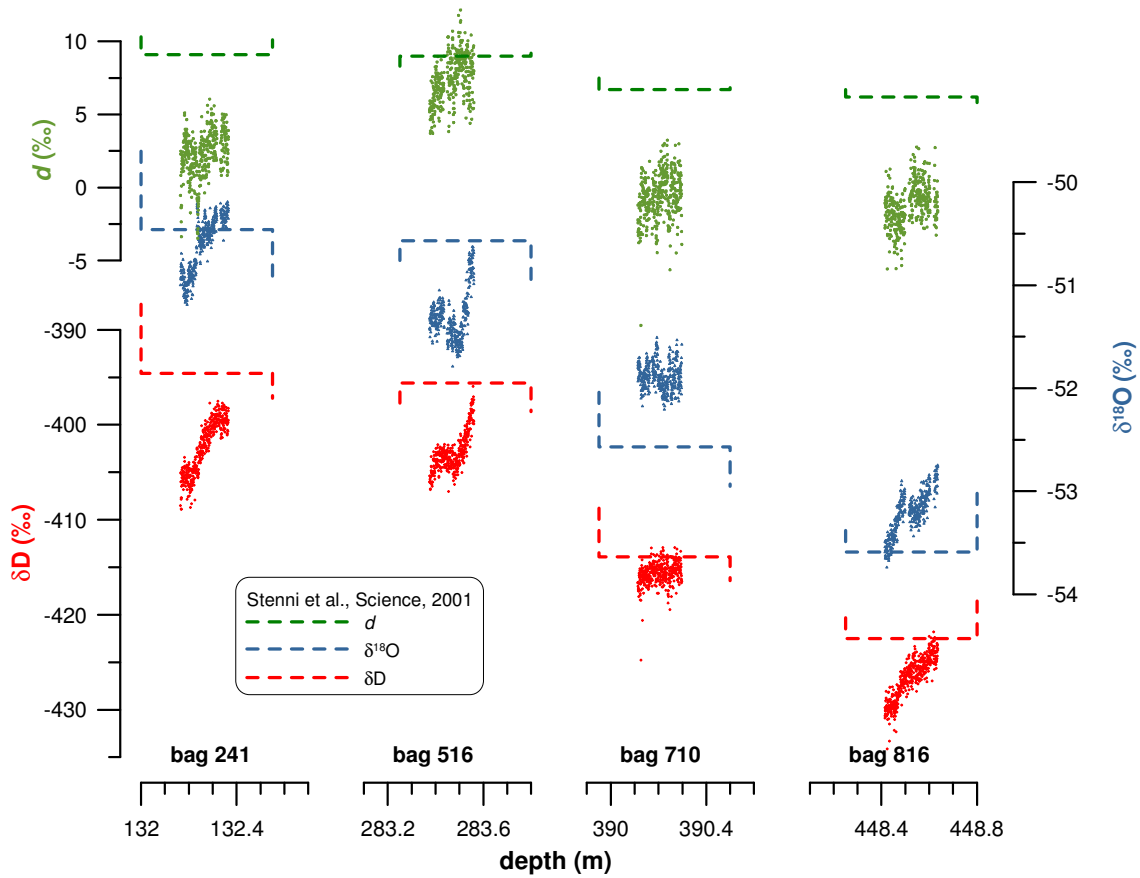
Figure 2.3: Comparison of the of Dome C ice measured with the combined on-line technique and conventional water isotope measurements. The on-line measurements samples, each between 23 and 27 cm long, are plotted in high resolution, whereas the conventional data has only bag mean resolution.

These measurements are the first truly continuous water isotope and deuterium excess determinations performed on ice cores. There is a good correlation between the on-line isotope data δ^{18}O and δD, that results in a fairly stable d-value over a single bag. However, a comparison of the results with existing conventional water isotope measurements [3] documents that there are some discrepancies. Except for one measurement (bag 516), the on-line d-values are more than $7^0/_{00}$ lower than expected. This is either due to low δD-values (bag 241 and bag 816) or due to high δ^{18}O values (bag 710). Hence, the accuracy of the on-line ice measurement is not as good as expected.

Until now, the causes for the discrepancies are unknown. Some potential influences are listed below, but none of them provides a satisfactory explanation. Further tests are required to improve the accuracy of on-line ice measurements.

- δ^{18}O and δD: Equilibration time depends on the temperature. Temperature variations are observed, but not only during ice measurements. Thus, it should affect sample and standard in the same way.

- δ^{18}O: Isotopic equilibration depends strongly on the pH-value of the water sample (pH should be below 7). However, all ice samples have pH between 5.7 and 6.

- δD: Can dissolved substances containing hydrogen influence δD?

- Another limitation is the fact, that only one of our working standards is close to the measured ice values (δ^{18}O = -53.76$^0/_{00}$; δD = -428.0$^0/_{00}$). The second working standard (δ^{18}O = -27.20$^0/_{00}$; δD = -210.4$^0/_{00}$) has significantly higher δ-values.

Bibliography

[1] C. Huber and M Leuenberger. Fast high-precision on-line determination of hydrogen isotope ratios of water or ice by continuous-flow isotope ratio mass spectrometry. *Rapid Communications in Mass Spectrometry*, 17:1319–1325, 2003.

[2] M. Leuenberger and C. Huber. On-line determination of oxygen isotope ratios of water or ice by mass spectrometry. *Analytical Chemistry*, 74:4611–4617, 2002.

[3] B. Stenni, V. Masson-Delmotte, S. J. Johnsen, J. Jouzel, A. Longinelli, E. Monnin, R. Röthlisberger, and E. Selmo. An oceanic cold reversal during the last deglaciation. *Science*, 293:2074–2077, 2001.

Chapter 3

New On-Line Extraction and Measuring Technique for Isotope Ratios of Trapped Air from Ice Cores

3.1 Continuous Extraction of Trapped Air from Bubble Ice or Water for On-Line Determination of Isotope Ratios

Christof Huber,[1] Markus Leuenberger[1] and Oliver Zumbrunnen[1]

Abstract

This paper describes the new continuous extraction system for trapped air from bubble ice for on-line determination of the isotopic composition of the main air components nitrogen and oxygen (δ^{15}N, δ^{18}O and δ^{17}O). The precision (1 SD) of standard measurements is $\sim$0.04$^0\!/\!_{00}$ for δ^{15}N, $\sim$0.1$^0\!/\!_{00}$ for δ^{18}O, and $\sim$0.15$^0\!/\!_{00}$ for δ^{17}O, respectively. Continuous measurements of nitrogen as well as oxygen isotope ratios can be performed with a spatial resolution of $\sim$3 cm and nearly the same precision as for the standards. However, the measured δ-values of ice samples were generally lower compared to ice measured with conventional techniques, due to a time dependent dissolution process of air in water associated with kinetic fractionation which affects standard and sample differently. By modeling the dynamics of the this dissolution process we found a reason for the lack in accuracy and propose an improvement of the system which will lead to a better accuracy of the ice measurements.

---

[1]Climate and Environmental Physics, Physics Institute, University of Bern, Sidlerstrasse 5, CH-3012 Bern, Switzerland

Continuous Extraction of Trapped Air from Bubble Ice or Water for On-Line Determination of Isotope Ratios

Christof Huber, Markus Leuenberger,* and Oliver Zumbrunnen

Climate and Environmental Physics, Physics Institute, University of Bern, Sidlerstrasse 5, 3012 Bern, Switzerland

We describe a new continuous extraction system for trapped air from bubble ice or water for on-line determination of the isotopic composition of the main air components nitrogen and oxygen ($\delta^{15}N$, $\delta^{18}O$, and $\delta^{17}O$). Studies of the composition of air from bubbles trapped in polar ice are providing fundamental information about ancient atmospheric composition and, therefore, are an important tool to learn more about Earth's climate. The new system proved to work reliably for standard air admixed and subsequently removed from a water stream. The precision (1 SD) of standard measurements is ~0.04‰ for $\delta^{15}N$, ~0.1‰ for $\delta^{18}O$, and ~0.15‰ for $\delta^{17}O$. Ice measurements with the new on-line system are promising. Continuous measurements of nitrogen as well as oxygen isotope ratios can be performed with a spatial resolution of ~3 cm and nearly the same precision as for the standards. However, the measured δ values of ice are generally lower, as compared to ice measured with conventional techniques, as a result of a time-dependent dissolution process of air in water associated with kinetic fractionation, which affects standard and sample differently. By modeling the dynamics of the this dissolution process, we found a reason for the lack of accuracy and propose an improvement of the system that will lead to a better accuracy of the ice measurements.

Studies of the composition of air from bubbles trapped in polar ice are providing fundamental information about ancient atmospheric composition and, therefore, is an important tool to learn more about Earth's climate. In this study, we focus on measurements of isotopic composition of the main air components, nitrogen and oxygen ($\delta^{15}N$, $\delta^{18}O$, and $\delta^{17}O$). $\delta^{18}O$ measured on O_2 is a proxy of continental ice volume and was used to synchronize cores from Greenland and Antarctica.[1] $\delta^{15}N$ can be used to correct for gravitational enrichment in the firn and allow us to determine temperature changes and ice age–gas age differences during abrupt surface temperature variations.[2–4] The

measurement of the O_2/N_2 ratios of air could provide constraints on the understanding of the carbon cycle. Furthermore, variations of the elemental ratios, $\delta O_2/N_2$, $\delta Ar/N_2$, and $\delta Ar/O_2$ can provide valuable information about processes during bubble close-off and ice storage.

Several different methods to extract air from ice exist. However, certain air components require a specific technique in order to retrieve accurate information. For instance, CO_2 quickly reacts with H_2O by the carbonate reaction; therefore, a dry extraction method is necessary to measure CO_2 and its isotopic composition in ice.[5,6] An easier way to release the air is by melting the ice. This wet extraction was successfully used by several groups for methane,[7] nitrogen,[8] oxygen,[9] and argon,[4] which do not react with H_2O, and surprisingly, also for N_2O.[10] Conventional wet extraction systems deal with ice samples weighting 15–50 g.[2,8] The ice samples are melted under vacuum and are then refrozen. Extracted gases are condensed into a sample tube at very low temperature. Usually, a second melt-freeze cycle is necessary to extract all of the air from the ice. After this process, the air in the sample tube is analyzed in a isotope ratio mass spectrometer (IRMS). Our conventional system is limited to a maximum of ~8 samples/day.

Here, we present a new on-line melt extraction method which is able to accelerate the procedure. The air is extracted and analyzed continuously from the ice. The new technique allows the simultaneous and continuos determination of the isotopic and elemental ratios $\delta^{15}N$, $\delta^{18}O$, $\delta^{36}Ar$, $\delta O_2/N_2$, $\delta Ar/N_2$, and $\delta Ar/O_2$ within minutes. This new technique offers a real alternative to the proven method.

METHODS

Melting Device. Figure 1 shows the schematic setup of our melt extraction system. We used the melting device developed

---

* Corresponding author. Phone: ++41 31 631 44 70. Fax: ++41 31 631 87 42. E-mail: leuenberger@climate.unibe.ch.

(1) Bender, M.; Sowers, T.; Dickson, M.-L.; Orchardo, J.; Grootes, P.; Mayewski, P. A.; Meese, D. A. *Nature* **1994,** *372,* 663–666.

(2) Lang, C.; Leuenberger, M.; Schwander, J.; Johnsen, S. *Science* **1999,** *286,* 934–937.

(3) Leuenberger, M. C.; Lang, C.; Schwander, J. *J. Geophys. Res.* **1999,** *104,* 22163–22170.

(4) Severinghaus, J. P.; Sowers, T.; Brook, E. J.; Alley, R. B.; Bender, M. L. *Nature* **1998,** *391,* 141–146.

(5) Friedli, H.; Lötscher, H.; Oeschger, H.; Siegenthaler, U.; Stauffer, B. *Nature* **1986,** *324,* 237–238.

(6) Leuenberger, M.; Siegenthaler, U.; Langway, C. C. *Nature* **1992,** *357,* 488–490.

(7) Chappellaz, J.; Barnola, J.-M.; Raynaud, D.; Korotkevich, Y. S.; Lorius, C. *Nature* **1990,** *345,* 127–131.

(8) Sowers, T. A.; Bender, M. L.; Raynaud, D. *J. Geophys. Res.* **1989,** *94,* 5137–5150.

(9) Bender, M.; Sowers, T.; Labeyrie, L. *Glob. Biogeochem. Cycles* **1994,** *8,* 363–376.

(10) Flückiger, J.; Dällenbach, A.; Blunier, T.; Stauffer, B.; Stocker, T. F.; Raynaud, D.; Barnola, J.-M. *Science* **1999,** *285,* 227–230.

a) Extraction System
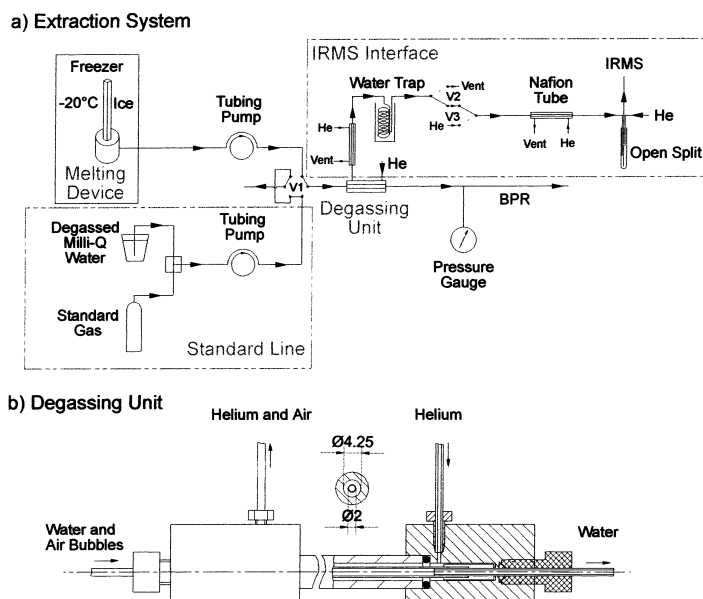
b) Degassing Unit

Figure 1. (a) Schematic setup of the extraction system. The system consists of the sample line with the melting device, the standard line, the degassing unit, and the IRMS interface. (b) The degassing unit, as described in the Methods Section.

for the continuos flow analysis system (CFA)[11] that was used for in situ analysis of chemical properties of the ice on several European drilling projects in Antarctica (EPICA) and Greenland (GRIP).[12,13] Part of the procedure is the same as the one described in our previous papers about new techniques for the on-line determination of oxygen and hydrogen isotope ratios of water or ice.[14,15] The melting device is placed in a freezer set to a temperature of -20 °C. An ice bar of $10-100$ cm in length with a square area of 2×2 cm is slightly forced onto the heated melting device, where the ice continuously melts. The meltwater and the released air of the clean inner ice fraction (cross-section 1 cm^2) is permanently drained off by a tubing pump. The design of the melting device prevents contamination of the sample with ambient air, because only the innermost part of the core section, which is fully sealed against the atmosphere, is used for the analyses (see Figure 2). To make sure that there is no contamination with the surrounding air, we performed a test with bubble-free ice (totally degassed ice produced from ultrapure water), which was melted in a CO_2 atmosphere. By measuring the electric conductivity of the meltwater, which increases when the water is contaminated with CO_2, the contamination can be determined as a function of the pump factor. The pump factor was defined as the pump rate of the tubing pump divided by the product of the melt velocity times the inner cross section of the melting device and determines thus how much of the inner core section is pumped off. We did not observe any contamination using pump factors below 1.2.
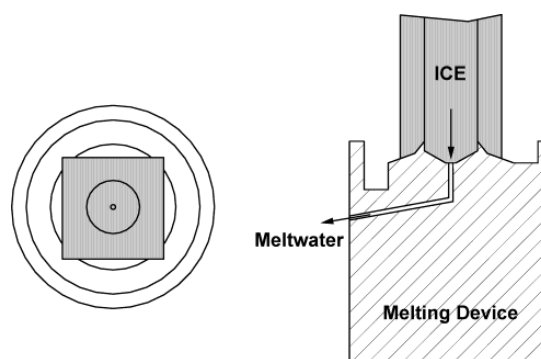
Figure 2. Detailed view of the melting device. The design of the melting device prevents contamination with ambient air, since only the inner part of the ice is used for the measurement.

Therefore, approximately one-quarter of the sample enters an opening in the center of the melting device and is passing through a tube ($\sim$100 cm long, i.d. 0.75 mm, material PEEK, Omnilab AG) to the multichannel tubing pump (Ismatec IP, Ismatec SA). We use PEEK tubing, since it is 10 times less oxygen permeable than Teflon (PTFE). The air bubbles have to pass the tubing pump to reach the degassing unit. This can lead to increased intensity variations of the signal as a result of difficulties of pumping a water—gas mixtures. Pumping of a water—gas mixture is a known and, to our knowledge, unsolved problem. We looked for many different types of pumps, of which the tubing pump turned out to be the best choice for our application.

Degassing Unit. In contrast to CFA, we are interested in the gas phase and not in the liquid phase. Therefore, the air bubbles that flow with the water flux have to be separated from the water.

(11) Sigg, A.; Fuhrer, K.; Anklin, M.; Staffelbach, T.; Zurmuhle, D. *Environ. Sci. Technol.* **1994**, *28*, 204−210.
(12) Fuhrer, K.; Neftel, A.; Anklin, M.; Maggi, V. *Atmos. Environ.* **1993**, *27A*, 1873−1880.
(13) Röthlisberger, R.; Bigler, M.; Hutterli, M.; Sommer, S.; Stauffer, B.; Junghans, H. G.; Wagenbach, D. *Environ. Sci. Technol.* **2000**, *34*, 338−342.
(14) Leuenberger, M.; Huber, C. *Anal. Chem.* **2002**, *74*, 4611−4617.
(15) Huber, C.; Leuenberger, M. *Rapid Commun. Mass Spectrom.* In press.

This separation occurs in the degassing unit (see Figure 1b). The degassing unit consists of a gas-permeable hydrophobic membrane (Accurel, Microdyn Techn. Inc.), 10 cm in length and 2 mm in diameter, that is placed into a plexiglass tube of the same length. Both membrane and plexiglass tube are fixed on aluminum bodies to seal it from ambient air. The volume between the membrane and the plexiglass tube is flushed with helium, which is used as a carrier gas. Seals consist of Teflon tubing and Delrin connectors (1/16-in. Delrin nut, Omnilab AG). The He flux is sealed with small Viton O-rings pressed onto the aluminum body. The water pressure (1.3–1.5 bar) drives the air bubbles through the membrane into the reverse flow of He (10–20 mL/min STP, 1.1–1.3 bar). Additionally, molecular diffusion forces a part of the dissolved air into the He as a result of the greater partial pressure in the water, as compared to the He. The longer the exchange time in the membrane unit is, the larger the amount of released dissolved air becomes. Using a 10-cm-long membrane, ~18–25% of the dissolved air is released. The water remains in the tube because of the hydrophobicity of the membrane and leaves the system through a PEEK tube (i.d. 0.5 mm). By adjusting the length of the PEEK tube, the water pressure in the membrane unit can be regulated according to the law of Hagen–Poiseuille.

IRMS Interface. Prior to the injection into the IRMS, the water vapor and the CO_2 are removed from the sample using a Nafion drying column (i.d. 0.36 mm, length 60 cm, Perma Pure Inc.) and a subsequent cold trap held at liquid nitrogen temperature ($T = -196$ °C). With a two-position switching valve (V2 and V3 in Figure 1) one can select between the bypass He and the system He flux. This allows us to determine the background signals of the IRMS and to remove the degassing unit and the water trap for maintenance without breaking the He flux of the interface, which connects our measuring system to the IRMS. Into this interface (a GP-Interface, Finnigan MAT), a second Nafion drying column (i.d. 0.36 mm, length 18 cm) is placed in front of the open split where the air–He mixture enters the IRMS capillary. The open split inlet provides a continuous flow of sample gas, ~0.35 mL/min STP, into the IRMS. The split ratio is 1:30–1:60, depending on the sample flux and the position of the capillaries. If necessary, the sample can be diluted with He using an additional capillary in the open split.

Standard Line. Fractionation between isotope species occurs as a result of slight differences in mass, solubility, mobility, and vapor pressure. Measurements of isotopic compositions are made relative to a known standard expressed in the δ notation,

$$\delta = (R_{sample}/R_{standard} - 1) \times 1000‰ \qquad (1)$$

where R is the abundance ratio of the isotopes. For example, for nitrogen, $R = {}^{15}N/{}^{14}N$. Since many isotope fractionations are difficult to quantify, we process samples and standard equally in order to eliminate the fractionation effects. We achieve this by generating bubbles of standard gas into a flow of degassed Milli-Q water (Ultrapure Water System, Millipore AG). Bubble generators are custom T-shaped plexiglass pieces with bore-hole diameters from 0.5 mm to 1 mm. The standard gas is injected through a thin fused-silica capillary that is immersed into the water flow. With the four-way valve V1 (4-way Teflon rotary valve, Rheodyne Inc.), we can switch between the sample and the standard stream.

Degassing of the Milli-Q water is known to be essential to prevent interference with dissolved air. We degas the water for at least 1 h using a simple water jet vacuum pump and a magnetic agitator. Subsequently, the water is stored in a bottle that is constantly flushed with He. After this procedure, the gas content of the water is >20 times lower than in air-saturated water (water in equilibrium with the atmosphere at 20°C), which is low enough to reach the desired accuracy.

Mass Spectrometry. A Finnigan MAT Delta Plus XL IRMS was used for the measurements of the isotopic ratios $\delta^{15}N$ and $\delta^{18}O$. This IRMS is equipped with the universal triple Faraday cup collector to record three mass/charge ratios simultaneously. With this IRMS, we are able to record either the nitrogen isotopes, mass/charge ratios 28 on cup 1 and 29 on cup 2, or the oxygen isotopes, mass/charge ratios 32 on cup 1 and 34 on cup 3, in a continuous mode.

For the most recent measurements, we had access to a Delta Plus XP equipped with eight Faraday cups, which permits simultaneous determination of the isotopic and elemental ratios of the major air components (N_2, O_2 and Ar, i.e., $m/z = 28, 29, 32, 33, 34, 36, 40,$ and 44).

Analysis Procedure. Since we measure in a fully continuous mode (on-line mode), we do not use a standard reference gas injection system (e.g., Conflow), but instead, we use a reference gas that passes through the entire system (see section Standard Line). The reference air standard is measured prior to and after a sample measurement for ~300–400 s. Sample analysis time varies between 200 and 1000 s, depending on the length of the ice sample. A 50-cm sample of ice at a melting velocity of 3 cm/min corresponds to 1000 s of analysis time. Therefore, the performance of the IRMS has to be stable or at least linear during an analysis time of 8–30 min.

CORRECTIONS

To reach the required precision the following corrections need to be applied.

Background Correction. We determine the background for the whole system at the start of each measurement by flushing the sample capillary with pure helium (valve V2 in "vent" and valve V3 in "He" position). The background is assumed to be constant during measurements.

Signal Intensity Imbalance Effect. Measured isotope ratios are slightly sensitive to variations of the signal intensity of the ion beam. For our system, the signal intensities of the standard and the sample are not exactly balanced. Furthermore, short time variations of the signal intensity due the injection of single bubbles into the He carrier gas flux can reach ~10% of the mean value. Therefore, the measured δ values have to be corrected for the signal intensity imbalance effect according to

$$\delta_{intensity-corrected} = \delta_{measured} - kI \qquad (2)$$

where I is the signal intensity of the main mass/charge 28, and k is the linear correction coefficient. We determine the correction coefficient k for every single measurement by measuring the air standard at different signal intensity levels (different amounts of standard gas are admixed to the water in the bubble generator). Typical values for linear correction coefficient k are 0.05‰/V for $\delta^{15}N$ and 0.4‰/V for $\delta^{18}O$. These values are strongly dependent
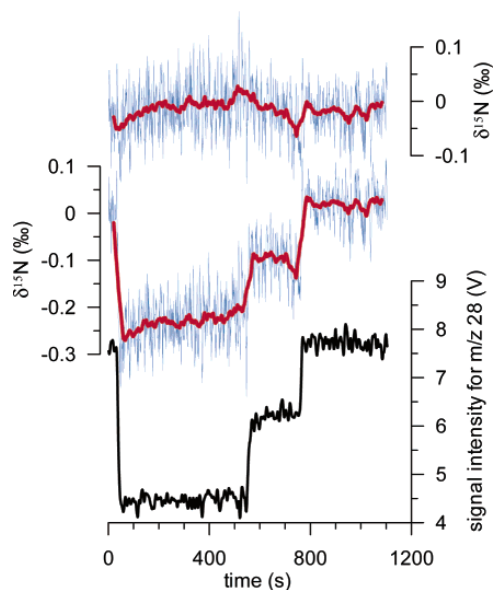
Figure 3. (Upper curve) Example of a background- and intensity-corrected $\delta^{15}N$ measurement of our working standard LK54 in Milli-Q water in full resolution (blue line) and smoothed (red line; 40-s running mean). (Middle curve) The same measurement but only background-corrected. (Bottom curve) The corresponding signal intensity of the mass/charge ratio 28 ($^{14}N_2$).

on the ion source settings. This correction thus includes ion source pressure imbalance effects as well as instrument nonlinearity effects which, however, potentially have the same origin. Figure 3 shows the effect of the intensity correction to the measured δ values.

Influence of the Elemental Composition on the Isotopic Ratios. It has been shown that measured isotopic ratios of a single element in a mixture of gases are sensitive to variations in the elemental ratios.[8] The amount of the influence depends on the instrument and the measuring parameters (e.g., focusing conditions, pressure in the ion source). Potential explanations for this effect are charge exchange between different elements, changed kinetic isotope effect for the ionization, and influence on the molecular flow of the different isotopes inside the ion source. For nitrogen and oxygen isotope ratios, one would expect mainly a sensitivity to variations in the O_2/N_2 ratio. With the Delta Plus XL IRMS, we cannot measure the O_2/N_2 ratio; therefore, these measurements are not corrected for the influence of the elemental composition.

For the measurements with the Delta Plus XP, we determine the influence of the elemental composition by adding various amounts of pure N_2 and O_2 to a standard gas, and measuring it against the pure standard gas. The measured deviation is the influence of the elemental composition. This leads to the following correction:

$$\delta_{el.\ comp.\ corrected} = \delta_{intensity\ corrected} - m(\delta O_2/N_2) \quad (3)$$

Typical values for the dependency m on $\delta O_2/N_2$ are 0.001‰/‰ for $\delta^{15}N$ and −0.01‰/‰ for $\delta^{18}O$.

Table 1. Comparison of Different Air Standards Measured with Different Techniques[a]

standard air	$\delta^{15}N$ (‰)	SD (‰)	n	$\delta^{18}O$ (‰)	SD (‰)	n	$\delta^{17}O$ (‰)	SD (‰)	n
dual-inlet[b]									
EG1	−2.55	0.01	61	3.27	0.02	61	1.70	0.11	14
EG2	−8.30	0.02	53	13.74	0.03	53	7.36	0.09	14
Luftstandard	−1.47	0.02	61	−31.75	0.10	61	−16.31	0.10	14
Keeling 340	−4.69	0.04	62	20.37	0.05	62	10.67	0.13	14
on-line mode[c]									
EG1	−2.54	0.02	17	3.31	0.08	17	1.89	0.16	17
EG2	−8.23	0.04	9	13.73	0.08	9	7.34	0.14	9
Luftstandard	−1.46	0.00	2	−31.66	0.08	2	−16.22	0.04	2
on-line in water[d]									
EG1	−2.55	0.03	49	3.33	0.08	9	1.96	0.09	3
EG2	−8.19	0.05	20	13.53	0.12	13	7.12	0.11	12
Luftstandard	−1.42	0.04	4	−31.11	0.04	4	−15.98	0.03	4
Keeling 340	−4.66	0.01	2	19.99		1			

[a] All δ values are measured against the working standard, LK54. [b] Measured with conventional dual-inlet technique. [c] Measured with the on-line technique (IRMS interface). Air is injected in a He carrier. [d] Measured with the entire on-line system. Air is injected in degassed water.

Drift Correction. Drifts are variations on time scales from minutes to hours due to (i) pump driven pressure (flux) oscillation of the water and air column in the system; (ii) room temperature and pressure changes; (iii) slow changes in the system properties, such as ice accumulation in the cold trap or condensation of water vapor on the surface of the tubing; (iv) surface desorption and absorption processes (memory effects); and probably more yet unknown effects. We correct drifts linearly between two standard measurements. Therefore, frequent standard measurements improve accuracy. To reduce drifts, we stabilize the room temperature to 20 ± 0.2°C.

Normalization to Atmosphere. Isotope ratio measurements should be referenced to the atmosphere. Our reference air standard (working standard LK54) is compressed dry air taken from the atmosphere. However, the isotopes could be fractionated as a result of the commercial compression process. We performed comparison measurements with atmospheric air sampled at Jungfraujoch using our new gas inlet system.[16] These measurements showed no significant deviations of the isotope ratios. Therefore, our working standard LK54 can be used as a reference for the atmosphere.

RESULTS AND DISCUSSION

Comparison of On-Line Mode versus Dual Inlet. To demonstrate the linearity and performance of the IRMS in the on-line mode, we first injected standard air over a thin fused-silica capillary directly into the He carrier gas stream connected with the IRMS interface. Thus, for these measurements, the standards were not injected into water. We measured different air standards (EG1, EG2, and Luftstandard) against our working standard LK54 using the on-line mode. A comparison of the on-line measurements with conventional dual inlet measurements of the same air standards is shown in Table 1. There is no significant difference between the on-line and the dual-inlet measurements. The on-

(16) Leuenberger, M.; Nyfeler, P.; Moret, H. P.; Sturm, P.; Huber, C. *Rapid Commun. Mass Spectrom.* 2000, *14*, 1543−1551.

line data match the dual inlet data within the error range. Note that for the on-line measurements, standard gas is measured directly from the high-pressure cylinder, whereas for the dual-inlet measurements, aliquots of the cylinder gas are decanted into smaller glass containers at atmospheric pressure. Therefore, small deviations could be explained by fractionations or contamination of the standard gas stored in these glass containers.

For the $\delta^{15}N$, the standard deviation (SD) of replicate on-line measurements is comparable to the SD of dual-inlet measurements, whereas for the oxygen isotope ratios, the variations of the on-line measurements are slightly larger. From these findings, we conclude that precision of air measurement using the on-line mode is <0.04‰ for $\delta^{15}N$, <0.1‰ for $\delta^{18}O$, and <0.2‰ for $\delta^{17}O$.

On-Line Measurements of Standard Air Extracted from Water. In the last section, we showed the feasibility of on-line air measurements using the IRMS interface shown in Figure 1. Therefore, we took a step forward and measured our secondary air standards EG1, EG2, Luftstandard, and Keeling 340 against our working standard LK54 using the entire system from Figure 1; i.e., the standard gas was permanently (~0.3 mL STP/min) injected into a water flow (3 mL/min) using a bubble generator and subsequently extracted from the water in the degassing unit into a He carrier stream connected with the IRMS interface. To be able to switch between sample and reference, we replaced the line from the melting device to the valve V1 with another standard line. In Figure 4, the $\delta^{15}N$ and $\delta^{18}O$ measurements of three different air standards versus LK54 are shown. All measurements are tabulated in Table 1. The precision is excellent: <0.05‰ for $\delta^{15}N$, ~0.1‰ for $\delta^{18}O$, and <0.15‰ for $\delta^{17}O$.

However, when comparing the on-line water data with the dual-inlet data (Table 1), it can be seen that the on-line δ values are smaller than the dual-inlet δ values. In Figure 5, the differences between the on-line and the dual-inlet δ values ($\delta_{on-line} - \delta_{dual-inlet}$) are plotted against the dual-inlet δ values. The following correlation's were found:

$$\delta^{15}N_{on-line} - \delta^{15}N_{dual-inlet} = -0.012 \times \delta^{15}N_{dual-inlet} - $$
$$0.007‰ \quad (R^2 = 0.584)$$

$$\delta^{18}O_{on-line} - \delta^{18}O_{dual-inlet} = -0.019 \times \delta^{18}O_{dual-inlet} + $$
$$0.051‰ \quad (R^2 = 0.989)$$

and

$$\delta^{17}O_{on-line} - \delta^{17}O_{dual-inlet} = -0.019 \times \delta^{17}O_{dual-inlet} + $$
$$0.070‰ \quad (R^2 = 0.582)$$

The offsets of these correlations are within the uncertainty range of the measurements. The nonzero slope can be explained by an incomplete degassing of Milli-Q water that is used to inject the standards. The residual gas content in the water leads to a slight dilution of the standard gas, since the dissolved air is mixed with the bubble air during the transport process and in the degassing unit (see below). The degassing process described in the Standard Line section reduces the amount of dissolved air in the water by a factor of ~20 or more. The solubility in water at 20°C and atmospheric pressure is 0.015 mL STP/mL of water for
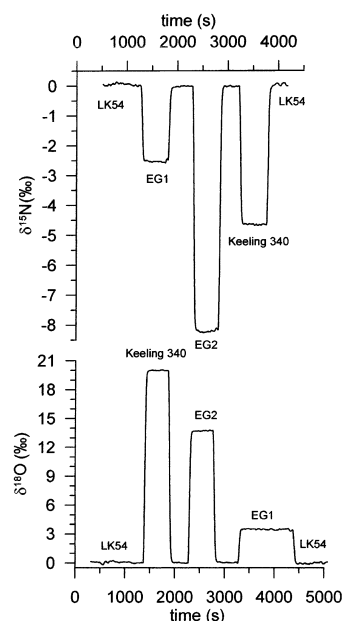
Figure 4. $\delta^{15}N$ (top) and $\delta^{18}O$ (bottom) measurement of EG1, EG2, and Keeling air standards versus the working standard LK54 (40-s running mean).
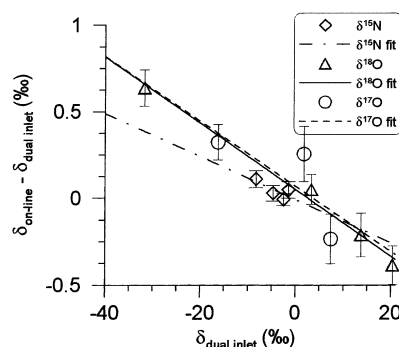
Figure 5. The differences between the on-line and the dual-inlet δ values ($\delta_{on-line} - \delta_{dual-inlet}$) are plotted against the dual-inlet δ values. The effect of incomplete air extraction on measured δ values is documented by the nonzero slopes of the fits plotted in this graph (see Table 1 and text for details).

nitrogen and 0.030 mL STP/mL of water for oxygen, respectively. Therefore, a residual gas content in the water of ~5–6% would lead to the observed slopes. However, the smaller the difference of the δ value between sample and reference, the better the accuracy of the measurements. For example, $\delta^{15}N$ values of polar ice samples are smaller than 1‰, and thus, the influence of the incomplete degassing is <0.012‰.

Ice Measurements. Finally, we analyzed Antarctic (Dome C) and Greenland (GRIP and Eurocore) ice samples with our new method. Before and after any ice sample, bubble-free ice was processed to precondition the melting device. A typical sequence of an ice measurement consists of (i) a calibration phase during which standard gas at different signal intensities is measured to obtain the parameters for the intensity imbalance correction and
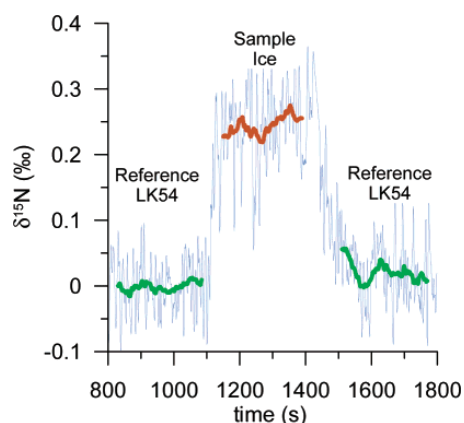
Figure 6. An example of an ice measurement (Eurocore, bag 231). First, the working standard LK54 is measured (green line, 40-s running mean). Subsequently, the 15-cm-long piece of ice is continuously melted and measured (red line, 40-s running mean), followed by a second sequence of the working standard LK54.
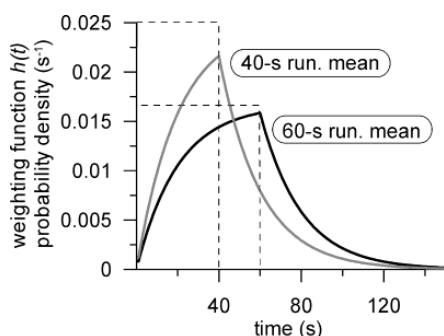
Figure 7. Weighting functions $h(t)$ according to eq 5 for a dispersion time, τ, of 20 s and running mean times, T_{rm}, 40 and 60 s.
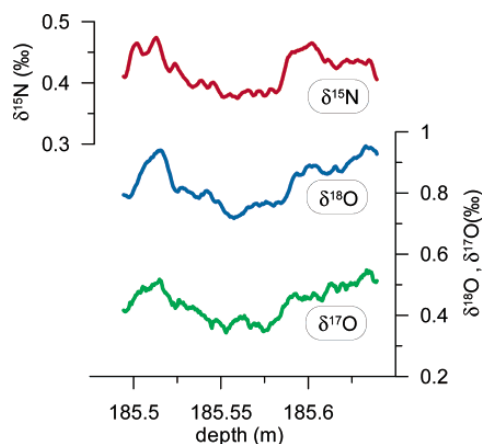
Figure 8. Simultaneous determination of $\delta^{15}N$, $\delta^{18}O$, and $\delta^{17}O$ of a 20-cm-long piece of an Antarctic ice core (Dome C, bag 338, gas age ~2787−2790 years BP). The data are smoothed using a 40-s running mean, corresponding to a spatial resolution of ~3 cm.

(ii) a sample determination phase during which the ice measurement is performed. An example of an ice measurement is given in Figure 6. First our working standard LK54 was measured for ~300 s. Subsequently, a 15-cm-long piece of ice (Eurocore, bag 231) was melted (3 cm/min) and continuously measured, followed by a second sequence of the working standard LK54. The measurements of the working standard prior to and after every ice measurement are used as a reference for the ice measurement and to detect possible changes in the system's properties (i.e., drifts) during the measurement.

Signal Dispersion and Mathematical Smoothing. Since standard and sample are processed successively through the same system, the measured signal is dispersed as a result of diffusion and turbulence during the process (memory effect). Signal dispersion has both a negative influence on the spatial resolution of the measurement and a positive influence on the signal variability because of a smoothing effect (i.e., a lowering of intensity signal variability). A good model for such a dispersion process is an ideal mixed volume, V, with an input flux, F_{in}, an input concentration, c_{in}, an output flux, F_{out}, and an output concentration, c_{out}. For the steady state, $F_{out} = F_{in}$, the output is an exponentially weighted mean of the input. The response to an input pulse $c_{in}(t) = \delta(t)$ is

$$g(t) = c_{out}(t) = \Theta(t)\frac{\exp(-t/\tau)}{\tau} \qquad (4)$$

with the dispersion time $\tau = V/F_{out}$. $\Theta(t)$ is defined as 0 for $t < 0$, 1 for $t > 0$, and is not defined at 0. The dispersion time of our system is ~20 s. To further smooth the signal, we applied a running mean to the output data. For a running mean over T_{rm} seconds, the following weighting function results.

$$h(t) = N\int_0^{T_{rm}}g(t-T)\,dT \quad \text{with} \quad \int_0^\infty h(t)\,dt = 1 \quad (5)$$

The weighting function $h(t)$ for a dispersion time, τ, of 20 s is plotted in Figure 7 for two different running mean times, T_{rm}, 40 and 60 s. The dispersion of the signal involves an asymmetric weighting function $h(t)$. The function $h(t)$ corresponds to the filter that is applied to the data. Smoothing of the signal as a result of dispersion and averaging has a direct influence on the spatial resolution of the ice measurement. The melt velocity of the ice is normally set to 3 cm/min. A 40-s running mean leads to a smoothing of the signal over more than 100 s, according to $h(t)$ (Figure 7). For $T_{rm} = 40$ s, the following integrals can be evaluated.

$$\int_0^\infty h(t)\,t\,dt = 40 \text{ s}; \quad \int_{10}^{70}h(t)\,dt = 0.85; \quad \int_0^{80}h(t)\,dt = 0.94$$

Therefore, the mean time lag is 40 s (note that accidentally, the time lag is the same as T_{rm}), and the spatial resolution of the averaged data is ~3 cm (85% of the signal stems from 3 cm of ice) to 4 cm (94% of the signal stems from 4 cm of ice).

Figure 8 shows a measurement of a 20-cm-long piece of an Antarctic ice core (Dome C, bag 338, gas age ~2787−2790 years BP) monitored with eight Faraday cups, which permits simultaneous determination of $\delta^{15}N$, $\delta^{18}O$, and $\delta^{17}O$. The data are smoothed using a 40-s running mean, corresponding to a spatial resolution of ~3 cm. All three curves show a similar pattern. The

Table 2. Ice Measurements Performed with the New On-Line Extraction Technique

ice/bag	gas age (years BP)	length (cm)	$\delta^{15}N$ (‰)	$\delta^{18}O$ (‰)	$\delta^{17}O$ (‰)	$\delta^{18}O_{gravcorr}$ (‰)	$\delta^{17}O_{gravcorr}$ (‰)	$\delta^{15}N_{expected}$ (‰)
Eurocore/153	57	9	0.30					0.30[ref21]
Eurocore/231	247	15	0.24					0.30
Dome C/338	2788	20	0.42	0.84	0.44	−0.00	0.02	0.54[a]
GRIP/2442	8038	15	0.27					0.34[ref3]
GRIP/2442	8040	15	0.25					0.34
GRIP/2482	8468	17	0.22					0.34
GRIP/2482	8470	17	0.20					0.34
GRIP/2522	8482	20	0.23	0.12	−0.02	−0.34	−0.24	0.34
GRIP/2522	8484	20	0.22	0.07	−0.03	−0.37	−0.25	0.34
GRIP/2389 I	7760	28	0.21	0.08	0.05	−0.34	−0.16	0.34
GRIP/2389 II	7760	28	0.27	0.20	0.14	−0.34	−0.13	0.34
GRIP/2402	7829	21	0.20	0.00	0.04	−0.41	−0.17	0.34
GRIP mean			0.23	0.09	0.04	−0.36	−0.19	0.34
GRIP SD			0.03	0.07	0.07	0.03	0.05	

^{a} According to $[\exp(\Delta mgh/RT) - 1]1000‰$, with $T = 220$ K, $h = 100$ m, $\Delta m = 1 \times 10^{-3}$ kg.

variation of the isotope ratios are within the error range of ~0.04‰ for $\delta^{15}N$, ~0.1‰ for $\delta^{18}O$, and ~0.15‰ for $\delta^{17}O$. The heavy isotopes are enriched for both nitrogen and oxygen. This is due to the gravitational settling of the isotopes in the firn column.[3,17] The gravitation enrichment for the $\delta^{18}O$ values is twice as large as for $\delta^{15}N$ and $\delta^{17}O$ values, since the mass difference, Δm, between the heavy and the light isotope is 2 for $\delta^{18}O$ and 1 for $\delta^{15}N$ and $\delta^{17}O$. $\delta^{15}N$ is generally used to correct the oxygen isotope for gravitational enrichment.

$$\delta^{18}O_{gravcorr} = \delta^{18}O - 2\delta^{15}N \quad (6)$$

$$\delta^{17}O_{gravcorr} = \delta^{17}O - \delta^{15}N \quad (7)$$

Applying this correction to the data in Figure 8 leads to $\delta^{18}O_{gravcorr}$ and $\delta^{17}O_{gravcorr}$ values of 0‰ versus atmosphere, which is the value that is expected for this time period.[18] A compilation of all ice measurements performed with the new technique is given in Table 2.

Influence of Dissolution of Air in Water during the Transport Process. For GRIP ice covering the time periods 7800−8100 years BP and 8400−8600 years BP, we would expect $\delta^{15}N$ values of ~0.34‰ [3], $\delta^{18}O_{gravcorr}$ values between −0.3 and −0.4‰ [18], and $\delta^{17}O_{gravcorr}$ values between −0.15 and −0.2‰.[19] $\delta^{18}O_{gravcorr}$ and $\delta^{17}O_{gravcorr}$ correspond to the expected values. However, we measured significantly lower $\delta^{15}N$ values, (0.23 ± 0.03)‰, than expected, (0.34 ± 0.02)‰.[3] Remarkably, the variability of the oxygen isotope data is significantly reduced for the gravitation corrected data compared to the raw data.

This discrepancy between expected and measured $\delta^{15}N$ values can most probably be explained by a solubility influence that offsets the standard values. During the transport process of the air−water mixture from the melting device (ice sample) or the bubble generator (standard) through the pump to the degassing unit, part of the air will be dissolved in the water. An equilibrium

Figure 9. Model output of the dynamics of the dissolution process between air bubbles and water in a tube. The isotope fractionation of nitrogen $\delta^{15}N$ and oxygen $\delta^{18}O$ in the air bubble is plotted against the exchange time. Different exchange times for standard and ice sample lead to a Δ shift of the reference toward higher δ values, as compared to the sample.

between water and air bubble for which the water is saturated with air and the δ value of the dissolved air is slightly enriched comparing to the air in the bubbles can be established. The equilibrium enrichment is $\epsilon_{eq} = 0.68‰$ for ^{15}N and $\epsilon_{eq} = 0.73‰$ for ^{18}O at 20 °C.[20] Before the equilibrium is reached, a dynamic process of dissolution of air in water takes place in which the isotopic fractionation can be much higher than in the equilibrium and is strongly dependent on the exchange time (Figure 9). However, for those transient cases, fractionations should still be the same if exchange times for the sample and the standard are the same and, hence, cancel each other. Obviously, this was not the case for the ice measurements. The exchange time of ice sample is nearly twice as long as the exchange time of the standard gas because of the length of the tube (220 cm) from the melting device to the degassing unit, which is much longer than the tube (140 cm) from the bubble generator to the degassing unit. This leads to different fractionations of the ice sample and

(17) Schwander, J. In *The Environmental Record in Glaciers and Ice Sheets*; Oeschger, H., Langway, C. C., Jr., Eds.; John Wiley: New York, 1989; pp 53−67.

(18) Fuchs, A.; Leuenberger, M. *Geophys. Res. Lett.* **1996**, *23*, 1049−1052.

(19) Blunier, T.; Barnett, B.; Bender, M. L.; Hendricks, M. B. *Glob. Biogeochem. Cycles* **2002**, *16*, 10.1029/2001GB001460.

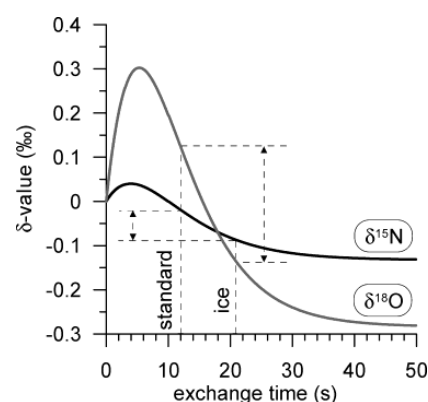(20) Knox, M.; Quay, P. D.; Wilbur, D. *Sel. Pap. Second Int. Symp. Gas Transfer Water Surf.* **1990**, 184−191.

(21) Schwander, J.; Barnola, J.-M.; Andrié, C.; Leuenberger, M.; Ludin, A.; Raynaud, D.; Stauffer, B. *J. Geophys. Res.* **1993**, *98*, 2831−2838.

Table 3. Solubility Influence Due to Different Lengths (Exchange Times) of the Sample and Standard Tubing

exchange time (s)	parameter	δ model (‰)	$\Delta\delta$ model (‰)	$\Delta\delta$ meas (‰)	difference (‰)
12	δ^{15}N	−0.05			
	δ^{18}O	−0.10			
	$\delta O_2/N_2$	−148.30			
	$\delta Ar/O_2$	−168.07			
	$\delta Ar/N_2$	−23.22			
21	δ^{15}N	−0.11	0.06	0.06	0.00
	δ^{18}O	−0.34	0.24	0.14	0.10
	$\delta O_2/N_2$	−176.74	28.44	28.03	0.41
	$\delta Ar/O_2$	−200.31	32.23	31.90	0.33
	$\delta Ar/N_2$	−28.62	5.41	3.43	1.98
34	δ^{15}N	−0.14	0.09	0.08	0.01
	δ^{18}O	−0.44	0.34	0.35	−0.00
	$\delta O_2/N_2$	−186.26	37.96	31.13	6.82
	$\delta Ar/O_2$	−211.09	43.02	40.39	2.63
	$\delta Ar/N_2$	−30.52	7.30	8.83	−1.52

the standard that causes a Δ shift of the reference toward enriched δ values, which would explain the lower ice δ^{15}N values.

The dynamics of the dissolution process can be evaluated for every gas species using a 2-box model. The first box in this model is the air bubble (with the volume, V_g; the δ value of the gas, δ_g; the pressure, p; and the gas concentration, c_g), and the second box is the water (with the water volume, V; the volume of dissolved gas, V_w; the δ value of the dissolved gas, δ_w; the solubility factor, s; the degree of saturation of dissolved gas, f, and the gas concentration in the water, c_w). There is a gas flux from the air bubble into the water, $F_{gw} = \alpha s p c_g$, and a reverse flux from the water into air bubble, $F_{wg} = \alpha c_w = \alpha V_w/V$, where α is a unknown proportionality constant (for a film model, this constant is the product of the exchange velocity and the surface area between the liquid and the gas phase). The δ value of the interchanging gas is fractionated as a result of the kinetic, ϵ_k, and equilibrium, ϵ_{eq}, fractionations. The following equations describe the dynamics of the process:

$$\frac{dV_g}{dt} = -\frac{dV_w}{dt} = -F_{gw} + F_{wg} \quad (8)$$

$$\frac{d\delta_g}{dt} \approx \frac{-F_{gw}\left(\epsilon_k + \frac{\epsilon_{eq}}{2}\right) + F_{wg}\left(\delta_w - \delta_g + \epsilon_k - \frac{\epsilon_{eq}}{2}\right)}{V_g} \quad (9)$$

$$\frac{d\delta_w}{dt} \approx \frac{-F_{wg}\left(\epsilon_k - \frac{\epsilon_{eq}}{2}\right) + F_{gw}\left(\delta_g - \delta_w + \epsilon_k + \frac{\epsilon_{eq}}{2}\right)}{V_w} \quad (10)$$

Figure 9 shows the model output for δ^{15}N and δ^{18}O. The following parameters were used to feed the model. All constants correspond to a temperature of 20 °C. $V_g(STP)/V = 0.1$, $V_w/V = 0$, $p = 1.3$ atm; δ^{15}N: $s = 0.015$ mL(STP)/mL(H$_2$O)atm, $\epsilon_{eq} = 0.68‰$,[20] $\epsilon_k = -1.2‰$,[20] $c_g = 0.78$; δ^{18}O: $s = 0.030$ mL(STP)/mL-(H$_2$O)atm, $\epsilon_{eq} = 0.73‰$,[20] $\epsilon_k = -2.8‰$,[20] $c_g = 0.21$. The proportionality constant α is set to 0.14 cm^3/s in order to best fit the measured values. Please note that α influences only the time scale in Figure 9 and not the magnitude of fractionation. The exchange times are ~12 s for the standard gas, and ~21 s for an ice sample.

These assumptions lead to a Δ shift of the reference of 0.06‰ for δ^{15}N, and of 0.24‰ for δ^{18}O toward higher values.

The measured GRIP data shows a strong correlation between oxygen and nitrogen isotope values ($\delta^{18}O_{measured} = 2.55\delta^{15}N_{measured} - 0.484‰$, $R^2 = 0.873$; and $\delta^{17}O_{measured} = 1.68\delta^{15}N_{measured} - 0.35‰$, $R^2 = 0.44$) supporting this explanation.

$$\delta^{15}N_{measured} = \delta^{15}N - \Delta \quad (11)$$

$$\delta^{18}O_{measured} = \delta^{18}O - m\Delta \quad (12)$$

$$\delta^{17}O_{measured} = \delta^{17}O - n\Delta \quad (13)$$

From eqs 11−13, one can find the following relation between measured oxygen and nitrogen isotope data:

$$\delta^{18}O_{measured} = \delta^{18}O - m\delta^{15}N + m\delta^{15}N_{measured} \quad (14)$$

$$\delta^{17}O_{measured} = \delta^{17}O - n\delta^{15}N + n\delta^{15}N_{measured} \quad (15)$$

From the measured correlation we find $m = 2.55 \pm 0.56$ and $n = 1.68 \pm 1.10$. Hence, by applying the correction for gravitational enrichment, the effect of the reference Δ shift is nearly canceled, which explains the lower variability of the corrected oxygen isotope data in Table 2.

$$\delta^{18}O_{gravcorr} = \delta^{18}O_{measured} - 2\delta^{15}N_{measured} = \delta^{18}O - 2\delta^{15}N - \Delta(m - 2) \quad (16)$$

$$\delta^{17}O_{gravcorr} = \delta^{17}O_{measured} - \delta^{15}N_{measured} = \delta^{17}O - \delta^{15}N - \Delta(n - 1) \quad (17)$$

However, the measured value of m is lower than the value we would expect from our model, $m_{model} = 0.24/0.06 = 4$. The reason for this discrepancy is not clear. The temperature dependence of the solubility, s, and the fractionations, ϵ_k and ϵ_{eq}, influence the parameter, m. Further measurements are required to solve this problem.

For the Dome C and Eurocore measurements, it is difficult to decide whether the measured values are offset, since only one or two values are available. But we would expect the same Δ shift as for the GRIP measurements.

From these findings, we conclude that an adjustment of the length of the tubing for the standard and the sample lines will help to prevent a Δ shift between the sample and the standard. First measurements with standard gas have proven this interpretation. As summarized in Table 3, the measured solubility influence due to different capillary lengths (hence, different exchange times) for the sample and standard path are in excellent agreement with model prediction. Furthermore, the exchange time should be increased to ~50−60 s by inserting a exchange tube after the 4-way valve (Figure 1) in order to reach more stable conditions close to the equilibrium (Figure 9), where slight differences in the exchange time do not affect the δ values.

CONCLUSIONS

We developed a new on-line system to determine the isotopic composition of the main air components, which proved to work

reliably for standard air admixed and subsequently removed from a water stream. Standard deviations of $\sim$0.04‰ for $\delta^{15}N$, $\sim$0.1‰ for $\delta^{18}O$, and $\sim$0.15‰ for $\delta^{17}O$ are comparable to conventional melt extraction systems. The ice measurements with the new on-line system are promising. Nitrogen as well as oxygen isotope ratios can be measured with a spatial resolution of $\sim$3 cm and nearly the same precision as the standards. Furthermore, the new system accelerates the procedure of extraction and measuring of ice samples. However, the accuracy of the ice measurements needs to be further improved to replace the conventional wet extraction system. By modeling the dynamics of the dissolution process between air bubbles and water during the transport through the system, we most probably have found the reason for the lack of accuracy in the time-dependent dissolution process associated with kinetic fractionation. Therefore, we are convinced that the proposed improvement of the system will lead to a better accuracy of the ice measurements.

Measurements of moderate accuracy are already possible. Such measurements could be useful in determining nitrogen and oxygen fractionations associated with biological activities in aquatic systems.

3.2 Measurements of Isotope and Elemental Ratios of Air from Polar Ice with a New On-Line Extraction Method

Christof Huber[1] and Markus Leuenberger[1]

Abstract

A recently developed continuous on-line extraction and analyzing technique for air trapped in ice cores has been improved and tested. The technique allows fast high resolution measurements of the isotopic and elemental ratios of the main air components nitrogen, oxygen and argon. Continuous measurements of up to 1 m long ice sections can be performed with a resolution of $\sim$3 cm (running average). For nitrogen and oxygen isotope ratios the accuracy and reproducibility is comparable to conventional melt extraction techniques. It depends on the desired resolution and the composition of the ice. For either pure bubble or complete bubble free ice the reproducibility and accuracy for a resolution of 3 cm is $\pm < 0.02^0/_{00}$ for δ^{15}N, $\pm < 0.05^0/_{00}$ for δ^{18}O, and $\pm < 0.06^0/_{00}$ for δ^{17}O, respectively. Furthermore, δAr/O$_2$ ($\pm 1^0/_{00}$), δO$_2$/N$_2$, δAr/N$_2$ (both ± 5–$8^0/_{00}$), and δ^{36}Ar (± 0.2–$0.3^0/_{00}$) can be determined as well. The precision of elemental ratios is good enough to resolve variations which are detected in ice at depths where air bubbles form clathrate hydrates. Surprisingly, at this depths the elemental ratios show roughly annual variations probably due to strong fractionations between air in clathrate hydrates and air in bubbles. Based on our measuring precision we cannot exclude similar effects for isotope ratios.

[1]Climate and Environmental Physics, Physics Institute, University of Bern, Sidlerstrasse 5, CH-3012 Bern, Switzerland

3.2.1   Introduction

Measurements of the isotopic and elemental composition of air trapped in polar ice is providing fundamental information about ancient climate. $\delta^{18}O$ measured on past atmospheric O_2 is a proxy of continental ice volume and can be used to synchronize cores from Greenland and Antarctica [4]. Fractionations of the isotope ratios of nitrogen, $\delta^{15}N$, and argon, $\delta^{36}Ar$, caused by gravitational settling and thermal diffusion in the firn column of polar ice sheets, have been used successfully to asses abrupt temperature changes in Greenland [16, 17, 19, 33]. Variations of the elemental ratios, O_2/N_2, Ar/N_2 and Ar/O_2 can provide valuable information about processes occurring during the bubble close-off process in the firn. Furthermore it has been shown, that O_2/N_2 from Antarctic ice cores varies coherently with local summertime insulation [3] and can be used as a tool to date old ice. In this study we improved our recently developed continuous on-line extraction and analyzing technique [11] resulting in an increased precision. Various measurements on different ice cores from Greenland (GRIP, NorthGRIP) and Antarctica (Dome C, DML) are performed. The potential of the new technique is discussed based on reproducibility tests and comparisons with data obtained using conventional extraction techniques [17, 19]. The new on-line melt extraction method is able to accelerate sample processing significantly. It allows the simultaneous and continuous determination of the isotopic and elemental ratios $\delta^{15}N$, $\delta^{18}O$, $\delta^{36}Ar$, $\delta O_2/N_2$, $\delta Ar/N_2$ and $\delta Ar/O_2$ within minutes, and offers a real alternative to conventional melt extraction systems.

3.2.2   Improvement of the Experimental Setup

The schematic setup of our extraction system and processing line is shown in Figure 3.1. The extraction procedure is described in detail in Huber et al. [11]. The ice sample is continuously melted on a melting device. Subsequently, the air is separated from the melt-water in a degassing unit. In order to avoid fractionations, samples and standard are processed equally in our system. In our earlier paper [11] a modification of the system was proposed to improve accuracy. Since the extraction of the gases from the water in the degassing unit (Figure 3.1) is not fully quantitative, the dissolution of air in water during the transport through the system can influence the measured δ-values. Hence in order to establish an equilibrium between water and dissolved air, the mixture of water and air bubbles passes an equilibration column (5 m long, i.d. 0.75 mm) prior to the degassing unit. This procedure helps to prevent kinetic fractionation effects between sample and standard since both are treated exactly the same way. It allows accurate measurements of the isotopic ratios, as well as of the Ar/O_2 ratio, since argon and oxygen have similar solubilities. In contrast, the accuracy for $\delta O_2/N_2$ and $\delta Ar/N_2$ is lower, due to different water solubilities. Here, only a complete degassing of the water would help to increase accuracy significantly.

3.2.3   Mass Spectrometry

A ThermoFinnigan Delta Plus XL IRMS was used for the measurements. This IRMS is equipped with a multi collector array of 8 Faraday cups, permitting the simultaneous determination of the isotopic and elemental ratios of the all major air components (N_2, O_2 and Ar i.e. $m/z = 28, 29, 32, 33, 34, 36, 40$ and 44). Without this outstanding ability of
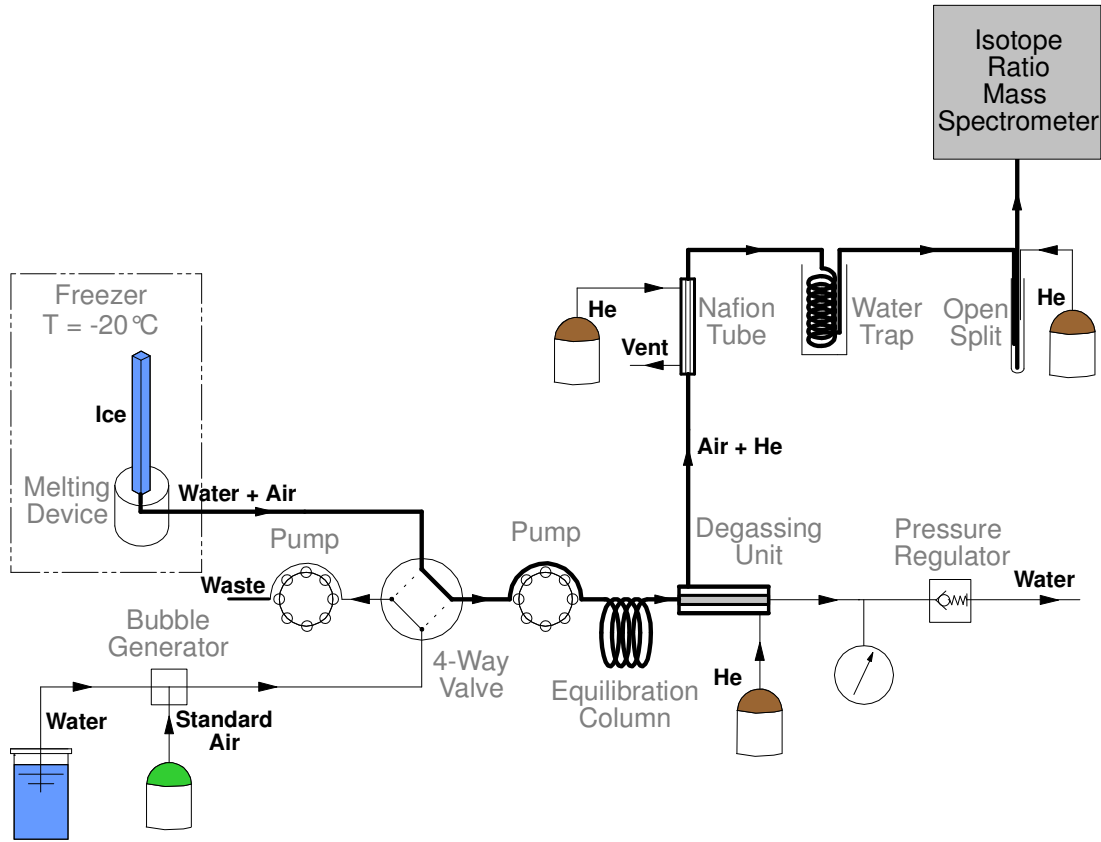
Figure 3.1: Schematic setup of the system. An ice bar of up to 100 cm in length with a square area of 2×2 cm is continuously melted (3 cm/min) on a heated melting device [35]. The design of the melting device prevents contamination of the sample with ambient air because only the innermost part of the core section is used for the analyses. In a separate line, tiny bubbles of standard gas are immersed into a flow of degassed Ultra Pure water. The air is separated from the water in the degassing unit, consisting of a gas-permeable hydrophobic membrane that is placed in a tube of the same length, which is constantly flushed with He. A pressure gradient between the water and the He of 0.1–0.3 bar, drives the air bubbles through the membrane into the reverse He carrier flow. Additionally, molecular diffusion forces about 10 to 20% of the dissolved air into the He. Better degassing efficiencies can be achieved using longer membranes, but this causes stronger signal dispersion and thus lower measurement resolution. Finally, water vapor and CO_2 are removed from the sample by a Nafion drying column and a subsequent cold trap held at liquid nitrogen temperature before the gas is introduced into the mass spectrometer via an open split.

the Delta Plus XL we would not been able to perform fully continuous measurements of all components synchronically. Due to small variations of isotopic compositions, measurements are expressed relative to a known standard in the δ-notation:

$$\delta = (R_{sample}/R_{standard} - 1) \times 1000^0/_{00} \tag{3.1}$$

where R is the abundance ratio of the isotopes, e.g. for nitrogen $R = {}^{15}N/{}^{14}N$. Isotope ratio measurements should be referred to modern atmospheric composition. Our reference air standard (working standard LK54) is compressed dry atmospheric air. We compared it with atmospheric air sampled at Jungfraujoch and measured with our new gas inlet system

[18]. These measurements showed no significant deviations of the isotope ratios, whereas for the elemental ratios the following offsets between LK54 and atmosphere were determined: $\delta O_2/N_2 = -3.91^0/_{00}$, $\delta Ar/N_2 = 3.92^0/_{00}$, and $\delta Ar/O_2 = 7.79^0/_{00}$).

In contrast to a standard reference gas injection system (e.g. Conflow), we use a reference gas that passes through the entire system instead. Reference air standard is measured prior and after each sample measurement. Sample analysis time may vary between 4 min and 20 min depending on the length of the ice sample. 55 cm of ice melted at a velocity of 3 cm/min corresponds to an analysis time of slightly more than 18 min. Therefore, the performance of the IRMS has to be stable or at least linear for a time period of up to 30 min.

To reach the required precision the following corrections have to be applied:

(i) Background correction: The background is determined daily by flushing the sample capillary with pure helium. Background signal is in the order of 0 to 15 mV depending on the collector cup. It is very stable. Since we use a cold trap at liquid nitrogen temperature, water vapor as well as CO_2 is removed from the sample. Thus an additional correction for the contribution of CO fragments from CO_2 to the ^{15}N signal is not necessary.

(ii) Signal intensity imbalance effect: Measured isotope ratios are slightly sensitive to variations of the signal intensity of the ion beam. For our system the signal intensities of the standard and the sample are not exactly balanced. Furthermore, variations of the signal intensity due to a varying gas content in the ice can reach more than 10% of the mean value. Therefore the measured δ-values have to be corrected for the signal intensity imbalance effect according to:

$$\delta^i_{intensity\,corrected} = \delta^i_{measured} - k^i \Delta I_{m/z28} \tag{3.2}$$

where i denotes the isotope ratio, $\Delta I_{m/z28}$ the difference of the signal intensity of the main mass/charge ratio 28 between sample and reference, and k^i the linear correction coefficient. We determine the correction coefficients k^i for each measurement sequence of one to four samples by introducing the air standard at three different signal intensity levels (different amounts of standard gas are admixed to the water in the bubble generator). Typical values for the coefficient k^i are $0.05^0/_{00}/V$ for $\delta^{15}N$, $0.5^0/_{00}/V$ for $\delta^{18}O$, $0.8^0/_{00}/V$ for $\delta^{17}O$ and $3^0/_{00}/V$ for $\delta^{36}Ar$, respectively. This values depend on the ion source settings. This correction thus includes ion source pressure imbalance effects as well as instrument non-linearity effects which, however, potentially have the same origin. For the elemental ratios $\delta O_2/N_2$, $\delta Ar/N_2$ and $\delta Ar/O_2$ the corrections are larger and more variable (about $10–20^0/_{00}/V$). The reason for this are differences in the water solubility between O_2, N_2, and Ar, that cause additional fractionations depending strongly on the ratio of dissolved to undissolved air in the water. This effect is at least an order of magnitude larger than the instrument non-linearity effects [11].

(iii) Chemical slope correction: It has been shown that measured isotopic ratios of a single element in a mixture of gases are sensitive to variations in the elemental ratios [38]. The amount of the influence depends on the instrument and the measuring parameters (e.g. focusing conditions, ion source pressure). Nitrogen and oxygen isotope ratios are sensitive to variations of the N_2/O_2 ratio, whereas argon isotope ratio depend on the N_2/Ar ratio. This leads to the following corrections:

$$\delta^i_{el.\,comp.\,corrected} = \delta^i_{intensity\,corrected} - m^i \delta N_2/O_2 \tag{3.3}$$
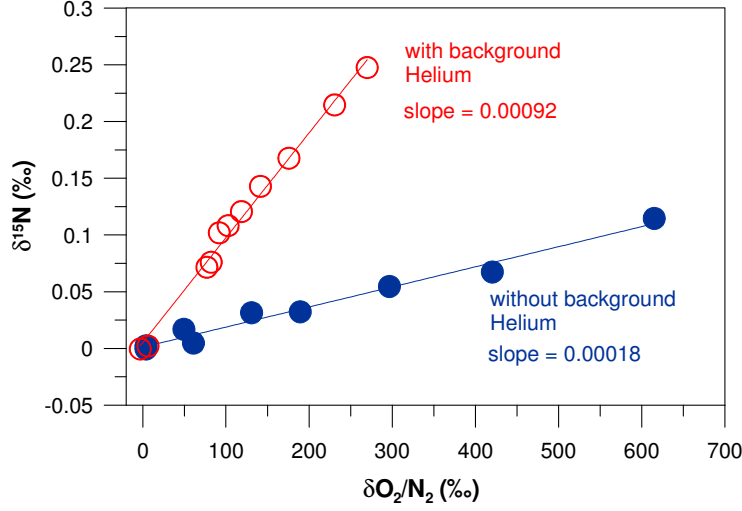
Figure 3.2: Determination of the "chemical slope" of $\delta^{15}N$, by adding increasing amounts of oxygen to a standard gas. The slope with background He (red open circles) is significantly larger than without background He (blue filled circles).

for i = ^{15}N, ^{18}O and ^{17}O, and

$$\delta^i_{el.\,comp.\,corrected} = \delta^i_{intensity\,corrected} - m^i \delta N_2/Ar \tag{3.4}$$

for i = ^{36}Ar, respectively. The chemical slope is determined every two weeks by measuring a mixture of various amounts of either pure N_2 or pure O_2 and standard gas against pure standard gas (see Figures 2 and 3). The gases are supplied to the IRMS using the bellows of the dual-inlet system. Typical values are $0.011\pm0.002^0/_{00}/^0/_{00}$ for $\delta^{17}O$, $0.022\pm0.002^0/_{00}/^0/_{00}$ for $\delta^{18}O$, and $0.083\pm0.006^0/_{00}/^0/_{00}$ for $\delta^{36}Ar$. For $\delta^{15}N$, the chemical slope is very low, only about 0.0005 to $0.001^0/_{00}/^0/_{00}$ (Figure 3.2). Generally, chemical slopes remain extraordinary stable. Despite parts of the ion source have been exchanged and the settings of the potentials have been changed several times, we did not detect major differences or trends during the last two years. Interestingly, the chemical slopes are influenced by the He background in the ion source. In an on-line system the sample is transported by a constant He carrier flux, which increases the ion source pressure more than one order of magnitude and alters the chemical slopes. Chemical slopes with He background are 2 to 4 times higher than without He background (Figures 3.2 and 3.3). The reason is unclear.

(iv) Drift correction: Signal drifts between two standard measurements (δ^i_{std-1} and δ^i_{std-2}) are corrected linearly with time.

$$\delta^i_{drift\,corrected} = \delta^i_{intensity\,corrected} - n^i \Delta t \tag{3.5}$$

with $n^i = (\delta^i_{std-2} - \delta^i_{std-1})/(t_2 - t_1)$. Δt is the time difference between the measurement and the standard (t_1). Hence, frequent standard measurements improve accuracy. To reduce drifts, we control the room temperature, and start to condition the ion source with air and He at least one hour prior to the start of the first measurement. For the typical duration of an ice measurement of 15 to 20 minutes, drift correction is linear and in the order of a few hundredths of a per mil.
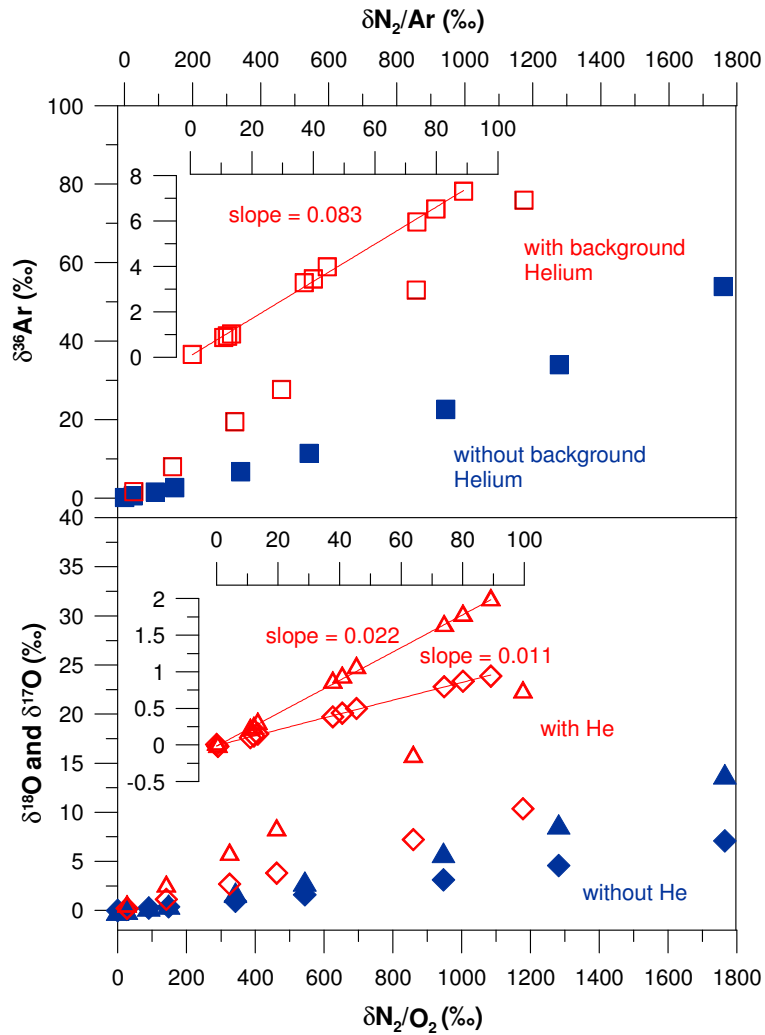
Figure 3.3: Determination of the "chemical slope" of $\delta^{18}O$ (diamonds), $\delta^{17}O$ (triangles), and $\delta^{36}Ar$ (squares), by adding increasing amounts of nitrogen to a standard gas. The slope with background He (red open symbols) is significantly larger than without background He (blue filled symbols).

In Figure 3.4 the effect of the different corrections on δ-values is shown for an on-line measurement. The signal is dispersed in our system due to diffusion and turbulences during the transport process (dispersion time is ~20 s). Additionally, in order to reduce noise, the 1 s data is smoothed by a 40 s running average. Thus, a maximal spatial resolution of about 3 cm can be achieved [11]. To avoid memory effects we reject the first and the last 40 s of each measurement. For a melt velocity of 3 cm/min this corresponds to an ice loss of 2 cm at either end.
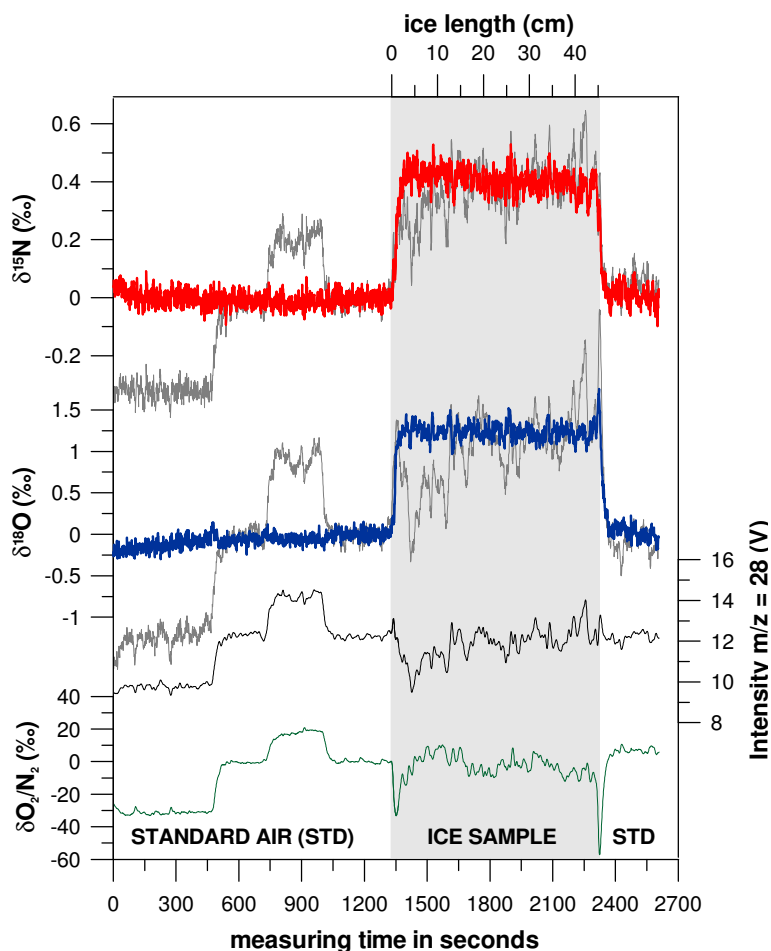
Figure 3.4: Example of an ice measurement. The upper two curves show raw (gray) and corrected δ^{15}N (red) and δ^{18}O (blue) values. The signal intensity (black) and the uncorrected $\delta O_2/N_2$ (green) ratio corresponds to the lower two curves. The measurement starts with a calibration procedure, i.e. standard air measured at three different signal intensities in order to extract the signal intensity imbalance effect. This takes about 15 to 20 minutes. After the calibration phase up to four ice samples can be measured one after another, sandwiched between standards. The standard measurements are needed as a reference and to determine the drift correction. O_2/N_2 and Ar/N_2 ratios are used to correct for chemical slope influences.

3.2.4 Measurements

To characterize our new on-line system and to assess reproducibility and accuracy of the measurements we analyzed samples from different ice cores drilled either in Greenland (GRIP, NorthGRIP, Dye-3) or in Antarctica (Dome C, DML).

Reproducibility from Replicate Measurements

We determined the reproducibility performing replicate measurements of ice taken at the same depth. We measured samples from a NorthGRIP firn ice core (NGRIP2001S-4) at depths between 95 and 98 m (just below the close off depth of about 70 m), from Dye-3 (159

m) and from the DML core (542 m). The accumulation rate at NorthGRIP is 17.5 cmH$_2$O/yr and the annual mean temperature is -31.7°C. The core has a very homogeneous bubble distribution and is therefore perfectly qualified for reproducibility studies. The DML core should be homogenous as well (6.7 cmH$_2$O/yr; -45.6°C), but our samples are from a depth interval where air bubbles are partly transformed into clathrate hydrates. Associated with this transfer are enormous fractionations, mainly of the elemental ratios, between clathrate hydrates and bubbles (see discussion below) [12, 13], manifested as strong variations of the measured elemental ratios (more than $\pm 50^0/_{00}$ for $\delta O_2/N_2$ and $\delta Ar/N_2$). Such variations reduce the precision of isotope ratio measurements due to uncertainties in the determination of the chemical slopes (eq. 3.3 and 3.4). Finally, Dye-3 is a very high accumulation core (50 cmH$_2$O/yr; -19.6°C). Summer temperature is relatively warm and melting of ice occurs frequently. In the used 1 m section we registered one large and two smaller melt events. Melt-layers reduce reproducibility since signal intensity decreases substantially during melt events. Furthermore, the shape of the melt-layers was not exactly horizontal, hence the influence was different for each sample. Therefore, those parts of the measurements which are obviously disturbed by melt-layers were rejected. We used the pooled standard deviation, s_{pooled}, as a measure of reproducibility [32]:

$$s_{pooled} = \sqrt{\frac{\sum (\delta_i - \overline{\delta_j})^2}{n - m}} \tag{3.6}$$

where s_{pooled} is the square root of the summed squared deviations of replicates δ_i from their respective means, divided by the degrees of freedom (the number of measured delta values n minus the number of means m). A compilation of the reproducibility (s_{pooled}) of the NorthGRIP, Dye-3, and DML measurements for three different average scenarios (1 cm, 3 cm, and 15 cm resolution) is shown in Table 3.1 and Figure 3.2.4. As one would expect, the longer the averaging interval the better the reproducibility, and for the Dye-3 and the DML ice the reproducibility is lower due to melt-layers and bubble hydrate fractionations.

Assessment of Accuracy by Comparison with Firn Air Measurements

The NorthGRIP firn core measurements can be used to assess the accuracy of the on-line technique. Atmospheric $\delta^{15}N$ and $\delta^{36}Ar$ are constant due to their long turnover times [20]. The enriched values of these ratios measured on air trapped in the ice reflect processes that occur in the diffusive firn column, where the gas isotopes are fractionated due to gravitational settling [8, 30, 28] and thermal diffusion [19, 31]. In 2001, firn air samples were taken at NorthGRIP, part of which were analyzed on our ThermoFinnigan Delta Plus XL IRMS using the conventional dual inlet technique (Table 3.2). The three deepest firn air samples correspond to the non-diffusive zone of the firn, hence, the isotopic ratios should agree with the values trapped in the ice, which indeed is nicely the case within an error range of 0.02$^0/_{00}$ for $\delta^{15}N$. The oxygen isotope ratios $\delta^{18}O$ and $\delta^{17}O$ agree within an error range of about 0.05$^0/_{00}$ to 0.06$^0/_{00}$. The $\delta^{17}O$ value of the firn samples of 0.41$^0/_{00}$ seems to be unrealistic high. A systematic error cannot be excluded. For $\delta^{36}Ar$, however, a large offset of 0.3$^0/_{00}$ is observed. It is known that the measurement of argon isotopes in an air mixture is extremely difficult, due to oxygen-argon-nitrogen interactions in the ion source. To achieve more accurate argon measurements the argon should be separated from the other air components, mainly from oxygen [32], and measured separately. In contrast to isotope
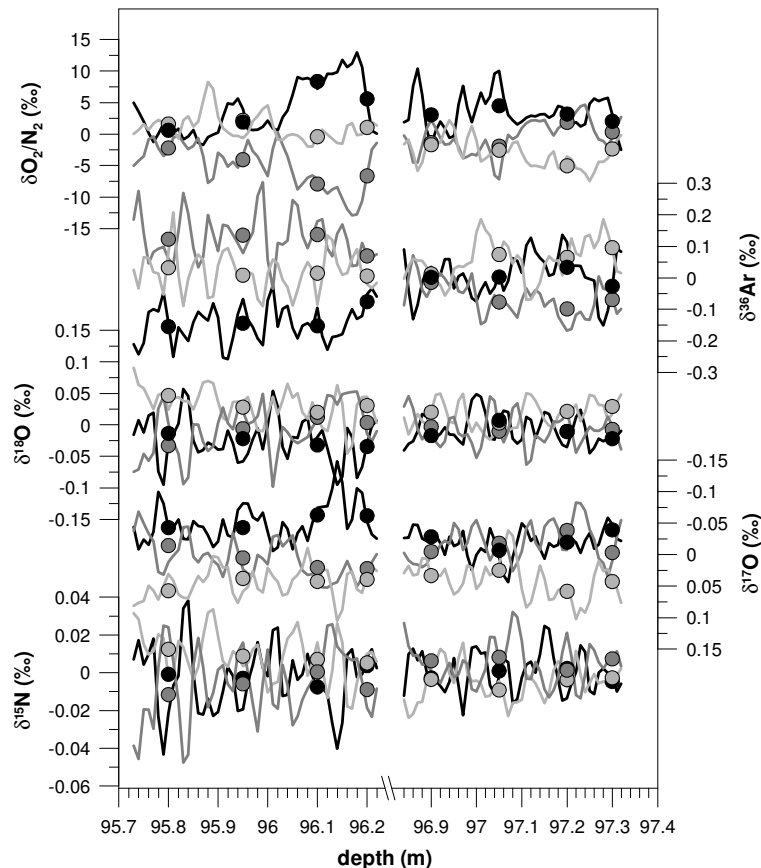
Figure 3.5: The deviation from the mean of three replicate measurements of two 55 cm sections of the NorthGRIP core (bag 175 and bag 177) as continuous lines (1 cm resolution) and as discrete points (15 cm averages). The reproducibility of the high resolution measurements (1–3 cm averages) is about $0.02^0/_{00}$ for $\delta^{15}N$, $0.05^0/_{00}$ for $\delta^{18}O$, $0.06^0/_{00}$ for $\delta^{17}O$, $0.2^0/_{00}$ for $\delta^{36}Ar$, 6–$7^0/_{00}$ for $\delta O_2/N_2$ and $\delta Ar/N_2$, and $1^0/_{00}$ for $\delta Ar/O_2$. It is better for the 15 cm averages (Table 3.1).

ratios, elemental ratio measurements from firn and ice cores cannot be compared directly, since elemental ratios are heavily fractionated during the bubble close off process [5].

Assessment of Accuracy by a Comparison with Measurements obtained from Conventional Wet Extraction Technique

A further test for the accuracy of the new on-line technique is to compare measurements with analyses performed with other methods. For this purpose we remeasured 10 GRIP ice samples from two events, the 8200 yr B.P. event [19] and the Dansgaard/Oeschger (D/O) event 19 [17], which were measured previously using our conventional wet extraction system.

For the D/O 19 event, five samples each between 20 and 30 cm long are compared to the [17] data (Figure 3.6). The on-line measurement agree nicely with the older data within an error range of $0.02^0/_{00}$ for $\delta^{15}N$, and $0.05^0/_{00}$ for $\delta^{18}O$, assuming an offset for the Lang et al. [17] $\delta^{15}N$ data of $-0.10^0/_{00}$. At the time of the Lang et al. [17] publication, the authors

Table 3.1: Reproducibility of NorthGRIP, Dye-3, and DML on-line measurements. Note: The reproducibility for 3 cm averages is only slightly better than for 1 cm averages. This is the case since the signal is smoothed due to dispersion and it corresponds to a running average over about 3 cm [11].
(A) b: pure bubble ice; ml: meltlayers; h + b: hydrates and bubbles.

ice	bag	resol. in cm	type ^{A} of ice	degree of freedom	pooled standard deviation in per mil						
					δ^{15}N	δ^{18}O	δ^{17}O	δ^{36}Ar	$\delta O_2/N_2$	$\delta Ar/N_2$	$\delta Ar/O_2$
NGRIP	175	1	b	100	0.021	0.05	0.059	0.16	6.1	6.4	1.1
NGRIP	177	1	b	100	0.014	0.032	0.047	0.1	4.5	4.8	0.9
Dye-3	160 A	1	b, ml	58	0.04	0.085	0.08	0.2	12.7	11.2	3.1
Dye-3	160 B	1	b, ml	80	0.025	0.093	0.062	0.16	12.6	16.2	6.3
DML	543	1	h + b	38	0.044	0.061	0.041	0.126	12.4	13.5	1.3
NGRIP	175	3	b	34	0.018	0.044	0.055	0.15	5.8	6.1	1
NGRIP	177	3	b	34	0.011	0.026	0.044	0.09	4.3	4.6	0.9
Dye-3	160 A	3	b, ml	20	0.037	0.077	0.073	0.16	12.1	10.9	2.8
Dye-3	160 B	3	b, ml	28	0.019	0.069	0.052	0.14	11.5	14.8	5.7
DML	543	3	h +b	12	0.039	0.052	0.036	0.116	12	13.1	1.2
NGRIP	175	15	b	8	0.009	0.033	0.051	0.13	5.5	5.9	0.7
NGRIP	177	15	b	6	0.005	0.014	0.032	0.06	3.2	3.5	0.4
Dye-3	160 A	15	b, ml	4	0.043	0.121	0.086	0.2	12.2	9.3	7.2
Dye-3	160 B	15	b, ml	6	0.012	0.052	0.038	0.12	4.8	8.1	4.5
DML	543	15	h + b	3	0.022	0.031	0.029	0.115	7.6	8.4	0.9

Table 3.2: Comparison of on-line measurements on the NorthGRIP firn ice core (NGRIP2001S-4) with NorthGRIP firn air measurements.

method	sample	depth [m]	δ^{15}N	δ^{18}O	δ^{17}O	δ^{36}Ar
dual inlet	NGRIP firn air 12	66.99	0.32	0.63	0.39	-1.37
dual inlet	NGRIP firn air 09	69.04	0.32	0.63	0.41	-1.27
dual inlet	NGRIP firn air 11	71.75	0.32	0.62	0.41	-1.31
		mean	**0.32**	**0.63**	**0.41**	**-1.32**
on-line	NGRIP ice 175	95.8	0.31	0.69	0.38	-1
on-line	NGRIP ice 175	95.95	0.31	0.66	0.34	-0.98
on-line	NGRIP ice 175	96.1	0.31	0.67	0.35	-1.03
on-line	NGRIP ice 175	96.2	0.31	0.72	0.39	-0.94
		mean	**0.31**	**0.69**	**0.36**	**-0.99**
on-line	NGRIP ice 177	96.9	0.29	0.64	0.33	-0.96
on-line	NGRIP ice 177	97.05	0.3	0.65	0.33	-0.95
on-line	NGRIP ice 177	97.2	0.3	0.66	0.37	-0.96
on-line	NGRIP ice 177	97.3	0.3	0.65	0.34	-0.98
		mean	**0.3**	**0.65**	**0.34**	**-0.96**

corrected their values based on bubble free ice standard measurements which were $0.108^0/_{00}$ shifted compared to the assigned value. Later we noticed that this shift was caused by a scale stretching problem and not by an absolute scale shift. Since the ice samples are close to our reference (ambient air) for which the scale stretching is negligible, the correction was mistakably applied. Consequences of these corrected values are that there is now a distinct disagreement between measured and modeled δ^{15}N values, measurements being lower. This points to either to a rather extensive convective zone as it is also seen for many other ice core during the glacial phase [37] or to a different accumulation rate during this time period.

The measurements of the 8200 yr BP event are plotted in Figure 3.7. The on-line data
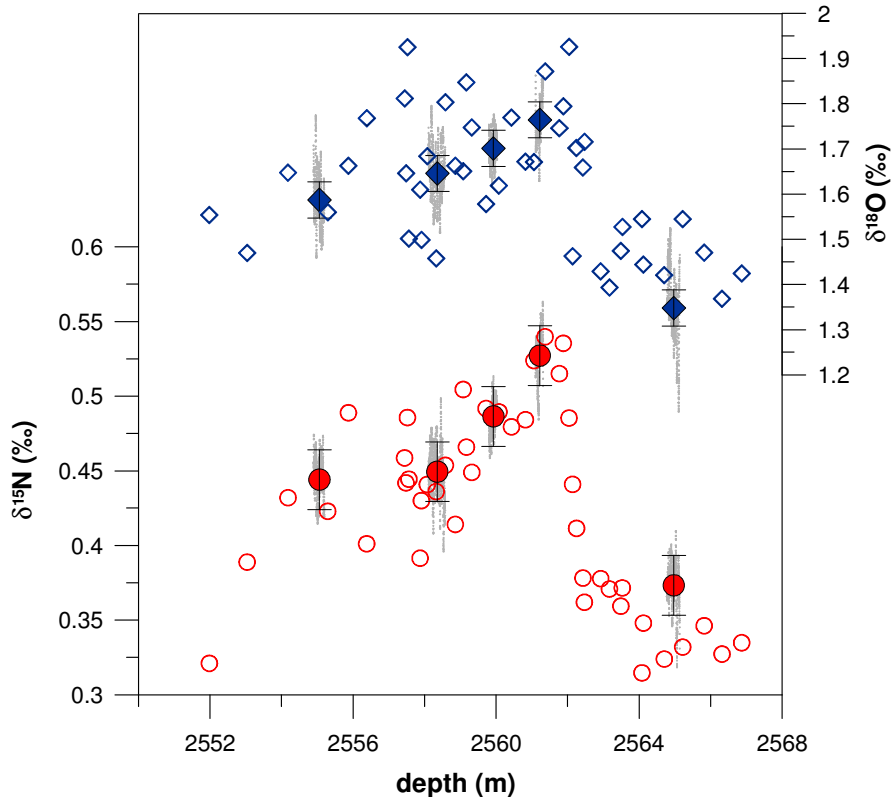
Figure 3.6: $\delta^{15}N$ and $\delta^{18}O$ during D/O event 19 measured on the GRIP ice core. Measurements performed with the new on-line technique are plotted in high resolution (light gray dots) and as measurement averages (filled red circles for $\delta^{15}N$ and blue diamonds for $\delta^{18}O$). Error bars are $\pm 0.02\%_{00}$ for $\delta^{15}N$ and $\pm 0.04\%_{00}$ for $\delta^{18}O$, respectively. Open circles and diamonds correspond to the values measured using the conventional wet extraction technique [17].

matches the conventional measurements within an error range of $0.04\%_{00}$ for $\delta^{15}N$ and $0.08\%_{00}$ for $\delta^{18}O$, respectively. The ice originates from the bubble to clathrate hydrates transformation zone (Figure 3.8). Therefore, the precision of the on-line isotope is reduced due to large elemental ratio variations typical for ice from the transformation zone (see next section).

Two Examples for Applications of On-Line Ice Measurements

At shallow depths air is stored in ice as bubbles. Deeper down in the ice, the gases are gradually transformed into clathrate hydrates [25], and both, bubbles and clathrate hydrates coexist. Finally, the deep ice is completely bubble free and all gases are trapped in clathrate hydrates. Raman spectra measurements of the O_2/N_2 ratio on air-bubbles and clathrate hydrates over the transition zone revealed strong fractionation effects between clathrate hydrates and bubbles [12, 13]. To investigate the influence of the phase transformation on ice core data, we analyzed several GRIP ice samples from depths between 100 and 2500 m (Figure 3.8). We found higher variable elemental ratios in the transformation zone, with
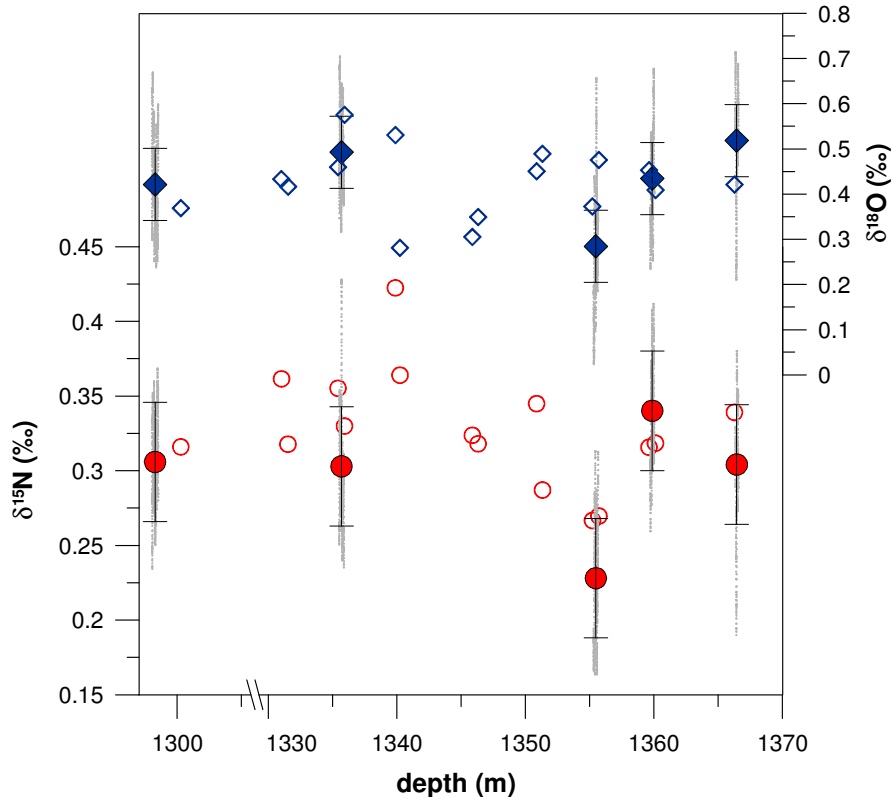
Figure 3.7: δ^{15}N and δ^{18}O during 8200 yr B.P. event measured on the GRIP ice core. Measurements performed with the new on-line technique are plotted in high resolution (light gray dots) and as measurement averages (filled red circles for δ^{15}N and blue diamonds for δ^{18}O). Error bars are $\pm 0.04^0/_{00}$ for δ^{15}N and $\pm 0.08^0/_{00}$ for δ^{18}O, respectively. Open circles and diamonds correspond to the values measured by conventional wet extraction technique [19].

surprisingly quasi-annual oscillations similar as for Ca^{2+} data (Figure 3.9). Though it is difficult to imagine a process that causes seasonal variations of elemental ratios, a possible explanation could be a fractionation of the air between clathrate hydrates and bubbles. In ice with high dust content, formation of clathrate hydrates will probably start earlier than in pure ice (nucleation effect). Therefore, our highly resolved on-line measurements indicate that seasonal variations of dust input could trigger a seasonal variability of the clathrate hydrate formation rate. Isotope ratios seem not to be affected.

Atmospheric oxygen isotope ratio δ^{18}O$_{atm}$ is influenced by δ^{18}O$_{sw}$ of seawater, and therefore by the ice volume and by the biospheric activity [7, 9]. Since oxygen is well mixed in the atmosphere, the δ^{18}O$_{atm}$ data can be used to synchronize timescales of different ice cores from Greenland and Antarctica [6, 4, 40]. Figure 10 represents a compilation of atmospheric oxygen data from different ice cores. There is a very good agreement (error range $<0.05^0/_{00}$) between the on-line data and the existing data. However, differences between the different timescales are obvious, that documents the potential to use δ^{18}O$_{atm}$ as a synchronization tool.
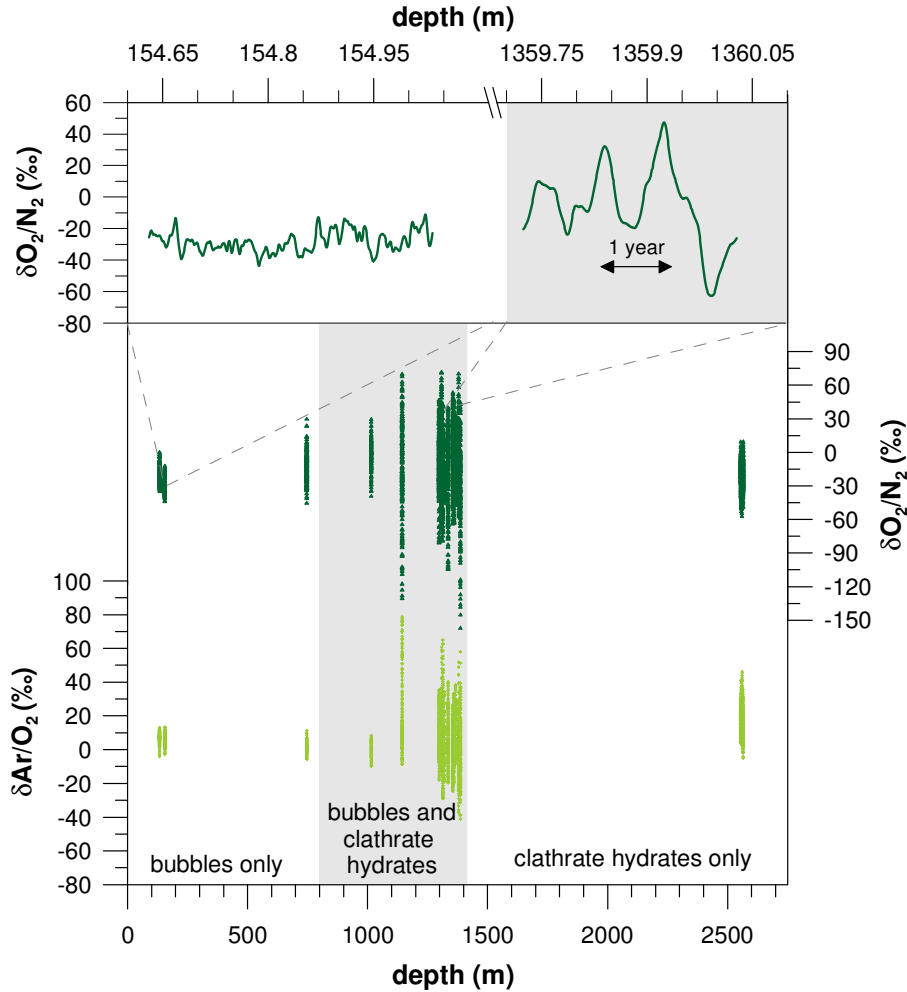
Figure 3.8: Lower Panel: The effect of bubble-clathrate hydrate transformation documented by $\delta O_2/N_2$ and $\delta Ar/O_2$ variations measured on GRIP ice. The variability is much larger than the natural variability, which is only a few per mil. However, for pure bubble ice as well as for pure clathrate hydrate-ice the variability seems to be lower than for the transformation zone. Upper panel: A zoom of $\delta O_2/N_2$ for pure bubble ice and ice from the transformation zone.

3.2.5 Conclusions

We improved and tested our new on-line technique [11] for continuous extraction and determination of the isotopic and the elemental composition of the main air components, in order to get better measurement reproducibility and accuracy. The new technique allows rapid analyses with high resolution. It proved to work reliably for nitrogen and oxygen isotope ratios. Measurement precision depends on the resolution and the composition of the ice. For either pure bubble or complete bubble free ice the reproducibility and accuracy of 15 cm averages is 0.01–0.02$^0/_{00}$ for $\delta^{15}N$, 0.03–0.05$^0/_{00}$ for $\delta^{18}O$, and 0.04–0.06$^0/_{00}$ for $\delta^{17}O$, respectively. This is comparable to precisions obtained by our conventional melt extraction technique [17, 19]. Furthermore, $\delta Ar/O_2$ (uncertainty of about $\pm 1^0/_{00}$), $\delta O_2/N_2$,
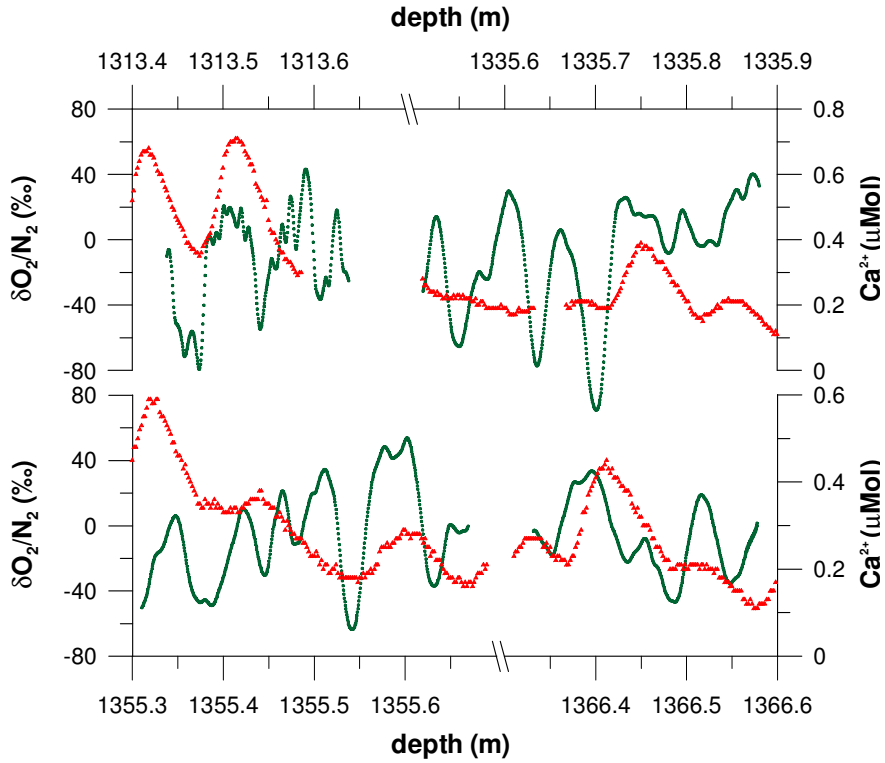
Figure 3.9: $\delta O_2/N_2$ (green dots) and Ca^{2+} (red triangles) [10] on GRIP ice from the transformation zone from bubbles to clathrate hydrates. The variations of both records look similar.

$\delta Ar/N_2$ (both ±5–$8^0/_{00}$), and $\delta^{36}Ar$ (±0.2–$0.3^0/_{00}$) can be measured. However, precision of $\delta^{36}Ar$, $\delta O_2/N_2$ and $\delta Ar/N_2$ is not yet satisfactory and should be further improved. The new technique accelerates the procedure of extraction and analyses of ice samples. Up to 16 samples can be measured a day, each between 20 to 55 cm long (corresponding to 5–17 3 cm single samples). A maximal spatial resolution of $\sim$3 cm can be achieved with about half the precision of the 15 cm averages. Hence, very highly resolved air measurements can be performed in a short time. It is now possible to measure $\delta^{15}N$ and $\delta^{18}O_{atm}$ over entire ice cores helping to synchronize chronologies, to assess gas age-ice age differences, and to calibrate the paleothermometry for rapid temperature changes. Additionally, interesting questions regarding the integrity of ice cores on very short time scales can be investigated using the new technique. For example, high resolution measurements on GRIP ice from the bubble to clathrate hydrate transformation zone revealed quasi-annual variations of the O_2/N_2 and Ar/N_2 ratios, probably due to fractionations between air in bubbles and air in clathrate hydrates.
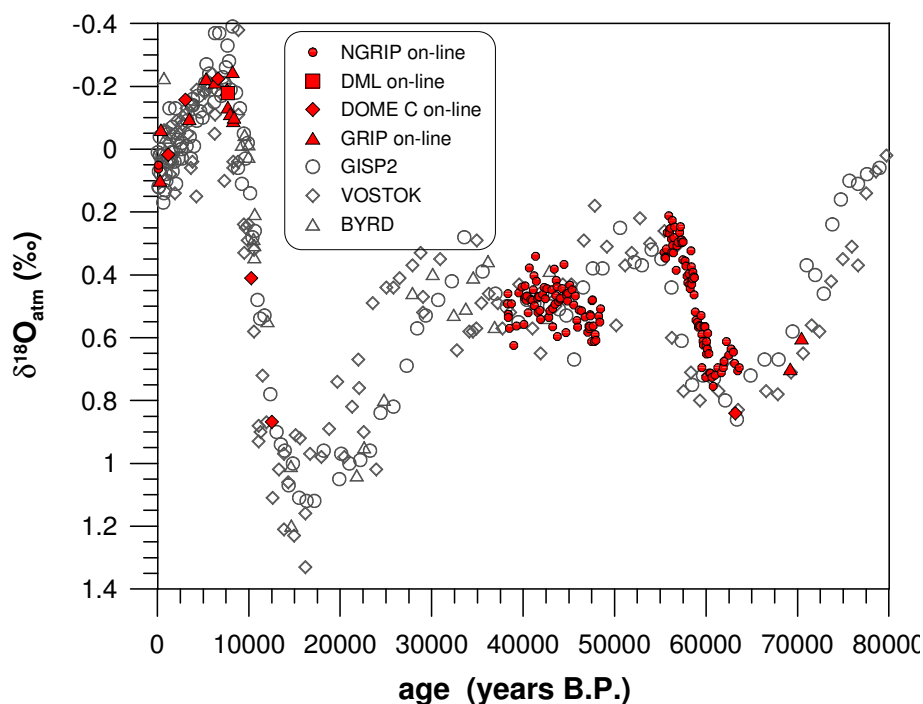
Figure 3.10: Atmospheric oxygen data from GISP2, BYRD, and Vostok is plotted together with a compilation of our on-line measured data from the NorthGRIP, GRIP, Dome C, and DML ice cores. The measurements are corrected for gravitational settling, using the $\delta^{15}N$ ($\delta^{18}O_{atm} = \delta^{18}O - 2 \cdot \delta^{15}N$). Furthermore the NorthGRIP measurements are corrected for the effect of thermal diffusion using a dynamic firn densification model that incorporates molecular and thermal diffusion (Huber et al., in preparation, 2004) [17, 19, 29]. The different data is plotted on their individual chronologies. GRIP: ss09 [10, 15, 29]; NorthGRIP: ss09sea [14, 24], Dome C: EDC2 tentative timescale [23]; DML: tentative timescale constructed by adjusting the DML timescale to Dome C by comparing the records of electrical conductivity of both cores (J. Schwander, 2004) [26, 34]; Vostok: GT4 [27, 36]; GISP2: [1, 2, 4, 21, 22]; BYRD: [39]. NorthGRIP data older than 40 kyr BP shows a age shift of 2000 to 3000 years, NorthGRIP being older. Accounting for this age offset the NorthGRIP record agrees nicely to the GISP2 and Vostok values.

Bibliography

[1] R B Alley, C A Shuman, D A Meese, T J Gow, K C Taylor, K M Cuffey, J J Fitzpatrick, P M Grootes, G A Zielinski, M Ram, G Spinelli, and B Elder. Visual-stratigraphic dating of the Greenland Ice Sheet Project 2 ice core: Basis, reproducibility, and application. *J. Geophys. Res.*, 102(C12):26.367–26.381, 1997.

[2] R.B. Alley, D.A. Meese, C.A. Shuman, A.J. Gow, K.C. Taylor, P.M. Grootes, J.W.C. White, M. Ram, E.D. Waddington, P.A. Mayewski, and G.A. Zielinski. Abrupt increase in greenland snow accumulation at the end of the Younger Dryas event. *Nature*, 362(6420):527–529, 1993.

[3] M Bender. Orbital tuning chronology for the Vostok climate record supported by trapped gas composition. *Earth and Planetary Science Letters*, 204:275–289, 2002.

[4] M. Bender, T. Sowers, M-L Dickson, J. Orchardo, P. Grootes, P. A. Mayewski, and D. A. Meese. Climate correlations between Greenland and Antarctica during the past 100000 years. *Nature*, 372:663–666, 1994.

[5] M Bender, T Sowers, and V Lipenkov. On the concentraion of O_2, N_2, and Ar in trapped gases from ice cores. *Journal of Geophysical Research*, 100(D9):18651–18660, 1995.

[6] M L Bender, T Sowers, J M Barnola, and J Chappellaz. Changes in O_2/N_2 ratio of the atmosphere during recent decades reflected in the composition of air in the firn at Vostok station. *Geophys. Res. Lett.*, 21:189–192, 1994.

[7] Michael Bender, Todd Sowers, and L Labeyrie. The dole effect and its variations during the last 130'000 years as measured in the Vostok ice core. *Glob. Biogeochem. Cycles*, 8(3):363–376, 1994.

[8] H. Craig, Y. Horibe, and T. Sowers. Gravitational separation of gases and isotopes in polar ice caps. *Science*, 242:1675–1678, 1988.

[9] M. Dole, G. A. Lane, D. P. Rudd, and D. A. Zaukelies. Isotopic composition of atmospheric oxygen and nitrogen. *Geochimica et Cosmochimica Acta*, 6:65–78, 1954.

[10] K Fuhrer, A Neftel, M Anklin, and V Maggi. Continuous measurements of hydrogen peroxide, formaldehyde, calcium and ammonium concentrations along the new GRIP ice core from Summit, central Greenland. *Atmospheric Environment*, 27A:1873–1880, 1993.

[11] C. Huber, M. Leuenberger, and O. Zumbrunnen. Continuous extraction of trapped air from bubble ice or water for on-line determination of istotope ratios. *Analytical Chemistry*, 75(10):2324–2332, 2003.

[12] T Ikeda, T Hondoh, T Fukumura, H. Fukazawa, and S Mae. Variation in N_2/O_2 ratio of occluded air in Dome Fuji antarctic ice. *J. Geophy. Res.*, 1006(D16):17,799–17,810, 2001.

[13] T Ikeda, H Kukazawa, S Mae, L Pepin, P Duval, B Champagnon, V Lipenkov, and T Hondoh. Extreme fractionation of gases caused by formation of clathrate hydrates in Vostok antarctic ice. *Geophys. Res Lett.*, 26(1):91–94, 1999.

[14] S. J. Johnsen, D. Dahl-Jensen, N. Gundestrup, J. P. Steffensen, H. B. Clausen, H. Miller, V. Masson-Delmotte, A. E. Sveinbjörnsdottir, and J. White. Oxygen isotope and palaeotemperature records from six Greenland ice-core stations: Camp Century, Dye3, GRIP, GISP2, renland and NorthGRIP. *Journal of Quaternary Science*, 16(4):299–307, 2001.

[15] Sigfus Johnsen, Dorthe Dahl-Jensen, Willi Dansgaard, and Niels Gundestrup. Greenland palaeotemperatures derived from GRIP bore hole temperature and ice core isotope profiles. *Tellus*, 47B:624–629, 1995.

[16] A. Landais, N. Caillon, C. Goujon, A. Grachev, J.M. Barnola, J. Chappellaz, J. Jouzel, V. Masson-Delmotte, and M. Leuenberger. Quantification of rapid temperature change during DO event 12 and phasing with methane inferred from air isotopic measurements. *Earth and Planetary Science Letters*, 225:221–232, 2004.

[17] C. Lang, M. Leuenberger, J. Schwander, and S. Johnsen. 16°C rapid temperature variation in central Greenland 70000 years ago. *Science*, 286:934–937, 1999.

[18] M. Leuenberger, P. Nyfeler, H.P. Moret, P. Sturm, and C. Huber. A new gas inlet system for an isotope ratio mass spectrometer improves reproducibility. *Rapid Communications in Mass Spectrometry*, 14:1543–1551, 2000.

[19] M. C. Leuenberger, C. Lang, and J. Schwander. Delta 15N measurements as a calibration tool for the paleothermometer and gas-ice age differences: a case study for the 8200 B.P. event on GRIP ice. *Journal of Geophysical Research*, 104(D18):22163–22170, 1999.

[20] A. Mariotti. Atmospheric nitrogen is a reliable standard for natural 15N abundance measurements. *Nature*, 303:685–687, 1983.

[21] D A Meese, A J Gow, R B Alley, P M Grootes, M Ram, K C Taylor, G A Zielinski, J F Bolzan, P A Mayewski, and E D Waddington. The GISP2 depth-age scale: Method and results. *J. Geophys. Res.*, 102(C12):26.411–26.423, 1997.

[22] D.A. Meese, A.J. Gow, P. Grootes, P.A. Mayewski, M. Ram, M. Stuiver, K.C. Taylor, E.D. Waddington, and G.A. Zielinski. The accumulation record from the GISP2 core as an indicator of climate change throughout the holocene. *Science*, 266:1680–1682, 1994.

[23] EPICA Community Members. Eight glacial cycles from an antarctic ice core. *Nature*, 429:623–628, 2004.

[24] NorthGRIP Members. High resolution climate record of the northern hemisphere reaching into the last glacial interglacial period. *Nature*, 431:149–151, 2004.

[25] S L Miller. Clathrate hydrates of air in antarctic ice. *Science*, 165:489–490, 1969.

[26] E. Monnin, E. J. Steig, U. Siegenthaler, K. Kawamura, J. Schwander, B. Stauffer, T. F. Stocker, J. M. Barnola, B. Bellier, D. Raynaud, and H. Fischer. Evidence for substantial accumulation rate variability in Antarctica during the holocene through synchronization of CO_2 in the Taylor Dome, DomeC and DML ice cores. *Earth and Planetary Science Letters*, 224:45–54, 2004.

[27] J. R. Petit, J. Jouzel, D. Raynaud, N. I. Barkov, J.-M. Barmola, I. Basile, M. Bender, J. Chappellaz, M. Davis, G. Delaygue, M. Demotte, V. M. Kotlyakov, M. Legrand, V. Y. Lipenkov, C. Lorius, L. Pépin, C. Ritz, E. Saltzman, and M. Stievenard. Climate and atmospheric history of the past 420000 years from the Vostok ice core, Antarctica. *Nature*, 399:429–436, 1999.

[28] J. Schwander. The transformation of snow to ice and the occlusion of gases. In H. Oeschger and C C Langway Jr., editors, *The Environmental Record in Glaciers and Ice Sheets*, pages 53–67. John Wiley, New York, 1989.

[29] J. Schwander, T. Sowers, J-M Barnola, T. Blunier, B. Malaizé, and T. Fuchs. Age scale of the air in the summit ice: Implication for glacial-interglacial temperature change. *J. Geophys. Res.*, 102(D16):19483–19494, 1997.

[30] J Schwander, B Stauffer, and A Sigg. Air mixing in firn and the age of the air at pore close-off. *Annals of Glaciology*, 10:141 – 145, 1988.

[31] J. P. Severinghaus and E. J. Brook. Abrupt climate change at the end of the last glacial period inferred from trapped air in polar ice. *Science*, 286:930–934, 1999.

[32] J. P. Severinghaus, A. Grachev, B. Luz, and N. Caillon. A method for precise measurement of argon 40/36 and krypton/argon ratios in trapped air in polar ice with applications to past firn thickness and abrupt climate change in Greenland and at siple dome, Antarctica. *Geochimica et Cosmochimica Acta*, 67(3):325–343, 2003.

[33] Jeffrey P Severinghaus, T Sowers, E J Brook, R B Alley, and M L Bender. Timing of abrupt climate change at the end of the Younger Dryas interval from thermally fractionated gases in polar ice. *Nature*, 391:141–146, 1998.

[34] U. Siegenthaler, E. Monnin, K. Kawamura, R. Spahni, J. Schwander, B. Stauffer, T. F. Stocker, J. M. Barnola, and H. Fischer. Supporting evidence from the EPICA Dronning Maud Land ice core for atmospheric CO_2 changes during the past millennium. *Tellus*, page in press, 2004.

[35] A. Sigg, K. Fuhrer, M. Anklin, T. Staffelbach, and D. Zurmuhle. A continuous analysis technique for trace species in ice cores. *Environmental Science and Technology*, 28:204–210, 1994.

[36] T. Sowers, M. Bender, L. Labeyrie, D. Martinson, D. Raynaud, J.J. Pichon, and Y.S. Korotkevich. A 135.000-year Vostok-specmap common temporal framework. *Paleoceanography*, 8(6):737–766, 1993.

[37] T Sowers, M Bender, D Raynaud, and Y S Korotkevich. $\delta^{15}N$ of N_2 in air trapped in polar ice: A tracer of gas transport in the firn and a possible constraint on ice age-gas age differences. *J. Geophys. Res.*, 97:15683–15697, 1992.

[38] T A Sowers, M L Bender, and D Raynaud. Elemental and isotopic composition of occluded O_2 and N_2 in polar ice. *J. Geophys. Res.*, 94:5137–5150, 1989.

[39] Todd Sowers and Michael Bender. Climate records covering the last deglaciation. *Science*, 269:210–214, 1995.

[40] Todd Sowers, Michael Bender, Dominique Raynaud, Y.S. Korotkevich, and Joe Orchardo. The δ^{18}O of atmospheric O_2 from air inclusions in the Vostok ice core: timing of CO_2 and ice volume changes during the penultimate deglaciation. *Paleoceanography*, 6(6):679–696, 1991.

Chapter 4

Gas Fractionation in the Firn Column

4.1 Evidence for Gas Fractionation in Firn Air Derived from Noble Gases, Oxygen, and Nitrogen Measurements

Christof Huber,[1] Urs Beyerle,[1,2] Markus Leuenberger,[1] Jakob Schwander,[1] Rolf Kipfer,[3,4] Renato Spahni,[1] Jeff P. Severinghaus[5] and Karin Weiler[1]

Abstract

We present elemental and isotopic measurements of noble gases (He, Ne, Ar, Kr, and Xe), oxygen and nitrogen of firn air from two sites. The first set of samples was taken in 1998 at the summit of the Devon Ice Cap in the eastern part of Devon Island (75°N, 82°W, altitude: 1800 m a.s.l.). The second set was taken in 2001 at NorthGRIP location (North Greenland) (75°N, 42°W, 2960 m a.s.l.). He and Ne are heavily enriched relative to Ar with respect to the atmosphere in the air near the close-off depth at around 50-70 m. The enrichment increases with depth and reaches the maximum value in the deepest samples just above the zone of impermeable ice where no free air could be extracted anymore. Similarly, elemental ratios of O_2/N_2, O_2/Ar and Ar/N_2 are increasing with depth. In contrast but in line with expectations, isotopic ratios of $^{15}N/^{14}N$, $^{18}O/^{16}O$, and $^{36}Ar/^{40}Ar$ show no significant enrichment close to the close-off depth. The observed isotopic ratios in the firn

---

[1] Climate and Environmental Physics, Physics Institute, University of Bern, Sidlerstrasse 5, CH-3012 Bern, Switzerland

[2] Present address: Paul Scherrer Institute PSI, CH-5232 Villingen, Switzerland

[3] Dep. Water Resources and Drinking Water, EAWAG, CH-8600, Dübendorf, Switzerland

[4] Isotope Geology, ETH Zürich, CH-8092 Zürich, Switzerland

[5] Scripps Institution of Oceanography, University of California, San Diego, La Jolla, California 92093-0244, USA

air column can be explained within the uncertainty ranges by the well-known processes of gravitational enrichment and thermal diffusion. To explain the elemental ratios, however, an additional fractionation process during bubble inclusion has to be considered. To verify and quantify this additional processes a firn air model is formulated and fitted to the data. We found a very similar close-off fractionation behavior of the different molecules at both sites. For smaller gas species (mainly He and Ne) the fractionation is linearly correlated to the molecule size, whereas for diameters greater than about 3.6 Å the fractionation seems to be orders of magnitudes smaller or even negligible. An explanation for this size dependent fractionation process could be gas diffusion through the ice lattice. At Devon Island the enrichment at the bottom of the firn air column is about four times higher compared to NorthGRIP. We explain this by lower firn diffusivity at Devon Island, most probably due to melt layers, resulting in significantly reduced back diffusion of the excess gas near the close-off depth. The results of this study considerably increase the understanding of the processes occurring during air bubble inclusion near the close-off depth in firn and can help to improve the interpretation of direct firn air measurements, as well as air bubble measurements in ice cores, which are used in numerous studies as paleo proxies.

4.1.1   Introduction

The top of ice sheets consists of a porous and therefore permeable firn layer. This firn layer, where atmospheric air is moving primarily by molecular diffusion, is normally 50-100 m deep [31]. At the bottom of the firn column the firn is continuously transformed into ice trapping the atmospheric air in bubbles. Measurements of the entrapped air from ice cores has been used successfully in numerous studies as a climate archive, e.g. to reconstruct greenhouse gas concentration histories [7, 8, 10, 14, 19, 26], to asses the amplitude of rapid temperature changes by measuring isotopic fractionation of N_2 and Ar isotope ratios caused by the process of thermal diffusion in the firn column [22, 23, 25, 34, 38], or to date ice cores using measurements of O_2 isotope ratios as well as elemental ratios of N_2/O_2 [2, 27]. Other studies have reconstructed atmospheric concentration histories of various gases from air sampled directly from the firn [1, 9, 12, 13, 15, 30]. Other recent studies have been concentrated on the processes that can alter the composition of atmospheric air moving from the surface to the close-off depth where the air is finally trapped in bubbles. This study focuses on the mechanisms occurring during bubble inclusion within the firn-ice transition zone. Up to now three processes are known which modify the composition of atmospheric air in the firn column. These processes are (i) the concentration diffusion [29, 41], (ii) the gravitational enrichment [11, 31], and (iii) the thermal diffusion [33, 36]. Firn air samples were taken from two different sites. A broad variety of concentrations and isotopic ratios of inert atmospheric gases were analyzed and compared with model prediction. Isotopic ratios agreed very well with theory. However, some elemental ratios significantly differ from the model prediction and could only be explained by assuming an additional size dependent fractionation during bubble inclusion, as discussed by Bender et al. [5], Battle et al. [1], Severinghaus and Brook [35], Severinghaus and Battle [32], Bender [2], Leuenberger et al. [24], and Severinghaus et al. [37].

4.1.2 Sampling and Analysis

Firn air samples were taken by the "bladder method" basically described by Schwander et al. [30]. A borehole was drilled into the ice sheet to the desired sampling depth, and then a bladder was lowered to the bottom of the borehole and inflated to block a small volume below the bladder from above. The bladder was 3 m long, made of natural rubber, with aluminum flanges and a "Bender-baffle" system at the lower end. Pumps located at the surface extracted the firn air from the small volume beneath the bladder and compressed it into flasks for later gas analysis. Three DEKABON 1/4-inch tubes made the connection between the bladder and the surface. One tube was used to inflate the bladder, one for purging and the last for sampling. The quality of the sampling was continuously monitored with an infrared CO_2 analyzer. Filling of flasks was started after reaching a stable CO_2 level. After taking the sample, the bladder was removed from the borehole and drilling to the next sampling depth was performed. The first drilling site is located at the summit of the Devon Ice Cap (approximately 75°N, 82°W, altitude: 1800 m asl.), in the east part of Devon Island (North-West Territories of Canada). This small ice cap has survived the glacial retreat since the Last Glacial Maximum. Accumulation rate is of the order of 30 cm of water equivalent per year. Despite a fairly low mean annual temperature of -23°C, summer melting is quite frequent at this site, generating ice layers of 0.5 to 6 cm thickness, with largely varying horizontal extent (a few cm to a few m). The Devon Island firn air sampling was carried out in April 1998 during the FIRETRACC project. Successful sampling was achieved to a depth of 59 m. "Impermeable" ice was found at about 62 m. Sampling below 59 m was not possible both because of very low flow rate and because of unstable CO_2 levels. The second set of samples was taken between May and June 2001 in the center of Greenland at the NorthGRIP (North GReenland Icecore Project) location (75.10°N, 42.38°W, altitude: 2960 m asl.). The average air temperature at NorthGRIP is -31.6°C and the average ice accumulation rate is 19 cm H_2O per year. The deepest sample for our gas analysis was taken at 71.75 m. "Impermeable" ice conditions were found below about 78 m (Table 4.1). Vertical profiles of CO_2 concentration and density of Devon Island and NorthGRIP firn are shown in Figure 4.1. Density has been determined by cutting the firn core into 0.55 m pieces

Table 4.1: Characteristics of the two sampling sites (Devon Island, NorthGRIP) used in the firn air model.

	Unit	Devon Island	NorthGRIP
Location		75°N, 82°W	75.1°N, 42.3°W
Altitude	(m)	1800	2960
Mean air temperature	(°C)	-23	-31.7
Mean atmospheric pressure	(hPa)	792	665
Accumulation rate	(cm H_2O/yr)	27.6	17.5
Firn density at surface	(g/cm^3)	0.4	0.32
Firn density at close-off	(g/cm^3)	0.838	0.811
Close-off depth	(m)	59	70

(bags) and measuring weight and dimensions of these bag samples. Flasks filled with firn air were analyzed mass spectrometrically at Climate and Environmental Physics, Physics Institute of the University of Bern (Switzerland) and at Isotope Geology of the ETH Zürich (Switzerland) in collaboration with the Swiss Federal Institute of Environmental Science and
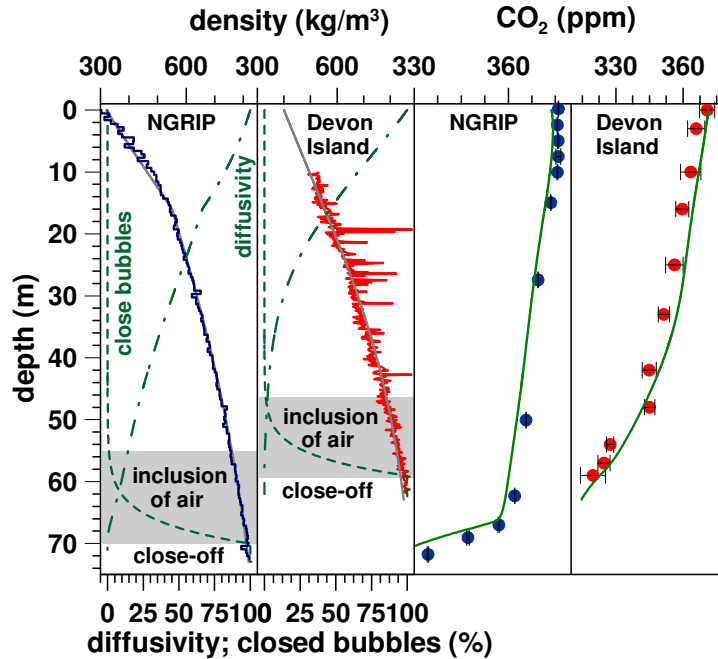
Figure 4.1: (First and second panel from the left) Firn density profile of NorthGRIP (left) and Devon Island (right), measured (colored lines) and modeled (gray lines), respectively. Additionally, the modeled relative diffusivity (chain dotted line) and the portion of closed bubbles (dashed line) are plotted versus depth. The lock-in zone where the bubble formation takes place is marked as shaded area. (Third and fourth panel from the left) CO_2 measurements (colored dots) and model fit (green line) of NorthGRIP (left) and Devon Island (right).

Technology (EAWAG). Ratios of nitrogen ($^{15}N/^{14}N$), oxygen ($^{18}O/^{16}O$) and argon isotopes ($^{36}Ar/^{40}Ar$) and elemental ratios of O_2/N_2, Ar/O_2 and Ar/N_2 were measured by isotope ratio mass spectrometry IRMS in Bern. We used a ThermoFinnigan Delta Plus XL IRMS for the NorthGRIP samples. Devon Island samples were measured on a MAT-250. Samples and standards were measured with using a dual inlet system. Absolute concentration of noble gas isotopes (^4He, ^3He, ^{20}Ne, ^{40}Ar, ^{86}Kr, ^{136}Xe) and corresponding elemental ratios were measured on a statically operated mass spectrometer at the ETH Zürich. The analytical technique is comparable to the procedure developed for the measurement of noble gases in water samples [6]. Due to the used mass spectrometric methods and the different abundances of the measured gas species, the analytical errors are two orders of magnitudes smaller for $\delta^{15}N$, $\delta^{18}O$, O_2/N_2 Ar/O_2 and Ar/N_2 ratios (typically between 0.01 to 0.05$^0\!/_{00}$) compared to the static measured noble gas isotopes (typically between 4 to 15$^0\!/_{00}$). One measurement, of ^{86}Kr from 42 m depth at Devon Island was rejected because of an unusual jump in the stability of the spectrometer (in this measurement ^{86}Kr was more then 9% higher than all other ^{86}Kr measurements). Unusual high He concentration were measured in the two uppermost Devon Island samples, 21% He excess compared to atmospheric concentration at 3 m and 7% excess He at 16 m, whereas at 33 m the He non-atmospheric excess has be completely vanished (0.1±1%). These two exceptional measurements can be explained by the fact that the DEKABON tubing used for sampling was leak-checked using pure He before leaving for the field. Although the tubes were flushed by several tens of liters

before sampling some non-atmospheric He had obviously remained in the DEKABON tubes contaminating the first samples taken. Therefore the helium measurements from Devon Island at 3 and 16 m are not considered in the following discussion.

4.1.3 Firn Air Model

The transport of gas in porous firn can be described with a one-dimensional diffusion equation [29, 36, 41]:

$$\frac{\partial C}{\partial t} = \frac{\partial}{\partial t}\left(D(z,T)\left[\frac{\partial C}{\partial z} - \frac{\Delta mg}{RT} + \Omega\frac{\partial T}{\partial z}\right]\right) \qquad (4.1)$$

where C is the concentration of the species, t is time, z is depth, D is the effective molecular diffusivity of gas in porous snow [31, 30, 40], T is temperature, Δm is mass difference of the gas to the mass of air, g is gravitational acceleration, R is the ideal gas constant, and Ω is the thermal diffusion sensitivity. In equation 4.1 the movement of gas is determined by molecular diffusion (driven by the concentration gradient $\partial C/\partial z$), by gravitational settling ($\Delta mg/RT$), and by thermal diffusion ($\Omega\partial T/\partial z$). As first order approximation, we did not take into account seasonal atmospheric temperature variations. In this simplified model the temperature in the firn column, which is equal to the mean annual atmospheric temperature, does not change with depth or time ($\partial T/\partial z = 0$). Therefore thermal diffusion is not considered and eq. 4.1 reduces to

$$\frac{\partial C}{\partial t} = \frac{\partial}{\partial t}\left(D(z,T)\left[\frac{\partial C}{\partial z} - \frac{\Delta mg}{RT}\right]\right) \qquad (4.2)$$

Eq. 4.2 will fail to reproduce the gas concentrations at the upper part of the firn because seasonal atmospheric temperature variations are penetrating down to about 5-10 m depth affecting the gas concentration at the top of the firn due to thermal diffusion. However, thermal diffusion is only relevant down to a depth of about 20-30 m [36]. Since we are mainly interested in the gas concentration near the close-off depth the simplified eq. 4.2 is justified. More detail about modeling firn gas movement considering thermal diffusion can be found in [36]. To calculate the gas diffusion and inclusion process in the firn we used an extended version [40] of the one dimensional diffusion model of Schwander et al. [30]. In this model the firn column is divided into a fixed number of boxes (usually 2000), where each of the boxes contains the same mass of air such we can handle the gas flow by concentration exchange (eq. 4.2). The length of the boxes thus increases with depth. The size of the boxes was determined with an approximation of the firn porosity using a density formula by Herron and Langway [17] and the relation of Schwander et al. [29]. The gas concentration is mixed vertically between the boxes by pure molecular diffusion and the effect of gravity (eq. 4.2), as well as vertical advection due to accumulation of new surface snow. In the lock-in zone bubbles start to form and are separated from the open firn column. The closed porosity is related to density by the empirical relation from Schwander et al. [31, 29]. As discussed in more detail below, an additionally process during bubble inclusion had to be implemented for this study, in order to explain the measured data. Air tends to escape from the closing bubble due to a compression overpressure. We assumed a constant fractionation of the gas during bubble inclusion. The concentration C_{closed}^i in the

newly formed bubble depends on the concentration C^i in the surrounding firn as follows:

$$C^i_{closed} = \alpha^i C^i \tag{4.3}$$

where α^i is the fractionation factor for each gas species i. We assumed that the proportion between the volume of closed bubbles V_{closed} and the volume of open pores V_{open} in a given depth, is a function of the firn density ρ, the open and closed porosity [40].

$$V_{open} + V_{closed} = V \tag{4.4}$$

Hence, to observe mass balance

$$V_{open}C^i_{open} + V_{closed}C^i_{closed} = VC^i \tag{4.5}$$

the concentration of the remaining gas in the open pore volume C^i open has to be:

$$C^i_{open} = C^i\Big(V_{closed}(1 - \alpha^i) + V_{open}\Big)V^{-1}_{open} \tag{4.6}$$

To constrain the model, we used the CO_2 firn air measurements (Figure 4.1). The model was forced with atmospheric CO_2 concentration since 1750 from ice core data and measurements from Point Barrow. Modeling the CO_2 profile is a good tool to adjust the parameters of the relation between diffusivity and open porosity used in the model [30, 40] The diffusivity profile found for CO_2 was then scaled linearly to the other gases (Table 4.2). Thereafter the concentrations of the other gases and isotopes were modeled in order to best fit the measured data by varying only the fractionation factor α^i. Atmospheric noble gas, oxygen and nitrogen concentrations, were assumed to be constant with time. This is a simplification mostly for of O_2/N_2 ratios, which alters seasonally due to photosynthesis and respiration processes, which is not important here as seasonal variations are not considered. Furthermore, the few atmospheric O_2/N_2 reconstructions suggests that the long term increase of atmospheric O_2/N_2 due to fossil fuel burning, is only about $0.01\%_0$/yr [4, 20]. As the fractionation effect discussed in this study shows variations of 2 to $10\%_0$, this latter effect can be neglected.

Table 4.2: Molecular properties used in the model and close-off fractionations factors. (A) Collision diameter are the and Lenard Jones potential values derived from viscosity data [28]. (B) Diffusion coefficient of trace gas in air relative to CO_2

Molecule	Mole Mass	Collision [A] Diameter (Å)	D/D$_{CO_2}$ [B]	Close-off fractionation factor α^i				
				NorthGRIP		Devon Island		Mean
				Mean	Error	Mean	Error	
CO_2	44	3.941	1	1		1		1
Xe	131	4.047	0.775	1		1		1
N_2	28	3.798	1.21	1		1		1
Kr	84	3.655	0.944	1		1		1
Ar	40	3.542	1.22	0.9975	0.0005	0.9945	0.0015	0.996
O_2	32	3.467	1.29	0.986	0.002	0.9855	0.0015	0.986
Ne	20	2.82	2.03	0.55	0.05	0.64	0.04	0.595
He	4	2.551	4.53	0.35	0.05	0.425	0.075	0.388

4.1.4 Results

Isotopic Ratios

Both NorthGRIP and Devon Island firn air samples show the expected linear increase in $\delta^{15}N$, and $\delta^{18}O$ with depth due to gravitational settling. Since the gravitational enrichment is proportional to the mass difference, Δm of the isotopes, $\delta^{36}Ar$ is affected 4 times as much as $\delta^{15}N$ (eq. 4.1). Deviations from the gravitational enrichment line were observed at both sampling sites at the top of the firn air column (Figure 4.2 and Figure 4.3) due to thermal diffusion driven by the seasonal temperature gradients. In the present study, however, we are mainly interested at the bottom of the firn air column. We did not detect any close-off fractionation for the isotopic ratios. This is confirmed by many different firn air studies at various sites in Greenland as well as in Antarctica [30, 41].
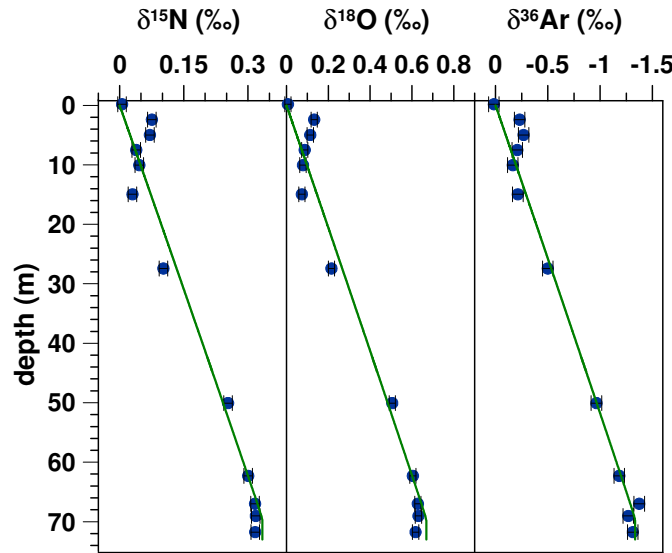
Figure 4.2: $\delta^{15}N$, $\delta^{18}O$, and $\delta^{36}Ar$ data from NorthGRIP. Measurements (dots) and model (solid line). The data shows a nice thermal effect in the upper 30 m. The model does only account for gravitational settling but not for thermal diffusion. Therefore the data and model disagree on the first 30 m.

Elemental Ratios

Measurements and model results of the elemental ratios from NorthGRIP and Devon Island are shown in Figure 4.4 to Figure 4.7. Model and measurements differ in the top 30 m because thermal diffusion is not included in the model. Below 30 m the linear gravitational signal as well as the close-off fractionation can be seen in the data and are reproduced by the model. O_2/N_2, Ar/N_2, He/Ar, Ne/Ar, Ne/He ratios show fractionations of different strengths during the inclusion process, whereas Kr/Ar and Xe/Ar seem not to be affected. Analytical errors of Kr/Ar and Xe/Ar, however, are too large to obtain a nice fit. The close-off enrichments are about 4 times more pronounced at Devon Island than at NorthGRIP. The ratio of Ne/He shows a interesting behavior, since at the close-off it is slightly enriched
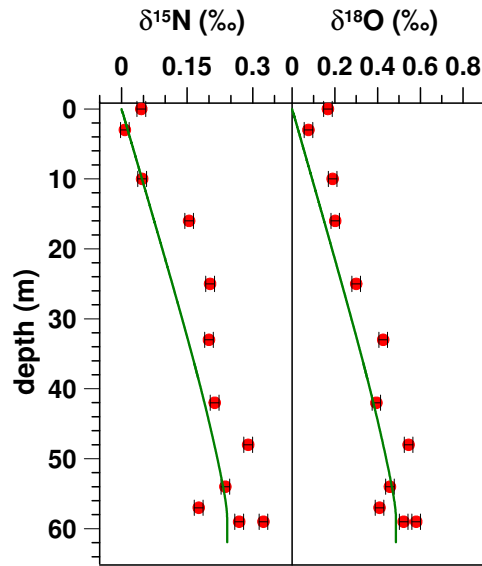
Figure 4.3: $\delta^{15}N$ and $\delta^{18}O$ data from Devon Island. Measurements (dots) and model (solid line). The model does only account for gravitational settling but not for thermal diffusion. Therefore the data and model disagree on the first 30 m. The quality of the data is not that good as for NorthGRIP (Figure 4.2).

at NorthGRIP but strongly depleted at Devon Island.
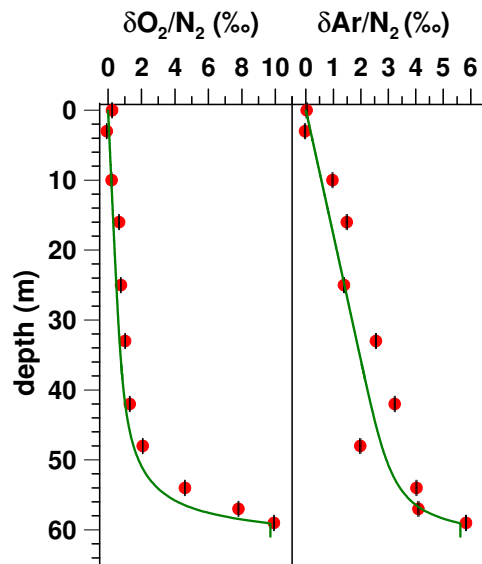
Figure 4.4: $\delta O_2/N_2$ and $\delta Ar/N_2$ measurements from Devon Island. The curves are the diffusion model with adjusted close-off fractionation.

Although the data from NorthGRIP and Devon Island are rather different, we found very similar close-off fractionation factors for both sites from the fitting of our model output to the data (Figure 4.8). This might indicate a universal physical process of bubble inclusion.
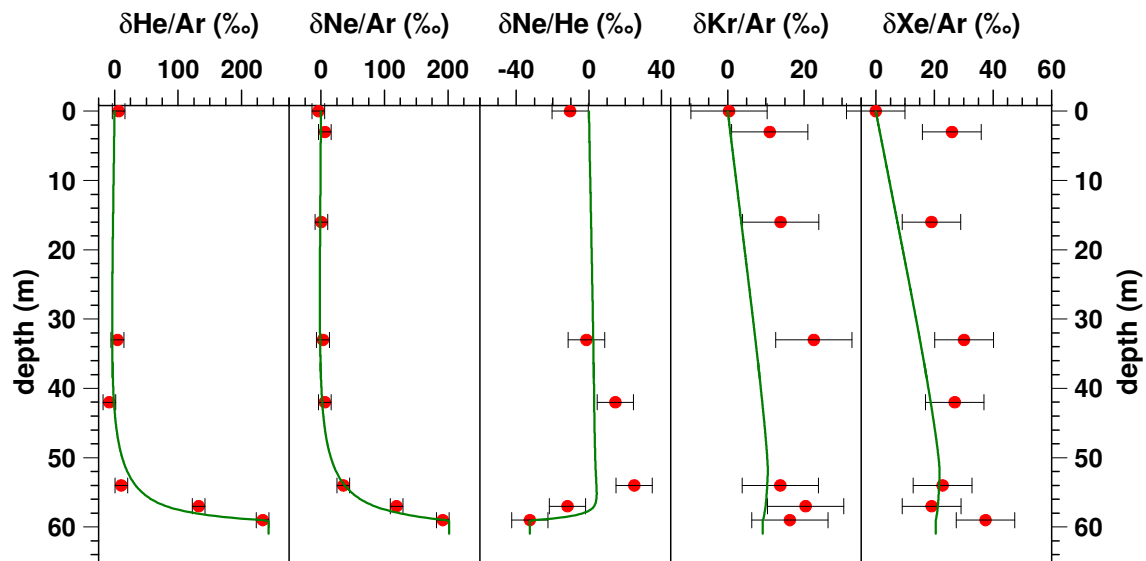
Figure 4.5: Noble gas ratio measurements from Devon Island. The curves are the diffusion model with adjusted close-off fractionation.
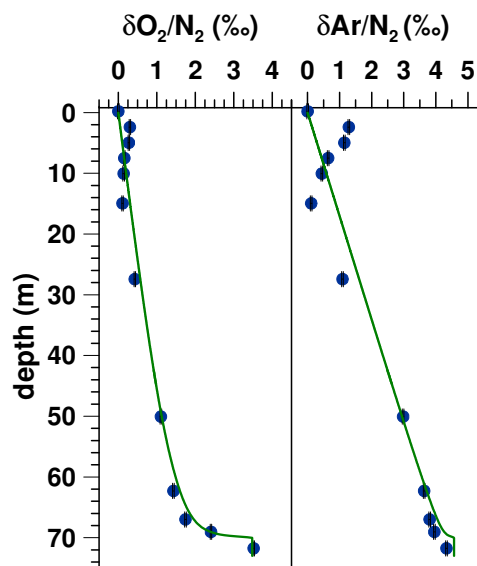
Figure 4.6: $\delta O_2/N_2$ and $\delta Ar/N_2$ measurements from NorthGRIP. The curves are the diffusion model with adjusted close-off fractionation.

However, we do not expect these fractionation factors to be fundamental physical constants, but rather they should be affected by the speed of the bubble close-off process and are a complicated integral of the gas fractionation with the bubble pressure and close-off history. The model is able to reproduce the 4 times stronger enrichments of the He/Ar and Ne/Ar at Devon Island compared to NorthGRIP, as well as the different Ne/He evolutions at
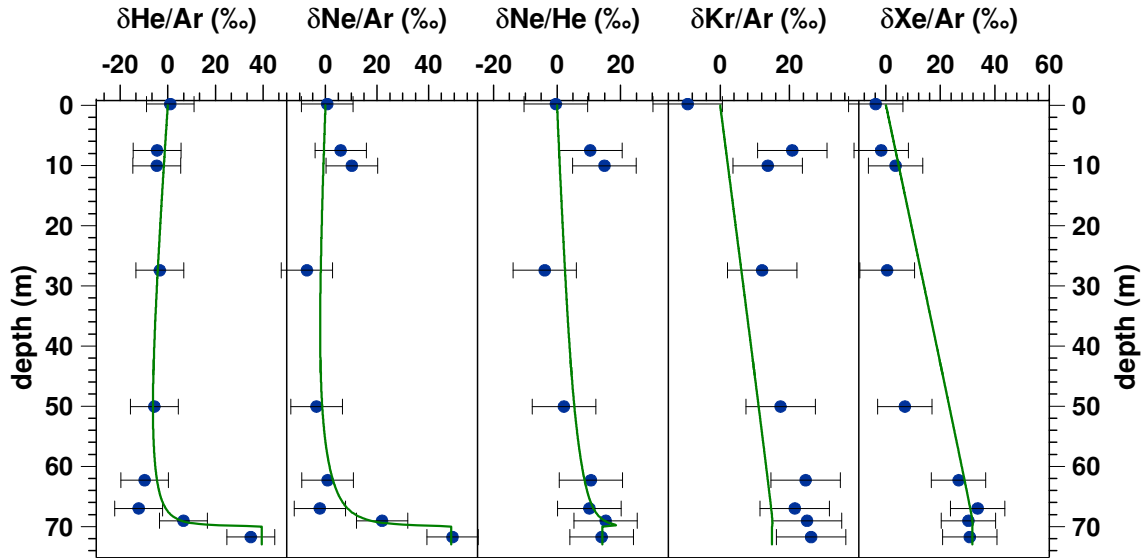
Figure 4.7: Noble gas ratio measurements from NorthGRIP. The curves are the diffusion model with adjusted close-off fractionation.

both sites. The reason for this differences can be found in the lower firn diffusivity at Devon Island due to intense layering, obtained by frequent meltwater events. This is nicely documented in the density profile (Figure 4.1), which is much smoother for NorthGRIP than for Devon Island. Impermeable dense summer layers damp the diffusion in the firn column and hence reduce the exchange of the gases with the free atmosphere. This causes a stronger enrichment of the expelled gases from the closing bubbles in the firn, since the excess gas can not escape easily to the atmosphere by back diffusion. Intense layering can cause a decoupling of air from the upper part of the firn column and thus lead to even stronger enrichments. Reduced diffusion also explains the strange behavior of the Ne/He ratios. He is more affected by the close-off fractionation than Ne, which leads to a depletion of the Ne/He ratio at Devon Island. In contrast, at NorthGRIP the Ne/He ratio is enriched at the bottom of the firn. This is because molecular diffusion of He in air is more than two times faster than of Ne in air (Table 4.2), hence the He concentration gradient is balanced by back diffusion to the surface at NorthGRIP, whereas at Devon Island reduced diffusivity due to meltlayers keeps the He at the bottom of the firn.

Close-off fractionation is strongest for the small and light elements He and Ne, and it is non existent for the large and heavy gases Xe and Kr, at least within our measurement precision. Plotting the close-off fractionation for the different species against their molecular diameter (Figure 4.8, Table 4.2) indicates a critical size of about 3.6 Å above which close-off fractionation seems to stop. The dependency of the close-off fractionation on molecular mass is not a steady function since O_2 (mass 32 g/mol) and Ar (40 g/mol) show stronger fractionation than the lighter N_2 (28 g/mol). The close-off fractionations factors obtained from the both sites agree within the uncertainty range.

In order to test the uniformity of our findings, we compared our model output for O_2/N_2 and Ar/O_2 to firn air samples from three Antarctic sites Dome C, Dronning Maud Land (DML),
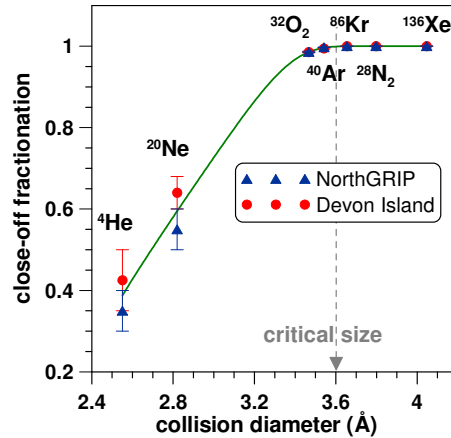
Figure 4.8: Close-off fractionation from the model fits of NorthGRIP (triangles) and Devon Island (dots), plotted against their molecular diameter [28]. Close-off fractionation is strongest for small molecules, and is decreasing with increasing size. We did not detect a close-off fractionation for molecules larger than the critical size of about 3.6±0.1 Å.

and Berkner Island (Figure 4.9) (firn sampling within the framework of CRYOSTAT). The model parameters were calibrated again fitting the CO_2 profile. Then the model was run using the mean close-off fractionations from Devon Island and NorthGRIP (Table 4.2). The agreement between model and data is good for the very low accumulation (only 2.5 cm H_2O/yr) site of Dome C. However, Berkner Island and to a lesser extent DML data, show extremely strong close-off fractionations which could not be reproduced by the model. This is probably due to extensive non-diffusive zones as a result of impermeable layers in the firn column. The non diffusive zone seems to start at about 50 m at Berkner Island and about 71 m at DML. This is supported by isotope ratio measurements of the four deepest samples from Berkner Island and the deepest sample at DML, respectively. The gravitational enrichment of $\delta^{15}N$ and $\delta^{18}O$ stops at this depths, whereas the samples were taken down to a depth of 63 m (Berkner Island), and 74 m (DML), respectively. Our model fails to reproduce this data, due to the smoothed diffusion profile prescribed by a smooth density profile. To improve the model, the density profile must be changed from a smooth function with depth, towards a more realistic, highly (annually) variable dependence. Such a model modification, could help to improve the accuracy of reconstructions of atmospheric O_2/N_2 from firn air.

4.1.5 Discussion

The phenomenon of close-off fractionation has been discussed by several authors [1, 2, 5, 32, 37]. Earlier workers also noticed a size-dependent fractionation during artifactual gas loss that may occur during ice sample retrieval or storage [3, 11, 39]. It is important to note that this artifactual (human-caused) process is distinct from the natural process described in this work, and will not be discussed further.

During the close-off process of an air bubble the pressure in the closing bubble increases and
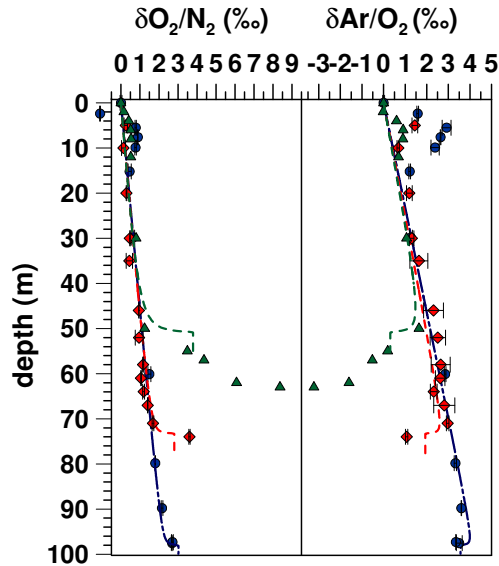
Figure 4.9: $\delta O_2/N_2$ and $\delta Ar/O_2$ measurements and model predictions from the Antarctic sites Dome C (dots), DML (diamonds), and Berkner Island (triangles). For the model predictions the mean close-off fractionation from Table 4.2 were used. The Berkner Island data shows extremely strong close-off fractionation. This is probably due a very long non-diffusive zone due to impermeable layers. This is supported by constant values of the isotope ratios for the deepest four measurements. Our model fails to reproduce this data, since layering is not yet implemented.

part of the air is forced out of the bubble into the surrounding pore space. It is not clear what could cause the observed size dependence of this expelling procedure. Some kind of diffusion, such as diffusion through tiny channels in the firn structure or even through the ice matrix is probably involved. Different diffusion processes have been discussed in prior literature (Poiseuille diffusion, molecular diffusion, effusion, Knudsen diffusion, steric diffusion) [3, 11], but none of them can explain the detected size dependent behavior properly.

Molecular diffusion occurs in the presence of partial pressure gradients. It is important when the diameter of the channel is much bigger than the size of the molecules, thus the molecules collide much more frequently with each other than with the walls of the medium. Fractionation due to molecular diffusion depends mainly on the inverse square root of the reduced mass, m, divided by the squared diameter, d: $D_{molecular} \sim m^{-1/2}d^{-2}$. It cannot explain the observed fractionation (Figure 4.8, Table 4.2) since otherwise isotope ratios should show a significant (detectable) fractionation. Furthermore a critical diameter cannot be explained by molecular diffusion. Molecular diffusion, however, is the driver of the back diffusion of excess gases expelled in the firn column and hence it is very important for the interpretation of the measured profiles.

Effusion is happening when the gas collides mainly with the walls in contrast to molecular diffusion, e.g. a collapsing balloon expelling the gas. Effusion depends only on the

square root of the mass ratio off different gases but not on the molecular size: $D_{effusion} \sim (m_1/m_2)^{1/2}$.

Knudsen diffusion occurs when the molecules collide predominantly with the walls rather than with each other. Knudsen diffusion is inversely proportional to the square root of its mass: $D_{knudsen} \sim m^{-1/2}$. Neither effusion nor Knudsen diffusion can explain the size dependency, as well as the unaffected isotope ratios, observed during the lock-in process.

Steric (activated) diffusion is important when the size of the molecules is of the same order as the size of the channel. Then the diffusivity depends on both the diameter and the mass of the molecule: $D_{steric} \sim m^{-1/2}e^{(-E/kT)}$ where $E = E_0 + ad$ is the activation energy required to jump from one crystal-site to the next (see for example [21]). Diffusion through the ice can be regarded as steric diffusion [18, 42]. Hence steric or activated diffusion could be a driver of the observed close-off fractionation, however there is still a mass dependence involved.

The clear detection of a critical size of 3.6 Å implies diffusion through channels of about the same dimension. However, an outlet from a closing bubble is not expected to develop a critical size, since it changes its dimension steadily from open to closed. Furthermore, a uniform behavior of the firn structure close-off region (the same channel dimensions at different sites) seems unrealistic, since physical conditions (temperature, accumulation) can be very different from site to site. Thus, we favor an explanation by diffusion through the ice matrix. Diffusion coefficients of gases in ice show a size dependence similar to our findings beside for Ar and O_2 [18]. However, diffusion through the ice matrix is very slow (far less than 1 mm/yr) [18, 42]. Therefore, a wall of few millimeters can inhibit gas penetration substantially. But, one can imagine that a newly formed bubble is sealed from the open pores by only a thin film of ice crystals. The overpressure in the bubble forces the gases to migrate through the ice structure. Diffusion through ice must behave in a uniform way, because the crystalline structure depends not much on temperature and pressure. At the pressure and temperature conditions of polar firn, normal ice (1h) with a hexagonal crystalline structure is formed (Figure 4.10). The crystal may be thought of as consecutive sheets lying on top of each other. For a very thin wall of ice such a crystal structure is forming hexagonal channels, which could serve as connections for the air from the bubble to the open pore volume. The distance between two neighboring oxygen atoms is about 2.75 Å [16]. The dimensions of the hexagonal passages in the ice matrix each formed by six H_2O molecules is similar to the critical size of about 3.6 Å (4.5-4.6 Å minus the dimension of the H_2O molecules of about 1-2 Å) (Figure 4.10). Therefore, a size dependent fractionation seems probable. Molecules larger than the channels are not able to pass the ice film, whereas small molecules like He pass easily. From bubble air measurements on ice cores it is known that He, as well as Ne are not captured properly in ice cores, whereas N_2, Ar, and O_2 concentrations seem to remain unchanged, at least in the inner part of the core. But, regarding a small film of ice only, O_2 and Ar have a slightly higher probability to pass than N_2, which could cause the enrichments in the firn in the close-off region. Diffusion coefficients of gases in ice show a of size dependence. Further investigations concerning this theory have to be carried out, in addition better experimental determinations of the diffusion constants of the main air components through ice would be very valuable.
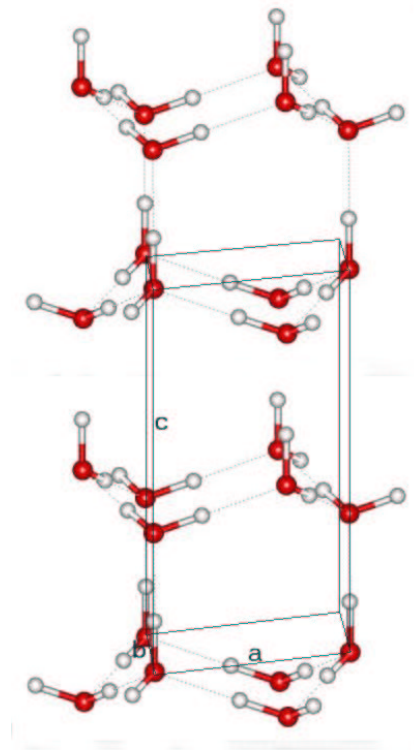
Figure 4.10: Hexagonal ice (1 h) unit cell. The unit cell may be considered as a group of four molecules (two above and two below); two and two halves of which make up the hexameric box. The crystallographic c-axis is in the vertical direction. The hexagonal crystal has unit cell dimensions 4.511 Å (a, b) and 7.351 Å (c) (90°, 90°, 120°, 4 molecules). The distance between two neighboring oxygen atoms (red globes) is about 2.75 Å [16].

4.1.6 Conclusions

The enrichment of elemental ratios near the close-off region measured in the firn air from Devon Island and NorthGRIP, can be modeled assuming a constant close-off fractionation of the air remaining in the closed bubble. The strong similarities found at both sites indicates an universal physical process causing this close-off fractionation. Our model approach is able to explain and predict the general shape of the firn air profiles from various different sites. However, it fails when the firn density structure has impermeable layers which cause large non-diffusive zones at the bottom of the firn. This has to be implemented into a future model. Close-off fractionations for different gases depend strongly on the collision diameter. The mass of the molecule is less important, since the effect on isotope ratios is very low. The critical size of about 3.6 Å seems to be the upper limit to which molecules fractionate during the close-off process in the firn. A possible explanation for this could be the diffusion of molecules through channels in the ice lattice. From our findings we believe that the effect of close-off fractionation is nonexistent or at least very small for isotope ratios and for large molecules, like Xe, Kr, N_2, CO_2, CH_4, and N_2O. This is an important confirmation for the integrity of polar ice cores as a climate archive of the ancient atmospheric composition of these gases.

Bibliography

[1] M Battle, M Bender, T Sowers, P P Tans, J H Butler, J W Elkins, J T Ellis, T Cornway, N Zhang, P Lang, and A D Clarke. Atmospheric gas concentrations over the past century measured in air from firn at the South Pole. *Nature*, 383:231–235, 1996.

[2] M Bender. Orbital tuning chronology for the Vostok climate record supported by trapped gas composition. *Earth and Planetary Science Letters*, 204:275–289, 2002.

[3] M Bender, T Sowers, and V Lipenkov. On the concentraion of O_2, N_2, and Ar in trapped gases from ice cores. *Journal of Geophysical Research*, 100(D9):18651–18660, 1995.

[4] M. L. Bender, J T Ellis, P. P. Tans, R. J. Francey, and Lowe D. Variability in the O_2/N_2 ratio of southern hemisphere air, 1991-1994: Implications for the carbon cycle. *Glob. Biogeochem. Cycles*, 10(1):9–21, 1996.

[5] M L Bender, T Sowers, J M Barnola, and J Chappellaz. Changes in O_2/N_2 ratio of the atmosphere during recent decades reflected in the composition of air in the firn at Vostok station. *Geophys. Res. Lett.*, 21:189–192, 1994.

[6] U. Beyerle, W. Aeschbach-Hertig, D. M. Imboden, H. Baur, T. Graf, and R. Kipfer. A mass spectrometric system for the analysis of noble gases and tritium from water samples. *Environmental Science & Technology*, 34:2042–2050, 2000.

[7] T Blunier, J Chappellaz, J. Schwander, J. M. Barnola, T Desperts, B. Stauffer, and D. Raynaud. Atmospheric methane record from a Greenland ice core over the last 1000 years. *J. Geophys. Res.*, 20(20):2219–2222, 1993.

[8] E J Brook, T Sowers, and J Orchardo. Rapid variations in atmospheric methane concentration during the past 110,000 years. *Science*, 273:1087–1091, 1996.

[9] J. H. Butler, M. Battle, M. L. Bender, S. A. Montzka, A. D. Clarke, E. S. Saltzman, J. P. Sucher, J. P. Severinghaus, and J. W. Elkins. A record of atmospheric halocarbons during the twentieth century from polar firn air. *Nature*, 399:749–755, 1999.

[10] J. Chappellaz, T Blunier, D Raynaud, J M Barnola, J Schwander, and B Stauffer. Synchronous changes in atmospheric CH_4 and Greenland climate between 40 and 8 kyr BP. *Nature*, 366:443–445, 1993.

[11] H. Craig, Y. Horibe, and T. Sowers. Gravitational separation of gases and isotopes in polar ice caps. *Science*, 242:1675–1678, 1988.

[12] D. M. Etheridge, L. P. Steele, R. J. Francey, and R. L. Langenfelds. Atmospheric methane between 1000 AD and present: Evidence for antropogenic emission and climate variability. *J. Geophys. Res.*, 103:15,979–15,993, 1998.

[13] D M Etheridge, L P Steele, R L Langenfields, R J Francey, J M Barnola, and V I Morgan. Natural and anthropogenic changes in atmospheric CO_2 over the last 1000 years from air in antarctic ice and firn. *J. Geophys. Res.*, 101:4115–4128, 1996.

[14] J. Flückiger, T. Blunier, B. Stauffer, J. Chappellaz, R. Spahni, K. Kawamura, J. Schwander, T. F. Stocker, and D. Dahl-Jensen. N_2O and CH_4 variations during the last galcial epoch: Insight into global processes. *Glob. Biogeochem. Cycles*, GB 1020:doi:10.1029/2003GB002122, 2004.

[15] R. J. Francey, M. R. Manning, C. E. Allison, S. A. Coram, D. Etheridge, R. L. Langenfelds, D. C. Lowe, and L. P. Steele. A history of delta C-13 in atmospheric CH_4 from the Cape Grim air archive and Antarctic firn air. *J. Geophys. Res*, 104:23,631–23,643, 1999.

[16] A. Goto, T. Hondoh, and S. Mae. The electron density distribution in ice 1h determined by single-crystal x-ray diffractometry. *J. Chem. Phys.*, 93(2):1412–1417, 1990.

[17] M M Herron and Jr. Langway, C C. Firn densification: An empirical model. *J. Glaciol.*, 25:373–385, 1980.

[18] T Ikeda, H Kukazawa, S Mae, L Pepin, P Duval, B Champagnon, V Lipenkov, and T Hondoh. Extreme fractionation of gases caused by formation of clathrate hydrates in Vostok antarctic ice. *Geophys. Res Lett.*, 26(1):91–94, 1999.

[19] A. Indermühle, T. F. Stocker, F. Joos, H. Fischer, H. J. Smith, M. Wahlen, B. Deck, D. Mastroianni, J. Tschumi, T. Blunier, and B. Stauffer. Holocene carbon-cycle dynamics based on CO_2 trapped in ice at Taylor Dome, Antarctica. *Nature*, 398:121–126, 1999.

[20] C. D. Keeling, S C Piper, and M. Heimann. Global and hemispheric CO_2 sinks deduced from changes in atmospheric O_2 concentration. *Nature*, 381:218–221, 1996.

[21] J. Kärger and D.M. Ruthven. Diffusion in zelolites and other microporous solids. *John Wiley & Sons, Inc. New York*, 1992.

[22] A. Landais, N. Caillon, C. Goujon, A. Grachev, J.M. Barnola, J. Chappellaz, J. Jouzel, V. Masson-Delmotte, and M. Leuenberger. Quantification of rapid temperature change during DO event 12 and phasing with methane inferred from air isotopic measurements. *Earth and Planetary Science Letters*, 225:221–232, 2004.

[23] C. Lang, M. Leuenberger, J. Schwander, and S. Johnsen. 16°C rapid temperature variation in central Greenland 70000 years ago. *Science*, 286:934–937, 1999.

[24] M. Leuenberger, P. Nyfeler, and J. Schwander. Isotopic and elemental ratio measurements on air from NorthGRIP firn air sampling 2001 (abstract). *Geophysical Research Abstracts*, 4:EGS02–A–01299, 2002.

[25] M. C. Leuenberger, C. Lang, and J. Schwander. Delta 15N measurements as a calibration tool for the paleothermometer and gas-ice age differences: a case study for the 8200 B.P. event on GRIP ice. *Journal of Geophysical Research*, 104(D18):22163–22170, 1999.

[26] E. Monnin, A. Indermühle, A. Dällenbach, J. Flückiger, B. Stauffer, T. F. Stocker, D. Raynaud, and J.-M. Barnola. Atmospheric CO_2 concentrations over the last glacial termination. *Science*, 291:112–114, 2001.

[27] J. R. Petit, J. Jouzel, D. Raynaud, N. I. Barkov, J.-M. Barmola, I. Basile, M. Bender, J. Chappellaz, M. Davis, G. Delaygue, M. Demotte, V. M. Kotlyakov, M. Legrand, V. Y. Lipenkov, C. Lorius, L. Pépin, C. Ritz, E. Saltzman, and M. Stievenard. Climate and atmospheric history of the past 420000 years from the Vostok ice core, Antarctica. *Nature*, 399:429–436, 1999.

[28] R. C. Reid and T. K. Sherwood. The properties of gases and liquids. *McGraw-Hill, New York*, 1966.

[29] J. Schwander. The transformation of snow to ice and the occlusion of gases. In H. Oeschger and C C Langway Jr., editors, *The Environmental Record in Glaciers and Ice Sheets*, pages 53–67. John Wiley, New York, 1989.

[30] J. Schwander, J M Barnola, C Andrié, M Leuenberger, A Ludin, D Raynaud, and B Stauffer. The age of the air in the firn and the ice at summit, Greenland. *J. Geophys. Res.*, 98:2831–2838, 1993.

[31] J Schwander, B Stauffer, and A Sigg. Air mixing in firn and the age of the air at pore close-off. *Annals of Glaciology*, 10:141 – 145, 1988.

[32] J. Severinghaus and M. Battle. Ninety per mil enrichment of neon in firn air at SouthPole (abstract). *Geophysical Research Abstracts*, 4:EGS02–A–00510, 2002.

[33] J Severinghaus and T Sowers. Thermal diffusion as a temperature-change indicator in ice core climate records (abstract). *Eos Trans. AGU*, 76(46):Fall Meet. Suppl., F291, 1995.

[34] J. P. Severinghaus and E. J. Brook. Abrupt climate change at the end of the last glacial period inferred from trapped air in polar ice. *Science*, 286:930–934, 1999.

[35] J. P. Severinghaus and E. J. Brook. Do atmospheric gases fractionate during air bubble closure in polar firn and ice? (abstract). *EOS Trans. AGU*, 81:S20, 2000.

[36] J. P. Severinghaus, A. Grachev, and M. Battle. Thermal fractionation of polar firn by seasonal temperature gradients. *Geochemistry Geophysics Geosystems*, 2:2000GC000146, 2001.

[37] J. P. Severinghaus, A. Grachev, B. Luz, and N. Caillon. A method for precise measurement of argon 40/36 and krypton/argon ratios in trapped air in polar ice with applications to past firn thickness and abrupt climate change in Greenland and at siple dome, Antarctica. *Geochimica et Cosmochimica Acta*, 67(3):325–343, 2003.

[38] Jeffrey P Severinghaus, T Sowers, E J Brook, R B Alley, and M L Bender. Timing of abrupt climate change at the end of the Younger Dryas interval from thermally fractionated gases in polar ice. *Nature*, 391:141–146, 1998.

[39] T A Sowers, M L Bender, and D Raynaud. Elemental and isotopic composition of occluded O_2 and N_2 in polar ice. *J. Geophys. Res.*, 94:5137–5150, 1989.

[40] R. Spahni, J. Schwander, J. Flückiger, B. Stauffer, J. Chappellaz, and B. Raynaud. The attenuation of fast atmospheric CH_4 variations recorded in polar ice cores. *Geophysical Research Letters*, 30(11):1571, doi:10.1029/2003GL017093, 2003.

[41] C M Trudinger, I G Enting, D M Etheridge, R J Francey, V A Levchenko, L P Steele, D Raynaud, and L Arnaud. Modelling air movement and bubble trapping in firn. *J. Geophys. Res.*, 102(D6):6747–6763, 1997.

[42] T. Uchida, S. Mae, T. Hondoh, V. Y. Lipenkov, P. Duval, and J. Kawabata. Growth process of air-hydrates and diffusion of air molecules in deep ice sheet. *Proceedings of the NIPR Symposium on Polar Meteorology and Glaciaology*, 8:140–148, 1994.

Chapter 5

The NorthGRIP Ice Core

5.1 High resolution Climate Record of the Northern Hemisphere reaching into the last Glacial Interglacial Period

North Greenland Ice-Core Project (NorthGRIP) Members[1]

Abstract

A new deep drilling operation has been completed in 2003 in North Greenland at the NorthGRIP site (75.10°N, 42.32°W), 324 km North-North-West of the summit site where the GRIP and GISP2 ice cores were retrieved. The site and resulting climate records are unique in a number of ways. Eemian ice is found at the base of the core, and the ice isotope values imply substantially warmer (by 5°C) conditions than present day at that time. The base of the ice sheet is melting at NorthGRIP, resulting in dramatically reduced layer thinning at the bottom of the core, undisturbed ice stratigraphy throughout the core, and nearly annual resolution of climate records at 120,000 yr BP. The full ice isotopic record compared with the GRIP and GISP2 corresponding profiles reveals both general similarities and striking differences. There is, in particular, a large and well marked latitudinal climatic gradient between the NorthGRIP and Summit sites that appears to be modulated by the extent of the Laurentide ice sheet, and thus related to its impact on atmospheric circulation. The Bølling warming in NorthGRIP appears as an abrupt climate change of about 10°C in a decade or less, in contrast to the more gradual, centennial scale warming seen in the Summit cores. In support of ice sheet models, there is no indication of significant changes in the altitude of the Greenland ice sheet in the NorthGRIP area over the last 120,000 yr BP. As drilling concluded, basal melt water flooded the hole and froze into the bottom 45 m of the borehole, leaving behind a potential archive for future paleobiological and paleoenvironmental studies.

---

[1]A full list of the authors appears at the end of this paper

High-resolution record of Northern Hemisphere climate extending into the last interglacial period

North Greenland Ice Core Project members*

A full list of authors appears at the end of this paper

....

Two deep ice cores from central Greenland, drilled in the 1990s, have played a key role in climate reconstructions of the Northern Hemisphere, but the oldest sections of the cores were disturbed in chronology owing to ice folding near the bedrock. Here we present an undisturbed climate record from a North Greenland ice core, which extends back to 123,000 years before the present, within the last interglacial period. The oxygen isotopes in the ice imply that climate was stable during the last interglacial period, with temperatures 5 °C warmer than today. We find unexpectedly large temperature differences between our new record from northern Greenland and the undisturbed sections of the cores from central Greenland, suggesting that the extent of ice in the Northern Hemisphere modulated the latitudinal temperature gradients in Greenland. This record shows a slow decline in temperatures that marked the initiation of the last glacial period. Our record reveals a hitherto unrecognized warm period initiated by an abrupt climate warming about 115,000 years ago, before glacial conditions were fully developed. This event does not appear to have an immediate Antarctic counterpart, suggesting that the climate see-saw between the hemispheres (which dominated the last glacial period) was not operating at this time.

The two deep ice cores drilled at the beginning of the 1990s in central Greenland (GRIP[1–3] and GISP2[4,5], respectively 3,027 m and 3,053 m long) have played a key role in documenting rapid climate changes during the last glacial period. However, it quickly became clear that the bottom 10% of at least one (and most probably both) of these ice cores[4,6–9] was disturbed owing to ice folding close to the bedrock. The Central Greenland ice core records are fully reliable climate archives back to 105,000 years before present (105 kyr BP), but the disturbances mean that no reliable Northern Hemisphere ice core record of the previous interglacial (the Eemian climatic period) was known to exist in the Northern Hemisphere.

This situation motivated the search for a new drilling site where undisturbed ice from the last interglacial period[10], and even from the previous glacial period, would be accessible[11]. The North Greenland Ice Core Project (NGRIP) site, located at 75.10 °N and 42.32 °W with an elevation of 2,917 m and an ice thickness of 3,085 m (Fig. 1), was selected on the basis of three criteria that, when satisfied together, should produce dateable ice older than that found in central Greenland: a position on a ridge to reduce deformation by ice flow, flat bedrock, and a lower precipitation rate. The present accumulation rate is 0.19 m ice equivalent yr^{-1}, the annual mean temperature is -31.5 °C, and the ice near the base originates 50 km upstream of the ice ridge in the direction of Summit[12]. The NGRIP drilling started in 1996, and bedrock was reached in July 2003.

Dating of the NGRIP climate record

The climate record of the oxygen isotopic composition of the ice ($\delta^{18}O$) from the NGRIP ice core is shown in Fig. 2 (and is available as Supplementary Information). In cold glaciers where the basal ice temperature is below freezing, the annual ice layers typically thin towards zero thickness close to bedrock, and flow induced disturbances can limit the usefulness of the deepest part of ice cores[13]. In contrast, at NGRIP high rates of basal ice melting, estimated to be 7 mm yr^{-1} (refs 12, 14), remove the bottom layers, greatly restricting the thinning of the layers and the possibility of ice disturbances. Whereas the present-day accumulation is 15% lower at NGRIP than at GRIP, NGRIP annual layer thicknesses at 105 kyr BP (depth 2,900 m) are of the order of 1.1 cm, twice that of GRIP ice of this age.
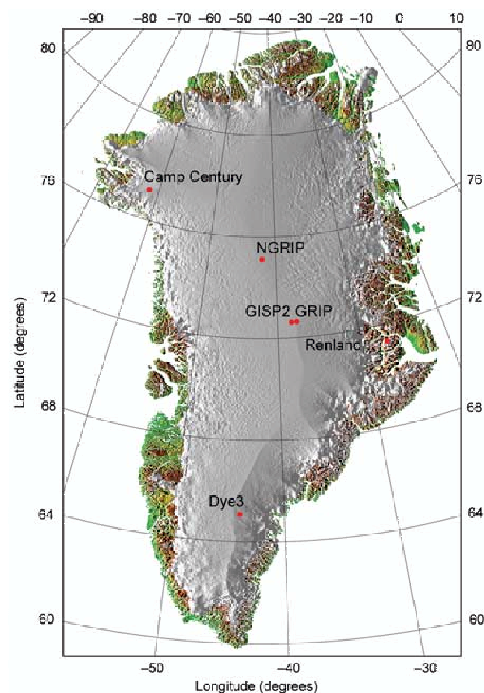
Figure 1 Map of Greenland, showing the locations of the deep ice core drilling sites. The sites GRIP (72.5 °N, 37.3 °W), GISP2 (72.5 °N, 38.3 °W), NGRIP (75.1 °N, 42.3 °W), Camp Century (77.2 °N, 61.1 °W), Dye3 (65.2 °N, 43.8 °W) and Renland (71.3 °N, 26.7 °W) are marked. The Greenland map was provided by S. Ekholm, Danish Cadastre.

   147

articles

The NGRIP isotopic record covers the Holocene, the entire last glacial period, and part of the Eemian period. The 24 abrupt and climatic warm Dansgaard–Oeschger (DO) events, or Greenland interstadials (GIS), initially numbered in the GRIP record[1,2] are very clearly identified (Fig. 2a, b), as are the climatic cold Greenland stadials (GS) that follow the DO events. The NGRIP core has been cross-dated to the GRIP core ss09sea chronology[15] down to 105 kyr BP using the high-resolution ice isotope profiles and volcanic events found in the ECM and DEP records[5,16]. Older ice is cross-dated to the Antarctic Vostok ice core records by using concentrations of methane and $\delta^{18}O$ of the entrapped air[9,17–22]. To determine if deep ice folding is a problem at NGRIP, we concentrate on the period corresponding to the marine isotope stage (MIS) 5d/5c transition dated around 105 kyr BP at Vostok (GT4 timescale). From methane and $\delta^{15}N$ air measurements, we confirm that this transition is the counterpart of the Northern Hemisphere stadial 25[18,21,23] that ends with the abrupt onset of DO 24 at the NGRIP depth of 2,940 m (Fig. 3). At this depth, methane concentrations in air exhibit a rapid increase from 450 to 650 p.p.b.v., a shift which is also observed in the Vostok data[24] (Fig. 3), and the $\delta^{15}N$ air signal, measured with a resolution of better than 100 yr, shows a rapid increase typical of DO events, resulting from thermal and gravitational fractionation processes. The increase in $\delta^{15}N$ and in methane concentration over the warming of DO 24 are both located 7 m deeper in the ice core than the corresponding $\delta^{18}O$ transition[25–27] (Fig. 3). This reflects the typical depth shift, or gas-age/ice-age difference, expected with normal firnification processes and later thinning through ice flow[28]. This supports our contention that the bottom ice is undisturbed by folding or ice mixing. We note that similar investigations on the GRIP core have confirmed that this record is indeed disturbed at the time of the 5d/5c transition[7,18], as in that core the isotope and gas transitions are located at the same depth.

Below DO 19 the NGRIP record is compared to the planktonic oxygen isotope record from marine core MD95-2045 drilled on the

Iberian margin[29] (Fig. 4). On the basis of strong similarities between these two records and ice modelling as well as $\delta^{18}O$ air measurements on the deepest parts of the core compared with Vostok, the basal part of the NGRIP record is dated to 123 kyr BP. Owing to the basal melting, the annual layer thickness of the ice from 2,700 to 3,085 m (90 to 123 kyr BP) thins much less than in the case of no melting, further making dating straightforward. At these depths, the depth scale is almost linearly proportional to time. Thus, we feel confident in interpreting the ice isotopic record at NGRIP as the first Northern Hemisphere ice core record of a highly detailed, undisturbed climate record of the late Eemian and the inception of the last glacial period.

Climate record of the late Eemian period

We first examine the implications arising from the relatively high (warm) and stable Eemian ice isotopic values found in the bottom 85 m of the ice core. As noted above, the annual layers are unusually thick, 1.0 to 1.6 cm, through this period of glacial interception and the latter part of the Eemian period, allowing a very detailed look at this key climatic period. The maximum isotopic value of $-32‰$ found for the Eemian in the NGRIP core corresponds to the highest values found in the GRIP and GISP2 ice cores. Although these other cores have disturbed chronologies for ice older than 105 kyr BP, they do contain Eemian age ice[15,18], and the maximum isotopic values can be assumed to represent the warmest Eemian climate[30]. Because both the present interglacial isotopic values ($-35‰$) and the Eemian values are similar in the GRIP, GISP2, and NGRIP ice, we infer that the ice from the bottom of the NGRIP core has sampled the warmest part of Eemian climate. This maximum isotopic value is 3‰ higher than the present value, and if attributed solely to temperature, implies at least a 5 K warmer temperature in the Eemian than at present[30–33]. It is notable that the 3‰ isotopic value difference between the present and the Eemian period seen at NGRIP, GRIP and GISP2 is also found in northern Greenland ice
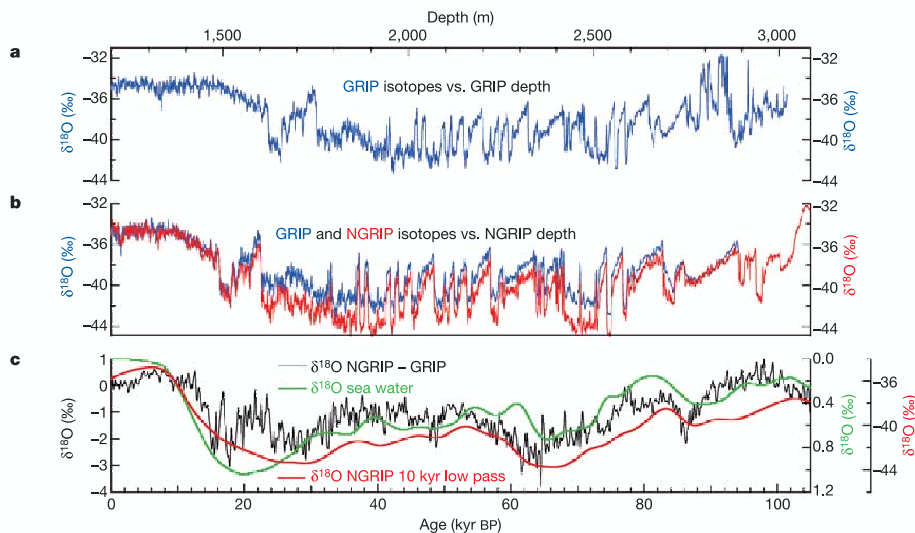
Figure 2 The NGRIP stable oxygen isotopic record compared to the GRIP record. **a**, The GRIP oxygen isotopic profile (blue) with respect to depth at GRIP. Isotopic values ($\delta^{18}O$) are expressed in ‰ with respect to Vienna Standard Mean Ocean Water (V-SMOW). The measurements have been performed on 55 cm samples with an accuracy of $\pm 0.1‰$. **b**, The NGRIP oxygen isotopic profile (red) with respect to depth at NGRIP. For comparison,

the GRIP record (blue) has been plotted on the NGRIP depth scale using the rapid transitions as tie points. **c**, The difference between the NGRIP and GRIP oxygen isotopic profiles plotted above on the GRIP2001/ss09sea timescale[15] in 50 yr resolution (black). The record is compared to a record representing sea level changes[39] (green) and a 10-kyr smoothed oxygen isotope profile from NGRIP (red).

cores nearer the coast, such as Camp Century (77.2 °N, 61.1 °W) in the west[15], and Renland (71.3 °N, 26.7 °W) in the east[15]. We conclude that the relative elevation differences during the Eemian in northern Greenland are thus not large, and further, as the Renland ice cap only is 325 m thick and cannot change elevation by more than 100 m, the absolute elevation changes between the Eemian and the present can only be of the order of 100 m. In contrast, the Dye3 ice core in south Greenland (65.2 °N, 43.8 °W) has an isotope difference of 5‰ (ref. 15), suggesting as much as 500 m lower elevation there. The Eemian isotopic values reported here paint a picture of an Eemian ice sheet with northern and central ice thicknesses similar to the present, while the south Greenland ice thickness is substantially reduced. This provides a valuable constraint for both future glaciological models of the Greenland Eemian ice sheet as well as models of sea level changes[30,34–36].

Climate record of the glacial inception

This high resolution NGRIP record reveals a slow decline in temperatures from the warm Eemian isotopic values to cooler, intermediate values over 7,000 yr from 122 to 115 kyr BP. The end of the last interglacial thus does not appear to have started with an abrupt climate change, but with a long and gradual deterioration of climate. Before full glacial values are reached, however, the record does reveal an abrupt cooling, with a first $\delta^{18}O$ decrease at about 119 kyr BP, followed by relatively stable depleted $\delta^{18}O$ levels, which we name here the Greenland stadial 26. The stadial is followed by an abrupt increase at ~115 kyr BP, the onset of DO 25[37] (Fig. 4). NGRIP is the first ice core climate record to so clearly resolve these rapid and large fluctuations in climate right at the beginning of the full glacial period. It is remarkable how well the features of the record compare with the marine planktonic isotope record from the margin of the Iberian coast, a proxy for the sea surface temperatures here. The features are thus believed to be large-scale features typical of the North Atlantic region[38]. It is significant that DO 25, while weak

(with an amplitude 25% of the following DO events), was similar in character to the following DO events, although it occurred at the time when the ice caps were first building up. Thus it seems difficult to call on melting ice or other large freshwater input to the North Atlantic to trigger this event, although clearly we need more information from this and future ice cores to fully understand this first abrupt climate change of the last glacial.

Regional climate differences in Greenland

We now focus on a detailed comparison of the NGRIP $\delta^{18}O$ ice profile with the GRIP ice isotopic record over their common part. Despite being only 325 km apart, these records have significant differences that illustrate the importance of regional variations in Greenland climate, even on quite long timescales. Figure 2b shows the NGRIP ice isotope profile. The GRIP record shown in Fig. 2a is plotted on the NGRIP depth scale using the DO events as references, so the two records can be compared. At first glance, the two records are very similar as expected, given the relative proximity of the cores. But closer inspection shows substantial differences between the records. Whereas NGRIP and GRIP have very similar $\delta^{18}O$ levels during the Holocene, glacial isotopic levels in the NGRIP record are systematically depleted by 1‰ to 2‰. The difference between these isotopic profiles (Fig. 2c) reaches maxima at about 15–20 kyr BP, 25–30 kyr BP and 60–70 kyr BP. The magnitude of the difference appears to be related to the Northern Hemisphere climate curve, as represented by a smoothed version of the NGRIP record, such that colder conditions have larger differences (Fig. 2c). The difference curve also compares relatively well to the global sea level curve[39], implying that the extent of the glacial continental ice sheets may help to explain the difference.

The difference curve only weakly traces the DO events, suggesting that the differences are not very well connected to processes operating on millennial timescales. A preliminary reconstruction of past temperatures based on the measured borehole temperatures
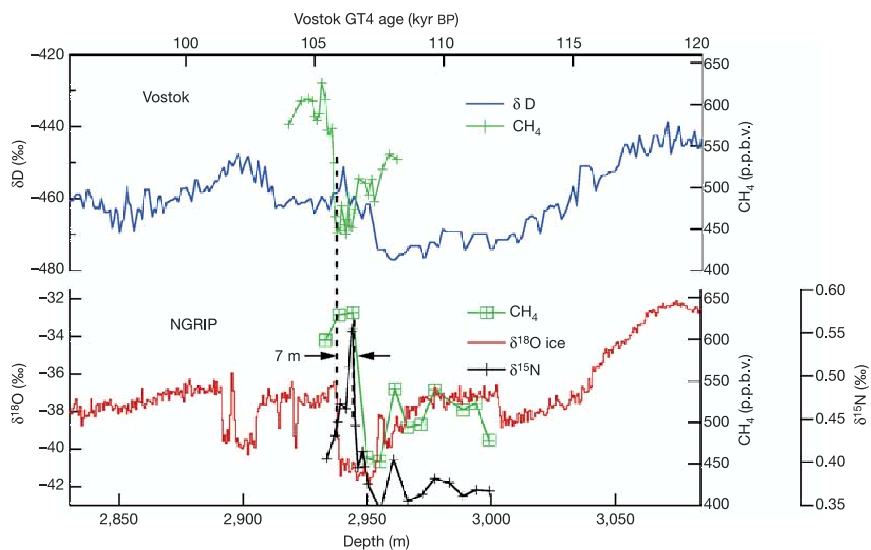
Figure 3 Comparison of ice core records from NGRIP and Vostok for NGRIP depths 2,830 to 3,085 m. The isotopic composition, δD, of the ice (blue) and of methane in the air (green) for Vostok are on the top, and the isotopic composition, $\delta^{18}O$, of the ice (red), methane (green) and δ15N (black) of the air for NGRIP are on the bottom. A 50-kyr resolution NGRIP record is available as Supplementary Information. The detailed Vostok methane profile combines published data and recent measurements performed to

examine the 5d/5c transition at Vostok[24]. The Vostok and NGRIP data are reported on their own scales, namely the GT4 timescale for Vostok (top axis) and the depth scale for NGRIP (bottom axis). These two independent scales have been simply shifted in order to match the sharp methane shift in Vostok with the sharp NGRIP warming at 2,940 m. Furthermore, matching of the two scales should result in the estimated mean 1.1 cm annual layer thickness for the NGRIP profile.

articles

at NGRIP supports this finding. Temperatures reconstructed at NGRIP during the Last Glacial Maximum are several degrees colder than those at GRIP and GISP2. The observed isotopic differences are large, given the relatively small distance between the two sites, and our finding that the two sites are believed to have only undergone small relative elevation changes during the glacial period[34,40]. Whereas the isotopic records in the central parts of East Antarctica[41] are rather similar and thus do not reveal large and significant climatically driven differences, the Greenland sites, located just 325 km apart, reveal major differences. Now that we are beginning to have a spatial distribution of deep ice core records, this brings into play a new source of palaeoclimatic information for these deep ice cores, that is, changes in geographical gradients with time. Our best theory is to postulate that the air masses reaching the two sites during the glacial had different sources. In response to the extent of the Laurentide ice sheet, sea ice and the extensive North Atlantic ice shelves, NGRIP has become further from the ocean, and may have seen a higher fraction of air coming over the northern side of the Laurentide ice sheet, bringing with it colder and more isotopically depleted moisture than GRIP might have seen[42,43]. Taken as a whole, the findings here suggest that the atmospheric water cycle over Greenland is substantially different between modern and glacial worlds.

Basal water under the ice

When drilling was completed at NGRIP, basal water flooded the deepest 45 m of the bore hole. Although we knew from temperature profiles taken in 2001–02 that the base of the ice sheet was at or very near the pressure melting point, liquid water was not seen in radar profiles done during site selection. The melt rate at the base at NGRIP is 7 mm ice yr^{-1}, so the geothermal heat flow appears to be as high as $140\,\mathrm{mW\,m}^{-2}$ ($70\,\mathrm{mW\,m}^{-2}$ from latent heat, and $70\,\mathrm{mW\,m}^{-2}$ conducted though the ice based on the measured bore temperature). This high geothermal heat flow value is atypical for Precambrian shields[44] believed to cover most of Greenland. The recent indications of bacterial life in and under Antarctic ice[45] have revealed that the Earth possibly contains a previously unrecognized cold biosphere that would be actively involved in biogeochemical processes. Thus Greenland, like Antarctica, is now known to have liquid water at its base in some locations, water that awaits further study for basal sediment composition and evidence of life in a truly extreme environment.

Implications for future palaeoclimatic studies

The first measurements available on the NGRIP core already provide a wealth of new and promising environmental information. Most importantly, the NGRIP core contains the first continuous record of the late Eemian and the interception of the last glacial period to be recorded in a deep Greenland ice core. The palaeoclimatic signal for Greenland now reaches 123,000 yr back in time, and reveals a stable and warm late Eemian period. The end of the Eemian is a slow decline to glacial, cooler, intermediate conditions, but the onset of abrupt climate changes, the DO events that mark the last glacial period, precedes full glacial conditions. The bottom ice at NGRIP is essentially undisturbed and annual ice layers are quite thick, a situation caused by basal melting which in turn results from an unexpectedly high geothermal heat flow in North Greenland. The additional knowledge that the central and northern ice sheet during the Eemian period was at the same elevation as present constrains modelled ice volumes and sea level changes during the Eemian and glacial period. This interpretation is only consistent with modelling studies of the ice sheet during the Eemian that, although predicting an overall smaller ice sheet in accord with higher observed sea levels during this time[34,35,46–48], allow for no large ice elevation change for the central Greenland ice. The next generation of models of the Greenland ice sheets should also include substantial melt under the northern part of the ice sheet as well as the northeast ice stream, important for the mass balance of the ice sheet[49,50].

The deepest ice should allow a detailed study of the last glacial inception, including greenhouse gases and atmospheric dust loading, and in future comparisons with Antarctic records we should be able to investigate in detail the sequence of climatic events and forcing between north and south during this key climatic period. We find that the 5d/5c Vostok time period is the counterpart of the Northern Hemisphere stadial 25 that ends with the abrupt onset of DO 24 at the NGRIP depth 2,940 m. The north–south teleconnection observed here is similar in behaviour to all the following events (DO events 1–23), and behaves as predicted by the simple thermodynamic see-saw model[23]. In contrast, the weak stadial 26 followed by the abrupt onset of DO 25 is not opposed by an Antarctic reversal. This could be due to dating uncertainties between the two cores, but it could also be information on the timing of the onset of the teleconnection during the building of the ice caps and the cooling of the climate. When did the north–south climate see-saw begin? Is there information waiting to be found that can tell us how glacial periods begin, and whether we are in danger of entering one in the near future? New and detailed measurements from the EPICA Antarctica ice cores are expected to clarify this observation. And finally, is there life at the base of the Greenland ice sheet? These are some of the many questions that await further study of the new NGRIP ice core. □

1. Johnsen, S. J. *et al.* Irregular glacial interstadials recorded in a new Greenland ice core. *Nature* **359**, 311–313 (1992).
2. Dansgaard, W. *et al.* Evidence for general instability of past climate from a 250-kyr ice-core record. *Nature* **364**, 218–220 (1993).
3. Greenland Ice-Core Project (GRIP) Members. Climate instability during the last interglacial period recorded in the GRIP ice core. *Nature* **364**, 203–208 (1993).
4. Grootes, P. M., Stuiver, M., White, J. W. C., Johnsen, S. J. & Jouzel, J. Comparison of oxygen isotope records from the GISP2 and GRIP Greenland ice cores. *Nature* **366**, 552–554 (1993).
5. Taylor, K. C. *et al.* Electrical conductivity measurements from the GISP2 and GRIP Greenland ice cores. *Nature* **366**, 549–552 (1993).
6. Bender, M. *et al.* Climate correlations between Greenland and Antarctica during the last 100,000 years. *Nature* **372**, 663–666 (1994).
7. Fuchs, A. & Leuenberger, M. δ^{18}O of atmospheric oxygen measured on the GRIP Ice Core document stratigraphic disturbances in the lowest 10% of the core. *Geophys. Res. Lett.* **23**, 1049–1052 (1996).
8. Johnsen, S. J. *et al.* The δ^{18}O record along the Greenland Ice Core Project deep ice core and the
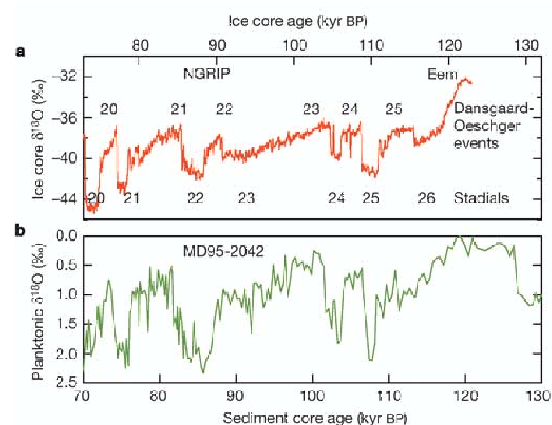
Figure 4 The NGRIP isotopic profile from the Supplementary Information (**a**) compared with the planktonic isotopes in the Iberian margin sediment core MD95-2024[29] (**b**). The Greenland Dansgaard–Oeschger events (interstadials) are numbered along with the associated stadials. The two age scales are independent and seem to match within a few kyr.

articles

problem of possible Eemian climatic instability. *J. Geophys. Res.* **102**, 26397–26410 (1997).

9. Chappellaz, J., Brook, E., Blunier, T. & Malaizé, B. CH_4 and $\delta^{18}O$ of O_2 records from Antarctic and Greenland ice: A clue for stratigraphic disturbance in the bottom part of the Greenland Ice Core Project and Greenland Ice Sheet Project 2 ice cores. *J. Geophys. Res.* **102**, 26547–26557 (1997).

10. Dahl-Jensen, D. *et al.* The NorthGRIP deep drilling program. *Ann. Glaciol.* **35**, 1–4 (2002).

11. Dahl-Jensen, D. *et al.* A search in north Greenland for a new ice-core drill site. *J. Glaciol.* **43**, 300–306 (1997).

12. Dahl-Jensen, D., Gundestrup, N., Gorgineni, P. & Miller, H. Basal melt at NorthGRIP modeled from borehole, ice-core and radio-echo sounder observations. *Ann. Glaciol.* **37**, 207–212 (2003).

13. Alley, R. B. *et al.* Comparison of deep ice cores. *Nature* **373**, 393–394 (1995).

14. Grinsted, A. & Dahl-Jensen, D. A Monte Carlo-tuned model of the flow in the NorthGRIP area. *Ann. Glaciol.* **35**, 527–530 (2002).

15. Johnsen, S. J. *et al.* Oxygen isotope and palaeotemperature records from six Greenland ice-core stations: Camp Century, Dye-3, GRIP, GISP2, Renland and NorthGRIP. *J. Quat. Sci.* **16**, 299–307 (2001).

16. Clausen, H. B. *et al.* A comparison of the volcanic records over the past 4000 years from the Greenland Ice Core Project and Dye3 Greenland ice cores. *J. Geophys. Res.* **102**, 26707–26723 (1997).

17. Blunier, T. *et al.* Asynchrony of Antarctic and Greenland climate change during the last glacial period. *Nature* **394**, 739–743 (1998).

18. Landais, A. *et al.* A tentative reconstruction of the last interglacial and glacial inception in Greenland based on new gas measurements in the Greenland Ice Core Project (GRIP) ice core. *J. Geophys. Res.* **108**, doi:10.1029/2002JD003147 (2003).

19. Flückiger, J. *et al.* N_2O and CH_4 variations during the last glacial epoch: Insight into global processes. *Glob. Biogeochem. Cycles* **18**, doi:10.1029/2003GB002122 (2004).

20. Suwa, M., von Fischer, J. & Bender, M. Age reconstruction for the bottom part of the GISP2 ice core based on trapped methane and oxygen isotopes records. *Geophys. Res. Abstr.* **5**, 07811 (2003).

21. Caillon, N. *et al.* Estimation of temperature change and of gas age-ice age difference, 108 kyr BP, at Vostok, Antarctica. *J. Geophys. Res.* **106**, 31893–31901 (2001).

22. Petit, J. R. *et al.* Climate and atmospheric history of the past 420,000 years from the Vostok ice core, Antarctica. *Nature* **399**, 429–436 (1999).

23. Stocker, T. F. & Johnsen, S. J. A minimum thermodynamic model for the bipolar seesaw. *Paleoceanography* **18**, doi:10.1029/2003PA000920 (2003).

24. Caillon, N., Jouzel, J., Severinghaus, J. P., Chappellaz, J. & Blunier, T. A novel method to study the phase relationship between Antarctic and Greenland climate. *Geophys. Res. Lett.* **30**, doi:10.1029/2003GL017838 (2003).

25. Severinghaus, J. P., Sowers, T., Brook, E. J., Alley, R. B. & Bender, M. L. Timing of abrupt climate change at the end of the Young Dryas interval from thermally fractionated gases in polar ice. *Nature* **391**, 141–146 (1998).

26. Chappellaz, J. *et al.* Synchronous changes in atmospheric CH_4 and Greenland climate between 40 and 8 kyr BP. *Nature* **366**, 443–445 (1993).

27. Brook, E. J., Sowers, T. & Orchardo, J. Rapid variations in atmospheric methane concentration during the past 110,000 years. *Science* **273**, 1087–1091 (1996).

28. Schwander, J. *et al.* Age scale of the air in the Summit ice: Implication for glacial-interglacial temperature change. *J. Geophys. Res.* **102**, 19483–19493 (1997).

29. Shackleton, N. J., Hall, M. A. & Vincent, E. Phase relationships between millennial-scale events 64,000–24,000 years ago. *Paleoceanography* **15**, 565–569 (2000).

30. Cuffey, K. M. & Marshall, S. J. Substantial contribution to sea-level rise during the last interglacial from the Greenland ice sheet. *Nature* **404**, 591–594 (2000).

31. Johnsen, S., Dahl-Jensen, D., Dansgaard, W. & Gundestrup, N. Greenland palaeotemperatures derived from GRIP bore hole temperature and ice core isotope profiles. *Tellus B* **47**, 624–629 (1995).

32. Cuffey, K. M. *et al.* Large arctic temperature change at the Wisconsin-Holocene glacial transition. *Science* **270**, 455–458 (1995).

33. Bennike, O. & Boecher, J. Land biotas of the last interglacial/glacial cycle, Jameson Land, East Greenland. *Boreas* **23**, 479–488 (1994).

34. Marshall, S. J. & Cuffey, K. M. Peregrinations of the Greenland Ice Sheet divide in the last glacial cycle: Implications for central Greenland ice cores. *Earth Planet. Sci. Lett.* **179**, 73–90 (2000).

35. Huybrechts, P. Sea-level changes at the LGM from ice-dynamic reconstructions of the Greenland and Antarctic ice sheets during the glacial cycles. *Quat. Sci. Rev.* **21**, 203–231 (2002).

36. Gregory, J. M., Huybrechts, P. & Raper, S. C. B. Threatened loss of the Greenland ice-sheet. *Nature* **428**, 616 (2004).

37. McManus, J. F., Oppo, D. W., Keigwin, L. D., Cullen, J. L. & Bond, G. C. Thermohaline circulation and prolonged interglacial warmth in the North Atlantic. *Quat. Res.* **58**, 17–21 (2002).

38. Khodri, M. *et al.* Simulating the amplification of orbital forcing by ocean feedbacks in the last glaciation. *Nature* **410**, 570–573 (2001).

39. Waelbroeck, C. *et al.* Sea-level and deep water temperature changes derived from benthic foraminifera isotopic records. *Quat. Sci. Rev.* **21**, 295–305 (2002).

40. Reeh, N., Oerter, H. & Thomsen, H. H. Comparison between Greenland ice-margin and ice-core oxygen-18 records. *Ann. Glaciol.* **35**, 136–144 (2002).

41. Watanabe, O. *et al.* Homogeneous climate variability across East Antarctica over the past three glacial cycles. *Nature* **422**, 509–512 (2003).

42. Charles, C. D., Rind, D., Jouzel, J., Koster, R. D. & Fairbanks, R. G. Seasonal precipitation timing and ice core records. *Science* **269**, 247–248 (1995).

43. Charles, C. D., Rind, D., Jouzel, J., Koster, R. D. & Fairbanks, R. G. Glacial-interglacial changes in moisture sources for Greenland: Influences on the ice core record of climate. *Science* **263**, 508–511 (1994).

44. Dawes, P. R. in *Geology of Greenland* (eds Escher, A. & Watt, W. S.) 248–303 (The Geological Survey of Greenland, Denmark, 1976).

45. Petit, J. R., Alekhina, I. & Bulat, S. A. in *Lessons for Exobiology* (ed. Gargaud, M.) (Springer, in the press).

46. Letréguilly, A., Huybrechts, P. & Reeh, N. Steady-state characteristics of the Greenland ice sheet under different climates. *J. Glaciol.* **37**, 149–157 (1991).

47. Letréguilly, A., Reeh, N. & Huybrechts, P. The Greenland ice sheet through the last glacial-interglacial cycle. *Palaeogeogr. Palaeoclimatol. Palaeoecol.* **90**, 385–394 (1991).

48. Kukla, G., McManus, J. F., Rousseau, D.-D. & Chuine, I. How long and how stable was the Last Interglacial? *Quat. Sci. Rev.* **16**, 605–612 (1997).

49. Fahnestock, M., Abdalati, W., Joughin, I., Brozena, J. & Cogineni, P. High geothermal heat flow basal melt, and the origin of rapid ice flow in central Greenland. *Science* **294**, 2338–2342 (2001).

50. Fahnestock, M. A. *et al.* Ice-stream-related patterns of ice flow in the interior of northeast Greenland. *J. Geophys. Res.* **106**, 34035–34045 (2001).

K. K. Andersen[1], N. Azuma[2], J.-M. Barnola[3], M. Bigler[4], P. Biscaye[5], N. Caillon[6], J. Chappellaz[3], H. B. Clausen[1], D. Dahl-Jensen[1], H. Fischer[7], J. Flückiger[4], D. Fritzsche[7], Y. Fujii[8], K. Goto-Azuma[8], K. Grønvold[9], N. S. Gundestrup[1]*, H. Mansson[10], C. Huber[4], C. S. Hvidberg[1], S. J. Johnsen[1], U. Jonsell[10], J. Jouzel[6], S. Kipfstuhl[7], A. Landais[6], M. Leuenberger[4], R. Lorrain[11], V. Masson-Delmotte[6], H. Miller[7], H. Motoyama[8], H. Narita[12], T. Popp[13], S. O. Rasmussen[1], D. Raynaud[3], R. Rothlisberger[4], U. Ruth[7], D. Samyn[11], J. Schwander[4], H. Shoji[14], M.-L. Siggard-Andersen[1], J. P. Steffensen[1], T. Stocker[4], A. E. Sveinbjörnsdóttir[15], A. Svensson[1], M. Takata[2], J.-L. Tison[11], Th. Thorsteinsson[16], O. Watanabe[8], F. Wilhelms[7] & J. W. C. White[13]

Affiliations for authors: 1, Niels Bohr Institute for Astronomy, Physics and Geophysics, University of Copenhagen, Juliane Maries Vej 30, DK-2100 Copenhagen OE, Denmark; 2, Nagaoka University of Technology, 1603-1 Kamitomioka-machi, Nagaoka 940-2188, Japan; 3, Laboratoire de Glaciologie et Géophysique de l'Environnement (CNRS), BP 96, 38402 St Martin d'Héres Cedex, France; 4, Climate and Environmental Physics, Physics Institute, University of Bern, Sidlerstrasse 5, CH-3012, Switzerland; 5, Lamont-Doherty Earth Observatory of Columbia University, Rte 9W - PO Box 1000, Palisades, New York 10964-8000, USA; 6, Institute Pierre Simon Laplace/ Laboratoire des Sciences du Climat et de l'Environnement, UMR CEA-CNRS, CE Saclay, Omme des Merisiers, 91191 Gir-Sur-Yvette, France; 7, Alfred-Wegener-Institute for Polar and Marine Research (AWI), Postfach 120161, D-27515 Bremerhaven, Germany; 8, National Institute of Polar Research, Kaga 1-9-10, Itabashi-ku, Tokyo 173-8515 Japan; 9, Nordic Volcanological Institute, Grensásvegur 50, 108 Reykjavik, Iceland; 10, Department of Physical Geography and Quaternary Geology, Stockholm University, S-106 91, Stockholm, Sweden; 11, Département des Sciences de la terre et de l'Environnement, Faculté des Sciences, CP 160/03, Université Libre de Bruxelles, 50 avenue FD Roosevelt, B1050 Brussels, Belgium; 12, Research Institute for Humanity and Nature, 335 Takashima-cho, Marutamachi-dori Kawaramachi nishi-iru, Kamigyo-ku, Kyoto 602-0878, Japan; 13, INSTAAR, Campus Box 450, University of Colorado, Boulder, Colorado 80309-0450, USA; 14, Kitami Institute of Technology, Koencho 165, Kitami, Hokkaido 090-8507 Japan; 15, Raunvísindastofnun Háskólans, Dunhagi 3, Iceland; 16, National Energy Authority, Grensvegur 9, IS-108 Reykjavík, Iceland

*Deceased

151

5.2 Isotope Calibrated Greenland Temperature Record over Marine Isotope Stage 3 and its Relation to CH$_4$

Christof Huber,[1] Markus Leuenberger,[1] Renato Spahni,[1] Jacqueline Flückiger,[1] Jakob Schwander,[1] Thomas F. Stocker,[1] Sigfus Johnsen,[2] Amaelle Landais[3] and Jean Jouzel[3]

Abstract

Greenland temperature variations on millennial time scales were characteristic for the last ice age. Abrupt warmings, known as Dansgaard-Oeschger (DO) events [18], can be traced in the $\delta^{18}O_{ice}$ record of Greenland ice cores. However, it has been shown that $\delta^{18}O_{ice}$ is not a direct temperature proxy [15]. Measurements of the isotopic composition of gases trapped in the ice can be used to calibrate the paleothermometer [33, 34, 35, 49, 51]. Here we present a continuous temperature record based on high resolution $\delta^{15}N$ measurements and firn model studies. It covers a sequence of 9 DO events (9–17) during the time period from 38 to 64 kyr BP. Temperature changes of 8 to 15°C were observed for these events. We can relate the discrepancy between the modern and the glacial $\delta^{18}O_{ice}$-T relationship to a combination of source temperature changes and changes in the annual distribution of precipitation. A detailed comparison of the temperature evolution with measurements of the atmospheric methane (CH$_4$) concentration shows that CH$_4$ and temperature rises at the onset of DO events are in phase. Furthermore, a strong correlation between both parameters on millennial and submillennial timescales supports the idea that even submillennial scale signals of the Greenland temperature record are at least hemispheric in their extent. On the other hand, differences in the shape of the CH$_4$ and temperature evolution during parts of the time point to a contribution of CH$_4$ source changes which depend not directly on northern temperature.

---

[1]Climate and Environmental Physics, Physics Institute, University of Bern, Sidlerstrasse 5, CH-3012 Bern, Switzerland

[2]Department of Geophysics, Juliane Maries Vej 30, University of Copenhagen, DK-2100, Copenhagen, Denmark

[3]IPSL/Laboratoire des Sciences du Climat et de l,Environnement, UMR CEA-CNRS, CEA Saclay, 91191 Gif-sur-Yvette, France

The climate over the last glacial period was characterised by numerous abrupt climate changes known as Dansgaard-Oeschger (DO) events [18]. They can be traced in paleorecords from the Arctic ice sheets, as well as from tropical and subtropical regions [1, 5, 52, 56]. DO events are most prominently represented in $\delta^{18}O_{ice}$, the oxygen isotope ratio record in Greenland ice cores. They have been related to shifts of the ocean thermohaline circulation (THC) [32, 42, 55]. DO events in Greenland typically start with a rapid warming of about 8°C up to 16°C within a few decades [33, 34, 49] followed by a more gradual cooling phase over several centuries and a rapid drop back towards cold stadial conditions. The long lasting DO events were preceded by massive ice surges from the northern ice sheets, documented by debris deposits known as Heinrich (H) events [24].

Water isotopes ($\delta^{18}O_{ice}$ or δD) are commonly used as a temperature proxy. Changes in isotopic composition of precipitation in polar regions are mainly related to changes of temperatures at the precipitation site. For Greenland a present day spatial $\delta^{18}O_{ice}$ to temperature ($\delta^{18}O_{ice}$-T) relation $\alpha_{spatial}$ of $0.67^0/_{00}$/K is determined [17]. However, for Greenland this present day spatial slope cannot be used to quantitatively interpret past climate shifts [15, 29]. $\delta^{18}O_{ice}$-T sensitivity α is varying over time, e.g. due to variations of the seasonal precipitation distribution [57] and/or changes occurring at the source region [6, 38] of precipitation. But measurements of the isotopic composition of nitrogen $\delta^{15}N$ and/or argon $\delta^{40}Ar$ on air trapped in ice cores can be used to calibrate the $\delta^{18}O_{ice}$-T relation, during an event of rapid temperature change [22, 34, 35, 49, 50]. Because atmospheric $\delta^{15}N$ is constant, changes of this air parameter trapped in ice reflect processes that occur in the firn column, where the gas isotopes are fractionated due to gravitation and thermal diffusion [51]. A rapidly changing surface temperature leads to a temperature gradient in the firn that forces the heavier isotopes to migrate towards the cold end resulting in a fractionation of the isotope signal trapped in the ice core. The original surface temperature change can be assessed comparing the measured isotope fractionation with firn model calculations. This approach has been used successfully to deduce rapid temperature changes for several DO events [33, 34, 35, 49, 51].

Here we present a reconstruction of the temperature evolution over 9 consecutive DO events 9 to 17 during Marine Isotope Stage (MIS) 3, based on high resolution $\delta^{15}N$ measurements on the ice core from the North Greenland Ice Core Project (NorthGRIP) [40], using a new on-line technique [25, 26]. This record is compared to existing high resolution CH_4 measurements from the NorthGRIP [21] (DO 12–9), and the GISP2 [3, 7] (DO 17–9) ice cores. Additionally we present new highly resolved CH_4 measurements from the NorthGRIP ice core for the time period of DO 17–15.

To assess past surface temperature evolution we use a combined dynamic firn densification, temperature and gas diffusion model [47] to calculate thermal and gravitational fractionations of isotopes trapped in the ice that can be compared to $\delta^{15}N$ measurements. The model input is the surface temperature, T_s, and the accumulation rate. Accumulation strongly depends on temperature. Hence it can be related to $\delta^{18}O_{ice}$ [29] by an empirical relation determined for present day conditions. However, the relations of the temperature as well as of the accumulation to $\delta^{18}O_{ice}$ are not exactly known for glacial conditions. In our model we tuned both parameters in order minimize the squared deviations between the model and the measurements. This leads to two conclusions. The relation between temperature and $\delta^{18}O_{ice}$ is not linear and should be revised. Our findings support a more complex relationship which

is influenced most probably by varying seasonal precipitation distribution and changes in the precipitation source region. The accumulation rates must be reduced by 20% compared to the assumptions made in the ice flow dating model for the ss09sea age scale [28, 40]. This correction has no influence on the depth-to-age relation of the NorthGRIP ice core, since the ice thinning function changes accordingly. A detailed description of the method and fitting procedure is given in the supplementary information. The tuning procedure yields the temperature evolution over the observed time period. The agreement between model and measurements is excellent for the magnitude of the δ^{15}N fractionation as well as for the timing of the events (Figure 5.1). This is strong evidence that the accumulation rate to temperature relation used in the model is correct, since otherwise either the magnitude or the timing of the events would disagree. Hence, we obtain an accurate determination of the ice-age to gas-age difference (Δage). This permits a direct comparison of the temperature and CH_4 with a time uncertainty of only about ± 50 years.

Greenland Temperature Evolution during MIS 3

In Figure 5.1 the surface temperature evolution over the time period from 64 and 38 kyr BP corresponding to nearly the complete MIS 3, is shown. MIS 3 is characterized by various abrupt temperature changes with amplitudes up to 15°C (in about 200 years). A typical rate of the temperature change at the beginning of DO events was 0.5±0.2°C/decade (Table 5.1). The amplitude of the temperature changes attributed to the different DO events are marked in Figure 1 and listed in Table 5.1. For the further discussion we distinguish three

Table 5.1: Rates of changes at the onset of DO events, Δage and Δdepth.
(A) Temperature and CH_4 amplitude change from start to top of DO event, respectively.
(B) Time from start to top of DO event.
(C) depth difference between the warming recorded in $\delta^{18}O_{ice}$ and in δ^{15}N

DO	ΔT (°C) [A]		Δt [B]	rate of change	ΔCH_4 [A]	rate of change	Δage	depth [C]
	mean	error	(yr)	(°C/decade)	(ppb)	(ppb/°C)	(yr)	(m)
9	9	3	560	0.16	78	8.7	1068	17.5
10	11.5	3	180	0.64	88	7.7	1129	17
11	15	3	580	0.26	112	7.5	1166	16
12	12.5	3	220	0.57	88	7	1053	13.5
13	8	3	220	0.36			836	13
15	10	3	240	0.42	163	16.3	923	13
16	9	3	180	0.5	121	13.4	668	11.5
17	12	3	180	0.67	185	15.4	1038	11.5

sequences: (i) DO 12–9, (ii) DO 14–13, (iii) DO 17–15. All three sequences have in common that peak temperatures were high for the first event and were constantly decreasing for subsequent ones. DO 12 and 17 were preceded by H-events 5 and 6, respectively [4, 24]. Event H-5.2, before DO 14, can not clearly be associated with a H-event, but some sediment proxies as well as sea level changes show clearly H-like behaviour [10, 24]. Beside these similarities, the three sequences were different. The sequence of DO events 12–9 started with the large event DO 12, followed by three smaller events. The sequence of DO 14–13 was characterized by a very long and stable warm phase (∼2500 yr) followed by a 2000 yr
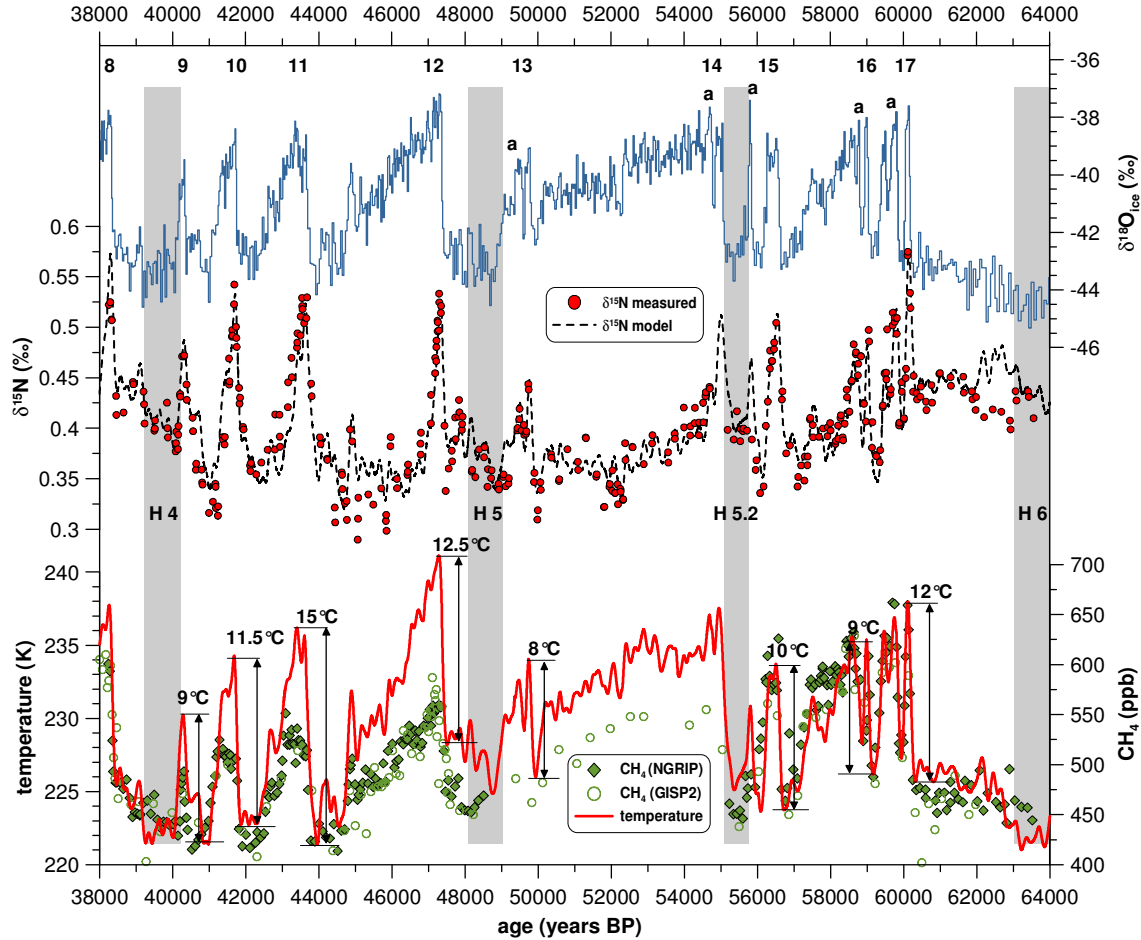
Figure 5.1: (Top panel) NorthGrip $\delta^{18}O_{ice}$ [40], (middle panel) NorthGRIP $\delta^{15}N$, (bottom panel) surface temperature (solid line), and CH_4 concentration from NorthGRIP [21] (filled diamonds) and GISP2 [3, 7] (open circles), for the time period of DO 8–17 (38 to 64 kyr BP). All curves are plotted on the GRIP2001/ss09sea [28] age scale. $\delta^{15}N$ measurements (dots) are compared to a model curve (dashed line). The temperature curve is deduced by fitting a firn densification and heat diffusion model [47] to the $\delta^{15}N$ data. Temperature is plotted as smoothed line (50 yr). Temperature changes associated with DO events are marked for each event except for DO 8 and DO 14 which could not be interpreted, due to the lack of $\delta^{15}N$ measurements. Heinrich (H) events are marked as shady bands.

period of intermediate temperatures and a very short cold interval before DO 13 started. On the other hand, the sequence of DO 17–15 was extremely unstable. Temperature was changing permanently with a frequency of about 400 yr and an amplitude of 7–12°C. In this time period, all events show a more or less pronounced second temperature peak (labelled with an "a" in the $\delta^{18}O$ record of Figure 5.1). Hence the temperature peaks were very narrow, e.g. DO 17 (width = 400 yr, from one cold phase to the next), DO 16 (300 yr), and DO 15a (200 yr), with warm phases of only a few decades. Nevertheless, the large DO events 12 and 17, which are preceded by H-events, show roughly the same temperature change of 12.5±3°C and 12±3°C, respectively. The 12.5°C temperature shift of DO 12 is in agreement with a 12°C change measured on the GRIP ice core [33]. In our calculation DO 14, which probably was also preceded by the Heinrich event H-5.2, shows a similar temperature jump.

Unfortunately, we did not yet have access to the samples covering the onset of DO 14. Therefore the temperature change of DO 14 cannot be evaluated and interpreted in detail. Interestingly, the largest temperature change is not observed for one of the large events, but for DO 11 with a 15±3°C temperature increase. However, it has to be taken into account, that for DO 11 the temperature rise was not as fast (580 years from start to top of peak) and steady as for the other events.

The Glacial $\delta^{18}O_{ice}$ to Temperature Relationship

Based on the idea of Boyle [6] who related the shift of the $\delta^{18}O_{ice}$-T relationship over the LGM-Holocene transition to changes of tropical sea surface temperatures (SST), different hypotheses regarding the discrepancy of the spatial and the temporal slope can be tested with our data. He assumed that the present day spatial relationship of $\sim 0.7^{0}/_{00}$/K accounts correctly for changes of the site temperature, when the source temperature remains constant, whereas changes of the source temperature influence the intercept of the $\delta^{18}O_{ice}$-T relationship but not the slope (Figure 5.2). Hence, the simultaneous change of both, the site and the source temperature, leads to an apparently lower slope of $\delta^{18}O_{ice}$-T relationship. Such calculations were made for the LGM-Holocene transition where the source temperatures were about 4–8°C cooler than at present [9, 43]. Based on our new data, we are now able to do the same for stadial-interstadial transitions. In Figure 5.2 $\delta^{18}O_{ice}$ corrected for changes of the oxygen isotopic composition of seawater, is plotted versus the isotope calibrated temperature. Our data suggests a similar behaviour of the $\delta^{18}O_{ice}$-T relationship during stadial-interstadial transitions as between LGM and Holocene. There is a good linear ($R^2 = 0.83$) relationship between $\delta^{18}O_{ice}$ and temperature with a mean slope of $0.37^{0}/_{00}$/K which is about half the present day spatial slope, corresponding to the values obtained by borehole temperature calibrations [29] for the last glacial to interglacial transition. A source temperature change leads to a shift of the line representing the modern $\delta^{18}O_{ice}$-T relationship on the horizontal axis in Figure 5.2.

$\delta^{18}O_{ice}$ does not depend on the mean annual temperature but on the precipitation weighted temperature. Since winter-to-summer temperature differences are large, seasonality has a strong impact on the isotopic composition of the snow. The glacial decrease in winter precipitation, predicted by GCM models [57], leads to a $\delta^{18}O_{ice}$ that is much higher than one would expect from the site temperature change alone. Hence, a seasonality change results in a shift of the modern $\delta^{18}O_{ice}$-T curve on the vertical axis of Figure 5.2. Thus seasonality variations can either compensate or amplify the effects of a changing source temperature on the $\delta^{18}O_{ice}$-T relation. For example, a lowering of the $\delta^{18}O_{ice}$ stadial-interstadial change by 3–$4^{0}/_{00}$ due to an increase of winter precipitation would be consistent with our measurements when constant source temperatures were assumed. Hence, every point in Figure 5.2 can be viewed as a linear combination of source temperature changes and changes in the distribution of precipitation throughout the year. If one parameter can be constrained the other can be inferred.

Assuming only minor variations of the seasonal distribution of precipitation, our findings would imply that source temperature changes of about 4–8°C for single DO events were in phase with site temperature variations on millennial timescales. This agrees nicely with reconstructions from the subtropical North Atlantic where temperature changes of 2–5°C where found during MIS 3, covarying with Greenland $\delta^{18}O$ of ice cores [43]. On the
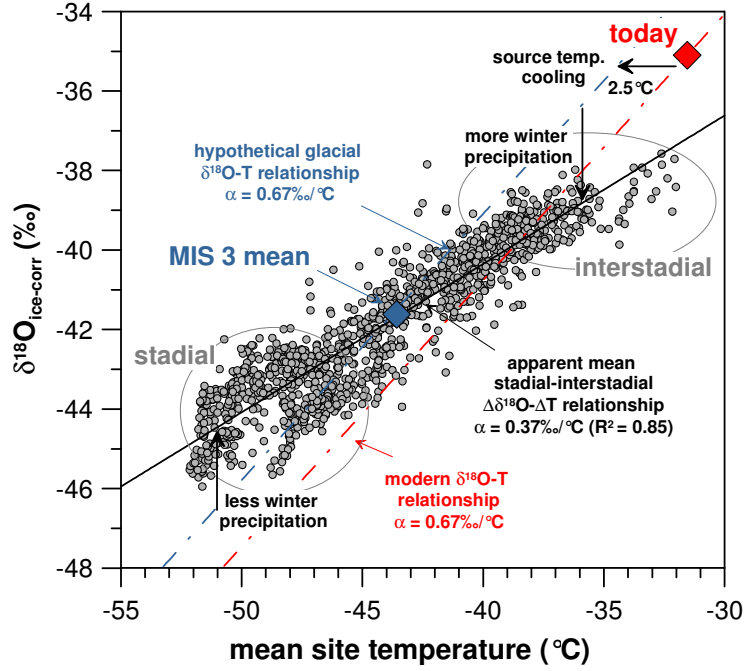
Figure 5.2: $\delta^{18}O_{ice}$ is plotted against the calibrated NorthGRIP temperature (grey dots). $\delta^{18}O_{ice}$ is corrected for changes of the oxygen isotopic composition of seawater. Since atmospheric $\delta^{18}O_{atm}$ variations reflect changes of oceanic $\delta^{18}O$ but delayed by about 1500–2500 years, we use the $\delta^{18}O_{atm}$ measurements from NorthGRIP ($\delta^{18}O_{atm} = \delta^{18}O_{measured} - 2 \cdot \delta^{15}N_{measured}$) shifted 2000 years toward older ages to correct for this effect. The curve with the modern $\delta^{18}O$-T slope ($\alpha = 0.67^0/_{00}/°C$) is plotted through the present day NorthGRIP value (red diamond) and through the mean value of our data (MIS 3 mean) (blue diamond). The data does not follow these curves. Offsets can be explained by a linear combination of source temperature changes and changes in the distribution of precipitation throughout the year.

other hand, it contradicts, however, measurements of the deuterium-excess (representing the source temperature) and the $\delta^{18}O_{ice}$ (representing the site temperature) on the GRIP ice core which are anticorrelated on millennial timescales [38]. This anticorrelation (Greenland cold, source region warm) could be the result of a southward shift of the moisture source during stadials, possibly due to extensive sea ice cover. A consistent explanation of the observed $\delta^{18}O_{ice}$-T relation with such a scenario requires large changes in the seasonality of precipitation between stadials and interstadials.

From our results we can conclude that on millennial timescales rapid temperature changes were most probably in phase with reorganisations of the seasonal precipitation distribution (the lower the temperature, the less winter precipitation) resulting in a reduction of the apparent slope of the $\delta^{18}O_{ice}$-T relationship compared to the present day value. If changes of the source temperatures can be constrained, for example by deuterium excess measurements [38], it is possible to quantify the strength of the seasonality changes.

CH_4 and Temperature

In parallel to nitrogen isotopes, CH_4 was measured on the NorthGRIP ice for the sequences of DO 12–9 [21] and DO 17–15 (new data). As shown by others before, the correlation between CH_4 and Greenland temperature is extraordinarily strong [3, 8, 11]. Usually such correlations were done using $\delta^{18}O_{ice}$ as a direct temperature proxy, which is not exactly true as showed above. Furthermore, additional uncertainties in the timing of both records arose from the Δage determinations. Here a much more direct comparison is possible, since both, temperature ($\delta^{15}N$) and CH_4, are gas species. Therefore, we can investigate the relative timing of CH_4 and temperature evolution. The timing uncertainty corresponds to the data resolution of about 50–100 years. We find that the CH_4 and temperature rises were in phase (within ± 50 yr) at the onset of the observed DO events (Figures 5.1 and 5.3).
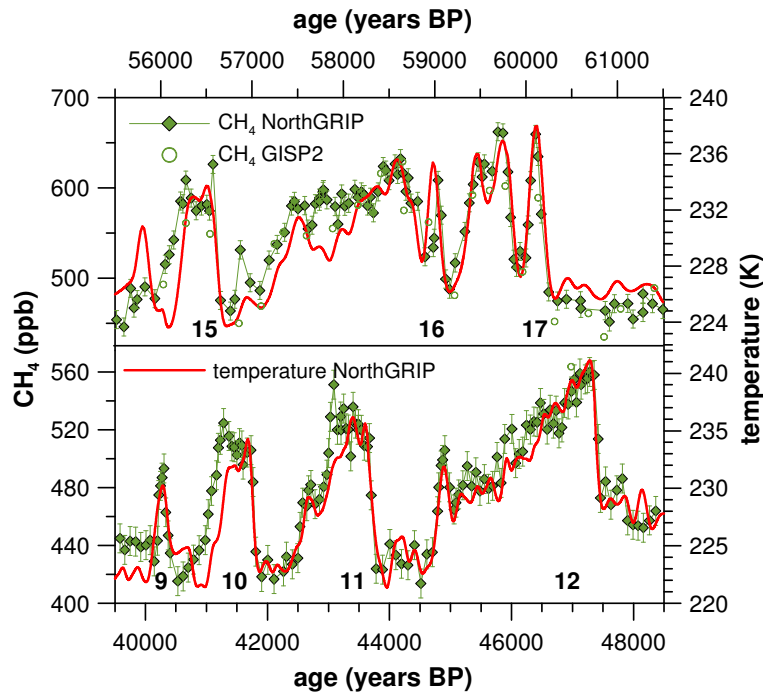
Figure 5.3: Calibrated NorthGRIP temperature evolution (solid line) compared to atmospheric methane concentration measurements (CH_4) from the NorthGRIP (ref. [21] and new measurements) and the GISP2 [8] ice cores. The data is plotted on the GRIP2001/ss09sea [28] age scale. (Top panel): Sequence of DO 17–15, 61.5 to 55.5 kyr BP. (Bottom panel): Sequence of DO 12–9, 48.5 to 39.5 kyr BP. Note that the scales of temperature and CH_4 are chosen different for the two panels. The CH_4 amplitudes are higher for DO 17–15 than for DO 12–9 [8, 21] (Figure 5.1).

The correlation between CH_4 and the calibrated temperature record is higher ($R^2 = 0.82$) than that between CH_4 and $\delta^{18}O_{ice}$ ($R^2 = 0.74$) for the sequence DO 12–9. This is most probably because $\delta^{18}O_{ice}$ includes apart from temperature other influences (precipitation distribution and/or source region movements) as discussed above. For the sequence DO 17–15, however, the correlation coefficient does not change significantly when using the calibrated temperature instead of $\delta^{18}O_{ice}$ ($R^2 = 0.72$ and 0.77, respectively) which could point to rather stable water cycle conditions. But the slope (rate of change in Table 5.1) of

the CH_4 to temperature dependency is changing substantially for the different periods. It is higher for DO 17–15 than for the period DO 12–9 (Table 5.1). This is in agreement with previous studies [8, 21] suggesting a possible link of the CH_4 amplitudes with the summer insolation of tropical to mid-northern latitudes.

The main preanthropogenic CH_4 sources are wetlands [8, 11, 12]. These CH_4 emissions are influenced by changes in precipitation and temperature driving extent and productivity of wetland ecosystems [58]. Today, main wetlands are located in the northern extra tropics, and the tropical region. DO events are recorded in different tropical paleo records as well. They indicate higher monsoon activity during the warm phase of DO events [1, 44, 56], implying enhanced CH_4 emissions. On the other hand, source distribution calculations, using the interpolar CH_4 gradient, indicate that the CH_4 increases during DO events are caused by sources mainly located north of 30°N [7, 20]. One probable contribution originates from rapid melting of large permafrost areas releasing large amounts of CH_4, stored under the ice, in parallel to temperature changes. Hence both, tropical and northern extra tropical sources could contribute to the observed CH_4 concentration variations, and we are not able to constrain either of them.

A detailed comparison of CH_4 with temperature for the two DO sequences 12–9 and 17–15 is shown in Figure 5.3. Note that the scales of temperature and CH_4 are chosen differently for the two panels in Figure 5.3, since the CH_4 amplitudes are higher for DO 17–15 than for DO 12–9 [8, 21]. For DO 17, 16, 12, and 11 even small submillennial temperature excursions have a clear counterpart in the CH_4 record. During the other presented DO events the correlation is less pronounced but still substantial. Similar features can be seen as well in the CH_4 record of the Greenland ice core GISP2 [3, 7] which is matched to the NorthGRIP (ss09sea) timescale using NorthGRIP CH_4. There is only one temperature peak that has no counterpart in CH_4 (DO 15a) which most probably was missed due to an insufficient sample resolution in both the CH_4 and the $\delta^{15}N$ record.

The presented DO events allow us for the first time to focus on the submillenial variability of CH_4 and Greenland temperature during the glacial period, since the timing uncertainty is <100 yr over the entire record. The most obvious discrepancies between CH_4 and temperature can be seen at the end of DO 10 and 15, where CH_4 decreases slower than temperature. Two possible explanations arise for this mismatch. First, other factors than temperature controlling wetland CH_4 emissions such as precipitation, water tables, vegetation changes could have remained unchanged or have not reacted immediately to temperature changes at the end of these DO events. Hence the wetland CH_4 emissions drops slower. Second, the Greenland temperature reconstruction is believed to be hemispheric in extent in agreement with recent modelling results [32]. However, different decrease rates between northern and tropical temperature which could result in a lag of ∼100 yr at the end of the decrease cannot be excluded. In this case tropical CH_4 sources behave differently from the northern ones. The question remains why not all DO events show this performance. Therefore, DO 10 and DO 15 should definitely be investigated further, i.e. by measuring the CH_4 stable isotope compositions, in order to constrain the origin of the CH_4 sources active during MIS 3.

5.2.1   Supplementary Information

Firn, the porous upper 50–100 m of an ice sheet, can be divided into three zones, distinguished by different properties of air movement. (i) The convective zone, where the air is well mixed with the atmosphere. (ii) The diffusive column, where the isotopic and elemental composition of the air is altered by diffusion, such as gravitational settling [14, 45] and thermal diffusion [34, 35, 51]. (iii) The non diffusive zone, where no vertical movement of the air occurs any more. Isotopic enrichment, i.e. for $\delta^{15}N$, at the bottom of the firn column due to gravitational settling, can be calculated using the barometric equation:

$$\delta = \left(e^{\Delta mgz/RT} - 1\right) \times 1000^0\!/\!00 \cong \Delta mgz/RT \times 1000^0\!/\!00 \tag{5.1}$$

where Δm is the mass difference between the isotope species, T is the mean firn temperature, z is the diffusive column height (DCH), g the gravitational constant, and R the ideal gas constant. Hence for stable climatic conditions the DCH can be obtained from nitrogen or argon isotope ratios measured in the ice core. The second process which alters the isotopic composition of the air in the firn diffusive column is thermal diffusion:

$$\delta = \left[\left(\frac{T_t}{T_b}\right)^{\alpha_T} - 1\right] \times 1000^0\!/\!00 \cong \Omega\Delta T \tag{5.2}$$

where ΔT is the temperature difference between the top (T_t) and the bottom (T_b) of the diffusive column, α_T is the thermal diffusion constant, and Ω the thermal diffusion sensitivity $(^0\!/\!00/°C)$ which both depend on the mean firn temperature. We used $\alpha_T = 4.61198 \cdot 10^{-3} \cdot ln(T/113.65K)$ [35]. Using the value from Grachev et al. [23] would lead to the same results. An abrupt surface temperature change, e.g. at the onset of a DO event, causes a temperature gradient in the firn column. Hence, the isotopic composition of the air is altered according to eq. 5.2, since gas diffusion is about 10 times faster than temperature conductance in the firn. After about 200 to 300 years stable climatic conditions are established again (no temperature gradient) hence the thermal signal disappears. To summarize: The isotopic enrichment measured on air from ice cores are twofold influenced, (i) by a gravitational settling, which depends mainly on the DCH, as well as (ii) by a thermal signal, which depends on the temperature gradient in the DCH (see Figure 5.4). These two effects can be separated by combined nitrogen and argon isotope measurements since both species are constant in the atmosphere [36].

The gravitational signal of $\delta^{15}N$ and $\delta^{40}Ar/4$ is the same, but the thermal diffusivities are different. Hence, the temperature gradient in the firn is proportional to $\delta^{15}N_{excess} = \delta^{15}N - \delta^{40}Ar/4$ [33, 49]. Another way is to use a combined firn densification, temperature and gas diffusion model [22, 47], to calculate the evolution of $\delta^{15}N$ theoretically and compare it to the measurements [34, 35]. Since the precision of our argon data is to low for the $\delta^{15}N_{excess}$ calculation [25], we follow second approach. The model needs as an input the accumulation and the surface temperature history. From this it calculates the firn temperature, the lock in depth (LID), which is the depth where the vertical diffusion stops, and the gas age-ice age difference Δage. Hence, the model can be fitted to the data by adjusting the input parameters. However, one has to keep in mind, that the model does not incorporate a potential convective zone in the firn, since the current understanding of the processes causing a convective zones is poor. In the following sections different approaches, which have been used to deduce past temperature evolution from our $\delta^{15}N$ data are discussed and compared with each other.
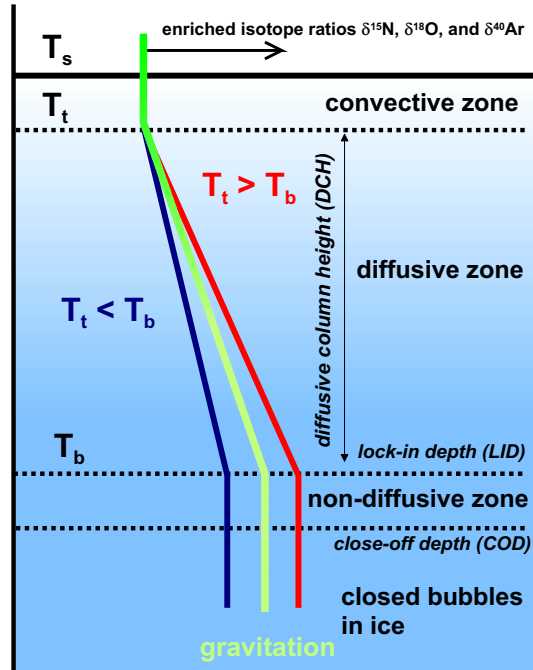
Figure 5.4: The different zones of the firn. The fractionation of nitrogen isotopic composition due to gravitational settling and thermal diffusion is shown.

Approach 1

The two model input parameters which can be tuned are the surface temperature and the accumulation rate. Accumulation rates and ice thinning (strain) are prescribed by the ice flow model dating of the core [30]. Hence when using a certain age scale, the accumulation rate is fixed and the only tuneable parameter is the temperature. However, age scales are never perfect and always under construction. In this study we use the ss09sea age scale, which is an improved GRIP age scale [28] adopted to NorthGRIP [40], and the ss06 age scale, which is at the moment the best NorthGRIP age scale available (S. Johnsen, personal communications 2004). Accumulation and thinning show relative differences of up to about 10% (Figure 5.5).

Using the accumulation rates given by the ss09sea age scale calculation, the surface temperature, T_s, is the only dependent variable. The following equation was used to derive the surface temperature: $T_s = (\delta^{18}O_{ice} + 35.1^0/_{00})\alpha^{-1} + 241.6$ K, where α is the $\delta^{18}O_{ice}$ to temperature sensitivity. We ran the model for different α scenarios ($\alpha = 0.30, 0.35, 0.40, 0.45, 0.50$). Since, α can change from one DO event to another it is not possible to find a single α scenario that matches the data for the entire time period. Hence, data and model should be fitted for short time periods of about 2000 years only. The best correlation between the model and the $\delta^{15}N$ data for a 2000 year time window was searched, varying α by linear interpolation between the different calculated scenarios. Thereafter the time window was shifted by 250 years and the procedure was repeated, until the all DO events were scanned. In order to get an error estimate for α and the convective zone depth, we tested the sensitivity of the fitting procedure to errors of the $\delta^{15}N$ measurements (Monte Carlo
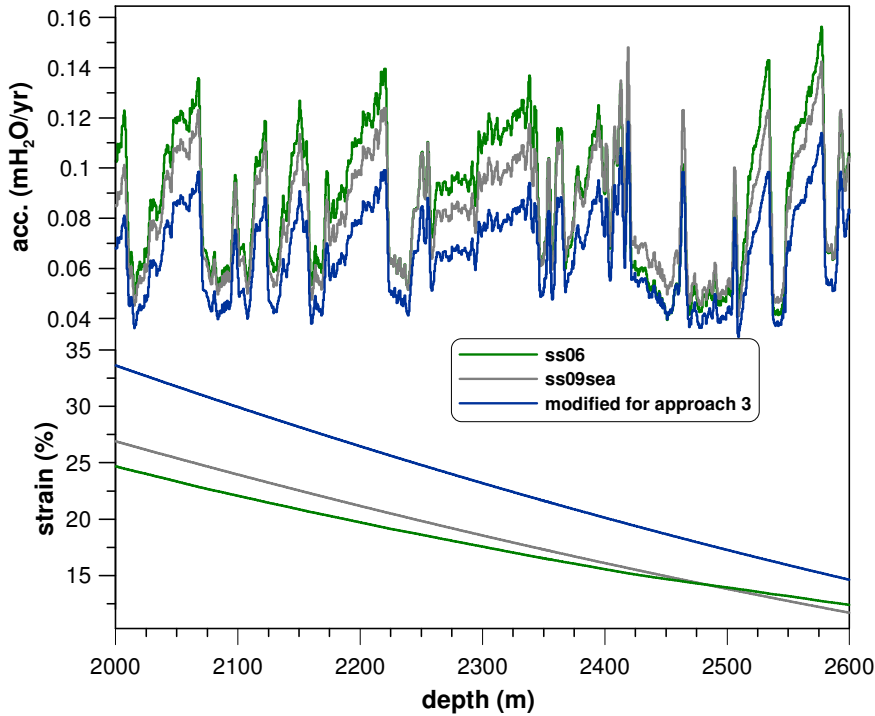
Figure 5.5: Comparison of the parameterisations of the accumulation rate and the ice thinning (strain) of the NorthGRIP age scales ss09sea (grey line) and ss06 (green line). Additionally modified accumulation rate scenario (ss09sea - 20%) and strain (ss09sea + 25%) used for the calculations in approach 3 are plotted (blue line).

simulations). For every time window 200 fits were performed. For each fitting procedure the $\delta^{15}N$ data was randomly modified by a Gaussian distributed standard error of $\pm 0.02^0/_{00}$. The model matches the data within this error range.

The result of this fitting procedure can be seen in Figure 5.6. The timing as well as the amplitudes of abrupt changes matches excellent. However, obviously the modelled $\delta^{15}N$ values are significantly higher $(0.07–0.1^0/_{00}$ than the measurements. This could be the result of a pronounced convective zone, that would reduce the diffusive column height (DCH = LID - convective zone) and hence the gravitational enrichment according to eq. 5.1. In order to explain an offset of $0.1^0/_{00}$, a convective zone of 20 m would be needed. For present-day conditions at Greenland, convective zones are inexistent or rather small (<5 m) [27, 46]. However, during glacial times convective zones could be significantly larger, e.g. due to increased wind pumping, lower accumulation rates associated with lower temperatures [13]. The Antarctic sites of Dome Fuji and Vostok have convective zones between 8–12 m. Severinghaus et al. [48] reported an Antarctic site were a deep (20 m) convective zone exists. As a result of the lack of winter accumulation deep cracks are formed in the firn. But, regarding the higher accumulation and temperatures in Greenland, convective zones of 20 m or more are very unlikely, even during glacials. A disagreement between data and model during glacials has been observed for other ice core as well. Measured $\delta^{15}N$ values at nearly all Antarctic sites are lower as predicted by the models. Additionally Schwander et

al. [47] found a similar behaviour for the Greenland cores GRIP and GISP2. On the other hand, two newer studies were able to model δ^{15}N properly at some parts of the GISP2 and GRIP cores [22, 33] assuming a small convective zone of 2 to 5 m.
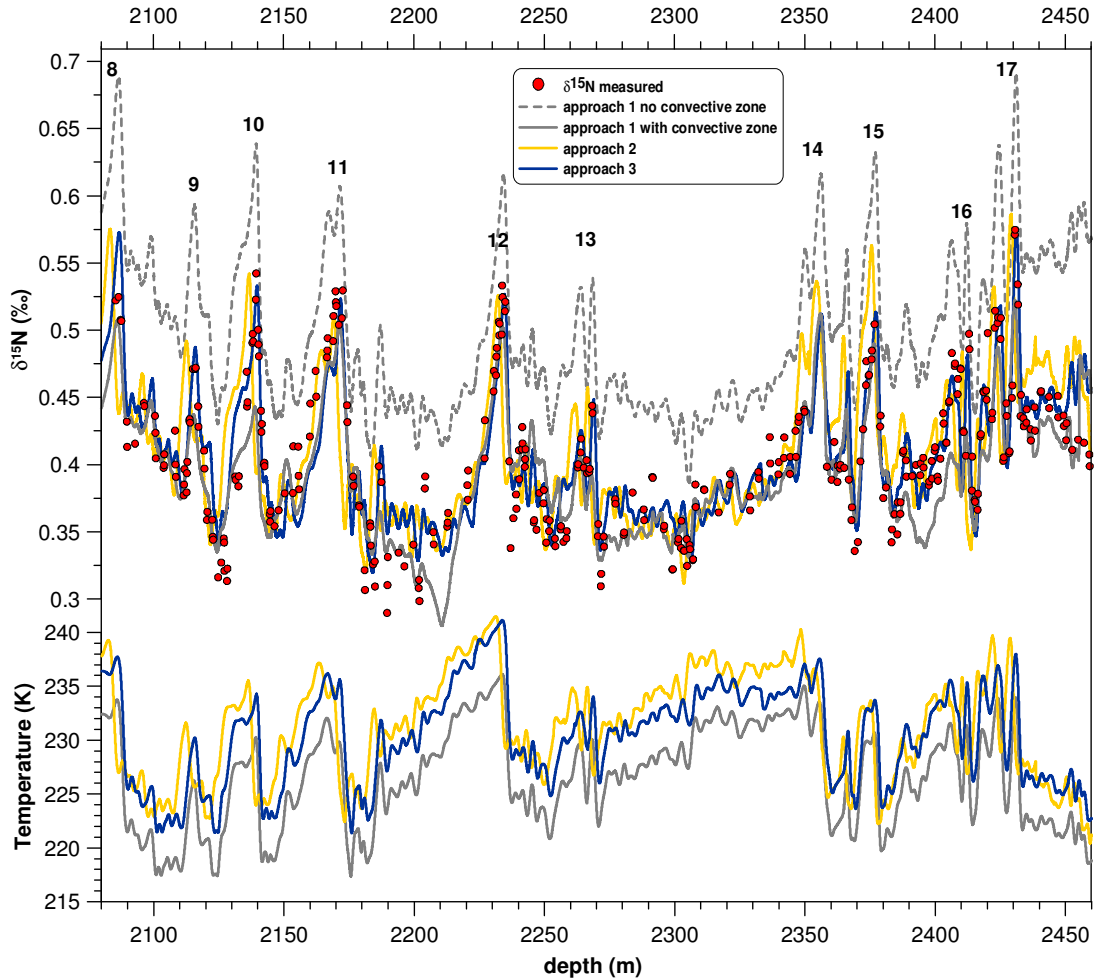
Figure 5.6: Top panel: δ^{15}N measurements (red dots) and firn model calculations versus ice depth. Bottom panel: Surface temperature evolution used as model input. The different approaches are described in the text.

An independent verification of the model findings can be done using the Δdepth. The Δdepth is the depth difference between an event recording in the gas phase, as δ^{15}N peak, and in the ice phase, as δ^{18}O$_{\text{ice}}$ peak. It depends on the LID at the time of bubble inclusion, and on the thinning of the ice with depth. From the age scale model we know the thinning function. Hence we are able to recalculate past LID. LID determined by the model, and the LID recalculated from Δdepth measurements agree within the error of the Δdepth calculation (Figure 5.7).

If the offset is interpreted as a convective zone, we have to correct the modelled δ^{15}N data. The gravitational enrichment is reduced by the offset. This leads to a perfect matching of
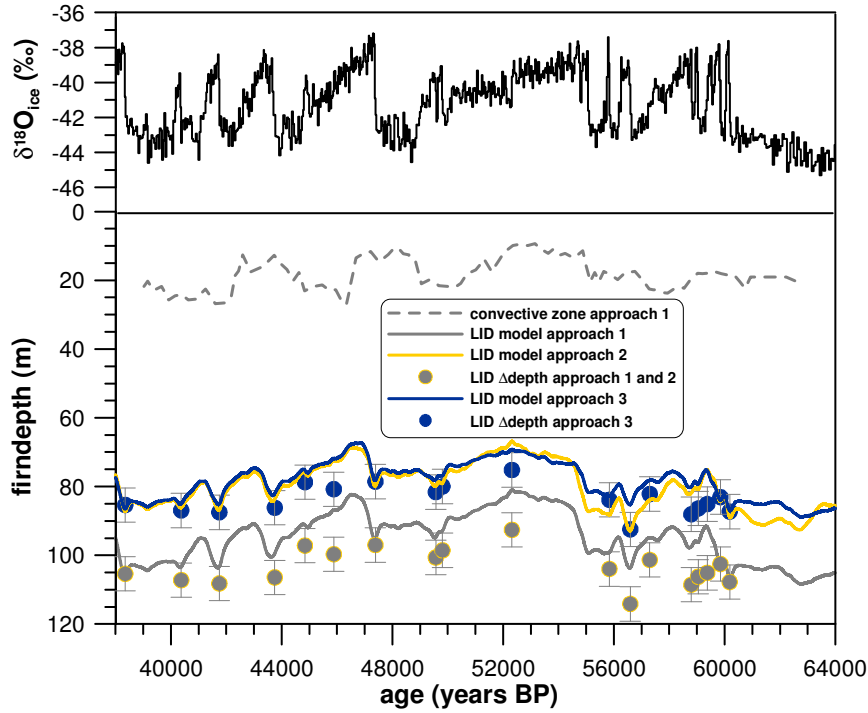
Figure 5.7: Top panel: $\delta^{18}O_{ice}$ of NorthGRIP on the ss09sea age scale. Bottom panel: Lock in depths (LID) for the different approaches determined by the firn densification model (solid lines), and calculated from Ddepth measurements using the ice thinning function (dots). The dashed line shows the size of the convective zone as calculated in approach 1.

model and data. However, by doing this a reduced ΔT has to be used for the for the thermal diffusion effect. At a depth of 10–20 m surface temperature signal is smoothed, reducing the thermal signal recorded in the nitrogen isotopes. The transfer of heat by vapour movement with the air flow is not able to level out the firn temperature to depth of 10 m or more [13]. The result of this correction is a reduction of the modelled $\delta^{15}N$ values, as shown in Figure 5.6. Short DO events are more affected by the smoothing process than longer ones. Though the depth of the convective zone accounts for only about 10–20% of the porous firn column, the temperature gradient is reduced by as much as 40%. In order to match the measured $\delta^{15}N$ data with the model, we would have to increase the surface temperature changes by up to 40% accordingly. Consequently, temperature changes for short events would become larger than for the long events. Such a scenario is very unlikely. All the more, Landais et al. [33] found a 12°C temperature change for DO 12 on the GRIP ice core, using the $\delta^{15}N_{excess}$ method, which agrees nicely with value we found in the uncorrected temperature scenario. An alternative explanation of the offset could be by an enlarged non-diffusive zone instead of a convective zone (Figure 5.4). A non-diffusive zone can be caused by inhomogeneities in the firn structure, due to different densities of summer and winter layers, as well as by crusts and melt-layers. Dense layers can cause a complete sealing of the firn column at depths far above the level where the mean firn diffusivity reaches zero values. Such layers would reduce the DCH. The model does account for a non-diffusive zone using empirical relations between firn density, open porosity, tortuosity and diffusivity [37, 46, 47]. Possible effects of layering

are not incorporated in the model. However, for glacial conditions an increased layering is very unlikely, since temperatures were much colder, accumulation rates were lower and winter precipitation was nearly absent [57]. Such conditions lead to a more homogeneous density structure of the firn, what contradicts the scenario of a larger non-diffusive zone.

Approach 2

From our calculations for approach 1 we found a clear anti-correlation between the offset and a. To calculate the temperature for approach 1, we assumed a linear relation of temperature and $\delta^{18}O_{ice}$: $T = \delta^{18}O_{ice}\ \alpha^{-1} + \beta$, where β was constrained by recent values for $\delta^{18}O_{ice}$ and temperature. The anti-correlation of the offset and α could be a result of this constraint. Hence, another way to circumvent the offset could be a shift in the absolute temperature. A 3.5°C mean temperature increase, reduces the DCH by 10 m and $\delta^{15}N$ by 0.05‰, respectively. Thus, the offset can be translated into an additional temperature shift. As a result of this offset corrected temperature scenario (Figure 5.6) the vertical offset indeed disappears, but now we have a disagreement in the timing between model and data. This timing problem is nicely documented in the Δdepth calculations (Figure 5.7), which disagree completely for the 2. approach.

Hence it is not possible to find a realistic temperature scenario with our model by using the accumulation rates of the ss09sea age scale model. The same calculation can be done with the ss06 age scale with the same conclusion. Therefore, possibly the parameterisation of the accumulation rates with $\delta^{18}O_{ice}$ is wrong for the observed time period.

Approach 3

The accumulation rate depends on temperature. In the parameterisation used in the age scale model, the accumulation rate is calculated from Approach 2: (corrected by the changing $\delta^{18}O$ of seawater), using an empirical relation based on measurements form various sites in Greenland [16, 19]. This relation describes recent climatic conditions. Hence, using the same relation for glacial conditions can only give a rough estimate of the accumulation rates at these times. Accumulation rates could likely be different. But, they can not be varied arbitrary, since otherwise the age scale of the ice core, which is constrained independently, changes. One way to avoid age scale conflicts is to change both, the accumulation rate and the ice thinning function, since the age scale depends only on the product of accumulation and thinning. Another way is to change only the slope of the accumulation to $\delta^{18}O$ dependency, but not the total amount of accumulation over a certain time period. Increasing the slope then corresponds to higher accumulation during warm times and lower accumulation during cold times. Thus, it will stretch and compress the age scale in the short term, but it will not affect it in the long term. The consequences of the latter accumulation modifications are documented in Figure 5.8. Three different accumulation scenarios (0.5×slope, 1×slope, 2×slope) are compared. The age scale is constrained at 35 kyr BP and at 65 kyr BP. The temperature scenario is calculated from $\delta^{18}O_{ice}$ using an α=0.4‰/°C. A reduction of the slope causes a stretching of the cold phases and a compression of the warm phases, respectively. The higher the slope, the longer the warm phases and the shorter the cold phases become. Hence, we can tune the length of the events if necessary. For example, the slight disagreement between data and model at the end of DO 10 (Figures 5.6 and 5.8) could

probably be solved by reducing the slope during this time interval. However, the offset in $\delta^{15}N$ between model and data remains nearly unchanged (about $0.1^0/_{00}$).
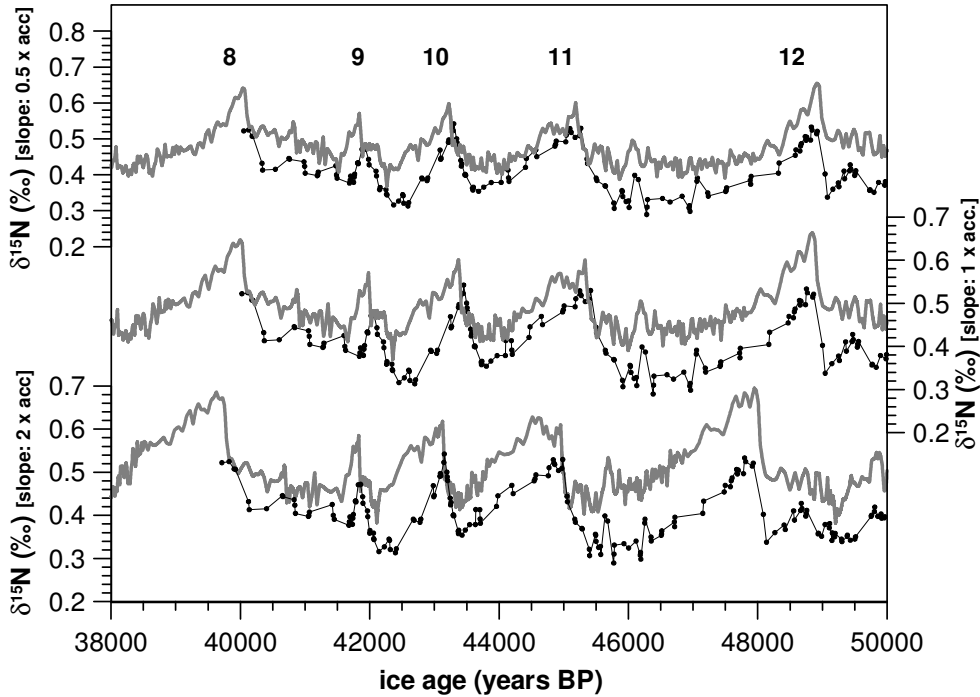
Figure 5.8: A comparison of three different accumulation scenarios ($0.5\times$slope, $1\times$slope, $2\times$slope) covering DO 8 to 12. Model output is plotted as grey lines, measurements as black lines and dots. The age scale was constrained at 35 kyr BP and at 65 kyr BP. The temperature scenario was calculated from $\delta^{18}O_{ice}$ using α $=0.4^0/_{00}$/K. It can be seen nicely, the higher the slope is, the longer the warm phases and the shorter the cold phases become.

The disagreement of the LID for approach 2 (Figure 5.6) between the model calculation and the Δdepth reconstruction is about 20% to 25% over the entire time period. The LID calculated from Δdepth is directly proportional to the thinning function. Hence, we have to reduce the ice thinning by about 25% as well to obtain a better agreement. In order to conserve the age scale, the accumulation rate must be adjusted accordingly. Results are shown in Figure 5.6. Accumulation is reduced by 20% compared to ss09sea (Figure 5.5). The temperature evolution bases on the Monte Carlo calculations from approach 1, but the absolute temperature is corrected by 4°C towards higher values. Furthermore some fine tuning has been done on the temperature evolution, in order to find the best fit (smallest square root deviations) between model and data. Now the agreement is excellent for both, the amplitudes as well as the timing of the events. Model matches the data within the analytical error range of $0.02^0/_{00}$. As expected, the LID of the model and the calculations by the Ddepth correspond within the uncertainty range of the Δdepth determination. These calculations are done under the assumption that the convective zone was zero.

Additional Information from Oxygen Isotopes

Parallel to $\delta^{15}N$ and $\delta^{36}Ar$ we determined $\delta^{18}O$ of O_2 on the NorthGRIP ice samples. From these measurements we can calculate the atmospheric oxygen isotope composition $\delta^{18}O_{atm}$, which can be compared with measurements from other ice cores from both hemispheres, since O_2 is well mixed in the atmosphere. $\delta^{18}O_{atm}$ is usually obtained using $\delta^{15}N$ to correct for gravitational effects. According to eq. 5.1 the gravitational enrichment of $\delta^{18}O$ is two times the enrichment of $\delta^{15}N$ ($\delta^{18}O_{atm} = \delta^{18}O - 2 \cdot \delta^{15}N$). This calculation underestimates $\delta^{18}O_{atm}$ at the time of rapid temperature changes, since the ratio of thermal diffusion factors of $\delta^{18}O$ and $\delta^{15}N$ is only 1.6, which is slightly lower than the effect of gravitation. However, the error is small compared to the analytical uncertainty of our measurements of $\pm 0.05^0/_{00}$, and can be neglected. The resulting $\delta^{18}O_{atm}$ record matches Vostok [31, 41, 53, 54] and GISP2 [2] $\delta^{18}O_{atm}$ data nicely (Figure 5.9) when the NorthGRIP age scale is shifted by 2000 ± 500 yr years towards younger ages. Note that the data is plotted on different age scales (NorthGRIP ss09sea ,Vostok GT4 [41], and GISP2 [39]) in Figure 5.9. These results are an independent constrain of the NorthGRIP ss09sea age scale. This shift of 2000 years has no impact on the conclusions of this paper, because it is more or less constant over the entire MIS 3.
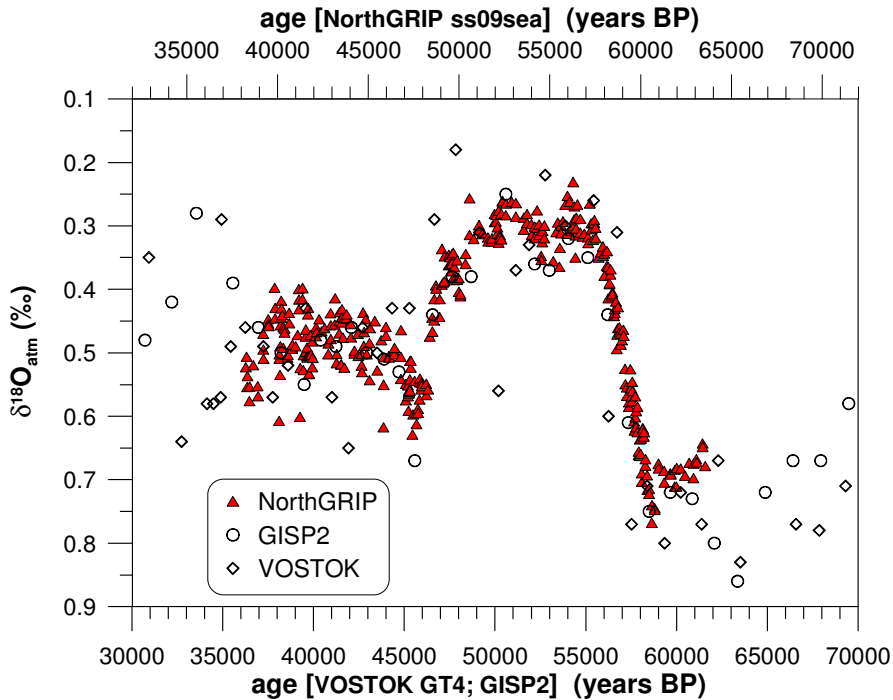
Figure 5.9: Atmospheric oxygen data $\delta^{18}O_{atm}$ from NorthGRIP (filled triangles) is plotted together with $\delta^{18}O_{atm}$ from the GISP2 (open circles) [2] and Vostok (open diamonds) [41, 53, 54] ice cores. The NorthGRIP $\delta^{18}O$ measurements were corrected for gravitational fractionation using $\delta^{15}N$. The different data is plotted on their individual age scales. The different age scales are offset, but not the $\delta^{18}O_{atm}$ values. After shifting the North GRIP ss09sea age scale by 2000 ± 500 yr, the data matches nicely within its error range of $\pm 0.05^0/_{00}$.

Bibliography

[1] M. A. Altabet, M. J. Higginson, and D. W. Murray. The effect of millenial-scale changes in Arabian Sea denitrification on atmospheric CO_2. *Nature*, 415:159–162, 2002.

[2] M. Bender, T. Sowers, M-L Dickson, J. Orchardo, P. Grootes, P. A. Mayewski, and D. A. Meese. Climate correlations between Greenland and Antarctica during the past 100000 years. *Nature*, 372:663–666, 1994.

[3] T. Blunier and E. Brook. Timing of millennial-scale climate change in Antarctica and Greenland during the last glacial period. *Science*, 291:109–112, 2001.

[4] G. C. Bond, W. Showers, M. Elliot, M. Evans, R. Lotti, I. Hajdas, G. Bonani, and S. Johnson. The North Atlantic's 1-2 kyr climate rhythm: Relation to Heinrich Events, Dansgaard/Oeschger Cycles and the Little Ice Age. In P. U. Clark, R. S. Webb, and L. D. Keigwin, editors, *Mechanisms of global climate change at millennial time scales*, volume 112 of *Geophysical Monograph*, pages 35–58. AGU, Washington, DC, 1999.

[5] Gerard Bond, Wallace Broecker, Sigfus Johnsen, Jerry McManus, Laurent Labeyrie, Jean Jouzel, and Georges Bonani. Correlations between climate records from North Atlantic sediments and Greenland ice. *Nature*, 365:143–147, 1993.

[6] E. A. Boyle. Cool tropical temperatures shift the global δ^{18}O-T relationship: An exlplanation for the ice core δ^{18}O-borehole thermometry conflict? *Geophysical Research Letters*, 3:273–276, 1997.

[7] E. J. Brook, S. Harder, J. Severinghaus, and M. Bender. Atmospheric methane and millennial-scale climate change. In P. U. Clark, R. S. Webb, and L. D. Keigwin, editors, *Mechanisms of global climate change at millennial time scale*, volume 112 of *Geophysical Monograph*, pages 165–175. AGU, Washington, DC, 1999.

[8] E J Brook, T Sowers, and J Orchardo. Rapid variations in atmospheric methane concentration during the past 110,000 years. *Science*, 273:1087–1091, 1996.

[9] I. Cacho, J. O. Grimalt, C. Pelejero, M. Canals, F.J. Sierro, J.A. Flores, and N. J. Shackleton. Dansgaard-Oeschger and Heinrich event imprints in Alboran Sea paleotemperatures. *Paleoceanography*, 14(6):668–705, 1999.

[10] J Chappell. Sea level changes forced ice breakouts in the last glacial cycle: new results from coral terraces. *Quaternary Science Reviews*, 21:1229–1240, 2001.

[11] J Chappellaz, J M Barnola, D Raynaud, Y S Korotkevich, and C Lorius. Ice-core record of atmospheric methane over the past 160'000 years. *Nature*, 345:127–131, 1990.

[12] J. Chappellaz, T Blunier, D Raynaud, J M Barnola, J Schwander, and B Stauffer. Synchronous changes in atmospheric CH_4 and Greenland climate between 40 and 8 kyr BP. *Nature*, 366:443–445, 1993.

[13] S C Colbeck. Air movement in snow due to windpumping. *J. Glaciol.*, 35(120):209–213, 1989.

[14] H. Craig, Y. Horibe, and T. Sowers. Gravitational separation of gases and isotopes in polar ice caps. *Science*, 242:1675–1678, 1988.

[15] Kurt M. Cuffey, Richard B. Alley, Pieter M. Grootes, John M. Bolzan, and Sridhar Anandakrishnan. Calibration of the δ^{18}O isotopic paleothermometer for central greenland, using borehole temperatures. *Journal of Glaciology*, 40(135):341–349, 1994.

[16] D Dahl-Jensen, S J Johnsen, C U Hammer, H B Clausen, and J Jouzel. Past accumulation rates derived from observed annual layers in the GRIP ice core from Summit, central Greenland. In W R Peltier, editor, *Ice in the Climate System*, pages 517–532. Springer-Verlag, Berlin, Heidelberg, 1993.

[17] W Dansgaard. Stable isotopes in precipitation. *Tellus*, 16:436–468, 1964.

[18] W. Dansgaard, S J Johnsen, H B Clausen, D Dahl-Jensen, N S Gundestrup, C U Hammer, C S Hvidberg, J P Steffensen, A E Sveinbjörnsdottir, J Jouzel, and G Bond. Evidence for general instability of past climate from a 250 kyr ice-core record. *Nature*, 364:218–220, 1993.

[19] W. Dansgaard, S.J. Johnsen, H.B. Clausen, and Jr. Langway, C.C. Time scale and ice accumulation during the last 125,000 years as indicated by the Greenland 18-O curve. *Geological Magazine*, 110:81–82, 1973.

[20] A. Dällenbach, B. Blunier, J. Flückiger, B. Stauffer, J. Chappellaz, and D. Raynaud. Changes in the atmospheric CH_4 gradient between Greenland and Antarctica during the last glacial and the transition to the Holocene. *Geophys. Res. Lett.*, 27(7):1005–1008, 2000.

[21] J. Flückiger, T. Blunier, B. Stauffer, J. Chappellaz, R. Spahni, K. Kawamura, J. Schwander, T. F. Stocker, and D. Dahl-Jensen. N_2O and CH_4 variations during the last galcial epoch: Insight into global processes. *Glob. Biogeochem. Cycles*, GB 1020:doi:10.1029/2003GB002122, 2004.

[22] C. Goujon, J. M. Barnola, and C. Ritz. Modeling the densification of polar firn including heat diffusion: Application to close-off characteristics and gas isotope fractionation for Antarctic and Greenland sites. *J. Geophys. Res*, 108:doi:10.1029/2002JD003319, 2003.

[23] A. Grachev and J. P. Severinghaus. Laboratory determination of thermal diffusion constants for $^{29}N_2/^{28}N_2$ in air at temperatures from -60 to 0°C for reconstruction of magnitudes of abrupt climate changes using the ice core fossil-air paleothermometer. *Geochimica et Cosmochimica Acta*, 67(3):345–360, 2003.

[24] S. R. Hemming. Heinrich Events: Massive late Pleistocene detritus layers of the North Atlantic and their global climate imprint. *Rev. Geophys*, 42(RG1005):doi:10.1029/2003RG000128, 2004.

[25] C. Huber and M. Leuenberger. Measurements of isotope and elemental ratios of air from polar ice with a new on-line extraction method. *Geochemistry Geophysics Geosystems*, in press, 2004.

[26] C. Huber, M. Leuenberger, and O. Zumbrunnen. Continuous extraction of trapped air from bubble ice or water for on-line determination of istotope ratios. *Analytical Chemistry*, 75(10):2324–2332, 2003.

[27] M. Hutterli and R. Röthlisberger. Atmosphere-to-snow-to-firn transport studies of HCHO at summit, Greenland. *Geophysical Research Letters*, 26:1691–1694, 1999.

[28] S. J. Johnsen, D. Dahl-Jensen, N. Gundestrup, J. P. Steffensen, H. B. Clausen, H. Miller, V. Masson-Delmotte, A. E. Sveinbjörnsdottir, and J. White. Oxygen isotope and palaeotemperature records from six Greenland ice-core stations: Camp Century, Dye3, GRIP, GISP2, renland and NorthGRIP. *Journal of Quaternary Science*, 16(4):299–307, 2001.

[29] Sigfus Johnsen, Dorthe Dahl-Jensen, Willi Dansgaard, and Niels Gundestrup. Greenland palaeotemperatures derived from GRIP bore hole temperature and ice core isotope profiles. *Tellus*, 47B:624–629, 1995.

[30] S.J. Johnsen and W. Dansgaard. On flow model dating of stable isotope records from Greenland ice cores. In E. Bard and W.S. Broecker, editors, *The Last Deglaciation: Absolute and Radiocarbon Chronologies. NATO ASI series*, volume I 2, pages 13–24. Springer Verlag, 1992.

[31] J Jouzel, N I Barkov, J M Barnola, M Bender, J Chappellaz, G Genthon, V M Kotlyakov, V Lipenkov, C Lorius, J R Petit, D Raynaud, G Raisbeck, C Ritz, T Sowers, M Stievenard, F Yiou, and P Yiou. Extending the Vostok ice-core record of palaeoclimate to the penultimate glacial period. *Nature*, 364:407–412, 1993.

[32] R. Knutti, J. Flückiger, T. F. Stocker, and A. Timmermann. Strong hemispheric coupling of glacial climate through freshwater discharge and ocean circulation. *Nature*, 430:851–856, 2004.

[33] A. Landais, N. Caillon, C. Goujon, A. Grachev, J.M. Barnola, J. Chappellaz, J. Jouzel, V. Masson-Delmotte, and M. Leuenberger. Quantification of rapid temperature change during DO event 12 and phasing with methane inferred from air isotopic measurements. *Earth and Planetary Science Letters*, 225:221–232, 2004.

[34] C. Lang, M. Leuenberger, J. Schwander, and S. Johnsen. 16°C rapid temperature variation in central Greenland 70000 years ago. *Science*, 286:934–937, 1999.

[35] M. C. Leuenberger, C. Lang, and J. Schwander. Delta 15N measurements as a calibration tool for the paleothermometer and gas-ice age differences: a case study for the 8200 B.P. event on GRIP ice. *Journal of Geophysical Research*, 104(D18):22163–22170, 1999.

[36] A. Mariotti. Atmospheric nitrogen is a reliable standard for natural 15N abundance measurements. *Nature*, 303:685–687, 1983.

[37] P Martinerie, V Y Lipenkov, D Raynaud, J Chappellaz, N I Barkov, and C Lorius. Air content paleo record in the vostok ice core (Antarctica): A mixed record of climatic and glaciological parameters. *J. Geophys. Res.*, 99:10565–10576, 1994.

[38] V. Masson-Delmotte, J. Jouzel, A. Landais, M. Stievenard, S. J. Johnsen, J. W. C. White, M. Werner, A. Sveinbjornsdottir, K. Fuhrer, and E. Cortijo. Rapid and slow reorganisation of the northern hemisphere hydrological cycle during the last glacial period as derived from the grip ice core deuterium-excess record. *Nature*, submitted 2004.

[39] D A Meese, A J Gow, R B Alley, P M Grootes, M Ram, K C Taylor, G A Zielinski, J F Bolzan, P A Mayewski, and E D Waddington. The GISP2 depth-age scale: Method and results. *J. Geophys. Res.*, 102(C12):26.411–26.423, 1997.

[40] NorthGRIP Members. High resolution climate record of the northern hemisphere reaching into the last glacial interglacial period. *Nature*, 431:147–151, 2004.

[41] J. R. Petit, J. Jouzel, D. Raynaud, N. I. Barkov, J.-M. Barmola, I. Basile, M. Bender, J. Chappellaz, M. Davis, G. Delaygue, M. Demotte, V. M. Kotlyakov, M. Legrand, V. Y. Lipenkov, C. Lorius, L. Pépin, C. Ritz, E. Saltzman, and M. Stievenard. Climate and atmospheric history of the past 420000 years from the Vostok ice core, Antarctica. *Nature*, 399:429–436, 1999.

[42] S. Rahmstorf. Ocean circulation and climate during the past 120,000 years. *Nature*, 419:207–214, 2002.

[43] J. P. Sachs and S. J. Lehman. Subtropical North Atlantic temperatures 60,000 to 30,000 years ago. *Science*, 286:756–759, 1999.

[44] Hartmut Schulz, Schmutz von Rad, and Helmut Erlenkeuser. Correlation between Arabian Sea and Greenland climate oscillations of the past 110,000 years. *Nature*, 393:54–57, 1998.

[45] J. Schwander. The transformation of snow to ice and the occlusion of gases. In H. Oeschger and C C Langway Jr., editors, *The Environmental Record in Glaciers and Ice Sheets*, pages 53–67. John Wiley, New York, 1989.

[46] J. Schwander, J M Barnola, C Andrié, M Leuenberger, A Ludin, D Raynaud, and B Stauffer. The age of the air in the firn and the ice at summit, Greenland. *J. Geophys. Res.*, 98:2831–2838, 1993.

[47] J. Schwander, T. Sowers, J-M Barnola, T. Blunier, B. Malaizé, and T. Fuchs. Age scale of the air in the summit ice: Implication for glacial-interglacial temperature change. *J. Geophys. Res.*, 102(D16):19483–19494, 1997.

[48] J. Severinghaus, M. Fahnestock, M. Albert, T. Scambos, and C. Shuman. Do deep convective zones exist in low-accumulation firn? (abstract). *Geophysical Research Abstracts*, 6:EGS04A–00821, 2004.

[49] J. P. Severinghaus and E. J. Brook. Abrupt climate change at the end of the last glacial period inferred from trapped air in polar ice. *Science*, 286:930–934, 1999.

[50] J. P. Severinghaus, A. Grachev, B. Luz, and N. Caillon. A method for precise measurement of argon 40/36 and krypton/argon ratios in trapped air in polar ice with applications to past firn thickness and abrupt climate change in Greenland and at siple dome, Antarctica. *Geochimica et Cosmochimica Acta*, 67(3):325–343, 2003.

[51] Jeffrey P Severinghaus, T Sowers, E J Brook, R B Alley, and M L Bender. Timing of abrupt climate change at the end of the Younger Dryas interval from thermally fractionated gases in polar ice. *Nature*, 391:141–146, 1998.

[52] N. J. Shackleton and M. A. Hall. Phase relationships between millenial-scale events 64,000-24,000 years ago. *Paleoceanography*, 15(565-569), 2000.

[53] T. Sowers, M. Bender, L. Labeyrie, D. Martinson, D. Raynaud, J.J. Pichon, and Y.S. Korotkevich. A 135.000-year Vostok-specmap common temporal framework. *Paleoceanography*, 8(6):737–766, 1993.

[54] Todd Sowers, Michael Bender, Dominique Raynaud, Y.S. Korotkevich, and Joe Orchardo. The δ^{18}O of atmospheric O_2 from air inclusions in the Vostok ice core: timing of CO_2 and ice volume changes during the penultimate deglaciation. *Paleoceanography*, 6(6):679–696, 1991.

[55] T. F. Stocker and O. Marchal. Abrupt climate change in the computer: is it real? *Proceeding of the US National Academy of Science*, 97(4):1362–1365, 2000.

[56] Y. J. Wang, H. Cheng, R. L. Edwards, Z. S. An, J. Y. Wu, C.-C. Shen, and J. A. Dorale. A high-resolution absolute-dated late pleistocene monsoon record from Hulu Cave, China. *Science*, 294:2345–2348, 2001.

[57] M. Werner, M. Heimann, and G. Hoffmann. Isotopic composition and origin of polar precipitation in present and glacial climate simulations. *Tellus*, 53B:53–71, 2001.

[58] Q. Zhuang, J. M. Melillo, D. W. Kicklighter, R. G. Prinn, A. D. McGuire, P. A. Steudler, B. S. Felzer, and S. Hu. Methane fluxes between terrestrial ecosystems and the atmosphere at northern high latitudes during the past century: A retrospective analysis with a process-based biogeochemistry model. *Global Biogeochemical Cycles*, 18(GB3010):doi: 10.1029/2004GB002239, 2004.

Appendix A

Data

A.1   North Greenland Ice Core Project (NorthGRIP)

On-line air measurements performed along the North Greenland Ice Core Project (North-GRIP) ice core. All measurements are expressed against atmospheric air. The measurements cover DO events 9–17. The gas age is based on the ss09sea ice timescale. It is obtained by adjusting the parameters of a dynamic firn densification and diffusion model in order to best fit the $\delta^{15}N$ data. $\delta^{15}N$ and $\delta^{18}O$ measurements are published, the rest is unpublished data. For details see section 5.2. The measurements are performed with the new improved on-line system (section 3.2). The maximal data resolution is about 3 cm. The measurements presented in this table are averages over 10–20 cm.

Bag	Depth (m)	$\delta^{15}N$ ($^0/_{00}$)	$\delta^{18}O$ ($^0/_{00}$)	$\delta^{17}O$ ($^0/_{00}$)	$\delta^{36}Ar$ ($^0/_{00}$)	$\delta O_2/N_2$ ($^0/_{00}$)	$\delta Ar/N_2$ ($^0/_{00}$)	$\delta Ar/O_2$ ($^0/_{00}$)	Gas Age (yr BP)
3792	2085.50	0.522	1.567	0.818	-1.75	-21.2	-10.1	11.1	38'256
3794	2086.60	0.525	1.556	0.824	-1.90	-11.1	1.5	12.6	38'296
3796	2087.43	0.508	1.569	0.801	-1.71	-20.0	-8.3	11.7	38'329
3796	2087.66	0.507	1.551	0.777	-1.71	-22.3	-12.8	9.5	38'339
3800	2089.79	0.432	1.440	0.742	-1.53	-14.2	-1.1	13.1	38'456
3800	2089.91	0.413	1.380	0.716	-1.53	-12.9	-2.1	10.8	38'464
3806	2092.94	0.416	1.351	0.683	-1.71	-10.6	2.0	12.7	38'659
3812	2096.34	0.446	1.444	0.789	-1.53	-4.3	9.1	13.4	38'916
3812	2096.49	0.444	1.456	0.783	-1.54	-8.8	4.6	13.5	38'927
3820	2100.60	0.436	1.342	0.720	-1.58	-8.3	3.6	11.9	39'206
3820	2100.75	0.424	1.342	0.679	-1.69	-11.3	1.1	12.5	39'222
3820	2100.89	0.405	1.318	0.679	-1.52	-27.3	-17.2	10.2	39'235
3826	2103.89	0.398	1.242	0.652	-1.53	-9.0	2.7	11.8	39'503
3826	2104.02	0.400	1.253	0.644	-1.57	-13.1	-0.4	12.8	39'514
3826	2104.15	0.408	1.273	0.641	-1.57	-8.8	3.4	12.2	39'523
3834	2108.30	0.425	1.248	0.692	-1.40	8.1	21.5	13.7	39'848
3834	2108.45	0.400	1.246	0.673	-1.34	-7.5	2.2	10.1	39'860
3834	2108.60	0.391	1.211	0.652	-1.30	-14.0	-4.5	10.1	39'872
3840	2111.60	0.377	1.362	0.778	-1.79	-52.1	-44.0	8.1	40'086
3840	2111.75	0.385	1.280	0.740	-1.84	-43.0	-34.8	8.2	40'095

<div align="center">Continuation on next page</div>

Data from the NorthGRIP ice core – continuation

Bag	Depth (m)	$\delta^{15}N$ $(^0\!/_{00})$	$\delta^{18}O$ $(^0\!/_{00})$	$\delta^{17}O$ $(^0\!/_{00})$	$\delta^{36}Ar$ $(^0\!/_{00})$	$\delta O_2/N_2$ $(^0\!/_{00})$	$\delta Ar/N_2$ $(^0\!/_{00})$	$\delta Ar/O_2$ $(^0\!/_{00})$	Gas Age (yr BP)
3840	2111.90	0.397	1.296	0.721	-1.79	-28.5	-19.9	8.7	40'104
3842	2112.70	0.379	1.294	0.720	-1.54	-31.9	-22.5	9.8	40'148
3842	2112.85	0.394	1.277	0.703	-1.60	-29.0	-20.8	8.6	40'156
3842	2113.00	0.402	1.261	0.710	-1.55	-24.1	-15.6	9.2	40'164
3844	2113.79	0.433	1.310	0.712	-1.80	-32.5	-23.3	9.6	40'202
3844	2113.92	0.434	1.286	0.738	-1.76	-33.4	-25.7	8.3	40'208
3844	2114.05	0.431	1.292	0.730	-1.76	-27.6	-19.4	8.9	40'215
3846	2115.12	0.471	1.383	0.755	-1.96	-29.6	-20.1	9.7	40'265
3848	2116.01	0.471	1.434	0.763	-1.81	-29.1	-19.1	10.0	40'313
3848	2116.19	0.472	1.403	0.723	-1.93	-16.9	-5.4	11.6	40'322
3850	2117.14	0.443	1.349	0.727	-1.86	-24.2	-11.9	12.4	40'382
3850	2117.30	0.428	1.324	0.735	-1.85	-26.1	-14.8	11.5	40'392
3854	2119.42	0.410	1.328	0.743	-1.71	-26.0	-16.4	9.7	40'549
3854	2119.58	0.397	1.297	0.705	-1.58	-25.2	-17.7	7.6	40'562
3856	2120.54	0.359	1.155	0.610	-1.22	-20.5	-12.9	7.6	40'638
3856	2120.70	0.365	1.183	0.646	-1.19	-27.9	-20.8	7.1	40'649
3860	2122.60	0.359	1.208	0.694	-0.93	-33.7	-26.9	6.8	40'797
3860	2122.75	0.346	1.186	0.688	-0.83	-34.3	-28.9	5.4	40'810
3860	2122.90	0.344	1.175	0.664	-0.85	-33.1	-27.8	5.3	40'822
3864	2124.83	0.316	1.122	0.605	-0.93	-29.0	-23.9	5.2	40'998
3866	2126.04	0.327	1.126	0.595	-0.99	-24.2	-17.7	6.5	41'106
3868	2126.99	0.345	1.089	0.586	-1.16	-6.3	1.7	8.0	41'172
3868	2127.12	0.342	1.100	0.590	-1.19	-4.5	3.7	8.2	41'180
3868	2127.24	0.321	1.073	0.569	-1.09	-4.7	3.1	7.8	41'188
3870	2128.24	0.313	1.227	0.688	-0.83	-37.8	-29.8	7.8	41'242
3870	2128.40	0.323	1.169	0.659	-0.90	-26.1	-18.6	7.5	41'250
3876	2131.40	0.391	1.198	0.620	-1.31	-29.8	-24.8	5.0	41'375
3876	2131.54	0.389	1.175	0.621	-1.29	-28.9	-24.8	4.0	41'382
3878	2132.62	0.384	1.295	0.726	-1.29	-34.2	-27.4	6.7	41'424
3878	2132.79	0.391	1.286	0.718	-1.35	-27.5	-20.6	6.8	41'431
3884	2135.80	0.469	1.412	0.811	-1.59	-37.3	-28.3	9.1	41'546
3884	2135.95	0.443	1.385	0.785	-1.37	-37.2	-29.8	7.4	41'552
3884	2136.09	0.446	1.356	0.748	-1.58	-31.6	-23.3	8.3	41'557
3888	2138.00	0.491	1.486	0.797	-1.65	-33.3	-23.3	10.1	41'627
3888	2138.15	0.497	1.486	0.775	-1.71	-28.5	-17.9	10.7	41'634
3888	2138.30	0.492	1.491	0.776	-1.73	-22.5	-11.4	11.2	41'640
3890	2139.29	0.523	1.485	0.765	-1.78	-27.2	-15.7	11.8	41'684
3890	2139.41	0.542	1.514	0.801	-1.83	-30.7	-17.9	13.1	41'691
3892	2140.19	0.500	1.534	0.853	-1.60	-42.0	-31.4	10.7	41'737
3892	2140.32	0.489	1.485	0.819	-1.65	-31.5	-21.1	10.4	41'746
3892	2140.45	0.481	1.494	0.811	-1.62	-35.6	-25.4	10.3	41'755
3894	2141.30	0.440	1.352	0.745	-1.48	-29.6	-19.4	10.2	41'820
3894	2141.45	0.424	1.354	0.775	-1.44	-34.5	-24.3	10.2	41'833
3894	2141.60	0.430	1.363	0.714	-1.49	-31.7	-20.5	11.2	41'848
3896	2142.39	0.400	1.323	0.725	-1.38	-34.8	-25.0	9.8	41'917
3896	2142.53	0.401	1.284	0.658	-1.67	-29.8	-20.3	9.5	41'929
3896	2142.67	0.399	1.305	0.675	-1.58	-24.6	-14.4	10.3	41'941
3900	2144.62	0.363	1.200	0.665	-1.49	-31.2	-22.6	8.8	42'120

Continuation on next page

Data from the NorthGRIP ice core – continuation

Bag	Depth (m)	$\delta^{15}N$ ($^0/_{00}$)	$\delta^{18}O$ ($^0/_{00}$)	$\delta^{17}O$ ($^0/_{00}$)	$\delta^{36}Ar$ ($^0/_{00}$)	$\delta O_2/N_2$ ($^0/_{00}$)	$\delta Ar/N_2$ ($^0/_{00}$)	$\delta Ar/O_2$ ($^0/_{00}$)	Gas Age (yr BP)
3900	2144.76	0.358	1.175	0.645	-1.42	-27.2	-20.3	7.0	42'132
3900	2144.90	0.365	1.199	0.648	-1.46	-31.1	-23.3	7.8	42'146
3903	2146.46	0.354	1.155	0.627	-1.66	-18.8	-10.2	8.5	42'292
3906	2147.90	0.365	1.189	0.665	-1.37	-10.0	1.1	11.1	42'430
3910	2150.40	0.379	1.218	0.633	-1.34	-16.5	-5.0	11.6	42'603
3916	2153.53	0.379	1.260	0.664	-1.32	-27.3	-17.8	9.6	42'799
3916	2153.69	0.414	1.312	0.684	-1.43	-22.2	-11.7	10.5	42'809
3920	2155.59	0.413	1.264	0.749	-1.37	-17.9	-6.2	11.8	42'926
3920	2155.74	0.392	1.240	0.700	-1.35	-18.1	-7.2	10.9	42'934
3920	2155.89	0.382	1.242	0.701	-1.22	-19.6	-10.0	9.6	42'942
3928	2160.05	0.421	1.297	0.690	-1.62	-18.3	-6.7	11.8	43'155
3928	2160.23	0.445	1.305	0.692	-1.81	-11.7	2.2	14.2	43'164
3932	2162.27	0.470	1.455	0.828	-1.85	-18.8	2.8	21.4	43'256
3932	2162.51	0.450	1.403	0.739	-1.73	-6.4	10.8	16.5	43'265
3940	2166.60	0.480	1.429	0.780	-1.62	-17.7	-4.3	13.6	43'408
3940	2166.75	0.485	1.419	0.751	-1.74	-14.2	-0.9	13.4	43'413
3940	2166.89	0.494	1.424	0.751	-1.84	-18.1	-5.8	12.4	43'418
3944	2168.98	0.492	1.502	0.826	-1.86	-18.0	-2.9	15.1	43'502
3944	2169.10	0.511	1.540	0.873	-1.91	-15.2	2.0	17.4	43'508
3946	2169.90	0.529	1.489	0.790	-1.78	-12.8	1.6	14.5	43'544
3946	2170.05	0.521	1.493	0.844	-1.74	-19.8	-6.0	13.9	43'550
3946	2170.20	0.518	1.480	0.858	-1.76	-22.8	-10.7	12.2	43'557
3948	2171.15	0.504	1.484	0.827	-1.73	-17.7	-3.0	14.2	43'602
3950	2172.33	0.509	1.464	0.803	-1.74	-17.8	-5.4	12.5	43'661
3951	2172.66	0.530	1.583	0.868	-2.02	-16.0	5.2	21.5	43'680
3954	2174.31	0.444	1.334	0.727	-1.64	-12.2	-0.1	12.2	43'794
3954	2174.45	0.432	1.303	0.703	-1.57	-13.2	-1.3	12.0	43'808
3958	2176.64	0.391	1.237	0.723	-1.27	-16.9	-5.6	11.3	44'032
3958	2176.83	0.384	1.244	0.672	-1.47	-11.2	0.7	11.9	44'050
3962	2178.89	0.370	1.241	0.704	-1.14	-31.2	-20.5	10.8	44'228
3962	2179.01	0.369	1.234	0.689	-1.20	-27.5	-16.7	10.9	44'238
3966	2181.08	0.321	1.113	0.567	-1.34	-22.5	-14.3	8.2	44'438
3966	2181.20	0.307	1.118	0.569	-1.29	-22.1	-13.4	8.7	44'451
3970	2183.17	0.356	1.215	0.693	-1.17	-27.4	-16.5	11.0	44'629
3970	2183.29	0.354	1.228	0.681	-1.17	-27.8	-17.0	10.9	44'639
3970	2183.41	0.340	1.210	0.672	-1.18	-30.5	-19.9	10.7	44'649
3972	2184.27	0.326	1.088	0.550	-1.19	-21.1	-12.6	8.5	44'717
3973	2184.93	0.328	1.145	0.632	-1.10	-16.7	-7.3	9.4	44'762
3973	2185.05	0.309	1.086	0.592	-0.99	-21.9	-13.2	8.7	44'770
3976	2186.53	0.399	1.245	0.601	-1.50	-19.8	-5.7	14.1	44'858
3978	2187.48	0.387	1.276	0.703	-1.23	-30.0	-18.0	11.9	44'915
3982	2189.69	0.290	1.122	0.688	-0.86	-37.7	-32.3	5.3	45'067
3982	2189.82	0.310	1.105	0.667	-0.95	-20.9	-14.3	6.5	45'076
3982	2189.95	0.331	1.124	0.647	-1.08	-10.9	-1.7	9.2	45'084
3990	2194.12	0.334	1.119	0.546	-1.19	-21.0	-13.7	7.4	45'357
3994	2196.32	0.324	1.176	0.665	-0.83	-34.7	-28.1	6.6	45'493
4000	2199.80	0.340	1.161	0.592	-1.32	-14.5	-6.5	8.2	45'711
4004	2201.80	0.308	1.233	0.778	-0.71	-47.1	-43.1	4.2	45'837

Continuation on next page

Data from the NorthGRIP ice core – continuation

Bag	Depth (m)	δ^{15}N ($^0/_{00}$)	δ^{18}O ($^0/_{00}$)	δ^{17}O ($^0/_{00}$)	δ^{36}Ar ($^0/_{00}$)	$\delta O_2/N_2$ ($^0/_{00}$)	$\delta Ar/N_2$ ($^0/_{00}$)	$\delta Ar/O_2$ ($^0/_{00}$)	Gas Age (yr BP)
4004	2201.95	0.314	1.179	0.716	-0.96	-40.5	-36.9	4.1	45'846
4004	2202.10	0.298	1.104	0.624	-1.14	-34.4	-29.6	5.6	45'854
4008	2204.18	0.382	1.224	0.626	-1.25	-13.6	-4.3	9.3	45'964
4008	2204.31	0.391	1.255	0.658	-1.27	-19.8	-11.0	8.8	45'971
4014	2207.44	0.350	1.205	0.706	-1.15	-34.0	-28.1	6.2	46'138
4014	2207.59	0.341	1.189	0.685	-1.18	-26.3	-19.4	7.3	46'146
4024	2212.80	0.354	1.205	0.638	-1.38	-22.2	-14.3	7.9	46'428
4024	2212.95	0.357	1.216	0.690	-1.28	-25.1	-17.5	7.6	46'437
4024	2213.10	0.364	1.220	0.676	-1.32	-25.1	-17.7	7.5	46'444
4038	2220.50	0.385	1.311	0.743	-1.20	-38.0	-32.8	5.2	46'784
4038	2220.65	0.374	1.254	0.682	-1.33	-26.5	-19.7	6.8	46'791
4038	2220.80	0.396	1.255	0.643	-1.43	-17.9	-11.8	6.0	46'797
4050	2227.09	0.405	1.384	0.801	-1.30	-33.5	-24.7	9.0	47'069
4050	2227.23	0.433	1.415	0.794	-1.60	-23.1	-13.6	9.5	47'074
4056	2230.56	0.454	1.477	0.806	-1.60	-33.3	-22.7	10.8	47'184
4056	2230.70	0.470	1.490	0.800	-1.54	-29.9	-19.7	10.3	47'189
4058	2231.50	0.466	1.524	0.825	-1.55	-29.6	-17.4	12.3	47'215
4058	2231.65	0.480	1.524	0.832	-1.48	-31.4	-20.4	11.2	47'219
4058	2231.80	0.487	1.538	0.826	-1.59	-23.1	-10.1	13.1	47'224
4060	2232.60	0.506	1.573	0.840	-1.65	-31.5	-20.0	11.7	47'249
4060	2232.75	0.496	1.551	0.805	-1.70	-26.3	-13.6	12.8	47'254
4060	2232.89	0.505	1.572	0.834	-1.66	-27.9	-15.5	12.4	47'260
4062	2233.70	0.497	1.553	0.818	-1.62	-29.2	-18.2	11.1	47'288
4062	2233.85	0.533	1.608	0.858	-1.73	-28.7	-16.7	12.1	47'294
4062	2234.00	0.525	1.562	0.801	-1.85	-11.8	2.2	14.0	47'300
4064	2234.92	0.514	1.552	0.825	-1.76	-28.0	-16.5	11.6	47'343
4064	2235.05	0.521	1.555	0.810	-1.77	-24.0	-14.2	9.8	47'349
4067	2236.61	0.402	1.434	0.758	-1.38	-28.3	-16.6	11.9	47'440
4068	2237.08	0.338	1.272	0.712	-1.18	-38.3	-31.6	6.8	47'472
4070	2238.16	0.360	1.265	0.668	-1.22	-15.3	-7.5	7.8	47'556
4072	2239.19	0.378	1.351	0.727	-1.37	-30.4	-19.7	10.8	47'640
4072	2239.31	0.367	1.347	0.748	-1.31	-27.1	-17.4	9.6	47'651
4074	2240.29	0.411	1.409	0.765	-1.41	-27.3	-15.5	12.1	47'734
4074	2240.42	0.389	1.373	0.784	-1.23	-29.4	-19.8	9.9	47'745
4076	2241.43	0.411	1.396	0.768	-1.49	-26.7	-14.1	12.8	47'828
4076	2241.56	0.428	1.402	0.758	-1.70	-23.2	-10.1	13.3	47'838
4076	2241.69	0.416	1.372	0.740	-1.62	-24.7	-13.3	11.6	47'849
4078	2242.53	0.398	1.354	0.727	-1.39	-24.9	-15.5	9.5	47'915
4078	2242.66	0.404	1.356	0.718	-1.47	-24.6	-14.5	10.2	47'925
4078	2242.79	0.411	1.375	0.732	-1.44	-29.4	-18.8	10.8	47'936
4084	2245.99	0.357	1.263	0.755	-1.31	-35.6	-27.8	7.9	48'189
4084	2246.11	0.359	1.284	0.755	-1.20	-38.8	-31.8	7.0	48'199
4086	2247.03	0.352	1.261	0.718	-1.29	-14.6	-4.7	9.9	48'285
4088	2248.13	0.379	1.233	0.653	-1.47	-15.8	-6.6	9.2	48'388
4091	2249.70	0.371	1.187	0.674	-1.40	-18.4	-7.9	10.5	48'524
4091	2249.85	0.381	1.229	0.701	-1.43	-19.5	-7.9	11.6	48'536
4093	2250.80	0.342	1.133	0.620	-1.19	-25.5	-17.6	7.9	48'618
4093	2250.95	0.359	1.134	0.634	-1.22	-28.8	-22.7	6.1	48'630

Continuation on next page

Data from the NorthGRIP ice core – continuation

Bag	Depth (m)	$\delta^{15}N$ (⁰/₀₀)	$\delta^{18}O$ (⁰/₀₀)	$\delta^{17}O$ (⁰/₀₀)	$\delta^{36}Ar$ (⁰/₀₀)	$\delta O_2/N_2$ (⁰/₀₀)	$\delta Ar/N_2$ (⁰/₀₀)	$\delta Ar/O_2$ (⁰/₀₀)	Gas Age (yr BP)
4095	2251.90	0.350	1.095	0.586	-1.35	-1.5	10.2	11.7	48'718
4095	2252.05	0.358	1.115	0.596	-1.34	-18.4	-8.9	9.4	48'732
4099	2254.10	0.345	1.133	0.644	-1.10	-30.7	-22.2	8.5	48'919
4099	2254.24	0.339	1.094	0.622	-1.10	-30.0	-23.2	6.8	48'931
4103	2256.29	0.352	1.040	0.538	-1.48	-31.1	-24.5	6.5	49'051
4103	2256.41	0.354	1.101	0.613	-1.39	-22.1	-14.0	8.0	49'058
4105	2257.39	0.342	1.074	0.583	-1.23	-20.7	-14.2	6.5	49'117
4107	2258.50	0.345	1.078	0.578	-1.39	-25.3	-16.6	8.6	49'193
4107	2258.65	0.350	1.049	0.573	-1.39	-25.4	-18.3	7.0	49'203
4115	2262.90	0.398	1.158	0.649	-1.50	-28.3	-18.9	9.4	49'434
4115	2263.06	0.400	1.146	0.619	-1.63	-19.3	-8.8	10.5	49'441
4117	2264.00	0.409	1.167	0.626	-1.51	-21.1	-12.2	8.9	49'488
4117	2264.14	0.419	1.200	0.674	-1.53	-27.1	-17.1	10.0	49'495
4119	2265.19	0.398	1.167	0.638	-1.43	-28.9	-20.2	8.6	49'551
4121	2266.26	0.403	1.166	0.640	-1.55	-37.6	-30.4	7.1	49'613
4121	2266.43	0.393	1.131	0.610	-1.60	-22.7	-14.5	8.1	49'623
4123	2267.30	0.394	1.171	0.645	-1.47	-32.4	-23.7	8.7	49'673
4123	2267.44	0.397	1.136	0.590	-1.61	-18.8	-8.4	10.3	49'682
4125	2268.40	0.444	1.273	0.731	-1.45	-30.0	-20.1	9.9	49'735
4125	2268.55	0.438	1.241	0.664	-1.55	-25.7	-15.9	9.9	49'744
4129	2270.60	0.347	1.078	0.594	-1.23	-21.8	-11.5	10.3	49'891
4129	2270.74	0.356	1.066	0.595	-1.34	-18.4	-9.7	8.6	49'903
4131	2271.70	0.309	1.002	0.565	-1.24	-45.6	-41.5	4.2	49'982
4131	2271.86	0.319	1.041	0.590	-1.09	-37.9	-32.4	5.6	49'994
4133	2272.80	0.346	1.104	0.674	-1.00	-27.9	-19.6	8.3	50'066
4133	2272.94	0.339	1.085	0.662	-1.19	-24.8	-14.7	10.1	50'076
4141	2277.21	0.374	1.108	0.608	-1.39	-22.5	-10.6	11.9	50'358
4141	2277.35	0.371	1.086	0.577	-1.35	-19.7	-9.6	10.1	50'366
4147	2280.50	0.348	0.952	0.544	-1.43	-24.5	-15.3	9.1	50'573
4147	2280.65	0.349	1.013	0.573	-1.41	-17.7	-7.8	9.9	50'582
4153	2283.91	0.379	1.079	0.632	-1.27	-30.7	-21.6	9.0	50'805
4161	2288.20	0.367	1.040	0.561	-1.44	-27.7	-18.2	9.5	51'088
4161	2288.35	0.359	1.016	0.542	-1.34	-26.0	-18.9	7.0	51'098
4167	2291.50	0.391	1.095	0.628	-1.36	-31.4	-21.0	10.4	51'303
4167	2291.66	0.390	1.092	0.646	-1.34	-29.5	-20.0	9.5	51'312
4175	2295.90	0.352	1.022	0.579	-1.34	-28.5	-17.9	10.6	51'594
4175	2296.04	0.354	1.033	0.593	-1.33	-29.8	-19.7	10.1	51'604
4181	2299.20	0.322	0.968	0.551	-1.16	-40.6	-34.9	5.8	51'805
4181	2299.35	0.322	0.964	0.538	-1.14	-33.5	-27.3	6.2	51'815
4185	2301.40	0.342	0.965	0.537	-1.31	-23.8	-15.4	8.3	51'955
4185	2301.55	0.345	0.983	0.560	-1.22	-24.5	-16.7	7.7	51'965
4187	2302.50	0.338	0.969	0.524	-1.31	-23.7	-14.3	9.4	52'027
4187	2302.64	0.358	0.999	0.558	-1.17	-31.3	-23.9	7.4	52'037
4189	2303.59	0.336	0.984	0.551	-1.18	-41.6	-35.9	5.6	52'101
4189	2303.75	0.336	0.974	0.556	-1.16	-32.9	-26.1	6.8	52'112
4191	2304.70	0.344	0.965	0.586	-1.12	-36.3	-29.1	7.3	52'178
4191	2304.86	0.325	0.976	0.561	-1.26	-27.3	-18.0	9.3	52'188
4193	2305.80	0.340	0.994	0.559	-1.01	-40.6	-34.3	6.3	52'250

Continuation on next page

Data from the NorthGRIP ice core – continuation

Bag	Depth (m)	$\delta^{15}N$ ($^0/_{00}$)	$\delta^{18}O$ ($^0/_{00}$)	$\delta^{17}O$ ($^0/_{00}$)	$\delta^{36}Ar$ ($^0/_{00}$)	$\delta O_2/N_2$ ($^0/_{00}$)	$\delta Ar/N_2$ ($^0/_{00}$)	$\delta Ar/O_2$ ($^0/_{00}$)	Gas Age (yr BP)
4193	2305.95	0.337	0.992	0.559	-1.05	-33.4	-26.5	6.8	52'260
4195	2306.98	0.329	0.938	0.512	-1.31	-30.9	-22.5	8.4	52'323
4195	2307.14	0.330	0.981	0.533	-1.22	-33.8	-26.3	7.5	52'333
4197	2308.00	0.385	1.031	0.577	-1.22	-21.4	-13.1	8.2	52'384
4197	2308.14	0.368	0.999	0.535	-1.33	-21.0	-11.9	9.0	52'393
4203	2311.30	0.382	1.046	0.559	-1.36	-22.3	-13.3	9.0	52'581
4203	2311.44	0.381	1.027	0.554	-1.38	-20.1	-11.4	8.6	52'589
4213	2316.95	0.364	0.991	0.553	-1.22	-28.1	-20.0	8.1	52'892
4221	2321.21	0.385	1.034	0.605	-1.32	-27.0	-19.3	7.5	53'124
4221	2321.35	0.393	1.071	0.611	-1.24	-33.0	-25.3	7.7	53'132
4235	2328.89	0.376	1.058	0.599	-1.40	-25.3	-15.3	10.0	53'558
4235	2329.03	0.366	1.019	0.548	-1.28	-22.2	-13.5	8.7	53'565
4241	2332.20	0.394	1.084	0.637	-1.35	-29.6	-20.3	9.3	53'737
4241	2332.34	0.390	1.060	0.575	-1.42	-24.0	-14.7	9.3	53'744
4249	2336.60	0.420	1.138	0.636	-1.39	-25.1	-16.3	8.7	53'989
4249	2336.74	0.401	1.116	0.619	-1.29	-26.1	-18.2	7.8	53'996
4255	2339.89	0.393	1.105	0.598	-1.55	-12.3	-0.1	12.2	54'161
4255	2340.03	0.402	1.105	0.626	-1.46	-22.4	-13.9	8.5	54'169
4259	2342.01	0.405	1.113	0.576	-1.47	-29.4	-20.8	8.6	54'285
4259	2342.16	0.420	1.116	0.566	-1.65	-24.6	-15.7	8.8	54'293
4263	2344.30	0.393	1.100	0.582	-1.45	-35.3	-28.7	6.6	54'399
4263	2344.44	0.406	1.109	0.606	-1.47	-30.3	-22.9	7.4	54'406
4267	2346.50	0.425	1.198	0.690	-1.30	-28.9	-21.0	7.9	54'518
4267	2346.64	0.406	1.165	0.683	-1.36	-27.5	-19.1	8.4	54'527
4269	2347.60	0.432	1.189	0.630	-1.47	-12.7	-2.6	10.1	54'581
4269	2347.75	0.436	1.179	0.632	-1.56	-11.4	-0.4	11.0	54'590
4273	2349.80	0.441	1.201	0.620	-1.67	-25.1	-15.5	9.6	54'693
4273	2349.95	0.439	1.178	0.586	-1.68	-9.8	0.0	9.9	54'700
4289	2358.53	0.398	1.152	0.658	-1.23	-26.6	-18.2	8.5	55'189
4292	2360.28	0.389	1.088	0.592	-1.36	-16.2	-7.4	8.8	55'356
4294	2361.33	0.417	1.128	0.609	-1.39	-31.4	-23.1	8.3	55'442
4296	2362.52	0.387	1.139	0.682	-1.18	-30.6	-22.4	8.3	55'534
4296	2362.65	0.399	1.133	0.662	-1.20	-30.1	-22.3	7.8	55'545
4298	2363.55	0.397	1.094	0.623	-1.23	-27.5	-19.4	8.2	55'610
4298	2363.69	0.400	1.111	0.627	-1.25	-25.4	-16.4	9.1	55'620
4301	2365.16	0.398	1.088	0.592	-1.45	-28.2	-20.0	8.2	55'718
4304	2366.93	0.389	1.044	0.571	-1.26	-20.0	-12.5	7.5	55'852
4306	2367.94	0.359	1.030	0.575	-1.22	-23.5	-14.9	8.6	55'954
4306	2368.12	0.368	0.989	0.542	-1.33	-20.4	-11.7	8.7	55'975
4308	2369.17	0.336	0.934	0.490	-1.34	-23.1	-15.2	7.9	56'078
4310	2370.38	0.342	0.992	0.561	-1.17	-22.5	-14.1	8.4	56'172
4312	2371.37	0.402	1.105	0.624	-1.35	-20.5	-10.1	10.5	56'233
4314	2372.38	0.426	1.083	0.543	-1.59	-21.3	-12.7	8.5	56'287
4316	2373.51	0.459	1.208	0.683	-1.55	-26.3	-15.6	10.8	56'344
4316	2373.63	0.477	1.223	0.704	-1.60	-22.8	-12.2	10.6	56'350
4318	2374.55	0.466	1.247	0.714	-1.48	-34.3	-23.5	10.9	56'397
4318	2374.70	0.467	1.283	0.751	-1.45	-36.8	-25.3	11.7	56'406
4320	2375.65	0.478	1.261	0.724	-1.38	-28.7	-18.6	10.1	56'456

Continuation on next page

Data from the NorthGRIP ice core – continuation

Bag	Depth (m)	$\delta^{15}N$ ($^0/_{00}$)	$\delta^{18}O$ ($^0/_{00}$)	$\delta^{17}O$ ($^0/_{00}$)	$\delta^{36}Ar$ ($^0/_{00}$)	$\delta O_2/N_2$ ($^0/_{00}$)	$\delta Ar/N_2$ ($^0/_{00}$)	$\delta Ar/O_2$ ($^0/_{00}$)	Gas Age (yr BP)
4320	2375.79	0.485	1.257	0.690	-1.44	-26.6	-16.6	10.0	56'463
4322	2376.81	0.504	1.275	0.656	-1.71	-21.9	-10.3	11.7	56'518
4326	2378.95	0.428	1.167	0.747	-0.92	-42.0	-31.8	10.3	56'672
4326	2379.10	0.436	1.162	0.736	-0.79	-44.5	-35.6	8.9	56'687
4328	2380.16	0.375	1.067	0.628	-1.10	-37.7	-29.3	8.4	56'791
4330	2381.19	0.383	1.079	0.650	-0.99	-36.6	-26.7	10.0	56'893
4334	2383.35	0.342	1.002	0.517	-1.44	-15.0	-2.1	13.0	57'102
4334	2383.49	0.352	1.030	0.550	-1.30	-24.3	-12.9	11.5	57'117
4336	2384.43	0.363	0.991	0.542	-1.30	-10.4	0.6	11.1	57'199
4338	2385.55	0.348	0.992	0.537	-1.00	-22.3	-13.9	8.3	57'289
4338	2385.69	0.372	1.049	0.607	-0.97	-28.5	-20.3	8.3	57'300
4340	2386.65	0.363	1.049	0.610	-1.00	-35.9	-26.9	9.0	57'369
4340	2386.79	0.372	1.040	0.590	-1.11	-33.2	-24.2	9.1	57'379
4342	2387.72	0.409	1.113	0.623	-1.32	-28.8	-18.3	10.5	57'442
4342	2387.88	0.410	1.112	0.649	-1.22	-28.2	-19.2	9.0	57'452
4344	2388.85	0.403	1.109	0.589	-1.43	-25.8	-15.0	10.9	57'515
4344	2388.99	0.391	1.101	0.603	-1.29	-26.5	-16.0	10.6	57'525
4348	2391.27	0.391	1.132	0.659	-1.11	-33.2	-23.7	9.6	57'686
4351	2392.68	0.400	1.141	0.654	-1.21	-31.5	-21.7	9.8	57'795
4354	2394.34	0.392	1.116	0.614	-1.21	-26.1	-16.6	9.5	57'920
4354	2394.48	0.401	1.149	0.649	-1.22	-25.6	-15.5	10.3	57'930
4356	2395.45	0.405	1.154	0.658	-1.17	-28.0	-20.0	8.1	57'994
4356	2395.59	0.398	1.174	0.664	-1.16	-24.6	-16.3	8.5	58'004
4360	2397.65	0.384	1.132	0.633	-1.29	-25.6	-15.8	9.8	58'139
4360	2397.79	0.387	1.114	0.583	-1.51	-16.8	-7.1	9.8	58'148
4362	2398.75	0.403	1.169	0.628	-1.61	-24.0	-11.8	12.4	58'208
4362	2398.90	0.390	1.194	0.633	-1.58	-22.9	-9.9	13.2	58'217
4364	2399.85	0.410	1.213	0.723	-1.22	-34.3	-24.9	9.4	58'277
4364	2399.99	0.413	1.216	0.719	-1.29	-29.4	-19.6	9.8	58'286
4366	2400.96	0.391	1.158	0.597	-1.53	-13.1	-1.7	11.4	58'338
4366	2401.12	0.388	1.144	0.546	-1.65	-14.9	-5.0	9.9	58'346
4368	2402.07	0.404	1.220	0.659	-1.48	-26.2	-16.5	9.7	58'390
4370	2403.16	0.438	1.281	0.707	-1.36	-33.8	-25.5	8.3	58'446
4370	2403.30	0.431	1.269	0.688	-1.26	-34.3	-26.4	7.8	58'455
4372	2404.25	0.416	1.274	0.703	-1.37	-23.5	-12.0	11.6	58'511
4372	2404.39	0.416	1.275	0.704	-1.58	-19.2	-6.3	13.0	58'519
4374	2405.35	0.446	1.329	0.766	-1.33	-27.7	-17.8	10.0	58'575
4374	2405.49	0.447	1.326	0.741	-1.34	-22.8	-12.6	10.3	58'584
4376	2406.47	0.483	1.385	0.773	-1.41	-33.3	-23.6	9.9	58'637
4378	2407.55	0.473	1.441	0.856	-1.13	-38.1	-29.9	8.3	58'694
4378	2407.69	0.475	1.422	0.872	-1.07	-33.7	-25.0	8.8	58'701
4380	2408.65	0.452	1.366	0.747	-1.52	-31.9	-21.4	10.6	58'752
4380	2408.79	0.464	1.356	0.715	-1.57	-35.0	-26.4	8.6	58'761
4382	2409.75	0.472	1.403	0.760	-1.53	-32.7	-23.3	9.4	58'826
4382	2409.90	0.471	1.410	0.758	-1.50	-26.8	-17.4	9.5	58'837
4384	2410.85	0.425	1.338	0.750	-1.22	-34.3	-25.8	8.6	58'906
4384	2410.99	0.424	1.318	0.735	-1.35	-33.8	-25.7	8.1	58'916
4386	2411.87	0.407	1.293	0.694	-1.41	-29.5	-20.4	9.2	58'971

Continuation on next page

Data from the NorthGRIP ice core – continuation

Bag	Depth (m)	$\delta^{15}N$ ($^0/_{00}$)	$\delta^{18}O$ ($^0/_{00}$)	$\delta^{17}O$ ($^0/_{00}$)	$\delta^{36}Ar$ ($^0/_{00}$)	$\delta O_2/N_2$ ($^0/_{00}$)	$\delta Ar/N_2$ ($^0/_{00}$)	$\delta Ar/O_2$ ($^0/_{00}$)	Gas Age (yr BP)
4388	2413.05	0.497	1.458	0.814	-1.50	-25.8	-16.2	9.7	59'048
4388	2413.19	0.486	1.444	0.799	-1.40	-26.4	-18.3	8.2	59'058
4390	2414.15	0.381	1.287	0.674	-1.46	-18.6	-6.8	11.8	59'137
4390	2414.29	0.406	1.361	0.701	-1.37	-27.6	-15.8	11.9	59'150
4392	2415.22	0.374	1.302	0.721	-1.20	-24.7	-14.5	10.3	59'239
4392	2415.38	0.372	1.312	0.752	-1.15	-29.2	-19.8	9.4	59'255
4394	2416.35	0.366	1.318	0.797	-0.96	-38.6	-30.6	8.0	59'349
4394	2416.50	0.378	1.334	0.785	-1.01	-34.0	-26.2	7.8	59'363
4396	2417.45	0.421	1.397	0.778	-1.41	-43.7	-34.0	9.8	59'430
4396	2417.60	0.423	1.371	0.745	-1.38	-41.4	-33.5	7.9	59'438
4398	2418.55	0.455	1.465	0.803	-1.26	-33.5	-25.3	8.3	59'483
4398	2418.70	0.454	1.477	0.803	-1.24	-30.7	-22.2	8.6	59'489
4400	2419.65	0.455	1.486	0.803	-1.35	-32.7	-23.8	8.9	59'527
4400	2419.79	0.448	1.442	0.770	-1.45	-27.7	-19.3	8.5	59'533
4401	2420.23	0.498	1.556	0.867	-1.47	-29.0	-18.5	10.6	59'553
4404	2421.85	0.434	1.476	0.826	-1.26	-36.4	-27.5	9.0	59'641
4404	2422.00	0.439	1.500	0.832	-1.31	-32.2	-22.6	9.7	59'650
4406	2422.95	0.502	1.605	0.900	-1.52	-36.7	-27.0	9.8	59'702
4406	2423.09	0.514	1.597	0.876	-1.57	-43.3	-34.3	9.0	59'709
4408	2424.05	0.505	1.628	0.895	-1.58	-24.8	-14.8	10.1	59'756
4408	2424.20	0.509	1.610	0.873	-1.66	-24.1	-14.0	10.2	59'763
4410	2425.15	0.493	1.612	0.880	-1.52	-25.7	-16.1	9.7	59'812
4410	2425.29	0.509	1.603	0.877	-1.51	-24.3	-15.0	9.4	59'820
4412	2426.25	0.403	1.467	0.803	-1.30	-21.8	-12.6	9.2	59'877
4412	2426.40	0.405	1.466	0.776	-1.52	-10.4	0.4	10.8	59'887
4414	2427.35	0.446	1.528	0.844	-1.48	-22.4	-11.8	10.7	59'945
4414	2427.49	0.436	1.535	0.865	-1.31	-27.6	-16.9	10.8	59'954
4416	2428.45	0.408	1.476	0.780	-1.41	-30.5	-22.3	8.2	60'007
4416	2428.60	0.410	1.455	0.744	-1.54	-21.5	-14.0	7.5	60'014
4418	2429.53	0.450	1.589	0.863	-1.53	-31.6	-21.2	10.6	60'059
4418	2429.71	0.459	1.621	0.902	-1.43	-28.0	-18.2	9.9	60'068
4420	2430.64	0.571	1.761	0.970	-1.71	-35.7	-24.0	11.8	60'112
4420	2430.76	0.575	1.770	0.951	-1.71	-32.8	-22.6	10.3	60'120
4422	2431.75	0.534	1.700	0.908	-1.79	-17.9	-6.6	11.3	60'179
4422	2431.90	0.519	1.663	0.882	-1.87	-12.6	-1.5	11.1	60'189
4424	2432.85	0.436	1.550	0.824	-1.53	-21.0	-12.2	8.9	60'263
4424	2432.99	0.452	1.571	0.801	-1.69	-16.5	-7.0	9.6	60'275
4426	2433.94	0.435	1.562	0.828	-1.43	-25.5	-16.1	9.5	60'359
4426	2434.07	0.428	1.573	0.822	-1.32	-28.4	-20.4	8.0	60'370
4428	2435.08	0.431	1.576	0.883	-1.17	-31.4	-21.1	10.4	60'462
4428	2435.20	0.441	1.605	0.897	-1.23	-23.3	-13.8	9.5	60'474
4431	2436.69	0.426	1.620	0.926	-1.26	-39.7	-30.1	9.9	60'616
4431	2436.81	0.418	1.576	0.872	-1.33	-33.4	-24.4	9.4	60'628
4434	2438.25	0.443	1.630	0.927	-1.32	-30.0	-19.3	10.8	60'767
4434	2438.39	0.425	1.598	0.881	-1.32	-23.7	-12.8	10.9	60'782
4438	2440.55	0.454	1.582	0.811	-1.59	-20.6	-10.4	10.2	60'983
4438	2440.69	0.455	1.591	0.840	-1.51	-23.3	-14.8	8.6	60'996
4444	2443.73	0.450	1.587	0.837	-1.55	-24.8	-14.0	10.7	61'286
Continuation on next page									

Data from the NorthGRIP ice core – continuation

Bag	Depth (m)	$\delta^{15}N$ ($^0/_{00}$)	$\delta^{18}O$ ($^0/_{00}$)	$\delta^{17}O$ ($^0/_{00}$)	$\delta^{36}Ar$ ($^0/_{00}$)	$\delta O_2/N_2$ ($^0/_{00}$)	$\delta Ar/N_2$ ($^0/_{00}$)	$\delta Ar/O_2$ ($^0/_{00}$)	Gas Age (yr BP)
4444	2443.85	0.442	1.588	0.849	-1.49	-20.9	-10.2	10.7	61'298
4450	2447.15	0.451	1.592	0.880	-1.42	-31.0	-22.1	9.0	61'635
4450	2447.30	0.435	1.562	0.872	-1.40	-22.1	-13.9	8.2	61'651
4454	2449.35	0.436	1.584	0.860	-1.45	-14.5	-5.0	9.5	61'870
4454	2449.49	0.429	1.541	0.842	-1.40	-17.9	-9.8	8.1	61'886
4456	2450.34	0.418	1.547	0.855	-1.36	-20.9	-12.1	8.8	61'973
4456	2450.46	0.431	1.543	0.854	-1.31	-17.7	-9.6	8.1	61'986
4460	2452.68	0.411	1.504	0.765	-1.52	-25.7	-19.2	6.6	62'205
4464	2454.96	0.419	1.531	0.846	-1.40	-23.8	-15.2	8.7	62'440
4468	2457.21	0.416	1.506	0.842	-1.42	-24.3	-16.3	8.1	62'676
4472	2459.25	0.407	1.512	0.820	-1.32	-23.4	-15.8	7.6	62'912
4472	2459.40	0.399	1.472	0.781	-1.44	-22.5	-14.8	7.7	62'930
4474	2460.35	0.437	1.541	0.832	-1.35	-28.0	-19.9	8.1	63'066
4474	2460.49	0.427	1.527	0.812	-1.39	-17.2	-8.9	8.4	63'089
4478	2462.55	0.436	1.516	0.801	-1.51	-16.0	-6.9	9.1	63'408
4478	2462.69	0.431	1.510	0.843	-1.41	-22.2	-14.0	8.2	63'428
4480	2463.83	0.410	1.498	0.815	-1.36	-25.4	-18.3	7.3	63'559

A.2   NorthGRIP Firn Ice Core (NGRIP2001S-4)

Triplicate measurement (A–C) of the bag 175 and bag 177 of the NorthGrip firn ice core (NGRIP2001S-4). All measurements are expressed against atmospheric air. The data is published. For details see section 3.2. The measurements are performed with the new improved on-line system (section 3.2). The maximal data resolution is about 3 cm. The measurements presented in this table are averages over 15 cm.

Bag	Depth (m)	$\delta^{15}N$ ($^0/_{00}$)	$\delta^{18}O$ ($^0/_{00}$)	$\delta^{17}O$ ($^0/_{00}$)	$\delta^{36}Ar$ ($^0/_{00}$)	$\delta O_2/N_2$ ($^0/_{00}$)	$\delta Ar/N_2$ ($^0/_{00}$)	$\delta Ar/O_2$ ($^0/_{00}$)
175 A	95.80	0.314	0.679	0.334	-1.15	-21.0	-12.5	8.4
175 A	95.95	0.303	0.638	0.295	-1.12	-15.9	-9.6	6.3
175 A	96.10	0.303	0.640	0.288	-1.19	-6.1	0.2	6.2
175 A	96.20	0.318	0.687	0.327	-1.01	-17.9	-9.4	8.4
175 B	95.80	0.327	0.739	0.434	-0.96	-20.0	-12.1	7.9
175 B	95.95	0.315	0.688	0.375	-0.97	-15.7	-9.7	6.0
175 B	96.10	0.318	0.692	0.393	-1.02	-14.9	-9.2	5.5
175 B	96.20	0.320	0.752	0.428	-0.93	-22.4	-13.9	8.5
175 C	95.80	0.303	0.659	0.362	-0.87	-23.8	-17.6	6.2
175 C	95.95	0.300	0.654	0.343	-0.84	-21.9	-16.4	5.4
175 C	96.10	0.311	0.684	0.371	-0.90	-22.4	-16.9	5.3
175 C	96.20	0.306	0.725	0.411	-0.87	-30.1	-22.0	8.0
177 A	96.90	0.290	0.622	0.302	-0.95	-18.0	-12.1	5.8
177 A	97.05	0.305	0.653	0.323	-0.95	-14.9	-9.6	5.2
177 A	97.20	0.301	0.652	0.346	-0.93	-19.6	-14.0	5.5
177 A	97.30	0.296	0.629	0.300	-1.00	-19.3	-14.5	4.8
177 B	96.90	0.290	0.660	0.363	-0.94	-22.8	-17.5	5.2
177 B	97.05	0.295	0.649	0.355	-0.88	-21.9	-17.8	3.9
177 B	97.20	0.295	0.684	0.424	-0.89	-27.8	-22.4	5.2
177 B	97.30	0.298	0.681	0.383	-0.88	-23.7	-18.6	5.0
177 C	96.90	0.299	0.636	0.325	-0.97	-22.4	-16.3	5.9
177 C	97.05	0.313	0.636	0.312	-1.03	-21.3	-16.3	4.9
177 C	97.20	0.300	0.652	0.328	-1.06	-20.9	-14.7	6.0
177 C	97.30	0.308	0.644	0.337	-1.04	-21.0	-15.7	5.2

A.3 Greenland Ice Core Project (GRIP)

On-line air measurements performed on the Greenland Ice Core Project (GRIP) ice core. All measurements are expressed against atmospheric air. Bag 2361–2509 cover the 8'200 year event (Figure 3.7), whereas bag 4646–4664 cover DO-event 19 (Figure 3.6). The data is published. For details see section 3.2. Note that measurements of bag 242–2080 are not performed with the latest version of the on-line system (section 3.1). Hence, these measurements can be slightly offset due to a different dissolution fractionation of standard and sample. The rest of the measurements are performed with the improved on-line system (section 3.2). The maximal data resolution is about 3 cm. In this table only the measurements averages are listed.

Bag	Depth (m) Top – Bottom	$\delta^{15}N$ ($^0/_{00}$)	$\delta^{18}O$ ($^0/_{00}$)	$\delta^{17}O$ ($^0/_{00}$)	$\delta^{36}Ar$ ($^0/_{00}$)	$\delta O_2/N_2$ ($^0/_{00}$)	$\delta Ar/N_2$ ($^0/_{00}$)	$\delta Ar/O_2$ ($^0/_{00}$)
242	132.63 – 133.03	0.275	0.649	0.342	-0.81	-19.3	-11.4	6.8
282	154.63 – 155.03	0.306	0.545	0.351	-0.86	-28.4	-22.4	6.2
1357	745.94 – 746.22	0.272	0.441	0.283	-1.31	-12.8	-12.7	1.3
1847	1015.32 – 1015.53	0.314	0.413	0.205	-0.84	-3.1	-2.4	0.5
2080	1143.67 – 1143.98	0.328	0.440	0.249	-1.25	-15.1	4.7	20.9
2361	1298.03 – 1298.52	0.306	0.421	0.190	-1.26	-9.4	0.9	10.4
2379	1307.92 – 1308.43	0.281	0.428	0.235	-0.96	-13.5	-2.4	11.6
2429	1335.51 – 1335.88	0.303	0.493	0.288	-0.89	-10.0	-3.8	6.2
2465	1355.31 – 1355.67	0.228	0.284	0.166	-0.58	-5.2	-6.0	-0.9
2473	1359.72 – 1360.03	0.340	0.434	0.201	-1.16	-6.0	-0.6	5.1
2485	1366.33 – 1366.59	0.304	0.521	0.253	-1.24	-7.3	4.5	11.8
2509	1379.47 – 1379.80	0.290	0.466	0.203	-1.00	-1.9	1.2	3.1
4646	2554.89 – 2555.20	0.446	1.592	0.857	-1.76	-16.6	0.8	17.5
4652	2558.11 – 2558.58	0.449	1.650	0.938	-1.71	-28.0	-8.9	19.5
4655	2559.80 – 2560.03	0.486	1.700	0.923	-1.81	-26.2	-7.0	19.4
4657	2561.10 – 2561.32	0.527	1.769	0.966	-1.97	-27.3	-6.4	21.2
4664	2564.78 – 2565.14	0.373	1.351	0.780	-1.43	-19.3	-4.0	15.4

A.4   Dye-3 Ice Core, Greenland

Triplicate (I–III) measurement of bag 160 of the Dye-3 ice core. 160 A corresponds to the top 50 cm and 160 B the bottom 50 cm of the bag. All measurements are expressed against atmospheric air. The data is published. For details see section 3.2. The measurements are performed with the new improved on-line system (section 3.2). The maximal data resolution is about 3 cm. The measurements presented in this table are averages over 10 cm.

Bag	Depth (m)	$\delta^{15}N$ ($^0/_{00}$)	$\delta^{18}O$ ($^0/_{00}$)	$\delta^{17}O$ ($^0/_{00}$)	$\delta^{36}Ar$ ($^0/_{00}$)	$\delta O_2/N_2$ ($^0/_{00}$)	$\delta Ar/N_2$ ($^0/_{00}$)	$\delta Ar/O_2$ ($^0/_{00}$)
160 A I	159.07	0.242	0.506	0.223	-0.72	-15.2	-11.3	3.9
160 A I	159.17	0.243	0.546	0.280	-0.82	-19.4	-14.5	4.8
160 A I	159.27	0.288	0.537	0.204	-1.00	-14.5	-13.1	1.3
160 A I	159.37	0.276	0.463	0.125	-1.02	-20.1	-18.3	1.9
160 A II	159.07	0.161	0.357	0.132	-0.93	10.5	11.7	1.2
160 A II	159.18	0.233	0.466	0.141	-1.62	-0.9	3.5	3.8
160 A II	159.28	0.252	0.518	0.211	-1.22	-7.0	-1.7	5.3
160 A II	159.37	0.240	0.493	0.233	-0.99	-10.5	-4.9	5.6
160 A III	159.08	0.249	0.734	0.438	-0.81	-33.4	-17.4	16.8
160 A III	159.18	0.349	0.766	0.315	-1.46	-21.9	0.2	23.4
160 A III	159.28	0.327	0.700	0.337	-1.17	-29.2	-17.0	13.0
160 A III	159.37	0.274	0.520	0.211	-1.12	-26.7	-23.3	3.3
160 B I	159.52	0.218	0.460	0.185	-0.71	-15.2	-9.8	5.4
160 B I	159.62	0.232	0.435	0.178	-0.74	-5.0	-3.0	2.1
160 B I	159.72	0.244	0.483	0.208	-0.79	-6.9	-3.4	3.6
160 B I	159.82	0.262	0.599	0.304	-0.89	-18.0	-11.3	6.7
160 B II	159.52	0.229	0.460	0.217	-0.80	-15.9	-12.6	3.4
160 B II	159.62	0.238	0.463	0.204	-0.92	-10.7	-8.2	2.5
160 B II	159.72	0.243	0.497	0.230	-0.91	-15.1	-11.2	3.9
160 B II	159.82	0.278	0.572	0.250	-0.93	-17.5	-14.1	3.4
160 B III	159.52	0.209	0.512	0.254	-0.80	-10.2	-3.8	6.4
160 B III	159.62	0.207	0.462	0.206	-0.86	-6.0	-1.6	4.5
160 B III	159.72	0.220	0.652	0.337	-1.17	5.2	24.0	19.1
160 B III	159.82	0.280	0.672	0.313	-1.13	-21.2	-10.4	11.2

A.5   EPICA Dome Concordia Ice Core (EDC-96), Antarctica

On-line air measurements performed on the Dome Concordia (Dome C) EDC-96 ice core drilled in the framework of the European Project for Ice Coring in Antarctica (EPICA). All measurements are expressed against atmospheric air. The $\delta^{18}O_{atm}$ data is published (section 3.2). Note that the measurements are performed with the unimproved version of on-line system (section 3.1). Hence, the data can be slightly offset due to a different dissolution fractionation of standard and sample. The maximal data resolution is about 3 cm. In this table only the measurements averages are listed.

Bag	Depth (m) Top – Bottom	$\delta^{15}N$ ($^0/_{00}$)	$\delta^{18}O$ ($^0/_{00}$)	$\delta^{17}O$ ($^0/_{00}$)	$\delta^{36}Ar$ ($^0/_{00}$)	$\delta O_2/N_2$ ($^0/_{00}$)	$\delta Ar/N_2$ ($^0/_{00}$)	$\delta Ar/O_2$ ($^0/_{00}$)
241	132.16 – 132.43	0.490	0.998	0.486	-1.88	-18.0	-4.9	13.4
338	185.50 – 185.61	0.449	0.740	0.365	-1.49	-32.3	-5.9	27.0
516	283.37 – 283.56	0.485	0.746	0.336	-1.67	-28.1	-15.9	12.7
710	390.11 – 390.30	0.477	1.365	0.663	-1.71	-23.5	-8.8	15.2
816	448.41 – 448.64	0.421	1.709	0.894	-1.35	-27.0	-15.8	12.0
1921	1056.02 – 1056.35	0.406	1.653	0.863	-1.59	-14.2	2.1	16.5

A.6   EPICA Dronning Maud Land Ice Core (DML), Antarctica

Measurements performed on the Dronning Maud Land (DML) ice core drilled in the framework of the European Project for Ice Coring in Antarctica (EPICA). All measurements are expressed against atmospheric air. Bag 543 is measured in duplicate (A–B). The data of bag 543 is published (section 3.2). The measurements are performed with the new improved on-line system (section 3.2). The maximal data resolution is about 3 cm. The measurements presented in this table are averages over 10 cm.

Bag	Depth (m)	$\delta^{15}N$ ($^0/_{00}$)	$\delta^{18}O$ ($^0/_{00}$)	$\delta^{17}O$ ($^0/_{00}$)	$\delta^{36}Ar$ ($^0/_{00}$)	$\delta O_2/N_2$ ($^0/_{00}$)	$\delta Ar/N_2$ ($^0/_{00}$)	$\delta Ar/O_2$ ($^0/_{00}$)
485	484.37	0.381	0.498	0.169	-1.54	-7.2	4.0	11.4
485	484.47	0.392	0.493	0.182	-1.57	-7.5	2.5	10.2
485	484.57	0.379	0.499	0.245	-1.53	-14.4	-4.1	10.4
543 A	542.34	0.370	0.547	0.300	-1.18	-28.2	-21.9	6.3
543 A	542.44	0.423	0.652	0.350	-1.29	-18.7	-9.5	9.2
543 A	542.54	0.368	0.561	0.342	-1.14	-32.2	-23.9	8.3
543 A	542.61	0.379	0.536	0.300	-1.45	-52.4	-46.0	6.3
543 B	542.34	0.373	0.604	0.328	-1.159	-45.1	-38.6	6.4
543 B	542.44	0.336	0.503	0.272	-1.276	-33.2	-25.4	7.8
543 B	542.54	0.352	0.527	0.281	-1.473	-45.6	-39.0	6.6
543 B	542.61	0.367	0.569	0.338	-1.183	-42.5	-34.7	7.8

Publications

Articles published in reviewed journals

- Huber, C., and M. Leuenberger, Measurements of Isotope and Elemental Ratios of Air from Polar Ice with a New On-Line Extraction Method, *Geochemistry Geophysics Geosystems*, **in press 2004**

- NorthGRIP Members. High resolution Climate Record of the Northern Hemisphere reaching into the last Glacial Interglacial Period. *Nature*, 431, 147–151 **2004**

- Huber, C., M. Leuenberger, and O. Zumbrunnen, Continuous extraction of trapped air from bubble ice or water for on-line determination of isotope ratios, *Analytical Chemistry*, 75(10), 2324–2332, **2003**

- Huber, C., and M. Leuenberger, Fast high-precision on-line determination of hydrogen isotope ratios of water or ice by continuous-flow isotope ratio mass spectrometry, *Rapid Communications in Mass Spectrometry*, 17, 1319–1325, **2003**

- Leuenberger, M., and C. Huber, On-line determination of oxygen isotope ratios of water or ice by mass spectrometry, *Analytical Chemistry*, 74(18), 4611–4617 **2002**

- Leuenberger, M., P. Nyfeler, H.P. Moret, P. Sturm, and C. Huber, New gas inlet system for an isotope ratio mass spectrometer improves reproducibility, *Rapid Communications in Mass Spectrometry*, 14, 1552–1557, **2000**

Articles submitted to reviewed journals

- Huber, C., M. Leuenberger, R. Spahni, J. Flückiger, J. Schwander, T.F. Stocker, S.J. Johnsen, A. Landais, and J. Jouzel, Isotope Calibrated Greenland Temperature Record over Marine Isotope Stage 3 and its Relation to CH_4, *Nature*, **submitted 2004**

- Huber, C., U. Beyerle, M. Leuenberger, J. Schwander, R. Kipfer, R. Spahni, J. Severinghaus, and K. Weiler, Evidence for gas fractionation in firn air derived from noble gases, oxygen, and nitrogen measurements, *Earth and Planetary Science Letters* **submitted 2004**

- Landais, A., J.M. Barnola, V. Masson-Delmotte, J. Jouzel, J. Chappellaz, N. Caillon, C. Huber, M. Leuenberger, and S.J. Johnsen, A continuous record of temperature evolution over a whole sequence of Dansgaard-Oeschger during Marine Isotope Stage 4 (76 to 62 kyr BP), *Geophysical Research Letters*, **submitted 2004**

- Landais, A., V. Masson-Delmotte, J. Jouzel, D. Raynaud, S.J. Johnsen, C. Huber, M. Leuenberger, J. Schwander, and B. Minister, The glacial inception recorded in the NorthGRIP Greenland ice core: information from air isotopic measurements, *Climate Dynamics*, **submitted 2004**

Others

- Huber, C., and M. Leuenberger, Von der Idee zum Patent, *Uni Press: Forschung und Wissenschaft an der Universität Bern*, 121,30–32, **2004**

- Huber, C., Methoden zur kontinuierlichen massenspektrometrischen Messung von Isotopenverhältnissen an Luft, Wasser und Eisbohrkernen, Diploma thesis, *Philosophisch-naturwissenschaftlichen Fakultät der Universität Bern*, **2001**

Patent Applications

- Huber, C., and M. Leuenberger, Verfahren und Vorrichtung zur Bereitstellung einer gasförmigen Substanz für die Analyse von chemischen Elementen oder Verbindungen, *Offenlegungsschrift des Deutschen Patent- und Markenamtes*, DE 102 56 009 A1, **16.04.2002**

- Huber, C., and M. Leuenberger, Process and apparatus for providing a gaseous substance for the analysis of chemical elements or compounds, *United States Patent Application Publication*, US 2003/0228708 A1, **16.04.2003**

- Huber, C., and M. Leuenberger, Process and apparatus for providing a gaseous substance for the analysis of chemical elements or compounds, *UK Patent Application*, GB 2 389 903 A, **16.04.2003**

Acknowledgements

I had a very fruitful and enjoyable time at the Climate and Environmental Physics division (KUP) during the last 5 years. This is the merit of a lot of people at the KUP and elsewhere. Special thanks go to Markus Leuenberger, who was an excellent supervisor of my thesis. He offered me the time and the freedom which are essential for the development of new ideas. He was always open to discuss arising problems and supplied a lot of good ideas.

Many thanks to...

...Thomas Stocker - *thesis supervisor and head of the KUP*

...Markus Leuenberger, Peter Nyfeler, Patrick Sturm, Marc Eyer, Marc Filot, Francesco Valentino, Oliver Zumbrunnen, Lukas Lanz, and Clemens Lang - *the Isotope Team*

...Jacqueline Flückiger, Jakob Schwander, Renato Spahni, Karin Weiler, and Gregor Hausammann - *firn model and methane specialists of the A66 office*

...Doris Rätz - sectretary and administration

...Urs Beyerle, Reto Knutti, and Stefan Zoller - *computer and LaTeX support*

...Hanspeter Moret, Hans Riesen, Ivan Schärmeli, Kurt Grossenbacher, and Heiri Rufli - *workshop and electronic lab*

...Bernhard Stauffer, Eric Monnin, Matthias Bigler, Urs Siegenthaler, Thomas Blunier, Manuel Hutterli, Kaspar Plattner, Grégoire Floch, Stefan Gerber, Fortunat Joos, Regine Rötlisberger, Kenjji Kawamura, Simon Müller, Fabrice Lambert, Patrick Kaufmann, Christoph Raible, Manuel Renold, Bernhard Lehmann, José Corcho, Stefan Sommer, Rene Fischer, Thomas Wagner, André Dällenbach, Andreas Indermühle, Roland Purtschert, Mark Siddall, and the rest of the KUP - *discussions, coffee break, skiing days, excursions, apéro's*

...Amaelle Landais, Jean Jouzel, Sigfus Jonsen, Jeff Severinghaus, Gabrielle Dreyfus, Jérôme Chappellaz, Jean-Marc Barnola, Sophie Bernard, Luke Skinner, and Anita Scheiwiller - *external support*

Curriculum vitæ

Christof Huber, born in Bern, March 5. 1972

Education

1978-1983:	Primary school, Intragna (TI) and Bern
1983-1988:	Secondary school, Bern
1988-1992:	Apprenticeship in Engineering Mechanics, LWB Bern
1992-1995:	Studies in Mechanical Engineering at the School of Engineering and Architecture of Biel
1995:	Diploma in Mechanical Engineering (dipl. Ingenieur HTL)
1996-2001:	Studies in Physics at the University of Bern. Subsidiary subjects: Mathematics and Informatics.
2001:	Diploma at the research division of Climate and Environmental Physics,Physics Institute, University of Bern
2001-2004:	Ph.D. thesis at the research division of Climate and Environmental Physics, Physics Institute, University of Bern

Conference and summer school attendances

EGS XXVI General Assembly, Nice, 2002

Swiss Polar Research Summer School, Riederalp, 2002

EURESCO Conference , San Feliu de Guixols, 2003

AGU Fall Meeting, San Francisco, 2003

EGU General Assembly, Nice, 2004

JESIUM (Joint European Stable Isotope User Group Meeting), Vienna, 2004

Awards

Winner of the 2nd price of the DC Bank price for resarch and innovation, 2002

Winner of the "Isotopenpreis" donated by the Dr.-Karleugen-Habfast-Foundation, 2004